# Design of Improved Carbon Capture Solvents Using Molecular Simulation

by

Javad Noroozi

A thesis
presented to the University of Waterloo
in fulfillment of the
thesis requirement for the degree of
Doctor of Philosophy
in
Chemical Engineering

Waterloo, Ontario, Canada, 2021

**Examining Committee Membership**

The following served on the Examining Committee for this thesis. The decision of the Examining Committee is by majority vote.

| | |
|---|---|
| External Examiner: | Hans Hasse<br>Professor, Dept. of Mechanical and Process Engineering<br>University of Kaiserslautern, Germany |
| Supervisors: | William R. Smith<br>Professor, Department of Mathematics and Statistics<br>University of Guelph<br>Adjunct Professor, Department of Chemical Engineering<br>University of Waterloo |
| | Nasser Mohieddin Abukhdeir<br>Associate Professor, Dept. of Chemical Engineering<br>University of Waterloo |
| Internal Member: | Luis Ricardez Sandoval<br>Associate Professor, Dept. of Chemical Engineering<br>University of Waterloo |
| Internal Member: | Mark Pritzker<br>Professor, Dept. of Chemical Engineering<br>University of Waterloo |
| Internal-External Member: | Pierre-Nicholas Roy<br>Professor, Dept. of Chemistry, University of Waterloo |

## Author's Declaration

I hereby declare that I am the sole author of this thesis and this thesis consists of material all of which I authored. I have designed the computational framework, implemented and performed the calculations and analysed the data. I wrote the initial versions of the manuscripts and Prof. William R. Smith provided continual support and guidance throughout this work and contributed to the final manuscripts and editorial comments and corrections.

I understand that my thesis may be made electronically available to the public.

## Abstract

Study of the equilibrium compositions of complex chemically reacting systems by means of experimental measurements and thermodynamic modeling tools is of great interest and importance in chemistry, biology, and chemical engineering. Systems involving ionic species (especially aqueous electrolyte systems) are of particular significance and have long been studied using these approaches, but their modeling by means of molecular-based methodology is in its relative infancy. Carbon capture and storage (CCS) technology using post–combustion $CO_2$ capture (PCC) by reactive absorption with aqueous alkanolamine solvents is currently considered to be one of the most mature technologies to reduce greenhouse gas emissions by $CO_2$ capture from point sources. The discovery of more economically effective solvents is crucial to encourage its future deployment. Such systems usually involve a mixture of electrolyte species coexisting in an aqueous solution, an important aspect of which is their simultaneous chemical and phase equilibrium properties.

In this thesis, we develop a general predictive (requiring no experimental data) and computationally efficient molecular-based simulation framework for calculating these properties. The framework is based on an exact translation of molecular simulation methodology to the standard-state quantities of a conventional macroscopic electrolyte solution thermodynamic model. Its most important properties are the reaction equilibrium constants, $p$K, formed by linear combinations of the species standard–state chemical potentials, $\mu_i^\dagger(T,P)$. We calculate these quantities by a combination of *ab initio* electronic structure calculations using high–level composite methods in the gas phase and alchemical solvation free energy simulations using the General Amber Force Field (GAFF) employing thermodynamic integration in the solution phase. The resulting nonlinear equations of the thermodynamic model are then solved to predict the speciation and the $CO_2$ partial pressure, $P_{CO_2}$ in equilibrium with the solution. We also calculate the temperature dependence of the reaction $p$K values, allowing us to obtain the reaction standard heat values. Furthermore, the methodology also permits the calculation of species with very small solution concentrations, far exceeding the capability of existing experimental methodologies. Overall, we report results for 77 alkanolamines of interest to the PCC process.

We initially demonstrate the application of our framework to the reactive absorption of $CO_2$ in aqueous monoethanolamine (MEA) solvent as the well–studied "benchmark case", the first time that a quantitatively accurate predictive approach requiring no experimental data has been successfully applied to calculate all solution species concentrations and $P_{CO_2}$ for this system. Such systems typically involve small ions such as hydroxide ($OH^-$), hydronium ($H_3O^+$), carbonate ($CO_3^{-2}$) and bicarbonate ion ($HCO_3^-$) are challenging to model using classical force fields, due to their relatively high electron density. In a separate study,

we propose an approach to eliminate the need for simulation of such ions by combining an appropriate choice of the underlying system reactions with well–known experimental data for the binary $CO_2$-$H_2O$ system. We apply this approach to 7 primary and secondary amines, including MEA and observe significant improvement in both quantitative and qualitative agreement with experiment of the speciation and $P_{CO_2}$.

For amine solvent selection, an important property is its protonation reaction equilibrium constant, often referred to as its acidity, ($p\mathrm{K}_a$), and its temperature dependence. We assess the accuracy of our framework by focusing on $p\mathrm{K}_a$ calculations at 298.15K and its integration with a commonly recommended theoretical value of the hydrogen ion ($H^+$) hydration free energy. We find that the GAFF with AM1-BCC atomic charges is able to predict $p\mathrm{K}_a$ values for a set of 29 amines with absolute average deviation (AAD) of $\approx 0.73$ $p\mathrm{K}_a$ units, out–performing the commonly used universal solvation model based on solute electron density (SMD). To obviate the need for the ($H^+$) hydration free energy, we develop a classical force field for the hydronium ion ($H_3O^+$) based solely on the MEA $p\mathrm{K}_a$ at 298.15 K. We then use this force field to predict $p\mathrm{K}_a$ of a large set of 77 amines at 298.15K with an AAD with respect to experimental data identical to that of our previous study. Furthermore, using the derived $H_3O^+$ force field, we are able to predict the intrinsic proton hydration free energy as a function of temperature, which has previously only been available at 298.15 K. We also report a temperature–dependent function for the $p\mathrm{K}_a$ of all 77 amines.

Use of the $H_3O^+$ force field also allows us to take advantage of the iso–coulombic form of the protonation reaction to obtain improved predictions of the temperature dependence of $p\mathrm{K}_a$, which further leads to improved its protonation reaction enthalpy ($\Delta H^{prot}$) predictions. We find our prediction of the latter quantify to be in reasonable agreement with available experimental data, and provide evidence that the precision of the results arising from our predictive framework is comparable to or better than that of existing experimental methodologies for obtaining $\Delta H^{prot}$.

The reversion of carbamate ion ($RNHCO_2^-$) into bicarbonate ion is another major reaction in primary and secondary aqueous alkanolamine solvents. The equilibrium constant ($p\mathrm{K}_c$) of this reaction is extremely difficult to measure experimentally, due to the often extremely small species concentrations and the presence of proton exchanging pairs in solution, both of which are challenging for convectional NMR spectroscopic studies. In this thesis, we identify strongly bicarbonate forming amines, and calculate the temperature dependence of $p\mathrm{K}_c$ and its standard heat of reaction, $\Delta H^{carb}$. While there are significant uncertainties in the experimental $p\mathrm{K}_c$ values, our predictions are in good agreement with the few available measurements, taking into account the mutual simulation and experimental uncertainties. It is important to note that $\Delta H^{carb}$ for most of the species considered

have never been measured experimentally.

We conclude the thesis by indicating several important implications of our work, including predictions of the overall heat duty of the PCC process, extensions to solvent blends and other solvents, the ability to perform rapid solvent screening, and the calculation of individual species $\mu_i^{\dagger}(T, P)$ and corresponding $\overset{\dagger}{i}(T, P)$ standard–state enthalpy values.

**Acknowledgements**

I first thank my primary supervisor, Professor William R. Smith, whose expertise was invaluable in developing and applying the research described in this thesis.

I also express my gratitude to my co-supervisor Prof. Nasser Mohieddin Abukhdeir, who provided a great deal of support and assistance throughout my program, and for his thoughtful comments on this dissertation. I thank the additional members of my examining committee: Prof.Luis Ricardez Sandoval, Prof. Mark Pritzker, Prof. Pierre-Nicholas Roy and Prof. Hans Hasse (University of Kaiserslautern, Germany) for their time and effort in reading my Ph.D. proposal and thesis and for their valuable comments.

I thank my research group members, Dr. Braden D. Kelly, Dr. Weikai Qi, Nayereh Hatefi, Ryan Wilkins, Dr. Jiri Skvara and Leann Tran for stimulating discussions and for the enjoyable experiences during group meetings (when these were possible during pre–covid 19 times).

This work was supported by the Natural Sciences and Engineering Research Council of Canada (NSERC) by the award of International Strategic Partnership Program Grant STPGP 479466 to Professsor Smith. I also thank the grant partners: the Agence Nationale de la Recherche (ANR), and our industrial partner Dr. John Carroll of Gas Liquids Engineering Ltd. for their support of the project. The University of Waterloo Department of Chemical Engineering and the University of Guelph Department of Mathematics and Statistics are acknowledged for their financial and administrative support forduring my program. The SHARCNET (Shared Hierarchical Academic Research Computing Network) HPC consortium and Compute Canada are gratefully acknowledged for providing computational facilities, without which this project would not have been possible.

Finally, my special thanks go to my family, especially my lovely mom, who has been extremely supportive of me throughout my journey.

## Dedication

To my parents, for their endless love, support and encouragement.

# Table of Contents

**List of Figures** xiv

**List of Tables** xvii

**1 Introduction** 1

1.1 General Overview . . . 1
1.2 Motivation . . . 6
1.3 Outline of the Thesis . . . 10

**2 Background** 13

2.1 Statistical Mechanics . . . 13
2.2 Classical Molecular Simulation . . . 14
2.2.1 Force Field . . . 16
2.2.2 Boundary Conditions and Potential Truncation . . . 17
2.3 Molecular Dynamics Simulation . . . 19
2.4 Monte Carlo Simulation . . . 20
2.5 Residual Chemical Potential in Canonical Ensemble ($\mu^{res,NVT}(T,P,\mathbf{x})$) . . . 22
2.6 Ideal Gas Chemical Potential ($\mu_i^0(T,P^0)$) . . . 26
2.7 Chemical Potential Models for Solutions: the General Case . . . 27
2.8 Commonly Used Chemical Potential Models . . . 29
2.9 Translating Between Models . . . 31

2.9.1 $(T, \rho)$ and $(T, P)$ Models . . . 32
2.9.2 Henry $(T, P)$ Model and General $(T, \rho)$ Model . . . 34
2.9.3 Henry $(T, \rho)$ Model and General $(T, \rho)$ Model . . . 35
2.9.4 Henry $(T, P; x)$ Model and General $(T, \rho)$ Model . . . 36

**3 An efficient molecular simulation methodology for chemical reaction equilibria in electrolyte solutions: Application to $CO_2$ reactive absorption. 37**

3.1 Introduction . . . 39
3.2 Reaction Equilibrium Using Henry-Law-Based Chemical Potential Models . 41
3.3 Molecular-Based Calculation of $pK_j$ . . . 43
3.3.1 Relation to Ideal–Gas and Hydration Free Energy Quantities . . . 43
3.3.2 Ideal Gas (IG) Quantities . . . 45
3.4 Systems Studied and Computational Details . . . 46
3.4.1 Force Fields . . . 46
3.4.2 Hydration Free Energies . . . 48
3.4.3 QM Simulations . . . 49
3.5 Results and Discussion . . . 50
3.5.1 Ideal–Gas Quantities . . . 51
3.5.2 Intrinsic Hydration Free Energies . . . 54
3.5.3 $pK$ Values . . . 55
3.5.4 Davies Parameter A . . . 57
3.5.5 Solution Compositions . . . 57
3.5.6 $CO_2$ Partial Pressure . . . 61
3.5.7 Uncertainty Analysis . . . 61
3.6 Discussion . . . 62
3.7 Conclusions and Recommendations . . . 63
3.8 Acknowledgements . . . 64

**4 Accurate Prediction of Speciation in Aqueous Alkanolamine-$CO_2$ System Requiring No Solvent Experimental Data** **65**

4.1 Introduction . . . 67

4.2 Molecular–Based Thermodynamic Methodology . . . 70

4.3 Simulation Details . . . 73

4.3.1 Ideal Gas Reaction Free Energies . . . 73

4.3.2 Force Field Development and Hydration Free Energy Calculations . 73

4.4 Results and Discussion . . . 75

4.4.1 Ideal–Gas Standard Reaction Free Energies . . . 75

4.4.2 Equilibrium Constants $pK_1$ and $pK_2$ . . . 75

4.4.3 Effects of Different Partial Charge Methods on the $pK$ Values . . . 77

4.4.4 Carbamate Stability Constant, $K_2$ . . . 78

4.4.5 Consistency Tests for the Amine Protonation Constants . . . 82

4.4.6 Speciation . . . 83

4.4.7 $CO_2$ Solubility . . . 84

4.5 Effect of Amine Concentration on $CO_2$ Solubility . . . 87

4.6 Uncertainty Analysis . . . 89

4.7 Summary and Conclusions . . . 91

4.8 Acknowledgements . . . 92

**5 Prediction of Alkanolamine pKa Values by Combined Molecular Dynamics Free Energy Simulations and ab Initio Calculations** **93**

5.1 Introduction . . . 94

5.2 Thermodynamic Background . . . 96

5.3 Simulation Details . . . 101

5.3.1 Conformational Search and Ideal Gas Reaction Free Energies . . . 101

5.3.2 Partial Charges and Intrinsic Hydration Free Energy Calculations . 101

5.4 Results and Discussion . . . 102

5.4.1 Intrinsic Hydration Free Energies of Amine Species . . . . . 102
5.4.2 $p\mathrm{K}_a$ Calculations . . . . . 106
5.5 Summary and Recommendations . . . . . 113
5.6 Acknowledgements . . . . . 115

**6 Force–Field–Based Computational Study of the Thermodynamics of a Large Set of Aqueous Alkanolamine Solvents for Post–Combustion $CO_2$ Capture 116**

6.1 Introduction . . . . . 117
6.2 Thermodynamic Background . . . . . 123
6.2.1 Molecular–Based Framework for the Calculation of p$K_a$ and p$K_c$ . . 123
6.2.2 $H_3O^+$ FF Determination and the Proton Hydration Free Energy . . 125
6.3 Computational Details . . . . . 126
6.3.1 Ideal–Gas Reaction Free Energies and Conformational Search . . . 128
6.4 Results and Discussion . . . . . 128
6.4.1 Ideal-Gas Reaction Free Energy Changes, $\Delta G_j^0(T;P^0)$ . . . . . 128
6.4.2 Residual Reaction Free Energy Changes, $\Delta G_j^{\mathrm{res},NVT;\infty}(T,P)$ . . . . 129
6.4.3 Deprotonation Constant, p$K_a$ . . . . . 131
6.4.4 Temperature Dependence of p$K_a$ and the Deprotonation Standard Reaction Enthalpy . . . . . 134
6.4.5 Carbamate Reversion Constant, (p$K_c$) . . . . . 141
6.4.6 Effect of Structural Features on Carbamate Reversion . . . . . 143
6.4.7 Temperature Dependence of p$K_c$ and the Carbamate Reversion Standard Reaction Enthalpy ($\Delta H^{carb}$) . . . . . 144
6.4.8 Validation of the $H_3O^+$ Force Field Using its Prediction of the Proton Hydration Free Energy . . . . . 146
6.5 Conclusions and Recommendations for Future Work . . . . . 148

**7 Conclusions and Recommendations 151**

7.1 Summary . . . . . 151
7.2 Recommendations for Future Work . . . . . 153

**References** **156**

**APPENDICES** **187**

**A Supplementary Information for Chapter 3** **188**

A.1 Ideal–Gas Standard Chemical Potentials . . . . . 188

A.2 Force Field Parameters . . . . . 191

**B Supplementary Information for Chapter 4** **201**

**C Supplementary Information for Chapter 5** **213**

**D Supplementary Information for Chapter 6** **217**

# List of Figures


1.1 Schematic of $CO_2$ absorption process using aqueous amine solvent . . . . . 2

2.1 Schematics of bonded intermolecular interactions . . . . . 17
2.2 Illustration of periodic boundary condition . . . . . 18
2.3 Simplified flowchart of a typical molecular dynamics simulation . . . . . 20
2.4 Schematic representation of gradual insertion/deletion . . . . . 23

3.1 MP2/aug-cc pVTZ optimized gas phase geometry of ethanolamine, protonated ethanolamine and its carbamate form . . . . . 48
3.2 Mole fractions of the major solution species as a function of $CO_2$ loading, $L$, at the indicated temperatures and $P = 1$ bar for a 30 weight % aqueous MEA solution . . . . . 59
3.3 Partial pressure of $CO_2$ above the solution as a function of loading, $L$, at the indicated temperatures and $P = 1$ bar for a 30 weight % aqueous MEA solution . . . . . 60

4.1 Molecular structures of the studied alkanolamines . . . . . 70
4.2 Temperature dependence of the equilibrium constants for reactions R1 and R2 for the seven amines studied . . . . . 77
4.3 Speciation predictions (curves) for 30 wt% aqueous MEA and AMP solutions of $CO_2$ at $T = 298.15$ K and $P = 1$ bar, and their comparison with experimental data . . . . . 83
4.4 Speciation predictions (curves) for reactive absorption of $CO_2$ in 30 wt% amine aqueous solutions at $T = 298.15$ K and $P = 1$ bar . . . . . 85

4.5 Comparison of the $CO_2$ partial pressures in 30 weight% MEA, AMP, AMPD and 60% 2–AEE aqueous solutions using the Henry–law–based ideal–solution model . . . 86
4.6 CO2 solubility in 30 wt% and 16 wt% 2-AP . . . 87
4.7 Effect of amine concentration on the $CO_2$ solubility . . . 88
4.8 Uncertainty in the equilibrium compostion and $P_{CO_2}$ in 30 weight % MEA at 313.15 K . . . 90

5.1 Molecular Structures of the 29 alkanolamines investigated in this work . . . 103
5.2 Parity plot comparison of the neutral amine hydration free energies (in $kJ{\cdot}mol^{-1}$) against the corresponding SMD results . . . 105
5.3 Parity plot comparison of the amine cation hydration free energies (in $kJ{\cdot}mol^{-1}$) against the corresponding semi–empirical AM1–BCC results . . . 107
5.4 AM1–BCC calculated versus experimental p$K_a$ values for the 29 alkanolamine species considered in this work . . . 112

6.1 Molecular Structures of the alkanolamines considered in this work. . . . 121
6.2 Molecular Structures of the alkanolamines considered in this work (continued). 122
6.3 Ideal–gas reaction free energy change of the deprotonation reaction and the carbamate reversion reaction . . . 129
6.4 Infinite dilution residual chemical potential of the neutral 4IPB as a function of temperature from five replicate simulations at each temperature . . . 131
6.5 Calculated versus experimental p$K_a$ values for the 77 alkanolamine species considered in this work . . . 132
6.6 Deprotonation constant of MEA, AMP, 1-AP, DEEA as functions of temperature . . . 135
6.7 Deprotonation constant of MAE, 2-DIPA, 2-AP and 3DMA1P as functions of temperature . . . 136
6.8 Deprotonation constant of TBAE, 2-AEE, EAE and TEA as function of temperature . . . 137
6.9 Deprotonation constant of AEPD, AMPD, DEA and SAPD as function of temperature . . . 138

6.10 Deprotonation constant of, MDEA, EDEA, 2PIPM and t-BDEA as function of temperature . . . . . 139
6.11 Comparison of the equilibrium constant of the MEA carbamate reversion reaction (R2) of this work with the experimental data . . . . . 145
6.12 Intrinsic and absolute hydration free energy and enthalpy of the proton . . 147

# List of Tables


3.1 Values of the dimensionless ideal–gas free energy function . . . . . 51

3.2 Ideal–gas reaction free energies at 0 K . . . . . 52

3.3 Values of the fraction of the total population of the MEA conformers . . . 53

3.4 Water density and dimensionless species intrinsic hydration free energies . 55

3.5 Quantities contributing to $\Delta\widetilde{G}_j(T,P)$ . . . . . 56

3.6 Values of $\epsilon_{r,\mathrm{solv}}$ and $A$ in Davis model . . . . . 57

4.1 Predicted $pK$ values for reactions R1 and R2 from this work at the indicated temperatures and $P = 1$ bar . . . . . 76

4.2 Comparison of GAFF predicted intrinsic hydration free energies of the protonated, neutral and carbamate forms of MEA and AMP at $T = 298.15$ K using different sets of partial charges in conjunction with RESP . . . . . 77

4.3 Comparison of the predicted $pK$ values of reactions R1 and R2 for the MEA and AMP systems at $T = 298.15$ K using different sets of partial charges . 78

4.4 Comparison with literature data of calculated $pK_2$ for the carbamate reversion reaction R2 at $T = 298.15$ K (unless indicated otherwise) and $P = 1$ bar . . . . . 80

4.5 Prediction of the amine protonation constant $pK_8$ independently of knowledge of the proton ($H^+$) hydration free energy at 298.15 K . . . . . 82

5.1 Thermodynamic data . . . . . 104

5.2 $\Delta G^0$ of the reaction $RNH_3^+ = RNH_2 + H^+$ for 29 amines in kJ·mol$^{-1}$ at $T = 298.15$ K and $P = 1$ bar . . . . . 108

5.3 p$K_a$ values for the reaction $RNH_3^+ = RNH_2 + H^+$ using different charge models and from SMD continuum solvent simulations at $T = 298.15$ K and $P = 1$ bar. . . . 110

5.4 Comparisons with experiment of p$K_a$ values for the reaction $RNH_3^+ = RNH_2 + H^+$ using AM1–BCC and SMD continuum solvent simulations at $T = 298.15$ K and $P = 1$ bar . . . 111

6.1 Protonation and carbamate formation constants of the studied amines at $T = 298.15$ K . . . 132

6.2 Enthalpy of deprotonation of amines ($\Delta H^{deprot}$/kJ.mol$^{-1}$) in aqueous solution at 298.15 and 313.15 K . . . 141

6.3 Enthalpy of carbamate reversion ($\Delta H^{carb}$/kJ·mol$^{-1}$) of amines in aqueous solution at 298.15 . . . 145

6.4 Coefficients of the function $A + B/T + C\ln(T)$ fitted to $\Delta G^0_{R9}(T, P^0)/RT$, $\ln\left(\frac{\overline{\rho}_{\rm solv}(T,P)RT}{100P^0M_{solv}}\right)$, $\mu^{res,\infty}_{H_2O}/RT$ , $\mu^{res,\infty}_{HCO_3^-}/RT$, $\mu^{res,\infty}_{H_3O^+}/RT$ $\mu^{res,\infty}_{H^+}/RT$ terms in Eq.6.12 . . . 147

A.1 Dimensionless species Gibbs energy functions . . . 190

A.3 $RNH_3^+$ bond parameters . . . 191

A.2 $RNH_3$ non-bonded parameters . . . 191

A.4 $RNH_3^+$ angle parameters . . . 192

A.5 $RNH_3^+$ dihedral parameters . . . 193

A.6 $RNHCOO^-$ non-bonded parameters . . . 194

A.7 $RNHCOO^-$ bond parameters . . . 194

A.8 $RNHCOO^-$ angle parameters . . . 195

A.9 $RNCOO^-$ dihedral parameters . . . 196

A.10 $RNH_2$ non-bonded parameters . . . 197

A.11 $RNH_2$ bond parameters . . . 197

A.12 $RNH_2$ angle parameters . . . 198

A.13 $RNH_2$ dihedral parameters . . . 199

A.14 $HCO_3^-$ non-bonded parameters . . . 199

A.15 $HCO_3^-$ bond parameters . . . 199
A.16 $HCO_3^-$ angle parameters . . . 200
A.17 $HCO_3^-$ dihedral parameters . . . 200
A.18 $H_3O^+$ and $OH^-$ non-bonded parameters . . . 200

B.1 Constants of the equation $\ln K_1 = A + \frac{B}{T} + C \ln T$. . . . 201
B.2 Constants of the equation $\ln K_2 = A + \frac{B}{T} + C \ln T$. . . . 202
B.3 BAR predicted residual chemical potential (kJ/mol) of neutral ($RNH_2$), protonated ($RNH_3^+$) and carbamate forms ($RNHCO_2^-$) of the seven alkanolamines in TIP3P water at P=1.0 bar and T=298.15-353.15K . . . 202
B.4 BAR predicted residual chemical potential (kJ/mol) of the small molecules ($CO_2$, $H_2O$, $HCO3^-$ in TIP3P water at P=1.0 bar and T=298.15-353.15K 203
B.5 Ideal gas reaction free energy of the main reaction (R1 : $CO_2 + 2RNH_2 = RNHCO_2^- + RNH_3^+$) from different QM methods. . . . 204
B.6 Ideal gas reaction free energy of the carbamate reversion reaction (R2 : $RNHCO_2^- + H_2O = RNH_2 + HCO_3^-$) from different QM methods. . . . 205
B.7 Quantities contributing to the equilibrium constant of the reactions (R1 : $CO_2 + 2RNH_2 = RNHCO_2^- + RNH_3^+$) . . . 206
B.8 Quantities contributing to the equilibrium constant of the carbamate reversion reaction (R2 : $RNHCO_2^- + H_2O = RNH_2 + HCO_3^-$) . . . 207
B.9 Gaussian output of the ideal gas relative gibbs free energies (in Hartree) . . 208
B.10 Gaussian output of the ideal gas relative gibbs free energies (in Hartree) . . 209
B.11 Gaussian output of the ideal gas relative gibbs free energies (in Hartree) . . 210
B.12 Gaussian output of the ideal gas relative gibbs free energies (in Hartree) . . 211
B.13 Gaussian output of the ideal gas relative gibbs free energies (in Hartree) of the small molecules using different QM method . . . 212

C.1 The raw intrinsic hydration free energies (in $kJ \cdot mol^{-1}$) of the neutral forms of the 29 alkanolamines from different charge models and from SMD continuum solvent simulations at $T = 298.15$ K and $P = 1.0$ bar . . . 214

C.2 The raw intrinsic hydration free energies (in kJ·mol$^{-1}$) of the protonated ($RNH_3^+$) forms of the 29 alkanolamines from different charge models and from SMD continuum solvent simulations at $T = 298.15$ K and $P = 1.0$ bar 215

D.1 Coefficients of the fit to $\frac{\Delta G^{IG}}{RT} = A^0 + B^0/T + C^0 ln(T)$ of the ideal gas reaction free energy of the deprotonation reaction $RNH_3^+ + H_2O = RNH_2 + H_3O^+$ . . 217

D.2 Coefficients of the fit to $\frac{\Delta G^{IG}}{RT} = A^0 + B^0/T + C^0 ln(T)$ of the ideal gas reaction free energy of the carbamate reversion reaction $RNHCO_2^- + H_2O = RNH_2 + HCO_3^-$ . . . . . 220

D.3 Coefficients of the fit to $\frac{\mu_i{}^{res\infty}}{RT} = a^{res} + b^{res}/T + c^{res} ln(T)$ for the small molecules. . . . . 221

D.4 Coefficients of the fit to $\frac{\mu_i{}^{res\infty}}{RT} = a^{res} + b^{res}/T + c^{res} ln(T)$ of the neutral amines considered in this work. . . . . 221

D.5 Coefficients of the fit to $\frac{\mu_i{}^{res\infty}}{RT} = a^{res} + b^{res}/T + c^{res} ln(T)$ of the protonated amines considered in this work. . . . . 224

D.6 Coefficients of the fit to $\frac{\mu_i{}^{res\infty}}{RT} = a^{res} + b^{res}/T + c^{res} ln(T)$ of the carbamate form of the primary and secondary amines considered in this work. . . . . 226

D.7 Coefficients of the fit to $-\ln K = A + B/T + C ln(T)$ of the deprotonation reaction $RNH_3^+ + H_2O = RNH_2 + H_3O^+$. . . . . 227

D.8 Coefficients of the fit to $-\ln K = A + B/T + C ln(T)$ of the carbamate reversion reaction $RNHCO_2^- + H_2O = RNH_2 + HCO_3^-$ . . . . . 230

D.9 Reaction enthalpy (in kJ/mol) at T=313.15K for the amine de-protonation (R1) and carbamate reversion (R2) reactions. . . . . 231

# Chapter 1

# Introduction

## 1.1 General Overview

It is generally believed that anthropogenic $CO_2$ emission from fossil fuel-fired power plants (e.g., coal and natural gas) and other $CO_2$ point sources such as steel and cement manufacturing facilities are the main reason for the increase in the global temperature and the associated environmental issues. Annual global emissions of $CO_2$ increased by approximately 80% between 1970 and 2004, and based on the current scenario it is predicted to increase by 1% annually on average until 2040[1]. The problem of $CO_2$ atmospheric reduction is one of the grand challenges for the 21st century[2]. Since carbon-based fuels play a vital role in meeting global energy demand, a carbon-neutral process will require capture of the produced $CO_2$. This has prompted global collaborations to establish policies and initiate programs to foster and advance the growth of clean energy technologies such as Carbon Capture and Sequestration (CCS) to reduce the atmospheric concentrations of greenhouse gases[3, 4]. The Intergovernmental Panel on Climate Change (IPCC) predicts that $CO_2$ release to the atmosphere could be reduced by 80 - 90 % for a conventional power plant equipped with CCS technology[4]. In a typical CCS process, $CO_2$ is captured from large point sources and compressed for transport to deep underground formations for permanent storage. Among the capturing techniques (adsorption in nano-porous materials, membranes, cryogenic distillation, etc.) solvent absorption is the most widely used capturing method[5]. According to Li *et al.* [6], from a total of 1297 patents related to $CO_2$ capture approximately 37.5% are related to solvents.

Industrial scale CCS implementation requires a process control strategy (*e.g.*, Sandoval *et al.* [7, 8]), built on a model whose foundation is a kinetic model (*e.g.*, de Meyer *et al.*

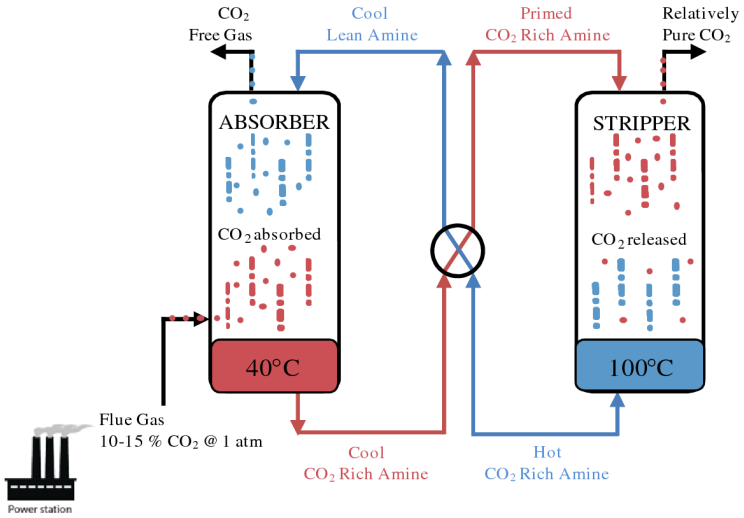


Figure 1.1: Schematic of $CO_2$ absorption process using aqueous amine solvent. Reprinted with permission from ref[10]. Copyright 2009 American Chemical Society.

[9]), which in turn requires a description of the equilibrium thermodynamics of the process. In this thesis, we focus on the thermodynamic properties of the solvent absorption process, which include the $CO_2$ solubility and its relationship to the vapour phase partial pressure of $CO_2$, and the chemical speciation in the absorbent solution.

The low partial pressure of $CO_2$ in typical flue gas (*i.e.*, in post-combustion $CO_2$ capture) prevents the use of physical solvents for a deep removal, and hence $CO_2$ must be absorbed chemically followed by solvent stripping in the later stages of the process by supplying heat to regenerate the solvent and release the absorbed $CO_2$. The most mature CCS technology currently used in industry is post-combustion capture using reactive absorption[11] by an aqueous solution of alkanolamines or amino acids. A schematic of the absorption process is shown in Fig.1.1. Equilibrium $CO_2$ solubility is a property of primary importance for the design of such processes and this is governed by the equilibrium constants and their temperature dependence for the involved underlying reactions. For the amine solvents these are commonly represented by the following set of reactions (or any linearly independent combination thereof):

$$\mathrm{RNH_3^+ + H_2O} = \mathrm{RNH_2 + H_3O^+} \quad \text{(R1)}$$
$$\mathrm{RNHCO_2^- + H_2O} = \mathrm{RNH_2 + HCO_3^-} \quad \text{(R2)}$$
$$\mathrm{CO_2 + 2H_2O} = \mathrm{HCO_3^- + H_3O^+} \quad \text{(R3)}$$
$$\mathrm{H_2O + HCO_3^-} = \mathrm{CO_3^{-2} + H_3O^+} \quad \text{(R4)}$$
$$\mathrm{2H_2O} = \mathrm{H_3O^+ + OH^-} \quad \text{(R5)}$$
$$\mathrm{CO_2} = \mathrm{CO_2(vap)} \quad \text{(R6)}$$

where $CO_2$ is absorbed primarily in the solution in the form of carbamate ($RNHCO_2^-$), bicarbonate ($HCO_3^-$) and carbonate ($CO_3^{-2}$) ions, in coexistence with the neutral ($RNH_2$) and protonated ($RNH_3^+$) amine species, water and its ionization products, and free $CO_2$.

The primary concern associated with the process is the high energy demand for solvent regeneration, in addition to solvent loss and equipment corrosion. The high energy intensity is partly due to the unavoidable parasitic energy loss of the water co-solvent and also to the large $CO_2$ absorption enthalpy due to formation of stable carbamate species ($RNHCO_2^-$). To partially overcome these deficiencies, a blend of amines or amine-functionalized solid materials is sometimes proposed[12, 13].

However, the physical and chemical properties of the amines must be understood in order to design an optimal absorption process. Unfortunately, little experimental data concerning the properties of the majority of potential amine solvents exist. This includes, for example, sterically hindered amines, which have been experimentally shown to be promising candidates to replace conventional amines due to their high $CO_2$ absorption capacity (similar to that of tertiary amines), coupled with reasonable reaction rates (100 times faster than tertiary amines) and relatively low heat of absorption[14, 15, 16]. However, the properties of these materials required for CCS process design[17] are not known.

Another attractive class of solvents gaining interest for carbon capture is ionic liquids (ILs), which do not need to be mixed with water. An IL is composed of a bulky cation (usually with a hydrophobic hydrocarbon tail) and a (typically) smaller anion. This structure hinders their crystallization, leading to a stable liquid state at ambient conditions. ILs have favourable features for gas separation, such as low volatility (thereby reducing solvent loss), high absorption capacity and low degradation rate, in addition to their task-specific tunability[18, 19]. The properties of ILs can be further tailored by varying the cation and anion structures. However, due to the vast number of potential cation and anion combinations, an experimental search for an ideal task-specific candidate is a laborious and expensive operation[20]. Furthermore, thermodynamic modeling using conventional

equations of state usually requires molecular parameters such as critical properties, which are not available or even experimentally measurable, due to thermal degradation at very high temperatures[21].

An ideal absorbent solution would have high $CO_2$ absorption capacity, a low regeneration energy requirement and fast reaction kinetics and mass transfer, in addition to other desirable chemical and physical properties. Upon chemical absorption, new species (usually a mixture of electrolytes) are formed, which complicates the modeling of thermodynamic and transport properties of the system using macroscopic approaches. For chemical absorption modeling, sophisticated equations-of-state such as the SAFT family of models or the NRTL require extensive sets of experimental data to fit their underlying parameters, such as reaction equilibrium constants and binary interaction parameters, which are not directly measurable[22, 23]. Furthermore, these macroscopic models require additional parameters to express the pressure and temperature dependencies of the parameters. Completely different multi-parameter macroscopic models must also be developed for the transport properties.

This scenario has opened attractive alternative avenues of research for developing improved solvents using more cost-effective theoretical approaches. In this context, high-throughput first principle atomistic simulations are emerging as a powerful tool to explore the vast chemical space of possibilities for designing and screening of potential solvent candidates for efficient carbon capture. Whereas even a couple of decades ago, atomistic simulation was practically unknown within the chemical engineering community, its applications have grown rapidly and is becoming a mainstream engineering tool[24]. The remarkable improvements in computer hardware and software capabilities over the past few decades have enabled researchers to probe the properties of complex molecular systems and develop and test state-of-the-art computational theories and algorithms[25]. Atomistic simulations with modern force-fields can predict macroscopic properties resulting from the behavior of matter at the atomic/subatomic scale and provide insight on the underlying molecular mechanisms for observed property behaviour, which is not possible using empirical equations of state.

Atomistic simulations may be classified in two categories: classical molecular mechanics (MM) simulations and quantum mechanical (QM) simulations. The former deals with generating a configurational trajectory for the atomic/molecular particles interacting classically via a force field that contains a relatively small number of parameters. The latter deals with the motion of electrons and nuclei based on the Schrödinger equation with few (or no) empirical parameters, but requires various approximations to make the problem computationally feasible. While MM can be applied to predict thermodynamics properties covering significant time and length scales, they cannot simulate the *kinetics* of chemical

bond formation (with notable exceptions such as reactive force fields[26]). The potentially more accurate *ab initio* QM methods are restricted to a handful of particles due to current computational limitations. This has led to the emergence of a third type of simulation methodology: Molecular Mechanics/Quantum Mechanics (MM/QM) simulations, which combine the accuracy of QM with the computational efficiency of MM to describe the system of interest more realistically than MM alone.[27].

MM simulation, which is the focus of this thesis, is divided into two types: molecular dynamics (MD) and Monte Carlo (MC). During MD simulation, the time evolution of particle trajectories is obtained by solving the classical Newton equations of motion; the MC technique generates atomistic trajectories based on stochastic moves and probabilities associated with random moves. The ergodic hypothesis guarantees the equality of the results of both approaches for the calculation of equilibrium properties. The grand challenge associated with both approaches is describing the interactions of the particles with a force-field (FF) that is sufficiently detailed to realistically mimic the behavior of the system of interest. A FF dictates how the energy and forces in a molecular system are computed from its atomic positions. The required FF parameter sets and functional forms for the atom types/functional groups present in the molecular structure are typically obtained from fitting to experimental properties of simple molecular systems in conjunction with QM calculations[28]. The parameters obtained in this way are used as building blocks to construct FFs for different and larger molecules or their mixtures, somewhat similar to the method of group contributions used in macroscopic thermodynamic modeling. This makes molecular modeling a powerful tool for rational chemical design and screening of a vast number of materials in an efficient cost-effective manner.

While atomistic simulations have been used extensively to investigate the behavior of non-reactive systems, there have been fewer studies on systems undergoing chemical reactions, and fewer still involving electrolytes as commonly encountered in a CCS process[29, 30, 31]. This is mainly because of the lack of a general-purpose molecular simulation methodology for reactive systems. Currently, the most widely used method is the reaction ensemble MC method of Smith and Triska [32] and its variants [33, 30, 29], which is computationally expensive for most systems of practical interest comprised of large molecules such as those encountered in CCS applications[30]. In this research, we first seek to develop and test new and computationally efficient algorithms for reactive $CO_2$ absorption using atomistic simulations for systems of practical interest for $CO_2$ capture such as aqueous alkanolamines solutions and ionic liquids (ILs). This requires the development of FFs for the molecular systems and testing them against available thermodynamic properties. In this thesis we apply such models to a wide range of potential solvents to assess their $CO_2$ removal capacity and to establish relationships between the molecular structure

and adsorption capacity. We will mainly be investigating the $CO_2$ solubility in these solvents, from which other essential quantities for solvent design may be obtained, such as the reaction absorption enthalpy. The findings of this research are also expected to have implications for other applications involving the molecular modeling of chemical reaction equilibria, particularly those involving electrolyte solutions.

## 1.2 Motivation

The current research project is primarily motivated by the lack of a computationally efficient molecular simulation framework for solving general chemical reaction equilibrium problems involving complex molecular systems such as those encountered in PCC systems. The scarcity of experimental data for the vast number of potential solvents for PCC (Post Combustion Capture) due to the difficulty and expense involved in experimental measurements of vapor–liquid equilibrium (VLE) properties of amine-$H_2O$-$CO_2$ systems has motivated us to develop and validate a new computational approach for the rapid screening of potential solvents. Properties of interest are reaction equilibrium constants and the species equilibrium concentration, including those present in minor concentrations or for hydrogen exchanging species which are difficult to measure experimentally by NMR techniques.

Molecular simulation has been widely used for the prediction of physical absorption of $CO_2$ and other small molecules in various solvents, and its modeling based on Henry constants has been the primary method of modeling solubility[34]. However, this neglects the fact that $CO_2$ undergoes chemical reaction with the solvent. Other than ourselves, the only workers to incorporate reactions in the solvent has been the groups of Maginn [30] and Vlugt[29], whose efforts for this purpose have been relatively unsuccessful. This is mainly due to the computational expense and complexity of the required Monte Carlo algorithms in the context of reactive systems.

Approaches relying on classical force fields to investigate chemical reaction equilibrium may be divided into two types. MD algorithms based on a so-called "reactive force field" allow the chemical identities of the molecules to be changed in the course of the simulations, by chemical bond formation and breaking. The reactive force field approach applies empirically based relationships involving bond distance, bond order and bond energy that model dissociation to separated atoms during the simulation. The application of this class of simulations is very limited, since such force fields parameters have been developed for only a few systems[26]. This is mainly because parameter development for this class of force fields is an extremely demanding and challenging task. A comprehensive review of

this category of methodology can be found in ref[35]. Another challenge associated with this type of simulation is the large free energy barrier between the product and the reactant molecules, which makes the sampling of "reactive events" using MD simulations extremely challenging, often requiring very long simulation times.

The second type of algorithm for simulation of reaction equilibrium is the "Reaction Ensemble Monte Carlo, REMC" method which is arguably the most widely used method. REMC is based on minimizing the Gibbs free energy of the system through a series of stochastic compositional changes using Monte Carlo moves. The REMC algorithm developed by Smith and Triska [32] and independently (in a less general form) by Johnson and Panagiotopoulos *et al.* [36] has been successfully applied to molecular systems undergoing chemical reactions. A comprehensive review of the methodology with basic examples can be found in ref[37]. The methodology may be combined with Gibbs Ensemble Monte Carlo simulation, enabling the simulation of combined reaction and phase equilibrium. A reaction move consists of randomly choosing a reaction with equal probability and performing a compositional change (by random deletion/insertion and/or alchemical change of products/reactants) in the system based on an integer change in the extent of reaction, followed by the acceptance or rejection of the move according to a particular transition probability. Similarly to macroscopic reaction equilibrium calculations, the methodology only requires a "species list" (chemical formulas of the reactant and products) and does not require a reaction set associated with a kinetic mechanism (the reaction set used may be chosen for computational convenience). The challenging part of the REMC simulation methodology is the implementation of the stochastic compositional change. This is done by a combination of alchemical and reactant/product molecule insertion/removal, and for dense systems with strong interactions, the free energy penalty of such moves are very large, resulting in low acceptance rates, requiring special system–specific algorithmic variants. REMC has been used to investigate complex chemical reactions, including propane metathesis[38], reaction in polymer models[39, 40], combined reaction and phase equilibrium[41], and xylene isomerization in nano-pores[42]. However, the Monte Carlo basis of the algorithm inhibits its computational efficiency and novel system-specific moves and acceptance probabilities are required for systems involving complex molecular structure. This has limited its applications primarily to the study of reactions in simple molecular systems such as ammonia synthesis [43, 44, 45, 46], nitric oxide dimerization [46, 47] and Lennard-Jonesium test systems.

A first-principles approach that does not require prior knowledge of the chemical identity of the product molecules has also been developed. Similarly to the case of macroscopic thermodynamic modeling using an EOS (equation-of-state) approach, a disadvantage of all FF-based approaches is the need for prior knowledge of the product molecules (*i.e.*, the

species list) to be able to obtain the thermodynamic equilibrium composition of the system. The recently proposed "first-principles "RxFPMC algorithm of Fetisov *et al.* solves this problem by employing an approximate QM simulation of the atoms of the system and an empirically based cluster analysis of its equilibrated atomic structure using a molecular identification criterion[48]. Even though the methodology does not require a "species list", the original applications have thus far been limited to a simple system involving N and O atoms. It is very computationally expensive, and its extension to larger molecules and their structural isomers will require more detailed identification criteria for particular species, somewhat analogously to the use of a "species list", as required in the REMC approach.

The lack of a generic and widely available simulation approach hinders the application of molecular simulations to complex molecular systems and to reactive systems in particular. Other notable studies to model the reactive absorption of $CO_2$ are based on single ideal–gas reactions and are approaches which are intrinsically unable to account for the effect of the solvent environment. This approach has been applied to a single isolated $CO_2$ molecule with various ionic liquid molecules in an attempt to predict their $CO_2$ capturing capability[49, 50, 49].

Although molecular simulation methodologies have been well established for calculation of the physical solubility of small gas molecules in complex systems based on free energy methods[34] or using Gibbs ensemble Monte Carlo simulation[51], there have been only a handful of studies of its application to reactive systems[52, 30, 29] which are of interest to CCS processes. In a notable recent study, Balaji *et al.* attempted to model the reactive absorption of $CO_2$ in an aqueous solution of ethanolamine using the REMC algorithm. The authors used an efficient Monte Carlo approach for molecular insertion/deletion moves (called "continuous fractional component Monte Carlo, CFCMC") to overcome the particle insertion/deletion issue in MC sampling[29]. However, we showed that they applied it erroneously for the considered system[53]. We emphasize that the employment of REMC for complex systems requires complicated system-dependent approaches, and it cannot be routinely applied to such systems. Furthermore, reactive systems in which some species have very small concentrations are extremely computationally expensive, and very long simulation times and/or large system sizes are required to observe sufficient numbers of successful reaction moves. Algorithmic complexity thus hinders their application to systems of practical interest for $CO_2$ capture. On the other hand, molecular dynamics simulations can be run efficiently on multiple processors for molecules of arbitrary complexity and system size; the missing ingredient has been the implementation of reaction moves.

Recently, Maginn *et al.* proposed a hybrid methodology based on a thermodynamic cycle to calculate the equilibrium loading of $CO_2$ in an aprotic heterocyclic anion (AHA) ionic liquid that reacts with $CO_2$ [52]. The core of the approach is a combination of the

MD simulation of the ion solvation free energies, the ideal–gas reaction free energy change in the vapour phase, the simulation of the solution enthalpy as a function of composition, and an analytical expression based on an ideal solution approximation to the solution entropy. The solution reaction free energy change was then calculated as a function of the extent of reaction to find the minimum of the Gibbs energy function. This approach can be computationally demanding, especially for systems with multiple reactions, since the required compositional space would become prohibitively large. Their thermodynamic cycle only allows for the concentration of chemically bound $CO_2$ to be calculated, and the physical solubility cannot be calculated using their approach. Additionally, the validity of the ideal solution approximation used for the entropy of mixing is questionable for other ILs or for different temperatures. In a subsequent study, they implemented the REMC algorithm for the same system using a united atom force field for the ionic liquid. This approach allows for the calculation of both chemically bound and physically bound $CO_2$ in the ILs; but at the cost of implementing a special system-dependent reaction move methodology. The computational complexity of MC algorithm development for novel molecular systems and the fact that its MC basis inhibits the implementation of significant parallelization hinder mainstream applications.

Most molecular simulation-based studies of systems relevant to $CO_2$ capture in the literature focus on reaction mechanism prediction (although this is irrelevant for prediction of reaction equilibrium) using ab initio approaches[54, 55, 56] and there have been few studies addressing quantitative prediction of absorption isotherms[52, 30, 29]. Most researchers have relied on the prediction of protonation constants [57, 58] and have tried to correlate them with the absorption capacity, the heat of regeneration and other quantities of interest to CCS. In this context, continuum solvent simulations, in which the solvent is treated as a dielectric medium and the solute is treated quantum mechanically, have been widely used to assess the performance of various alkanolamine solvents for $CO_2$ capture. However, such approaches lack information concerning the composition-dependence of free energies of absorption and are only applicable to the infinite dilution limit and for cases where the solvent is well characterized by a continuum model. For example, Svendsen[59] used continuum solvent simulations to investigate the temperature dependence of the enthalpy of protonation and carbamate formation of MEA and MDEA, two widely used solvents for $CO_2$ capture. The heat of absorption of $CO_2$ and reaction equilibrium constants estimated from continuum solvent simulations may be used in macroscopic thermodynamic equations of state such as UNIQUAC and NRTL for better design of post-combustion $CO_2$ capture solvents. However, continuum solvent simulations lack physical insight on molecular level interactions, are only applicable over the small range of temperatures at which they have been parameterized, and are available only for a limited number of solvents. Although they

are computationally less expensive than explicit solvent simulations, the accurate calculation of solvation free energy of a large flexible molecule is challenging as the contribution from different conformers in solution must be taken into account, which is also unaccounted for in this approach. In contrast to continuum solvent simulations, explicit solvent molecular simulation methods based on classical force fields can sample different conformers in solution, and the models are often transferable to the high temperature-pressure conditions usually encountered in CCS processes.

Macroscopic thermodynamic models have also been widely used for phase equilibrium, thermodynamic and transport property predictions for CCS processes. Recently, Vega *et al.* applied a molecular-based equation-of-state based on the Statistical Associating Fluid Theory (SAFT) to predict the phase behavior of reactive absorption in alkanolamine solutions[23, 22]. Although the SAFT-based equation-of-state has been successful in predicting thermodynamic properties of complex chemical systems, their application is hindered by the unavailability of the parameters for many molecular systems. Such models require extensive parameterization based on experimental measurement. Moreover, they are unable to correctly model chemical reactions (they use physical interatomic binding approximations).The aim of the research of this thesis is to fill an important gap in the literature by developing a generally applicable and computationally efficient molecular simulation approach for predicting the properties of systems encountered in CCS processes, with a minimal requirement for experimental data.

## 1.3 Outline of the Thesis

In this thesis we develop a general molecular simulation framework for prediction of vapour-liquid equilibrium in reactive systems with application to carbon capture using amine solvents. In Chapter 2, we describe the statistical mechanical derivation of the residual chemical potential $\mu^{res,NVT}$ in the canonical ensemble (specified temperature $T$ and density $\rho$), and how it can be obtained from alchemical free energy simulations. We describe several possible choices for the chemical potential model and translations between them. We provide an expression for the standard state chemical potential in the Henry-law-based model, $\mu^{\dagger}(T,P)$ (where $P$ is the pressure), based on $\mu^{res,NVT}$ and the ideal gas chemical potential, $\mu^{0,IG}(T;P^0)$ ($P^0 = 1$ bar is used). This expression allows us to calculate the reaction equilibrium constants, $p$K, as demonstrated in the subsequent chapters for different reactions involved in the amine-water-$CO_2$ system.

Our framework is a hybrid methodology that involves the calculation of species $\mu^{\dagger}(T,P)$ and reaction equilibrium constant values, which combines quantum chemical calculations

in the ideal–gas phase and explicit solvent molecular dynamics simulations in the liquid phase.

In Chapter 3, we show the computational details underlying the application of our framework. This involves coupling the simulation quantities with a macroscopic thermodynamic model to predict the reactive absorption properties. We apply the methodology to a benchmark system of 30 wt% monoethanolamine (MEA)-$H_2O$ solvent and predict speciation and $CO_2$ partial pressure above the solution as a function of temperature at a total pressure of 1.0 bar. This is the first time that explicit solvent classical force based molecular simulation has been successfully applied to this system. We use literature force fields to describe small solutes such as $OH^-$, $H_3O^+$, and the General Amber Force Field (GAFF) to model other solutes (neutral and protonated amine, carbamate and bicarbonate ions).

In Chapter 4, we propose an approach that combines our simulation data with readily available experimental reaction equilibrium data for the binary $CO_2$-$H_2O$ system, obviating the need for explicit simulation of the small ions $H_3O^+$, $OH^-$ and $CO_3^{-2}$. This improves our previously predicted results for the monoethanolamine (MEA)-$H_2O$ system and also provides accurate predictions for speciation and $CO_2$ solubility in six additional alkanolamine solvents.

In Chapter 5, we predict the dissociation constant ($p\mathrm{K}_a$) for a set of 29 amine solvents. These quantities are important with respect to solvent selection, since they strongly correlate with the absorption capacity, kinetics and the absorption heat in amine-water-$CO_2$ systems. We show that the GAFF with the semi-empirical AM1-BCC charges is able to predict this quantity with an average absolute deviation (AAD) of less that $0.72 p\mathrm{K}_a$ units, outperforming a commonly used continuum solvent method (SMD). Furthermore, we show that AM1-BCC also outperforms other partial charge methods used within the GAFF (based on B3LYP and HF electron density calculations). This study uses a theoretical value of the $H^+$ hydration free energy at $T = 298.15$ K based on the cluster-continuum calculations of Tissandier *et al.* [60] calculations. The limitation to this temperature is due to the lack of $H^+$ hydration free energy data at elevated temperatures.

In Chapter 6, we perform simulations of the $p\mathrm{K}_a$ and carbamate reversion equilibrium constants over a wide range of temperatures of interest for post–combustion $CO_2$ capture for a large and diverse set of 77 amines, using an iso-coulombic reaction set involving a new force field for the hydronium ion, $H_3O^+$. We find that using iso-coloumbic reactions provide improved temperature dependent predictions for the reaction equilibrium constants and hence the reactions enthalpie. Such reactions also provide improved speciation predictions, due to cancellation of ionic species activity coefficients in the reaction free energies.

The new $H_3O^+$ force field allows predictions of $pK_a$ at elevated temperatures, which were not previously possible using $H^+$, since its solvation free energy value is only available at 298.15 K. The new force field for $H_3O^+$ is obtained by adjusting a single parameter (the oxygen partial charge) to reproduce the well-known experimental MEA $pK_a$ value at 298.15 K. This allows pure predictions for MEA at higher temperatures and for the remaining 76 amines $pK_a$ at all temperatures. We furthermore calculate the protonation and the carbamate reversion reaction enthalpy of the amines. We express the temperature dependence of $pK_a$ and $pK_c$ by means of convenient analytical representations. Finally, we use the $H_3O^+$ force field to predict the intrinsic solvation free energy of the proton as a function of temperature. This is an important quantity of fundamental interest.

Chapter 6 summarizes the results of the thesis, and provides suggestions for future work.

# Chapter 2

# Background

## 2.1 Statistical Mechanics

(The following material is based on standard statistical mechanics textbooks (*e.g*, McQuarrie[61], Frenkel and Smit[62], and Allen and Tildesley[63]).

Equilibrium statistical mechanics is centered upon the mathematical statement:

$$\langle A \rangle = \int \int d\mathbf{r}^N d\mathbf{p}^N \mathcal{A}\left(\mathbf{r}^N, \mathbf{p}^N\right) \rho\left(\mathbf{r}^N, \mathbf{p}^N\right) \tag{2.1}$$

where the *expectation value*, $\langle A \rangle$ of the observable thermodynamic quantity $A$ is an average over all possible microstates available to the system. $\rho\left(\mathbf{r}^N, \mathbf{p}^N\right)$ is the probability of observing the system in microstate $r^N = (r_1, ..., r_N)$ and $p^N = (p_1, ..., p_N)$ , and $\mathcal{A}\left(\mathbf{r}^N, \mathbf{p}^N\right)$ is the value of the property $A$ when the system in that microstate. The variables $r^N$ and $p^N$ denote the sets of atomic positions and momenta. Hence, a microstate for a system of $N$ particles is specified by a point in a $6N$-dimensional phase space. The probability of finding a system at a certain microstate is proportional to exponential of the Hamiltonian as:

$$\rho\left(\mathbf{r}^N, \mathbf{p}^N\right) \propto \exp[-\beta \mathcal{H}\left(\mathbf{r}^N, \mathbf{p}^N\right)] \tag{2.2}$$

which is the energy of a point in phase space given by:

$$\mathcal{H}\left(\mathbf{r}^N, \mathbf{p}^N\right) = \mathcal{K}\left(\mathbf{p}^N\right) + \mathcal{U}\left(\mathbf{r}^N\right) = \sum_{i=1}^{N} \frac{p_i^2}{2m_i} + \mathcal{U}\left(\mathbf{r}^N\right) \tag{2.3}$$

while $m_i$ is the mass of the *ith* atom. The configurational potential energy $\mathcal{U}\left(\mathbf{r}^N\right)$ is generally approximated by invoking the pair-wise additivity approximation, where many-body effects are taken into account using an effective pair potential $u_{ij}$ . In the absence of any external field, it is given by:

$$\mathcal{U}\left(\mathbf{r}^N\right) = \sum_{i}^{N} \sum_{j>i}^{N} u_{ij}(\mathbf{r_i}, \mathbf{r_j}) \tag{2.4}$$

Evaluation of the integral in Eq.2.1 is generally extremely difficult because one must calculate all possible states of the system. Molecular simulation allows sampling of only a small portion of phase space which has the highest contribution to $\langle A \rangle$ by generating the most probable configurations of the system. For example, in a molecular dynamics simulation points in the phase space are visited sequentially in time and the time average of the quantity A is given by:

$$\langle A \rangle_{time} = \lim_{\tau \to \infty} \frac{1}{\tau} \int_{t=0}^{\tau} \mathcal{A}\left(\mathbf{r}^N, \mathbf{p}^N\right) dt \approx \frac{1}{M} \sum_{t=1}^{M} \mathcal{A}\left(\mathbf{r}^N, \mathbf{p}^N\right) \tag{2.5}$$

where $\tau$ is the simulation length, M is the number of time steps in the simulation. Although experimental observables are assumed to be ensemble averages (average over all possible microstates), according to the *ergodic hypothesis*, which states that *the time average equals the ensemble average*, if one allows the system to evolve in time indefinitely, that system will eventually pass through all possible states. Molecular simulation allows the approximation of the time average or equivalently the ensemble average using a reasonable amount of computer resource by generating a finite number of microstates.

## 2.2 Classical Molecular Simulation

Classical Molecular Dynamics (MD) and Monte Carlo (MC) simulations are computational tools widely used in material science and engineering. Both methods require a potential function or equivalently a force field (FF) with a specified mathematical form and its parameter sets to generate the sequential/time-dependent trajectory for the classical many-body particles/molecules interacting with each other. The mathematical form of the potential function depends on the nature of the interactions present in the system and the parameters are typically fitted to experimental thermodynamic properties such as vapor-liquid equilibrium data, critical and transport properties of the system[28].

In an MD simulation, the particle trajectories evolve with time based on the intermolecular forces. The equations of motion for the atoms is solved by initializing the atomic coordinates and velocities and solving Newton's equations of motion for the many-body system by numerical methods. The time evolution of an observable quantity is collected (time averaging) over millions of time steps. The simulation length usually spans from picoseconds to microseconds with a time step in the order of femtoseconds and a system size of thousands to millions of atoms. The appropriate system size is usually determined by empirically assessing the sensitivity of the quantity under investigation. Some thermodynamic properties might have strong system size dependency and one would need to increase the system size for more accurate estimation of such properties. Macroscopic constraints on the system such as pressure and temperature are controlled by periodically adjusting the simulation box size and the velocities of the atoms respectively[64, 62].

On the other hand, in an MC simulation, stochastic atomic/molecular movements, box volume changes and inter-box particle swaps (for multi-phase simulations) are performed to generate different configurations of the system. This process is repeated to generate a sequence of favorable configurations for the system to sample the structural and thermodynamic properties of the molecular system. The most important part of an MC algorithm is deriving the correct probability of moving from an prior configuration to a new configuration using statistical mechanics principles[62]. Since MC lacks any concept of time, dynamical properties (e.g. the diffusion coefficient) cannot be simulated.

Each method has its own advantages and disadvantages. For example, some molecular systems require longer time scales due to slow dynamics (e.g. solids) and MC may be preferred over MD simulations. Since in classical MD and MC simulation, bond rearrangement is not allowed (except for a certain class of force fields[26]) the chemical identity of each molecule in the simulation box remains unchanged over the course of the simulation. However, the existing molecular species may be replaced with new species (based on reaction stoichiometry) to change the composition of the system at desired steps and mimic the chemical reactions.

In this chapter, an overview of the basic principles and relations of MD and MC simulation are introduced along with explanations of various ensembles. We conclude by presenting general expressions for the chemical potential, a crucially important fundamental property for solubility and chemical reaction equilibrium calculations, are presented.

### 2.2.1 Force Field

In a classical simulation of a molecular system, atoms are treated as classical bodies represented by point particles carrying mass (m) and fixed electric charge (q) interacting through non-bonded potentials of electrostatic and van der Waals (vdW) forces.

All nonbonded intermolecular interactions between the pairs $ij$ separated by distance $r_{ij}$ are usually modeled using a standard 12-6 Lennard-Jones (LJ) plus coulombic potential with fixed point charges as

$$U_{\mathrm{ij}}\left(r_{ij}\right)=4\varepsilon_{ij}\left[\left(\frac{\sigma_{ij}}{r_{ij}}\right)^{12}-\left(\frac{\sigma_{ij}}{r_{ij}}\right)^{6}\right]+\frac{1}{4\pi\varepsilon_{0}}\frac{q_{i}q_{j}}{r_{ij}} \tag{2.6}$$

where $\varepsilon_{ij}$ and $\sigma_{ij}$ are the LJ energy and size parameters for atoms pair $ij$, respectively. These parameters commonly obtained from fitting to vapor-liquid equilibrium (VLE) measurements and thermodynamics properties such as virial coefficients, density, heat capacity, compressibility, hydration free energy, etc[28]. $q_i$ and $q_j$ are the atomic partial charge of atom $i$ and $j$. The partial charges for atoms in a molecule are obtained by minimizing the difference of the classical electrostatic potential and a accurate quantum mechanical derived electrostatic potential over many spatial grid points[65]. The use of fixed charges derived from *ab initio* calculation allows the electronic degrees of freedom to be replaced by effective computationally efficient coarse-grained interactions between the nuclei expressed via classical Coulomb's law.

Unlike LJ interactions are treated using Lorentz-Berthelot combining rules i.e.,

$$\sigma_{ij}=\frac{\sigma_{i}+\sigma_{j}}{2} \tag{2.7}$$

$$\epsilon_{ij}=\sqrt{\epsilon_{i}\epsilon_{j}} \tag{2.8}$$

As shown in Fig.2.1, bonded intra-molecular potentials describe bond vibrations, angle bending, and torsional movement within a molecule. For atoms $i$ and $j$ connected via a bond, the bond potential energy is modelled as a spring with a harmonic potential of the form:

$$U_{ij}=K_{bond}(r_{ij}-r_{0}) \tag{2.9}$$

Here, $K_{bond}$ is the bond stiffness constant and $r_0$ is its equilibrium length. Similarly for the angle potential for the three atoms $ijk$ is :

$$U_{ijk}=K_{angle}(\theta_{ijk}-\theta_{0}) \tag{2.10}$$

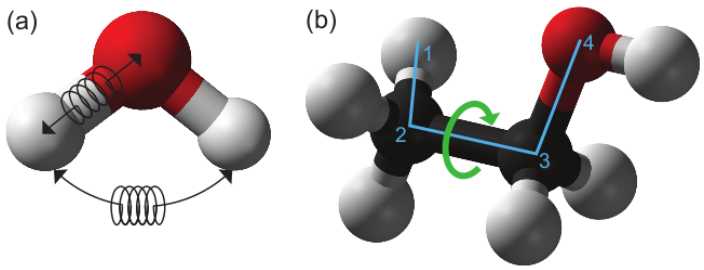


Figure 2.1: Schematics of bonded intermolecular interactions. Bonds and angles treated using harmonic potentials.

The dihedral potentials typically modelled using a cosine expansion:

$$U_{ijkl} = K_1[1+cos(\theta_{ijkl})]-K_2[1+cos(2\theta_{ijkl})+K_3[1+cos(3\theta_{ijkl})-K_4[1+cos(4\theta_{ijkl})] \quad (2.11)$$

The bonded parameters can be obtained from ideal gas quantum mechanical calculations and spectroscopic measurements[66]. The combination of the functional form of the model and specific values of its parameters is referred to as a "force field" (FF) . For different classes of compound various force fields with known parameters for a wide range of chemicals have been proposed. Examples of popular generic force fields are AMBER [67], OPLS [67],TraPPE[28], CHARMM [68] , GROMOS[69], DREIDING[70].

### 2.2.2 Boundary Conditions and Potential Truncation

Due to practical constraints in molecular simulation, the number of atoms in the simulation box is limited to a range from thousands to millions of atoms. This is still far from the thermodynamic limit and periodic boundary conditions are applied to the finite size simulation box to mimic the macroscopic limit. The schematic is shown in Fig.2.2. With this condition, when a particle leaves the central simulation box, its periodic image enters from the opposite face of the box. The central simulation box is artificially replicated throughout space and only the trajectory of the central box is tracked and stored in the memory; the periodic images follow the same trajectory as the central box. In a bulk fluid, the number of molecules affected by the wall is very small compared to the total number of molecules in a bulk experiment. Use of periodic boundary condition instead of a hard wall, eliminates the effect of a wall in a finite size simulation and mimics the bulk

behavior. For the calculation of the interaction potential at the position of atom $i$ due to ther atoms $j$ ( in the central box and its periodic images throughout the domain) the shortest distance is used, (this is sometimes called the minimum image convention). The pair-wise interactions distances that fall within a certain distance, $r_{cut}$ (the cut-off radius) are calculated using the potential function and the interactions with the rest of particles are treated using a mean field approximation. For the short-ranged VdW interaction, the second term in Eq.2.12 accounts for the truncation of the interaction beyond the cut-off distance. It is derived readily based on assuming a uniform number density beyond the cut-off radius, where the radial distribution function approaches unity and using the mean value of LJ parameter of the atoms in the system for potential energy function beyond the cut-off distance.

$$U_{total} = \sum_{i<j} U_{ij}(r) + \frac{N\rho}{2} \int_{r_{cut}}^{\infty} 4\pi r^2 U_{ij}(r) dr \tag{2.12}$$

Therefore the correction to the total potential energy due to truncation is :

$$U_{LR} = \frac{N\rho}{2} \int_{r_{cut}}^{\infty} 4\pi r^2 U(r) dr \tag{2.13}$$

For a "12-6 LJ" potential the correction is then:

$$U_{LR} = \frac{8}{9}\pi N\rho\sigma\varepsilon^3 \left[ \left( \frac{\sigma}{r_{cut}} \right)^9 - 3 \left( \frac{\sigma}{r_{cut}} \right)^3 \right] \tag{2.14}$$

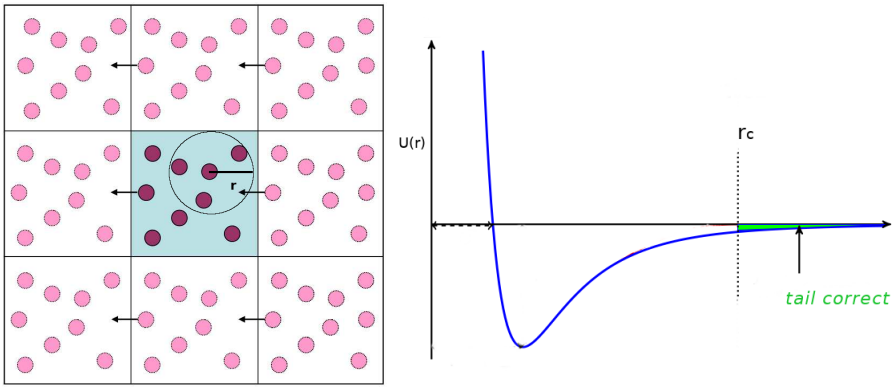


Figure 2.2: Illustration of periodic boundary condition

## 2.3 Molecular Dynamics Simulation

The basic idea of a MD simulation is to explore the phase space by generating sequential configurations of a molecular/atomic system by calculating intermolecular forces from potential functions and numerically integrating Newton's equations of motion. The classical atomic equations of motion can be expressed as:

$$m_i \ddot{\mathbf{r}}_i + \nabla_i \mathcal{U} = 0 \tag{2.15}$$

where $m_i$ is the mass and $\ddot{\mathbf{r}}_i$ is the acceleration of atom $i$. The force acting on atom $i$ is given by the negative gradient of the total potential function at position of particle $i$, $\mathcal{U}(\mathbf{r_{ij}})$, with respect to its position[62]:

$$\mathbf{f}_i = -\nabla_i \mathcal{U}(\mathbf{r_{ij}}) = -\frac{\partial \mathcal{U}(\mathbf{r_{ij}})}{\partial \mathbf{r}_i} \tag{2.16}$$

$\mathcal{U}(\mathbf{r_{ij}})$ is assumed to be pairwise additive:

$$\mathcal{U}(\mathbf{r_{ij}}) = \sum_{j \neq i} U_{ij}\left(\mathbf{r_{ij}}\right) \tag{2.17}$$

where $r_{ij}$ is the scalar distance between particles $i$ and $j$, and $U_{ij}$ is the pair potential specific to pair $(i, j)$. Therefore the force $\mathbf{f}_{ij}$ exerted on particle $i$ by means of its interactions with all other particles $j$ is given by :

$$\mathbf{f}_i = -\sum_{j=1}^{N} \frac{\partial U_{ij}\left(\mathbf{r_{ij}}\right)}{\partial \mathbf{r}_i} = \sum_{j=1}^{N} \mathbf{f}_{ij} \tag{2.18}$$

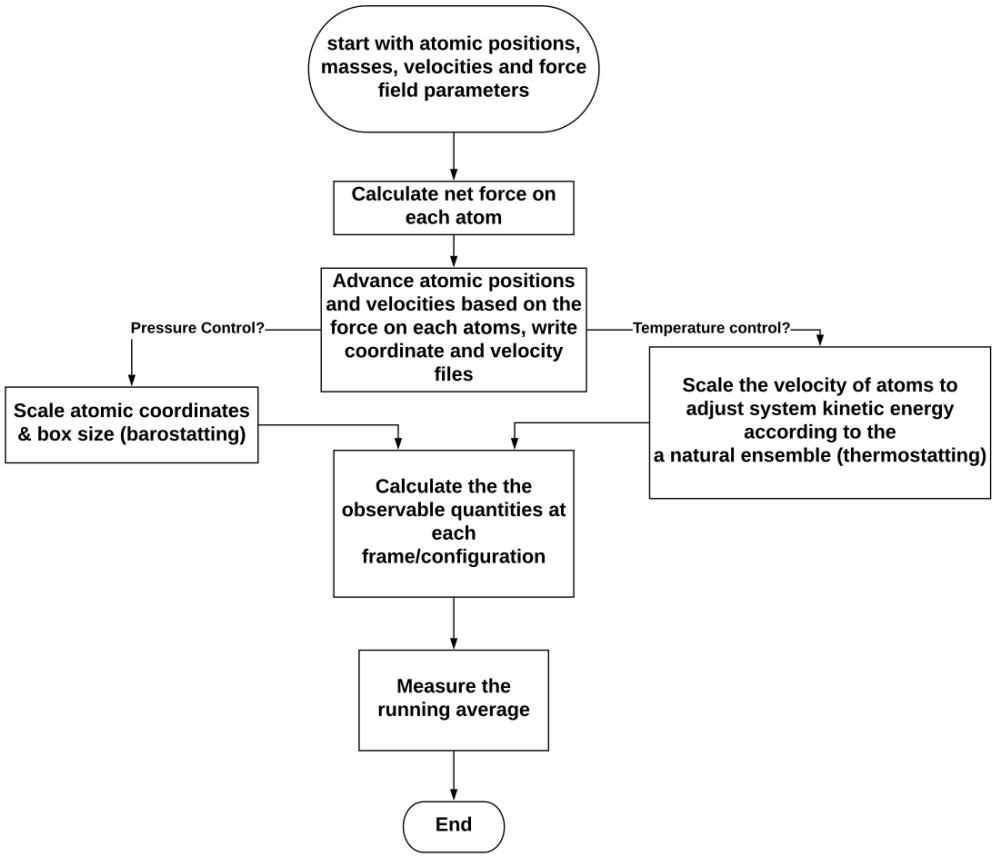


Figure 2.3: Simplified flowchart of a typical molecular dynamics simulation algorithm.

A typical molecular dynamics algorithm is shown in 2.3.

## 2.4 Monte Carlo Simulation

In a Monte Carlo simulation a sequences of random moves is performed on the molecules to achieve thermal (T), mechanical (P) and chemical ($\mu$) equilibrium depending on the ensemble used for the simulation. In a Canonical Ensemble (NVT), the simulation box is under constant volume (V), temperature and number of particles (N) in the course of simulation. Only particle random moves within the simulation box are allowed to achieve thermal equilibrium. Such a random move consists of randomly selecting one of the molecules and

translating (or rotating around) its center of mass by a certain extent $\alpha$. The value of $\alpha$ depends on the system and should be selected to achieve a reasonable number of successful moves. Rigid particle move is accepted according to the probability[62]

$$acc(o \rightarrow n) = min\left\{1, \exp[-\beta(U(n) - U(o))]\right\} \tag{2.19}$$

where $-\beta[(U(n) - U(o))]$ is the configurational potential energy change due to the particle move. To improve the efficiency of particle moves, an advanced algorithm such as multi-particle or force-biased MC may be used to speed up the calculations[71]. For flexible molecules, additional moves may be required to re-grow the molecule in different directions in addition to rigid body moves, to sample the intra-molecular part of the potential energy (due to bonds, angles and dihedrals) function. This can be extremely challenging for branched molecules in a dense environment, as the probability of successful molecular growth could be very small and special techniques such as configurational-biased Monte Carlo[72] has been developed to overcome this issue; however, due to algorithm complexity implementation of such approaches for new molecules is still challenging and focus of much ongoing research[73, 74].

Most experiments conducted under constant pressure and the NPT ensemble is ideal for mimicking the experimental conditions. In such an ensemble, the box volume is allowed to fluctuate during the simulations and the density is calculated based on the average value of the box volume $\langle V \rangle$. In addition to thermal equilibration, to achieve mechanical equilibration, the box volume change is also included as one the MC random moves. Each time the volume is changed by a small amount $dV$, the coordinates of the particles subsequently are scaled to accommodate the atoms. The volume change move is accepted according to the probability[62] :

$$\text{acc(o}\rightarrow n) = min\left\{1, \exp(-\beta[(U(n) - U(o)) + P(V(n) - V(o)) - N\beta^{-1} ln(\tfrac{V(n)}{V(o)})]\right\} \tag{2.20}$$

where $V(n) - V(o)$ is the volume difference of the old and new configurations. In a single particle move, only the interaction of the displaced particle with the rest of atoms need to be calculated for the probability calculation. In a volume change move, however, since the coordinates of all atoms are changed after the volume change, the interaction energy of all possible pairs must be calculated for the calculation of the probability function. This is the computationally expensive part of a Monte Carlo engine compared to MD simulations, which allow the simulation domain to be decomposed and calculations performed on several processors.

To simulate absorption/adsorption equilibrium the molecules must be transferred in and

out of the phase and this is achieved in a Grand Canonical Ensemble ($\mu VT$) simulation, where the volume of simulation box and the temperature are fixed and the number of molecules of different chemical species is allowed to fluctuate according to their prescribed chemical potentials. Particle swap between the chemical potential "reservoir" and the simulation box is accepted according to the probability[62] :

$$acc(o \rightarrow n) = min\left\{1, \frac{V}{\Lambda^3(N+1)} \exp(-\beta[(U(N+1) - U(N)) - \mu]\right\} \tag{2.21}$$

From this formula it can be seen that when system density is high ($\frac{V}{N+1}$ is small) or when the inserted particle interacts very strongly with the system ($\mu$ is large and negative) the probability of accepting a particle insertion becomes very low and the usual MC insertion algorithms are inefficient. For example, for strongly interacting particles such as ions in dense liquid water, the probability of such a move is virtually zero[62]. To circumvent this issue, "staged insertion/slow grow" algorithms such as Continuous Fractional Monte Carlo (for strongly interacting molecules) or Configurational Bias Monte Carlo (for branched and chain molecules) has been introduced into MC simulation programs[73, 74]. In a staged insertion/deletion, the interaction energy of the particle being inserted can be adjusted by a scaling parameter,$1 < \lambda < 0$ which controls the strength of interaction and the particle is fully grown over several stages which enhances the insertion/deletion probability.

## 2.5 Residual Chemical Potential in Canonical Ensemble ($\mu^{res,NVT}(T, P, \mathbf{x})$)

All chemical and physical phenomena are driven by the chemical potential. Other thermodynamic properties such as heat of absorption, vapor pressure and VLE properties are indirectly related to this quantity. Knowledge of the chemical potential for species in a reacting system allows the equilibrium concentrations to be calculated and subsequently, other transport and dynamical properties that depend on the composition to be predicted from the same molecular model.

Chemical potential is one of the most challenging and elusive properties to calculate in a simulation. Here we present a statistical mechanic-based derivation of the total chemical potential and how this quantity is calculated from an NVT ensemble simulation. For convenience, consider the simple case of a molecular system of composed $N_1$ solvent molecules

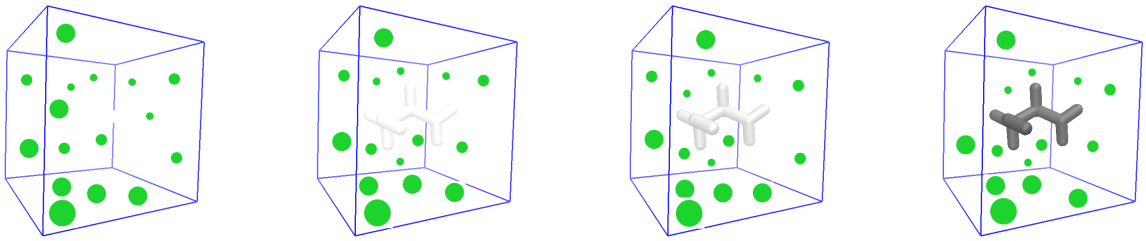

(a) $\lambda = 0$ (state A) (b) $\lambda = 0.3$ (c) $\lambda = 0.7$ (d) $\lambda = 1$ (state B)

Figure 2.4: Schematic representation of gradual insertion/ turning on the solute-solvent interactions.

and $N_2$ solute molecules. The chemical potential of component 2 is given by[75, 76]

$$\mu_2(N_1, N_2, T, V) = \left(\frac{\partial A}{\partial N_2}\right)_{T,V,N_1} = A(N_1, N_2 + 1, T, V) - A(N_1, N_2, T, V)$$
$$= -k_B T \ln \frac{Q(N_1, N_2 + 1, T, V)}{Q(N_1, N_2, T, V)} \tag{2.22}$$

$$\mu_2(N_1, N_2, T, V) = -k_B T \ln \left[\frac{Q(N_1, N_2 + 1, T, V)}{Q(N_1, N_2 + 1, T, V, \lambda = 1)} \frac{Q(N_1, N_2 + 1, T, V, \lambda = 1)}{Q(N_1, N_2 + 1, T, V, \lambda = 0)} \right.$$
$$\left. \frac{Q(N_1, N_2 + 1, T, V, \lambda = 0)}{Q(N_1, N_2, T, V)}\right] \tag{2.23}$$

where $Q$ represents the canonical partition function of the system. $Q(N_1, N_2, T, V, \lambda = 0)$ represents a hypothetical "state A" of the system where $N_1$ molecules of solvent and $N_2 + 1$ molecules of solute are present, where one of the $N_2$ molecules (call it the "guest molecule") is only interacting with itself (*i.e*, is an ideal gas molecule). $Q(N_1, N_2, T, V, \lambda = 1)$ represents a hypothetical "state B" of the system with $N_1$ molecules of solvent and $N_2 + 1$ molecules of solute, but all solute molecules are interacting with the rest of the system. The transition between state "state A" and "state B" is controlled by a coupling parameter $0 \leq \lambda \leq 1$. Since in "state A" the solute molecule is not interacting with the rest of the system,the partition function of the entire system (one ideal gas molecule and

$N_1 + N_2$ normal molecules) is the product of the individual partition functions as they are decoupled. [76]

$$\begin{aligned} Q(N_1, N_2 + 1, T, V, \lambda = 0) &= Q(N_1, N_2, T, V)Q(N_2 = 1, T, V) \\ &= Q(N_1, N_2, T, V)\Lambda_i^{-3}\langle V\rangle q_{int}(T) \end{aligned} \tag{2.24}$$

where the partition function of a single ideal gas molecule is used with

$$\frac{Q(N_1, N_2 + 1, T, V, \lambda = 0)}{Q(N_1, N_2, T, V)} = \Lambda_i^{-3} V q_{int}(T) \tag{2.25}$$

Similarly, the partition function of "state B" of the system can be obtained by multiplying the number of ways we can choose the "guest particle" by the partition function of $Q(N_1, N_2 + 1, T, V)$.

$$Q(N_1, N_2 + 1, T, V, \lambda = 1) = Q(N_1, N_2 + 1, T, V)N_2 \tag{2.26}$$

Combining Eqs.2.25-2.26 with Eq.2.22 yields:

$$\mu_2 = -k_B T \ln \frac{1}{N_2} - k_B T \ln \frac{Q(N_1, N_2 + 1, T, V, \lambda = 1)}{Q(N_1, N_2 + 1, T, V, \lambda = 0)} - k_B T \ln \Lambda_i^{-3}\langle V\rangle q_{int}(T) \tag{2.27}$$

Eq.2.27 may be rearranged to give:

$$\mu_2 = -k_B T \ln[\Lambda_i^{-3} q_{int}(T) \tfrac{k_B T}{P^0}] + k_B T \ln \tfrac{N_2 k_B T}{P^0 \langle V\rangle} - k_B T \ln \tfrac{Q(N_1, N_2+1, T, V, \lambda=1)}{Q(N_1, N_2+1, T, V, \lambda=0)} \tag{2.28}$$

In terms of mole fraction $x_2 = N_2/(N1 + N2)$, solution number density $\rho = (N_2 + N_1)/V$, and the standard state ideal gas chemical potential $\mu^0(T, P^0) = -k_B T \ln[\Lambda_i^{-3} q_{int}(T) \frac{k_B T}{P^0}]$, the chemical potential expression is:

$$\beta\mu_2 = \beta{\mu_2}^0(T, P^0) + \ln \frac{\rho k_B T}{P^0} + \ln x_2 - k_B T \ln \frac{Q(N_1, N_2 + 1, T, V, \lambda = 1)}{Q(N_1, N_2 + 1, T, V, \lambda = 0)} \tag{2.29}$$

Eq.2.29 relates the total chemical potential to quantities that can be calculated from molecular simulation of the free energy difference between two states. In the free energy perturbation calculation, the potential energy interaction of the "guest molecule" is $\lambda$-dependent such that with $\lambda = 0$ and $\lambda = 1$ we recover alchemical states A and B respectively. As

shown in Fig.2.4, one can go from state A to state B using any $\lambda$-dependent alchemical path and since the free energy is a state function, the free energy change would be the same. The parameter $\lambda$ scales the interaction potential of the "guest molecule" with the rest of the molecules. The $\lambda$-dependent canonical partition function of the system is:

$$Q(N_s^l, N_w, T, V, \lambda) = c \int_0^\infty \exp[-\beta U(\lambda)] dV \tag{2.30}$$

Differentiating Eq.2.30 with respect to $\lambda$ yields:

$$\frac{\partial \ln Q}{\partial \lambda} = \frac{\int_0^\infty -\beta U'(\lambda) \exp[-\beta U(\lambda)] dV}{\int_0^\infty \exp[-\beta U(\lambda)] dV} = \left\langle \frac{\partial U}{\partial \lambda} \right\rangle \tag{2.31}$$

where the bracket represents the ensemble average and $U(\lambda)$ is the interaction potential of the "guest molecule". Integrating from Eq.2.31 from $\lambda = 0$ to $\lambda = 1$ yields the following key equation which is calculated from molecular simulation at discrete values of the scaling parameter $\lambda$ by collecting the values of $\frac{\partial U}{\partial \lambda}$ over many configurations and $\lambda$ values.

$$-k_B T \ln \frac{Q(N_1, N_2 + 1, T, V, \lambda = 1)}{Q(N_1, N_2 + 1, T, V, \lambda = 0)} = \int_0^1 \left\langle \frac{\partial U}{\partial \lambda} \right\rangle d\lambda \tag{2.32}$$

The logarithmic term is referred to as canonical ensemble residual chemical potential $\mu_2^{res,NVT}(N1, N_2 + 1, T, \rho)$, or often refered to as conventional solvation/hydration free energy which is equivalent to the free energy of transfering the single molecule of type 2 to the solution of $N_1$ and $N_2$ molecules at the same volume. The residual chemical potential is the difference between the total chemical potential and its underlying ideality model. Note that this definition of the residual chemical potential is consistent with the density-based model of Eq.2.53 as both use the same underlying reference states.

$$\mu_2^{res,NVT}(N1, N_2 + 1, T, \rho) = \int_0^1 \left\langle \frac{\partial U_2}{\partial \lambda} \right\rangle d\lambda \tag{2.33}$$

This can be calculated by gradually turning on the interaction of the target molecule with the rest of the system using its $\lambda$-dependent interaction potential. To evaluate the residual chemical potential, the argument of the integral must be calculated at discrete values of the scaling parameter $\lambda$ and numerical integration yields the residual chemical potential. This is usually done in two separate steps, first growing the LJ interactions of the solute and then turning on the electrostatic interaction, and the total value is the sum of the two processes. At infinite dilution, $\mu_i^{res\infty,NVT}(P, T, \rho)$ maybe obtained using simulation of a

single solute molecule inserted into a box of solvent molecules.

## 2.6 Ideal Gas Chemical Potential ($\mu_i^0(T, P^0)$)

The ideal–gas chemical potential per particle of a species $i$ at $T$ and the standard state pressure $P^0$ relative to its atomic species at 0 K is calculated from its total partition function $q^0(T, V)$ using [76]:

$$\beta\mu_i^0(T, P^0) = -\ln[q_i^0(T, V)] \tag{2.34}$$

$q_i^0(T, V)$ maybe split into its translational, rotational, vibrational and electronic contributions,

$$q_i^0(T, V) = q_{\text{trans}} q_{\text{rot}} q_{\text{vib}} q_{\text{elect}} = q_{\text{trans}} q_{\text{int}} \tag{2.35}$$

where

$$q_{\text{trans}} = \frac{V}{\Lambda_i^3} = V\left(\frac{2\pi M_i k_B T}{h^2}\right)^{3/2} \tag{2.36}$$

$$q_{\text{rot}} = \frac{\pi^{1/2}}{\sigma}\frac{T^{3/2}}{(\phi_{r,x}\phi_{r,y}\phi_{r,z})^{1/2}} \tag{2.37}$$

$$q_{\text{vib}} = \prod_{j=1}^{3n-6}\frac{1}{1-\exp(\frac{-\phi_{vib,j}}{T})} \tag{2.38}$$

$$q_{\text{elect}} = \omega\exp(-\beta D_i) \tag{2.39}$$

where $D_i$ is the ground state energy level, and $\omega$ is its degeneracy. Defining

$$\hat{q}_i(T) = \frac{q_{\text{int}}(T)}{\Lambda_i^3} = \frac{q^0(T, V)}{V} \tag{2.40}$$

and using the ideal–gas law, $P^0V/kT = 1$, the ideal-gas chemical potential per particle relative to the molecule's atoms at 0 K may be expressed as:

$$\begin{aligned}\beta\mu_i^0(T; P^0) &= -\ln[\hat{q}_i(T)] + \ln\left(\frac{RT}{P^0}\right) + \beta D_i \\ &= \beta[G_i(T) - H_i(0)] - \beta\Delta H_{ai}(0)\end{aligned} \tag{2.41}$$

The sum of the first two terms gives the chemical potential with respect to the ground state of molecule $i$ at 0 K. When chemical reactions are considered, all $\mu_i$ must be measured with respect to a common energy level (taken as zero). $D_i$ may thus be measured with respect to the isolated atoms of the molecule (in which case, it is referred to as atomization energy, $\Delta H_{ai}$) or alternatively, with respect to the elements in their conventional standard states (the negative of which is referred to as the formation enthalpy, $\Delta H_{fi}$). In the context of chemical reactions, these terms are a major contribution to $\mu_i$.

## 2.7 Chemical Potential Models for Solutions: the General Case

(The material of this and the subsequent 2 sections is based on notes from the course CHE 725, "Research Topics in Chemical Process Analysis", taught by Prof. W. R. Smith in Winter 2018.)

Our goal in this section is to consider the mathematical forms for chemical potential models commonly used in practice. We will begin with a very general form satisfied by any model, and then focus on the common cases of these models. Using this approach facilitates the understanding of how to translate among the different forms. This is particularly important for understanding the translation of the form commonly used in statistical mechanics and molecular simulations to the formns commonly used for experimental descriptions. It also facilitates the ability to develop and use new forms suited to particular situations.

A mathematical model for the chemical potential model, $\mu_i$, of a species in a solution phase can be expressed in an infinite number of ways. We will describe the three steps involved in developing a specific model. These steps involve choices regarding overall thermodynamic variables among the set $\{T, P, \rho, V, \ldots\}$, the concentration variable, $z$, the reference state, $\mathbf{z}^0$, and the specification of an underlying ideal solution reference model.

We start with the following general expression for a $\mu_i$ model:

$$\mu_i = \mu_i^{\text{ref}}(\eta_1, \eta_2; \mathbf{z}^{0i}) + RT \ln a_i(\eta_1, \eta_2; \mathbf{z}) \tag{2.42}$$

where $\eta_1$ and $\eta_2$ are the overall thermodynamic variables, $\mathbf{z}$ is the composition vector, $(z_1, z_2, \ldots, z_N)^T$, $R$ is the universal gas constant, $\mu_i^{\text{ref}}(\eta_1, \eta_2; \mathbf{z}^{0i})$ is the chemical potential in the reference state (the state at which the activity is unity) at $(\eta_1, \eta_2)$ and concentration $\mathbf{z}^{0i}$, and $a_i$ is the *activity* of species $i$. $\xi_1$ and $\xi_2$ are intensive variables, and $(T, P)$ and $(T, \rho)$

are common choices. Note that the reference state composition may be different for each species. The main reason for the mathematical form of Eq. (2.42) is that it qualitatively conforms to the mathematical form of the expression for a mixture of ideal gases, discussed in the previous section.

In order to understand the origins of the different chemical potential models used in practise, and to understand how to generate new models that may be useful in particular circumstances, we first write Eq. (2.42) in several general forms, from which particular cases emerge. To this end, we first express $a_i$ in terms of an underlying *ideality model*. This is accomplished by writing the activity term as the product of a concentration and an *activity coefficient*, $\gamma_i(T, P; \mathbf{z})$, resulting in

$$\mu_i = \mu_i^{\text{ref}}(\eta_1, \eta_2; \mathbf{z}^{0i}) + RT \ln(z_i/z_i^0) + RT \ln \gamma_i(\eta_1, \eta_2; \mathbf{z}) \tag{2.43}$$

This can also be written as

$$\mu_i = \mu_i^{\text{ref}}(\eta_1, \eta_2; \mathbf{z}^{0i}) + RT \ln(z_i/z_i^0) + \mu_i^{\text{res}}(\eta_1, \eta_2; \mathbf{z}) \tag{2.44}$$

where $\mu_i^{\text{res}}(\eta_1, \eta_2; \mathbf{z})$ is the *residual chemical potential*. The residual chemical potential and its corresponding activity coefficient are thus related by

$$\mu_i^{\text{res}}(\eta_1, \eta_2; \mathbf{z}) = RT \ln \gamma_i(\eta_1, \eta_2; \mathbf{z}) \tag{2.45}$$

defined to satisfy the limiting behaviour

$$\lim_{\mathbf{z} \to \mathbf{z^{0i}}} \mu_i^{\text{res}}(\eta_1, \eta_2; \mathbf{z}) = 0 \tag{2.46}$$

$$\lim_{\mathbf{z} \to \mathbf{z}^{0i}} \gamma_i(\eta_1, \eta_2; \mathbf{z}) = 1 \tag{2.47}$$

The first two terms of Eqs. (2.43) and (2.44) comprise an *ideality model*, and we may write Eq. (2.44) as

$$\mu_i = \mu_i^{\text{id}}(\eta_1, \eta_2; \mathbf{z}^{0i}) + \mu_i^{\text{res},z}(\eta_1, \eta_2; \mathbf{z}) \tag{2.48}$$

where

$$\mu_i^{\text{id}} = \mu_i^{\text{ref}}(\eta_1, \eta_2; \mathbf{z}^{0i}) + RT \ln(z_i/z_i^0) \tag{2.49}$$

$\mu_i^{\text{res},z}(T, P; z_i)$ thus encapsulates the departure from the underlying ideality model.

## 2.8 Commonly Used Chemical Potential Models

Three steps are involved in the construction of a specific form of chemical potential model, which are as follows:

1. The first step is to choose the overall thermodynamic variables. For illustrative purposes in the following, we choose $(T, P)$ thermodynamic variables. This is sometimes called the Lewis-Randall framework, named after the two workers who published a pioneering chemical engineering textbook [77]) almost a century ago.

2. The second step is to choose a concentration variable, which may be different for different species in the phase. The commonest choices are mole fraction $x_i$, density, $\rho_i$, and molality, $m_i$. $x_i$ and $m_i$ are defined by:

$$x_i = \frac{n_i}{\sum_j n_j} \tag{2.50}$$

$$m_i = \frac{1000 n_i}{n_{\text{solv}} M_{\text{solv}}} \tag{2.51}$$

   where $n_i$ is the number of moles of species $i$, $n_{\text{solv}}$ is the number of moles of solvent, and $M_{\text{solv}}$ is its molecular weight. The density variable is defined by

$$\rho_i = \frac{n_i}{V} \equiv x_i \rho \tag{2.52}$$

   where $V$ is the total volume of the system and $\rho = n_T/V$ is the solution density. $\rho_i$ is sometimes replaced by the symbol $c_i$, and called a *concentration*.

3. The final, and perhaps the most important, choice is that of the reference state, $\mathbf{z}^{0i}$. The commonest cases are

   (a) Pure substance $i$ in its ideal gas state at $T$ and a reference state pressure $P^0$ or a reference state density $\rho^0$

   (b) Pure substance $i$ in its pure state at $(T, P)$ or at $(T, \rho^0)$.

   (c) Substance $i$ in a hypothetical state related to its properties at infinite dilution in the solvent; for historical reasons this is referred to as a Henry model. We will show its relationship to so–called Henry constants for vapour–liquid phase equilibrium, which are commonly used in chemical engineering.

Choice (a) is particularly useful, since the reference state properties depend only on $T$. This choice results in the following $\mu_i$ models:

$$\mu_i^{(T,\rho;\boldsymbol{x})} = \mu_i^{\phi}(T;\rho^0) + RT\ln\left(\frac{\rho_i}{\rho^0}\right) + \mu_i^{\mathrm{res},T,\rho,\boldsymbol{x}}(T,\rho,\boldsymbol{x}) \tag{2.53}$$

$$\mu_i^{(T,P;\boldsymbol{x})} = \mu_i^{0}(T;P^0) + RT\ln\left(\frac{x_i P}{P^0}\right) + \mu_i^{\mathrm{res},T,P,\boldsymbol{x}}(T,P,\boldsymbol{x}) \tag{2.54}$$

$\rho^0$ and $P^0$ are the respective reference state values of the concentration and pressure. The conventional choice for $P^0$ is $P^0 = 1$ bar (100 kPa), although prior to 1980, the convention was $P^0 = 1$ atm. (101.325 kPa); this is an important consideration when one uses older thermodynamic data based on the latter convention.

The first model is sometimes used by experimentalists, but is particularly useful in statistical mechanics, and we shall see that it is the most important model relevant to molecular simulation. Note also that the numerical value of $\mu_i^{\phi}(T;\rho^0)$ depends on the choice of units for $\rho$. For both models, the residual chemical potentials are defined to approach zero as the mole fraction of the substance approaches unity. Notice that, in that limit, the logarithmic terms vanish, and only the ideal gas reference state value remains.

Choice (b) leads to the following $\mu_i$ models:

$$\mu_i^{(T,\rho;\boldsymbol{x})} = \mu_i^{\omega}(T;\rho) + RT\ln x_i + \mu_i^{\mathrm{res},T,\rho,\boldsymbol{x}}(T,\rho,\boldsymbol{x}) \tag{2.55}$$

$$\mu_i^{(T,P;\boldsymbol{x})} = \mu_i^{*}(T;P) + RT\ln x_i + \mu_i^{\mathrm{res},T,P,\boldsymbol{x}}(T,P,\boldsymbol{x}) \tag{2.56}$$

The Choice (a) can be rearranged to yield

$$\mu_i^{(T,\rho;\boldsymbol{x})} = \left[\mu_i^{\phi}(T;\rho^0) + RT\ln\left(\frac{\rho}{\rho^0}\right)\right] + RT\ln x_i + \mu_i^{\mathrm{res},T,\rho,\boldsymbol{x}}(T,\rho,\boldsymbol{x}) \tag{2.57}$$

$$\mu_i^{(T,P;\boldsymbol{x})} = \left[\mu_i^{0}(T;P^0) + RT\ln\left(\frac{P}{P^0}\right)\right] + RT\ln x_i + \mu_i^{\mathrm{res},T,P,\boldsymbol{x}}(T,P,\boldsymbol{x}) \tag{2.58}$$

Grouping the terms in brackets as $\mu_i^{\omega}(T;\rho)$ and $\mu_i^{*}(T;P)$ thus give particular cases of Choice (b).

The Henry models of Choice (c) merit special attention. Three examples are

$$\mu_i = \mu_i^{\dagger}(T,P;m^0) + RT\ln\left(\frac{m_i}{m^0}\right) + \mu_i^{\mathrm{res},H(T,P,m)}(T,P;\boldsymbol{m}) \tag{2.59}$$

$$= \mu_i^{\omega_{\mathrm{H}}}(T,\rho;\rho^0) + RT\ln\left(\frac{\rho_i}{\rho^0}\right) + \mu_i^{\mathrm{res},H(T,\rho,x)}(T,\rho;\boldsymbol{\rho}) \tag{2.60}$$

$$= \mu_i^{*_{\mathrm{H}}}(T,P;x^0) + RT\ln\left(\frac{x_i}{x^0}\right) + \mu_i^{\mathrm{res},H(T,P,x)}(T,P;\boldsymbol{x}) \tag{2.61}$$

where the superscripts on the residual terms emphasize that they are specific to the underlying ideality models defined by the relevant first two terms on the right sides of the equal sign. For these models, For these models, the residual terms vanish as the species concentration approaches zero. When the residual terms are expressed in terms of activity coefficients as in Eq. (2.45), this is equivalent to defining the limiting value of its logarithm to also be zero. The underlying ideality model is thus obeyed only at extremely low concentrations, and only exactly in the limit of infinitely dilute solutions. As a result, the reference state quantities for these models refer to a hypothetical state where the species composition variable is equal to its reference state composition, respectively $\rho^0, x^0$ or $m^0$. For the models of Eqs. (2.56) and (2.59), the natural and universally used choices are $x^0 = 1$ and $m^0 = 1$ mol kg$^{-1}$ solvent, $\rho^0 = 1$ and the reference states are thus hypothetical ideal solutions at unit values of $x_i$ and $m_i$. This allows those models to be written as

$$\begin{aligned}\mu_i &= \mu_i^{*_{\mathrm{H}}}(T,P;x^0) + RT\ln x_i + \mu_i^{\mathrm{res},H(T,P,x)}(T,P;\boldsymbol{x}) \\ &= \mu_i^{\dagger}(T,P;m^0) + RT\ln m_i + \mu_i^{\mathrm{res},H(T,P,m)}(T,P;\boldsymbol{m})\end{aligned} \tag{2.62}$$

## 2.9 Translating Between Models

Translating between chemical potential models is often required, and in this section we describe a general methodology for performing this task. The underlying principle that facilitates the translation is the observation that given values of the overall thermodynamic variables and composition fixes the values of all other intensive properties of the phase. This is the *state postulate* for solutions, analogous to the corresponding postulate for pure substances, which states that all intensive properties are determined by setting any two independent intensive properties. We refer to the use of this principle for solutions as the *state consistency principle*.

A consequence of this principle for a system with specified $(T, P, \mathbf{x})$ and alternatively by specified $(T, \rho, \mathbf{x})$ must have the same values for all intensive properties. The species

chemical potentials are an example of such intensive properties, and this means that we can equate the alternative forms for the chemical potentials.

### 2.9.1 $(T, \rho)$ and $(T, P)$ Models

Here, we consider translating between the models of Eqs. (2.53) and (2.54). This is an important issue, since reference state ideal-gas chemical potentials are most commonly available as values of $\mu_i^0(T, P^0)$. The key is the observation that since both models entail the use of an underlying ideal–gas model, we can carry out the translation using the latter models, *i.e.*, when the residual terms vanish.

We thus consider the translation between the models

$$\mu_i = \mu_i^{\phi}(T; \rho^0) + RT \ln\left(\frac{x_i \rho}{\rho^0}\right) \tag{2.63}$$

$$\mu_i = \mu_i^0(T; P^0) + RT \ln\left(\frac{x_i P}{P^0}\right) \tag{2.64}$$

The state consistency principle allows us to equate the chemical potential expressions

$$\mu_i^{\phi}(T; \rho^0) + RT \ln\left(\frac{x_i \rho_i}{\rho^0}\right) = \mu_i^0(T; P^0) + RT \ln\left(\frac{x_i P}{P^0}\right) \tag{2.65}$$

We next use the fact that we are dealing with an ideal gas mixture, which satisfies

$$P = \rho RT \tag{2.66}$$

Substituting Eq. (2.66) in Eq. (2.65) gives

$$\mu_i^{\phi}(T; \rho^0) + RT \ln\left(\frac{\rho_i}{\rho^0}\right) = \mu_i^0(T; P^0) + RT \ln\left(\frac{x_i \rho RT}{P^0}\right) \tag{2.67}$$

which yields

$$\mu_i^{\phi}(T; \rho^0) = \mu_i^0(T; P^0) + RT \ln\left(\frac{RT\rho^0}{P^0}\right) \tag{2.68}$$

The general result for the model of Eq. (2.53) is thus

$$\mu_i^{(T,\rho;\boldsymbol{x})} = \mu_i^0(T; P^0) + RT \ln\left(\frac{RT\rho^0}{P^0}\right) + RT \ln\left(\frac{\rho_i}{\rho^0}\right) + \mu_i^{\mathrm{res},T,\rho,\boldsymbol{x}}(T, \rho, \boldsymbol{x}) \tag{2.69}$$

where $\rho$ is the density at the specified $(P, T)$. This is a deceptively simple result, and we must be aware that the numerical value of the second term depends on the density units used.

Some typical examples are (for $P^0 = 1$ bar $=10^5$ Pa at 298.15 K):

1. $\rho$ in mol m$^{-3}$:

$$\begin{aligned} RT \ln\left(\frac{RT\rho^0}{P^0}\right) &= \frac{(8.31446)(298.15)}{1000} \ln\left(\frac{(8.31446)(298.15)}{10^5}\right) \\ &= -9.165525708 \text{ kJ mol}^{-1} \end{aligned} \tag{2.70}$$

2. $\rho$ in mol L$^{-1}$:

$$\begin{aligned} RT \ln\left(\frac{RT\rho^0}{P^0}\right) &= \frac{(8.31446)(298.15)}{1000} \ln\left(\frac{(8.31446)(298.15)(1000)}{10^5}\right) \\ &= 7.958497407 \text{ kJ mol}^{-1} \end{aligned} \tag{2.71}$$

3. $\rho$ in particles m$^{-3}$:

$$\begin{aligned} RT \ln\left(\frac{RT\rho^0}{P^0}\right) &= \frac{(8.31446)(298.15)}{1000} \ln\left(\frac{(8.31446)(298.15)}{(6.022140857 \times 10^{23})(10^5)}\right) \\ &= -144.9005271 \text{ kJ mol}^{-1} \end{aligned} \tag{2.72}$$

4. $\rho$ in particles nm$^{-3}$:

$$\begin{aligned} RT \ln\left(\frac{RT\rho^0}{P^0}\right) &= \frac{(8.31446)(298.15)}{1000} \ln\left(\frac{(8.31446)(298.15)(10^{27})}{(6.022140857 \times 10^{23})(10^5)}\right) \\ &= 9.215680914 \text{ kJ mol}^{-1} \end{aligned} \tag{2.73}$$

We note in passing that these values will change slightly if the standard state pressure for the $\mu^0(T; P^0)$ value is $P^0 = 1$ atm. $= 1.01325$ bar, by the subtraction of the quantity $RT \ln(1.01325)$ from each of the above quantities. At 298.15 K, its value is

$$\frac{(8.31446)(298.15)}{1000} \ln 1.01325 = 0.03263 \text{ kJ mol}^{-1} \tag{2.74}$$

### 2.9.2 Henry $(T,P)$ Model and General $(T,\rho)$ Model

The Henry $(T,P)$ model of Eq. (2.61) is of widespread use in chemistry and chemical engineering, and $\mu_i^\dagger(T,P;m^0)$ values are available in compilations (*e.g.*, [78]). We consider the translation of this Henry model to the general density–based model of Eq. (2.69). Invoking the state consistency principle, we first equate the models to give

$$\left.\begin{array}{l} \mu_i^\dagger(T,P;m^0) + RT\ln\left(\frac{m_i}{m^0}\right) \\ +\mu_i^{\mathrm{res},H(T,P,m)}(T,P;\boldsymbol{m}) \end{array}\right\} = \left\{\begin{array}{l} \mu_i^0(T;P^0) + RT\ln\left(\frac{RT\rho^0}{P^0}\right) + RT\ln\left(\frac{\rho_i}{\rho^0}\right) \\ +\mu_i^{\mathrm{res},T,\rho,\boldsymbol{x}}(T,\rho,\boldsymbol{x}) \end{array}\right. \tag{2.75}$$

Substituting Eqs. (2.50)–(2.52) in Eq. (2.75) gives

$$\begin{aligned} \mu_i^\dagger(T,P;m^0) &= \mu_i^0(T;P^0) + RT\ln\left(\frac{RT\rho^0 n_{\mathrm{solv}} M_{\mathrm{solv}} m^0}{1000P^0 V(T,P;m)}\right) \\ &\quad +\mu_i^{\mathrm{res},T,\rho,\boldsymbol{x}}(T,\rho,\boldsymbol{x}) - \mu_i^{\mathrm{res},H(T,P,m)}(T,P;\boldsymbol{m}) \end{aligned} \tag{2.76}$$

We now take the limit of infinite dilution of species $i$, which causes $\mu_i^{\mathrm{res},H(T,P,m)}(T,P;\boldsymbol{m})$ to approach zero, giving the final result

$$\mu_i^\dagger(T,P;m^0) = \mu_i^0(T;P^0) + RT\ln\left(\frac{RT\rho_{\mathrm{solv}}(T,P)M_{\mathrm{solv}}\rho^0 m^0}{1000P^0}\right) + \mu_i^{\mathrm{res},T,\rho,\infty}(T,\rho_{\mathrm{solv}}) \tag{2.77}$$

where the notation $\infty$ indicates that the residual chemical potential refers to infinite dilution of species $i$ in the solvent (which contains all species except for species $i$ and is at the $(T,P)$ of the solution).

For a cation–anion pair, $\mu_i^\dagger(T,P)$ is given by

$$\begin{aligned} \mu_i^\dagger(T,P) &= \mu_{\mathrm{cat}}^0(T;P^0) + \mu_{\mathrm{an}}^0(T;P^0) + 2RT\ln\left(\frac{RT}{100P^0}\right) + 2RT\ln\left(\frac{\overline{\rho}_{\mathrm{solv}}(T,P)}{1000}\right) \\ &\quad +\mu_{\mathrm{cat}}^{\mathrm{res},NVT,\infty}[T,\rho_{\mathrm{solv}}(T,P)] + \mu_{\mathrm{an}}^{\mathrm{res},NVT,\infty}[T,\rho_{\mathrm{solv}}(T,P)] \end{aligned} \tag{2.78}$$

The $\ln(\gamma_i)$ is given by,

$$\mu_i^{\mathrm{res,H}}(T,P,\boldsymbol{m}) \equiv RT\ln\gamma_i(T,P,\boldsymbol{m}) \tag{2.79}$$

$$= RT\ln\left(\frac{x_{\mathrm{solv}}\rho_{\mathrm{soln}}(T,P;\boldsymbol{m})}{\rho^*_{\mathrm{solv}}(T,P)}\right) + \mu_i^{\mathrm{res},NVT}[T,\rho_{\mathrm{soln}}(T,P),\boldsymbol{x}] - \mu_i^{\mathrm{res},NVT,\infty}[T,\rho^*_{\mathrm{solv}}(T,P)] \tag{2.80}$$

where $x_{\mathrm{solv}}$ is the solvent mole fraction in the solution.

### 2.9.3 Henry $(T,\rho)$ Model and General $(T,\rho)$ Model

Proceeding as before, we first set the chemical potential models of Eqs. (2.60) and (2.69) equal to each other, giving

$$\left.\begin{array}{l}\mu_i^{\omega_{\mathrm{H}}}(T,\rho;\rho^0) + RT\ln\left(\frac{\rho_i}{\rho^0}\right) \\ +\mu_i^{\mathrm{res},H(T,\rho,x)}(T,\rho;\boldsymbol{\rho})\end{array}\right\} = \left\{\begin{array}{l}\mu_i^0(T;P^0) + RT\ln\left(\frac{RT\rho^0}{P^0}\right) + RT\ln\left(\frac{\rho_i}{\rho^0}\right) \\ +\mu_i^{\mathrm{res},T,\rho,\boldsymbol{x}}(T,\rho,\boldsymbol{x})\end{array}\right. \tag{2.81}$$

Taking the infinite dilution limit gives

$$\mu_i^{\omega_{\mathrm{H}}}(T,\rho;\rho^0) = \mu_i^0(T;P^0) + RT\ln\left(\frac{RT\rho^0}{P^0}\right) + \mu_i^{\mathrm{res},T,\rho,\infty}(T,\rho_{\mathrm{solv}}(T,P)) \tag{2.82}$$

Note that the values of $\mu_i^{\omega_{\mathrm{H}}}(T,\rho;\rho^0)$ and $\mu_i^{\dagger}(T,P;m^0)$ differ, according to

$$\mu_i^{\dagger}(T,P;m^0) = \mu_i^{\omega_{\mathrm{H}}}(T,\rho;\rho^0) + RT\ln\left(\frac{\rho_{\mathrm{solv}}(T,P)M_{\mathrm{solv}}m^0}{1000}\right) \tag{2.83}$$

For water as the solvent, at $T = 298.15$ K and $P^0 = 1$ bar (and $m^0 = 1$ mol kg$^{-1}$, the value of the final term in kJ mol$^{-1}$ using $\rho$ in mol L$^{-1}$ and the experimental water density of 55.342 mol L$^{-1}$ [79] is

$$\frac{(8.31446)(298.15)}{1000}\ln\left(\frac{(55.342)(18.01528)}{1000}\right) = -0.007444 \tag{2.84}$$

This is a very small quantity at ambient conditions, but it becomes significant at larger values of $T$. For example, at 373 C and 10 bar, the density of liquid water is 53.2 mol L$^{-1}$,

and the value is

$$\frac{(8.31446)(373)}{1000}\ln\left(\frac{(53.2)(18.01528)}{1000}\right) = -0.132 \tag{2.85}$$

### 2.9.4 Henry $(T, P; x)$ Model and General $(T, \rho)$ Model

Proceeding in the same way as previously, we obtain

$$\mu_i^{*\mathrm{H}}(T, P; x^0) = RT\ln\left(\frac{RT\rho_{\mathrm{solv}}}{P^0}\right) + \mu_i^{\mathrm{res},T,\rho,\infty}(T, \rho_{\mathrm{solv}}(T, P)) \tag{2.86}$$

# Chapter 3

# An efficient molecular simulation methodology for chemical reaction equilibria in electrolyte solutions: Application to $CO_2$ reactive absorption.



## Abstract

We develop a general molecular–based simulation algorithm for chemical reaction equilibria in liquids containing neutral and ionic species, which is based on the combination of classical force field and quantum mechanical methodologies. We show its application to the reactive absorption of $CO_2$ in aqueous monoethanolamine (MEA) solvent as a benchmark case, the first time that a quantitatively accurate predictive approach requiring no experimental data has been successfully applied to calculate all solution species concentrations

for this system, including the partial pressure of $CO_2$ above the solution. The reaction equilibrium composition is simulated using a variant of the recently developed ReMD algorithm (W.R. Smith and W. Qi, ACS Cent. Sci. **2018 4**, 1185–1193), which permits calculations involving very small species concentrations.

The $H_2O$–MEA–$CO_2$ benchmark system has been the subject of many previous studies based on macroscopic thermodynamic models, which primarily involve fitting their parameters (of which reaction $pK$ values are the most important) to experimental data. To make contact with such approaches, we show the translation of the molecular–based quantities to the direct prediction of these parameters, and calculate reaction equilibrium in the framework of a Henry–Law–based chemical potential model. We consider both the ideal solution form and its extension using the Davies equation for the species activity coefficients. We study a range of temperatures and $CO_2$ solution loadings in a 30 weight % MEA solution, and incorporate an Uncertainty Analysis in our methodology. The quality of the predictions from the simulations is comparable to that of the experimental results, and the extension of the approach to other electrolyte solutions is described.

## 3.1 Introduction

Calculation of the equilibrium composition of chemically reacting systems is of great interest and importance in chemistry, biology and chemical engineering. Systems involving ionic species (especially aqueous electrolyte systems) are of particular significance, and have long been studied using macroscopic thermodynamic tools [80, 81].

Carbon Capture and Storage (CCS) methodology applied to fixed $CO_2$ sources is currently considered to be one of the most advanced programs to reduce greenhouse gas emissions, and the development of more economically effective technologies is crucial to encouraging its future deployment (for reviews, see, *e.g.*, Kumoro *et al.* [82] and Song *et al.* [83]). Strategies based on $CO_2$ capture from point sources using reactive absorption in solvents is considered to be a viable option, and aqueous solutions of monoethanolamine (MEA, also referred to herein as $RNH_2$), where $R = (CH_2)_2OH$) were one of the first solvents used for this purpose. Its drawbacks include the large energy cost of regeneration from the $CO_2$–loaded, and this has spurred the search for improved solvents.

The search for such solvents has involved the use of chemical reaction equilibrium (CRE) calculations based on thermodynamic models for the involved aqueous $CO_2$–aqueous electrolyte solutions[84, 85, 86, 87, 88, 89, 90, 91, 92, 93, 94, 95]. Model development is complicated by the fact that its parameters are not directly measurable quantities, but must be obtained indirectly by fitting to experimental data. Thus, most $CO_2$ reactive absorption models in the experimental literature can be considered to be primarily correlations rather than predictions, and the resulting parameter values show considerable variation among different research groups.

A less expensive and more fundamentally based approach to CRE modeling involves the use of molecular–based methodology, which in principle requires little or no experimental data and is thereby predictive in nature. Several groups have focussed attention on the calculation of solution properties at infinite dilution (for example, reaction $pK$ values) using approximate quantum mechanical (QM) approaches (recent examples are the works of Gupta *et al.* [96] and Taranishi*et al.* [97]). Although such properties are important, these methods are computationally infeasible for calculating solution properties at higher concentrations due to their computational complexity.

Although classical force field (CFF) methodology has been used extensively for non–reacting systems, there have been relatively few studies of its application to systems undergoing chemical reactions, and fewer still involving systems containing reacting ionic species. CRE implementation by means of the Reaction Ensemble Monte Carlo (REMC) algorithm[32, 98] and its variants (for a review, see Turner *et al.* [99]) has been used

for multi–reaction plasma systems[100, 101], to a single-reaction ionic liquid system[102]. It has also been applied in a preliminary study of $CO_2$ solubility modeling in aqueous monoethanolamine involving four reactions[103], with which we make comparisons in this study. Since REMC implementation relies on a system–specific combination of alchemical and insertion moves, special system–dependent techniques such as Continuous Fractional Component (CFC) reaction moves[104, 105, 103, 106] must be used at liquid densities. However, the recent paper of Mullen *et al.* [102] found CFC to fail, and they replaced it with an alternative (system–dependent) approach. Another challenge in molecular-based CRE simulations is calculations involving very small species amounts (*e.g.*, concentrations of $10^{-4}$ or less), which at first sight would seem to require infeasibly large system sizes.

The recently developed ReMD algorithm of Smith and Qi[44], based on the relatively straightforward and system independent calculation of species chemical potentials using general–purpose Molecular-Dynamics (MD) software in conjunction with thermodynamic integration, was designed to overcome both of the above problems. Based on macroscopic thermodynamic principles, it minimizes the Gibbs energy by calculating an iterative sequence of compositions, which are used as reference states for an ideal solution extrapolation model. We apply it here to the case of the aqueous MEA–$CO_2$ system, using the infinite dilution reference state as the initial approximation and extrapolating the chemical potentials using the Henry Law ideality model or its extension incorporating the Davies equation for the activity coefficients[107]. This technique can also be used to calculate the concentrations of species present in very small concentrations. In this paper, we implement the ReMD algorithm using a combination of QM and MD procedures, resulting in an approach that is entirely predictive and utilizes no experimental data.

In the course of our study, we provide uncertainty estimates of the predicted partial pressure of $CO_2$ above the solution by propagating the uncertainties in the underlying parameters. We remark that the importance of uncertainty analysis applied to thermodynamic models of $CO_2$ reactive absorption has also recently been emphasized by Morgan*et al.* [108] and by others[109, 110].

The paper is organized as follows. The next section briefly reviews CRE calculation methodology in the context of conventional macroscopically based Henry-Law-based chemical potential models, and the subsequent section relates the relevant molecular simulation quantities to the macroscopic parameters and outlines the CRE calculation procedures. The following section describes the systems studied, and the relevant molecular models and simulation protocols used. The next section give our results and their discussion, followed by a section presenting our conclusions and recommendations.

## 3.2 Reaction Equilibrium Using Henry-Law-Based Chemical Potential Models

In Section 3.3, we translate our molecular simulation CRE model to the Henry–Law-based model, which is commonly used in macroscopic theoretical and experimental studies of electrolyte solutions and is briefly reviewed here.

$$\mu_i(T,P;\boldsymbol{m}) = \mu_i^{\dagger}(T;P) + RT\ln\left(\frac{m_i}{m^0}\right) + RT\ln\gamma_i(T,P;\boldsymbol{m});\quad i=1,2,\ldots,N_s \tag{3.1}$$

where $T$ is the absolute temperature, $P$ the pressure, $R$ the universal gas constant, $\mu_i(T,P;\boldsymbol{m})$ is the chemical potential of species $i$, $\boldsymbol{m}$ is the vector of molalities, $\gamma_i$ is the species activity coefficient, and $N_s$ is the number of solution species. $\mu_i^{\dagger}(T;P)$ is the standard state chemical potential of solute species $i$ in a hypothetical ideal solution of $m^0 = 1$ molal. In the $CO_2$-$H_2O$ system, we take $H_2O$ as the solvent and consider all other species to be solutes.

The chemical potential model for the solvent based on its pure component reference state is normally used:

$$\mu_{\text{solv}}(T,P;\boldsymbol{m}) = \mu_{\text{solv}}^{*}(T,P) + RT\ln a_{\text{solv}}(T,P;\boldsymbol{m}) \tag{3.2}$$

where $\mu_{\text{solv}}^{*}(T,P)$ is the chemical potential of the pure solvent at the solution $(T,P)$ and $a_{\text{solv}}$ is its activity in the solution.

Reaction equilibrium in a closed system at specified $(T,P)$ can be calculated by minimizing its Gibbs free energy subject to the conservation of mass constraints, the latter of which may be implemented by means of a set of $R$ linearly independent stoichiometric reactions, where

$$R = N_s - \text{rank}(\boldsymbol{A}) \tag{3.3}$$

$\boldsymbol{A}$ is the $N_s \times M$ matrix of chemical formulae and $M$ is the number of chemical elements[111]. It is important to note that the reaction set is independent of any underlying reaction mechanism, and may be selected based on numerical convenience.

The equilibrium composition is then determined by the solution of the equations

$$\Delta G_j \equiv \sum_{i=1}^{N_s} \nu_{ij}\mu_i = 0;\quad j=1,2,\ldots,R \tag{3.4}$$

where $\nu_{ij}$ is the stoichiometric coefficient of species $i$ in reaction $j$. Substitution of Eqs.

(3.1) and (3.2) in Eq. (3.4) yields the final working equations:

$$\frac{\Delta\widetilde{G}_j(T,P)}{RT} + \sum_{i=1}^{N_{\text{solu}}} \nu_{ij} \ln\left(\frac{m_i}{m^0}\right) + \sum_{i=1}^{N_{\text{solu}}} \nu_{ij} \ln\gamma_i(T,P;\boldsymbol{m}) + \nu_{\text{solv},j} \ln a_{\text{solv}}(T,P;\boldsymbol{m}) = 0 \quad (3.5)$$

where

$$\Delta\widetilde{G}_j(T,P) = \sum_{i=1}^{N_{\text{solu}}} \nu_{ij}\mu_i^{\dagger}(T,P) + \nu_{\text{solv},j}\mu_{\text{solv}}^{*}(T,P) \quad (3.6)$$

The $\widetilde{G}_j(T,P)$ values are commonly expressed in terms of equilibrium constants $K_j$ via

$$\ln(10) pK_j(T,P) = -\frac{\Delta\widetilde{G}_j(T,P)}{RT} \quad (3.7)$$

where $pK_j = -\log_{10}K_j$.

The solute activity coefficients $\gamma_i(T,P;\boldsymbol{m})$ in Eq. (3.1) may be modelled in various ways. In this paper, we consider (1) the ideal Henry-Law solution model with $\ln\gamma_i = 0$, and (2) the empirical Davies model [107]:

$$\ln(\gamma_i) = -z_i^2 A(T,P)\left(\frac{\sqrt{I}}{1+\sqrt{I}} - 0.3I\right) \quad (3.8)$$

where $z_i$ is the valence, and $A(T,P)$ is related to the pure solvent dielectric permittivity and density by [112, 113]

$$A(T,P) = 0.13287 \times 10^6 \frac{[\overline{\rho}_{\text{solv}}(T,P)]^{1/2}}{[\epsilon_{r,\text{solv}}(T,P)T)]^{3/2}} \quad (3.9)$$

where $\overline{\rho}_{\text{solv}}(T,P)$ is the density of the solvent in kg m$^{-3}$. $\epsilon_{r,\text{solv}}$ is the solvent relative static permittivity and $I$ is the solution ionic strength, defined by

$$I = \frac{1}{2}\sum_{i=1}^{N_s} m_i z_i^2 \quad (3.10)$$

$\ln a_{\text{solv}}$ in Eqs. (3.2) and (3.5) for these models is obtained by means of the Gibbs–Duhem

equation:

$$\ln a_{\rm solv}^{\rm Ideal} = -\left(\frac{1-x_{\rm solv}}{x_{\rm solv}}\right) \tag{3.11}$$

$$\ln a_{\rm solv}^{\rm Davies} = \frac{M_{\rm solv}}{1000}A(T,P)\left[2\left(\frac{1+2\sqrt{I}}{1+\sqrt{I}}\right)-4\ln(1+\sqrt{I})-0.3I^2\right]-\frac{1-x_{\rm solv}}{x_{\rm solv}} \tag{3.12}$$

## 3.3 Molecular-Based Calculation of $pK_j$

### 3.3.1 Relation to Ideal–Gas and Hydration Free Energy Quantities

$\mu_i^\dagger$ values for the solute species in Eq. (3.1) are calculated by molecular simulation using the following expression [114, 115, 116, 117] (see also Section 2 of the Supporting Information):

$$\mu_i^\dagger(T,P) = \mu_i^0(T;P^0)+\Delta G_i^{\rm hyd}(T,P)+\Delta G_i^{\rm corr}(T,P) \tag{3.13}$$

where $\mu_i^0(T;P^0)$ is the species ideal–gas standard chemical potential at $T$ and the reference state pressure $P^0 = 1$ bar, $\Delta G_i^{\rm hyd}(T,P)$ is its absolute hydration free energy, and $\Delta G_i^{\rm corr}$ is a (typically small in magnitude) correction term that includes [116] (1) a finite–size correction term to account for the size dependence of the simulations; (2) a correction for the mean effect of electrostatic interactions beyond the simulation cutoff distance, depending on the relative dielectric permittivity of the water model used in the simulation; (3) a quantum correction term.

$\Delta G_i^{\rm hyd}(T,P)$ is given by

$$\Delta G_i^{\rm hyd}(T,P) = \Delta G^{\rm std}(T,P)+\Delta G_i^{\rm intr}[T,\rho_{\rm solv}(T,P)] \tag{3.14}$$

where $\Delta G^{\rm std}(T;P^0)$ accounts for the change from the reference state pressure of $P^0 = 1$ bar in the ideal–gas state to a reference state solution concentration of 1 molal, $\Delta G_i^{\rm intr}$ is the intrinsic solvation free energy of species $i$, and $\rho_{\rm solv}(T,P)$ is the pure solvent density at the specified $(T,P)$. The first two quantities are given by

$$\Delta G^{\rm std}(T,P) = RT\ln\left(\frac{RT\overline{\rho}_{\rm solv}(T,P)m^0}{10^5P^0}\right) \tag{3.15}$$

$$\Delta G_i^{\rm intr}(T,P) = \mu_i^{{\rm res},NVT,\infty}[T,\rho_{\rm solv}(T,P)] \tag{3.16}$$

where $\overline{\rho}_{\rm solv}(T,P)$ is the pure solvent density in kg m$^{-3}$, $P^0$ is in bar, and $\mu_i^{{\rm res},NVT}[T,\rho(T,P)]$ is the residual chemical potential of species $i$ at infinite dilution in the pure solvent calculated by molecular simulation from Eq. (3.16).

Excluding the relatively small correction terms, $\mu_i^\dagger$ for a solute may be conveniently expressed as

$$\frac{\mu_i^\dagger(T,P)}{RT} = \frac{\mu_i^0(T;P^0)}{RT} + \ln\left(\frac{RT}{100P^0}\right) + \ln\left(\frac{\overline{\rho}_{\rm solv}(T,P)}{1000}\right) + \frac{\mu_i^{{\rm res},NVT}[T,\rho(T,P)]}{RT} \quad (3.17)$$

We remark that $\mu_i^\dagger(T,P)$ values for individual ions calculated from the above expressions are different from the "conventional" experimental values given in thermochemical tables (*e.g.*, Wagman *et al.* [78]); however, values for charge–conserving linear combinations of ions agree with the results using corresponding tabular values. Such linear combinations always occur in chemical reactions involving ions, as is the case in this study. (In order to match the conventional individual ionic values, a term involving the electrostatic Galvani potential at the vacuum/water interface, and a term involving the intrinsic hydration free energy of the proton must be included; see, *e.g.*, Majer *et al.* [118].)

The pure solvent chemical potential is given by

$$\frac{\mu_{\rm solv}^*(T,P)}{RT} = \frac{\mu_{\rm solv}^0(T;P^0)}{RT} + \ln\left(\frac{\rho_{\rm solv}(T,P)RT}{10^5P^0}\right) + \frac{\mu_{\rm solv}^{{\rm res},NVT}[T,\rho_{\rm solv}(T,P)]}{RT} \quad (3.18)$$

where $P^0$ is in bar, and $\rho$ is in units of mol m$^{-3}$. This may be rewritten as

$$\frac{\mu_{\rm solv}^*(T,P)}{RT} = \frac{\mu_{\rm solv}^\dagger(T;P)}{RT} + \ln\left(\frac{1000}{M_{\rm solv}m^0}\right) \quad (3.19)$$

$\Delta\widetilde{G}_j(T,P)$ and $pK_j(T,P)$ in Eqs. (3.6) and (3.7) can then be obtained from

$$\Delta\widetilde{G}_j(T,P) = \Delta G_j^\dagger(T,P) + \nu_{{\rm solv},j}RT\ln\left(\frac{1000}{M_{\rm solv}}\right) \quad (3.20)$$

where

$$\begin{aligned}
\Delta G_j^{\dagger} &= \Delta G_j^0(T;P^0) + RT\overline{\nu}_j \left[\ln\left(\frac{RT}{100P^0}\right) + \ln\left(\frac{\overline{\rho}_{\rm solv}(T,P)m^0}{1000}\right)\right] \\
&\quad + \Delta\Delta G_j^{\rm intr}(T,P) \qquad (3.21)\\
\overline{\nu}_j &= \sum_{i=1}^{N_s} \nu_{ij} \qquad (3.22)\\
\Delta G_j^0(T;P^0) &= \sum_{i=1}^{N_s} \nu_{ij}\mu_i^0(T;P^0) \qquad (3.23)\\
\Delta\Delta G_j^{\rm intr}(T,P) &= \sum_{i=1}^{N_s} \nu_{ij}\Delta G_i^{\rm intr}(T,P) \qquad (3.24)
\end{aligned}$$

### 3.3.2 Ideal Gas (IG) Quantities

The IG $\mu_i^0(T;P^0)$ values may be expressed in terms of statistical mechanical expressions and calculated from

$$\begin{aligned}
\mu_i^0(T;P^0) &= -RT\ln\left[\frac{q_i^0(T,V)}{V}\frac{RT}{P^0}\right] - \Delta H_{ai}(0) \\
&= [G_i(T) - H_i(0)] - \Delta H_{ai}(0) \qquad (3.25)
\end{aligned}$$

where $q_i^0(T,V)$ is the molecule's internal partition function and $\Delta H_{ai}(0)$ is its atomization energy at 0 K. Finally, we may write $\Delta G_j^0(T;P^0)$ as

$$\begin{aligned}
\Delta G_j^0(T;P^0) &= \sum_{i=1}^{N_s} \nu_{ij}[G_i(T) - H_i(0)] - \sum_{i=1}^{N_s} \nu_{ij}\Delta H_{ai}(0) \qquad (3.26)\\
&= \Delta_j[G(T) - H(0)] + \Delta G_j(0) \qquad (3.27)
\end{aligned}$$

where the quantities on the right are calculated at $P^0 = 1$ bar. The quantities in Eq. (3.26) may be obtained from quantum mechanical calculations, as described in Section 3.4.3.

## 3.4 Systems Studied and Computational Details

Our aqueous MEA-$CO_2$ system model contains the species $\{H_2O, RNH_2, CO_2, RNH_3^+, RNHCOO^-, H_3O^+, OH^-, HCO_3^-\}$ ($CO_3^{2-}$ is neglected as being vanishingly small), where $R = HO(CH_2)_2$. The $CO_2$ absorption process is modelled as a solution in equilibrium with a vapour phase at a total pressure of 1 bar, and we calculated solution compositions at several temperatures, solvent weight fractions, $\omega$ (kg MEA/kg solvent), and $CO_2$ loadings, $L$(mol $CO_2$/mol MEA).

### 3.4.1 Force Fields

All nonbonded intermolecular interactions were modeled using a standard 12-6 Lennard-Jones (LJ) plus Coulombic potential with fixed point charges

$$U_{\mathrm{nb}}\left(r_{ij}\right) = 4\varepsilon_{ij}\left[\left(\frac{\sigma_{ij}}{r_{ij}}\right)^{12} - \left(\frac{\sigma_{ij}}{r_{ij}}\right)^{6}\right] + \frac{1}{4\pi\varepsilon_0}\frac{q_i q_j}{r_{ij}} \tag{3.28}$$

where $\varepsilon_{ij}$ and $\sigma_{ij}$ are the LJ energy and size parameters, respectively, $q_i$ is the atomic partial charge of atom $i$, and $r_{ij}$ is the separation distance between atoms $i$ and $j$. Unlike intermolecular interactions were calculated using Lorentz-Berthelot combining rules. All intramolecular bonded and LJ parameters for MEA, $HCO_3^-$, $RNH_3^+$ and $RNHCOO^-$ were taken from the General Amber Force Field (GAFF)[119] in conjunction with the TIP3P water force field with the 1-4 LJ and electrostatic interactions scaled by 1/2 and 5/6 respectively. When combined with the GAFF, the TIP3 model has been shown to give better $\Delta G^{intr}$ than other water models. As far as the electrostatic interactions are concerned, no widely accepted standards for determination of the partial charges exist. However, it has been shown that the intrinsic hydration free energy strongly correlates with the solute dipolement and this varies across the theory levels/basis sets. Following Zhang *et al.* [120] to obtain the partial charges, the gas-phase geometry of each molecule was optimized at the MP2/cc-pVTZ level of theory/basis set, followed by a single point energy calculation on the gas-phase optimized structure at the B3LYP/6-311++g(d,p) level of theory/basis set using the Gaussian09 package[121]. The original GAFF used low–level HF/6-31G* to generate the electrostatic surface potential; however, as shown by Zhang *et al.* [120], B3LYP/6-311++G(d,p) yields very similar dipole moments and reasonable thermodynamic propoerties prediction for wide range of solvents. It is worth noting that the author scaled the original GAFF LJ parameter for improved predictions, however, we found that the LJ contribution to the $\Delta G^{intr}$ is very small (specially for the ionic species

considered here) compared to the contribution of the electrostatic interactions. The gas–phase geometries of the MEA, $RNH_3^+$ and $RNHCOO^-$ molecules are shown in Fig. 3.1. The partial charges were then obtained with the two stage restrained electrostatic potential (RESP) fitting method using the Antechamber package[119]. $CO_2$ was modelled using the TraPPE force field of Pottoff[122], although TIP3P/TraPPE combination is not the model of choice when it comes to $CO_2$-water interactions, we expect little variation of its intrinsic hydration free energy across the water models.

Finally, the partial charges for $H_3O^+$ and $OH^-$ ions were taken from the polarizable model used by Dang *et al.* [123]. The LJ parameters of these two ions were manually optimized to approximate the experimental hydration free energies of the individual ions referenced to the 1–molal gas phase and the Henry–Law 1–molal aqueous phase standard state at 298.15 K and 1 bar in TIP3 water according to

$$\Delta G_i^* = \Delta G_i^{\text{intr}} + z_i e \psi_s \tag{3.29}$$

where $\Delta G_i^{\text{intr}}$ is the species intrinsic hydration free energy calculated in this work, $z_i$ is its valence, $e$ is the electronic charge, and $\psi_s$ is the Galvani potential of TIP3P water, taken from Zhang *et al.* [115].

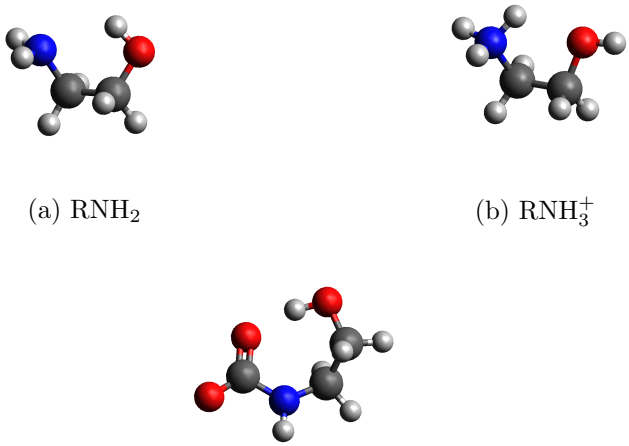

(a) $RNH_2$ (b) $RNH_3^+$

(c) $RNHCOO^-$

Figure 3.1: MP2/aug-cc pVTZ optimized gas phase geometry of ethanolamine (a), protonated ethanolamine (b) and its carbamate form (c) used in this study to derive RESP charges.

### 3.4.2 Hydration Free Energies

The initial structure was generated by adding a single ion/solute in a cubic box of 888 TIP3P water molecules employing periodic boundary conditions using Packmol[119]. A short energy minimization was followed by a 1 ns NVT simulation and a 10 ns NPT equilibration was performed to prepare the initial structure for the free energy calculations using an $NPT$ simulation. $\Delta G_i^{\text{intr}}$ was calculated by first linearly decoupling the electrostatic ion–water interactions according to

$$U_{\text{elec}}\left(r_{ij};m\right) = \lambda_m^{\text{elec}} \frac{1}{4\pi\varepsilon_0} \frac{q_i q_j}{r_{ij}} \tag{3.30}$$

over 12 equally spaced $\lambda$ windows $\{0.00, 0.05, 0.1, 0.2, 0.3, 0.4, 0.5, 0.6, 0.7, 0.8, 0.9, 1.00\}$ This was followed by decoupling the LJ ion-water van der Waals interactions over the 19 $\lambda$ $\{0.00, 0.05, 0.1, 0.15, 0.2, 0.25, 0.3, 0.35, 0.4, 0.5, 0.6, 0.65, 0.7, 0.75, 0.8, 0.85, 0.9, 0.95, 1.00\}$

windows using the soft-core potential

$$U_{\mathrm{LJ}}^{\mathrm{sc}}\left(r_{ij};m\right)=4\lambda_{m}^{\mathrm{LJ}}\varepsilon_{ij}\left\{\frac{\sigma_{ij}^{12}}{\left[\left(1-\lambda_{m}^{LJ}\right)\alpha_{LJ}\sigma_{ij}^{6}+r_{ij}^{6}\right]^{2}}-\frac{\sigma_{ij}^{6}}{\left[\left(1-\lambda_{m}^{LJ}\right)\alpha_{LJ}\sigma_{ij}^{6}+r_{ij}^{6}\right]}\right\} \tag{3.31}$$

where $\alpha_{\mathrm{LJ}}=0.5$

At each $\lambda$ window, we performed an 8 ns $NPT$ simulation to collect the derivative of the Hamiltonian every 0.2 ps, with the first 2.5 ns discarded from the analysis. The free energy change resulting from decoupling the particle from the solvent was calculated using the multi-state Bennett acceptance ratio method[124] as implemented into GROMACS 2018, with all post-processing performed by the Python script Pymbar[125]. The GROMACS stochastic dynamics integrator with time step of 2 fs and Langevin dynamics thermostat with friction coefficient of 1 ps were used. For $NPT$ simulations, the pressure was set to 1 bar using the Parrinello–Rahman barostat with a characteristic oscillation time of 5.0 ps and the compressibility set to $4.5\times10^{-5}$. Short–range LJ interactions were truncated at 1.2 nm and standard mean–field long–range corrections were applied for the energy and pressure truncation of these interactions. Long–range electrostatic interactions were evaluated with the smooth particle-mesh Ewald (SPME) method with tin–foil boundary conditions, with real space interactions truncated at 1.2 nm, a SPME B-spline of order 4, a grid spacing of 0.12 nm, and a relative accuracy of $10^{-5}$. (Following Joung and Cheatham[126], for single ion hydration the net charge of the simulation box was not set to zero, since this is implicitly accounted for when Ewald summation using tin–foil boundary conditions.) The solution free energy change calculation was followed by a single molecule simulation of the free energy in vacuum (in a non–periodic simulation box with infinite force–field cutoffs), which was subtracted from the free energy change calculation in the solution.

All GROMACS input files and force field parameters are provided in the Supplementary Information file.

### 3.4.3 QM Simulations

To obtain the initial structure of the flexible molecules (MEA, RNH3$^+$ and RNHCOO$^-$), a conformational search was initially performed with the MMFF94 force field using Spartan'18 software[127], and the resulting geometries were then further optimized at increasing QM levels of accuracy. For $RNH_3^+$ and RNHCOO$^-$, the energy differences between the lowest and next lowest energy conformers were found to be significant; therefore only the

lowest energy conformer was adopted for each of these molecules. For MEA, however, the energy differences were relatively small, and contributions from other conformations also were taken into account using Boltzmann averaging, as described in Results and Discussion section.

To calculate the IG quantities for each species at the temperature of the interest and 1 bar, the selected geometries were further optimized with quantum chemical methods followed by frequency calculations to ensure that the optimized structures were true minima on the potential energy surface (no negative eigenvalues in the Hessian matrix). All QM calculations were performed with Gaussian09[121]. To assess the sensitivity of the calculations to the QM method and to calculate uncertainty estimates, the $G(0)$ quantities were calculated using several theory levels and basis sets, namely wB97XD-aug-cc-pVTZ, wB97XD/6-311++(2d,2p), wB97X/6-311++G(3df,3pd), B3LYP/6-311++g(d,p), CAM-B3LYP/6-311++g(2d,2p), CAM-B3LYP-aug-cc-pVTZ, G4, CBS-APNO and CBS-QB3.

## 3.5 Results and Discussion

For the equilibrium calculations, we may use any set of 4 linearly independent reactions; we use the set

$$2\mathrm{RNH_2} + \mathrm{CO_2} = \mathrm{RNH_3^+} + \mathrm{RNHCOO^-} \quad \text{(R1)}$$

$$\mathrm{RNH_3^+} + \mathrm{H_2O} = \mathrm{H_3O^+} + \mathrm{RNH_2} \quad \text{(R2)}$$

$$\mathrm{RNHCOO^-} + \mathrm{H_2O} = \mathrm{RNH_2} + \mathrm{HCO_3^-} \quad \text{(R3)}$$

$$\mathrm{RNH_2} + \mathrm{H_2O} = \mathrm{RNH_3^+} + \mathrm{OH^-} \quad \text{(R4)}$$

The equilibrium compositions are obtained from the solution of Eqs. (3.5). The following two subsections describe our methodology for calculating the input quantities and estimating their uncertainties. We estimated the uncertainties in the resulting equilibrium

compositions by propagating those of the input quantities.

Table 3.1: Values of the dimensionless ideal–gas free energy function $[G(T) - H(0)]/RT$ at $T = 293.15$ K and $P^0 = 1$ bar for the species involved in the MEA-$CO_2$-$H_2O$ system. The second column contains values calculated in this work, the third column contains values calculated previously by Balaji *et al.* [103], and the fourth column contains results from the JANAF thermochemical tables[128].

| Species | $[G_i(T) - H_i(0)]/RT$[(a)] | $-\ln\left[\frac{q_i^0(T)RT}{P^0}\right]$ [(b)] | $[G_i(T) - H(0)]/RT$[(c)] |
|---|---|---|---|
| $RNH_3^+$ | -28.977 | -28.912 | - |
| $RNHCOO^-$ | -33.075 | -32.961 | - |
| $HCO_3^-$ | -27.250 | -27.233 | - |
| $H_3O^+$ | -19.118 | -19.097 | -19.083 |
| $OH^-$ | -17.166 | - | -17.272 |
| $RNH_2$[(d)] | -28.757 | -28.671 | - |
| $H_2O$ | -18.628 | -18.618 | -18.717 |
| $CO_2$ | -21.865 | -21.882 | -21.937 |

[(a)] This work. Calculated using Gaussian09[121] with B3LYP/6-311++G(d,p).
[(b)] Calculated using the $\hat{q}_i(T)$ values of Balaji *et al.* [103].
[(c)] Calculated from columns 4 and 5 of the JANAF thermochemical tables[128].
[(d)] Calculated for the lowest energy conformer at 293.15 K (see the text.)

### 3.5.1 Ideal–Gas Quantities

The only previous simulation study of the reactive absorption of $CO_2$ in the aqueous MEA system is that of Balaji *et al.* [103], who used the REMC algorithm[32, 98, 129], which also requires the ideal–gas quantities $\Delta G_j^0(T; P^0)$ in Eq. (3.26). They calculated the $[G_i(T) - H_i(0)]$ quantity, but neglected to include the atomization energy contribution. This is verified in Table 3.1 at $T = 293.15$ K, where our calculations of the former quantities are compared with their results and with available JANAF data[128]. It is seen that the three sets of $[G_i(T) - H_i(0)]$ results are in good agreement.

We found the values of $[G_i(T) - H_i(0)]/RT$ (the "thermal corrections") to be relatively insensitive to the QM method used, in contrast to the $\Delta G_j(0)$ results. In order to account

Table 3.2: Ideal–gas reaction free energies at 0 K, $\Delta G_j^0(0)$ of Eq. (3.27) in kJ mol$^{-1}$ at $P = 1$ bar for reactions R1–R4 in the text. For the indicated reaction, the final row gives the average value of the methods and the numbers in parentheses denote the standard deviations.

| Method | R1 | R2 | R3 | R4 |
|---|---|---|---|---|
| B3LYP/6-311++G(d,p) | 487.40 | 233.31 | 34.61 | 708.27 |
| wB97XD-aug-cc-pVTZ | 476.66 | 232.22 | 42.12 | 709.27 |
| wB97XD/6-311++(2d,2p) | 472.58 | 235.28 | 42.82 | 714.57 |
| CAM-B3LYP/6-311++(2d,2p) | 469.38 | 234.33 | 39.60 | 713.04 |
| G4 | 478.73 | 231.37 | 47.69 | 708.20 |
| CBS-APNO | 475.00 | 231.20 | 48.35 | 711.78 |
| CBS-QB3 | 474.55 | 234.43 | 49.10 | 720.72 |
| wB97X/6-311++G(3df,3pd) | 470.28 | 232.10 | 41.34 | 716.60 |
| CAM-B3LYP-aug-cc-pVTZ | 470.83 | 232.88 | 39.32 | 707.10 |
| Average(std) | 473.50(3.1) | 232.98(1.4) | 43.79(3.7) | 712.66(4.3) |

for the effects of this sensitivity, we calculated $\Delta G_j(0)$ required in Eqs. (3.25)–(3.27) in conjunction with the range of high–order methods indicated in Section 3.5.1, in addition to the commonly used B3LYP/6-311++G(d,p) method (*e.g.*, Gupta *et al.* [130, 131, 132]). For our reaction equilibrium calculations, we used the average values of $\Delta G_j^0(T; P^0)$ obtained from the eight indicated high–order methods shown in Table 3.2 and took the standard deviations as their uncertainty estimates. The results are shown in Table 3.2. It can be seen that the B3LYP/6-311++G(d,p) results differ markedly from those of the higher order methods, most importantly for reactions R1 and R3. The results indicated in the table are in agreement with others who have indicated that B3LYP/6-311++G(d,p) results are generally inferior to those of the higher order methods for amine–based systems; we thus excluded its results from our calculations.

It is important to account for the fact that larger molecules typically exhibit more than one locally stable structural isomer. The set of ideal–gas isomers can be treated by an exact "lumping procedure" [133, 134], whereby the set is replaced by a single species with a standard chemical potential $\mu_I^0(T; P^0)$ given by the Boltzmann-weighted sum of the $N_c$ conformer chemical potentials. The mole fraction of each conformer in the set is

$$x_i = \frac{\exp[-\mu_i^0(T; P^0)/RT]}{\sum_{j=1}^{N_c} \exp[-\mu_j^0(T; P^0)/RT]} \tag{3.32}$$

Table 3.3: Values of the fraction of the total population of the MEA conformers with the 13 lowest values of $\mu^0(T)$ at the temperatures considered in this work, calculated using M06/6-311++G(3df,3dp). The final row values of "Adjustment" refer to the argument of the logarithmic term in Eq. (3.36)

| Conformer | 293.15 | 298.15 | 313.15 | 333.15 | 353.15 |
|---|---|---|---|---|---|
| g'Gg' | 0.6177 | 0.6139 | 0.5746 | 0.5255 | 0.4811 |
| gGg' | 0.1279 | 0.1304 | 0.1413 | 0.1541 | 0.1650 |
| tGt | 0.0638 | 0.0640 | 0.0685 | 0.0737 | 0.0778 |
| gGt4 | 0.0506 | 0.0508 | 0.0552 | 0.0603 | 0.0647 |
| tGg | 0.0371 | 0.0373 | 0.0412 | 0.0459 | 0.0502 |
| gGg | 0.0330 | 0.0330 | 0.0362 | 0.0401 | 0.0436 |
| tGg' | 0.0254 | 0.0255 | 0.0288 | 0.0330 | 0.0369 |
| tTt | 0.0116 | 0.0117 | 0.0139 | 0.0112 | 0.0201 |
| g'Tt | 0.0091 | 0.0092 | 0.0109 | 0.0134 | 0.0159 |
| tTg | 0.0082 | 0.0083 | 0.0100 | 0.0124 | 0.0148 |
| gTg' | 0.0073 | 0.0074 | 0.0090 | 0.0170 | 0.0135 |
| gTg | 0.0072 | 0.0073 | 0.0089 | 0.0111 | 0.0134 |
| g'Gt | 0.0011 | 0.0012 | 0.0016 | 0.0022 | 0.0030 |
| Adjustment | 1.593 | 1.628 | 1.740 | 1.902 | 2.078 |

and

$$\mu_I^0(T;P^0) = \sum_{i=1}^{N_c} x_i \left[\mu_i^0(T;P^0) + RT\ln x_i\right] \tag{3.33}$$

$$= -RT\ln\left[\sum_{j=1}^{N_c} \exp[-\mu_i^0(T;P^0)/RT]\right] \tag{3.34}$$

For a given species, we first determined the conformer with the lowest chemical potential, $\mu_*^0(T;P^0)$, and the relative free energy differences of the other conformers from its minimum value, $\delta\mu_i^0(T;P^0)$, where

$$\delta\mu_i^0(T;P^0) = \mu_i^0(T;P^0) - \mu_*^0(T;P^0) \tag{3.35}$$

The standard chemical potential $\mu_I(T;P^0)$ of the isomer group is then calculated by rearranging Eq. (3.34) to the form

$$\frac{\mu_I^0(T;P^0)}{RT} = \sum_{i=1}^{N_c} \frac{\mu_i^0(T;P^0)}{RT} = \frac{\mu_*^0(T;P^0)}{RT} - \ln\left(\sum_{i=1}^{N_c} \exp\left[-\frac{\delta\mu_i^0(T;P^0)}{RT}\right]\right) \tag{3.36}$$

where $N_c$ is the number of conformers considered. We found that the final term was vanishingly small for all species except MEA, for which we found 13 conformers, the same set reported by Xie *et al.* [135] and by Novakovskaya and Rodnikova[136]. Table 3.3 shows the mole factions of the individual conformers and the final term of Eq. (3.36) at each temperature considered.

### 3.5.2 Intrinsic Hydration Free Energies

The intrinsic hydration free energies of the species, $\Delta G_i^{\text{intr}}(T;P)$ defined in Eq. (3.16) are shown in Table 3.4. As noted in Section 3.3, for our purposes we only require the charge-conserving linear combinations of the intrinsic hydration free energies, $\Delta G_j^{\text{intr}}$, that are calculated from the individual $\Delta G_i^{\text{intr}}(T;P)$ values. The individual $\Delta G_i^{\text{intr}}(T;P)$ values show relatively small uncertainties, which we propagated to the $\Delta G_j^{\text{intr}}$ quantities shown in Table 3.2.

Table 3.4: Water density and dimensionless species intrinsic hydration free energies, $\Delta G_i^{\text{intr}}(T,P)/RT$, defined in Eq. (3.16), at the temperatures, $T$, considered in this study and pressure $P = 1$ bar, using the TIP3P water model and the species FFs described in the text. A subscript indicates the uncertainty (one standard deviation) in the final number of digits.

| | 293.15 K | 298.15 K | 313.15 K | 333.15K | 353.15 K |
|---|---|---|---|---|---|
| $H_2O$ Density(kg $m^{-3}$) | $991.83_{98}$ | $987.35_{98}$ | $973.88_6$ | $954.31_9$ | $932.61_8$ |
| Species | | | | | |
| $RNH_3^+$ | $-98.35_4$ | $-96.43_4$ | $-95.67_4$ | $-89.13_3$ | $-83.51_3$ |
| $RNHCOO^-$ | $-150.90_8$ | $-148.10_8$ | $-143.96_9$ | $-134.34_7$ | $-125.20_7$ |
| $HCO_3^-$ | $-158.89_2$ | $-155.92_2$ | $-143.07_2$ | $-133.38_2$ | $-124.77_2$ |
| $H_3O^+$ | $-168.90_3$ | $-165.72_3$ | $-156.95_3$ | $-146.50_2$ | $-137.31_2$ |
| $OH^-$ | $-199.96_3$ | $-196.38_3$ | $-185.71_3$ | $-173.01_3$ | $-161.76_2$ |
| MEA | $-12.54_3$ | $-12.14_3$ | $-12.26_3$ | $-10.95_2$ | $-9.80_2$ |
| $H_2O$ | $-11.09_1$ | $-10.90_1$ | $-10.03_1$ | $-9.04_1$ | $-8.22_1$ |
| $CO_2$ | $0.39_1$ | $0.41_1$ | $0.67_4$ | $0.82_1$ | $0.93_1$ |

### 3.5.3 $pK$ Values

Table 3.5 shows the equilibrium constants and their constituent contributions for Reactions R1–R4 at the temperatures of this study, along with estimates of their uncertainties (one standard deviation). It is difficult to compare our $pK$ results with those of experiment, since the latter are typically obtained indirectly by fitting an activity coefficient model to experimental data, and the uncertainties are rarely discussed. Since Reaction R3 involving $HCO_3^-$ and $RNHCOO^-$ is one of the most important, we compare our $pK$ value at 298.15 in the table with its values from several sources[87, 137, 138, 139], which yield an average value of 1.58 with a standard deviation of 0.19. This overlaps with our pK value and its uncertainty range.

Table 3.5: Quantities contributing to $\Delta\widetilde{G}_j(T,P)$, defined in Eqs. (3.20)–(3.24) for reactions R1–R4 at the indicated temperatures and $P = P^0 = 1$ bar. $\Delta G_j^0(T;P^0)$ is calculated from Eq. (3.27) using the second column of this table and data in Tables 3.2–3.4, in conjunction with Eq. (3.36). $\Delta\Delta G_j^{\rm intr}$ is calculated from Eq. (3.24) and data in Table 3.4. Uncertainties are given in parentheses as one standard deviation.

| | $\frac{\Delta_j[G(T)-H(0)]}{RT}$ | $\frac{\Delta G_j^0(T;P^0)}{RT}$ | $\frac{\Delta\Delta G_j^{\rm intr}(T,P)}{RT}$ | $\ln K_j \equiv \frac{\Delta\widetilde{G}_j}{RT}$ | $pK_j \equiv -\log_{10}(K_j)$ |
|---|---|---|---|---|---|
| | | | 293.15 K | | |
| R1 | 17.33 | 212.53(1.27) | -224.56(0.11) | -15.22(1.28) | -6.61(0.55) |
| R2 | -0.27 | 94.85(0.57) | -72.00(0.06) | 18.83(0.58) | 8.18(0.25) |
| R3 | -4.30 | 13.20(1.52) | -9.44(0.09) | -0.26(1.52) | -0.11(0.66) |
| R4 | 1.24 | 294.09(1.76) | -274.68(0.06) | 15.40(1.77) | 6.69(0.77) |
| | | | 298.15 K | | |
| R1 | 17.36 | 209.34(1.25) | -220.67(0.11) | -14.52(1.26) | -6.31(0.55) |
| R2 | -0.27 | 93.23(0.56) | -70.52(0.06) | 18.69(0.57) | 8.11(0.25) |
| R3 | -4.28 | 12.90(1.49) | -9.06(0.09) | -0.18(1.50) | -0.08(0.65) |
| R4 | 1.25 | 289.22(1.73) | -269.78(0.06) | 15.43(1.74) | 6.70(0.75) |
| | | | 313.15 K | | |
| R1 | 17.44 | 200.41(1.19) | -209.78(0.12) | -12.61(1.20) | -5.48(0.52) |
| R2 | -0.26 | 88.67(0.54) | -66.66(0.06) | 17.99(0.54) | 7.81(0.23) |
| R3 | -4.23 | 12.03(1.42) | -8.51(0.10) | -0.49(1.42) | -0.21(0.62) |
| R4 | 1.26 | 275.53(1.65) | -255.94(0.06) | 15.57(1.65) | 6.76(0.72) |
| | | | 333.15 K | | |
| R1 | 17.54 | 189.77(1.12) | -196.29(0.09) | -9.80(1.12) | -4.26(0.49) |
| R2 | -0.25 | 83.22(0.51) | -62.19(0.04) | 17.01(0.51) | 7.39(0.22) |
| R3 | -4.16 | 11.01(1.34) | -8.08(0.08) | -1.09(1.34) | -0.47(0.58) |
| R4 | 1.27 | 259.19(1.55) | -239.24(0.05) | 15.94(1.55) | 6.92(0.67) |
| | | | 353.15 K | | |
| R1 | 17.63 | 180.35(0.06) | -184.64(0.09) | -7.60(1.06) | -3.30(0.46) |
| R2 | -0.25 | 78.36(0.48) | -58.10(0.04) | 16.25(0.48) | 7.06(0.21) |
| R3 | -4.10 | 10.08(1.26) | -7.53(0.08) | -1.46(1.26) | -0.64(0.55) |
| R4 | 1.29 | 244.73(1.46) | -224.53(0.04) | 16.19(1.47) | 7.03(0.64) |

Table 3.6: Values of $\epsilon_{r,\text{solv}}$ in Eq. (3.9) and $A$ in Eq. (3.8) at the temperatures of this study.

| $T$ | $\epsilon_{r,\text{solv}}$ | $A$ |
|---|---|---|
| 293.15 | 102.102 | 0.350 |
| 298.15 | 97.857 | 0.363 |
| 313.15 | 94.067 | 0.356 |
| 313.15 | 90.830 | 0.338 |
| 353.15 | 83.094 | 0.350 |

### 3.5.4 Davies Parameter A

$\epsilon_{r,\text{solv}}$ for TIP3P water was obtained using

$$\epsilon_{r,\text{solv}} = 1 + \frac{\beta\left(< \boldsymbol{M}^2 > - < \boldsymbol{M} >^2\right)}{3\epsilon_0 V} \tag{3.37}$$

where $\boldsymbol{M} = [M_x, M_y, M_z]$ is the total dipole moment and $\epsilon_0$ is the permittivity of free space. We equilibrated systems of 2000 water molecules for 2 ns and used 10 ns production periods in the NPT ensemble to obtain the system box size, which was followed by 10ns $NVT$ simulation to calculate $\epsilon_{r,\text{solv}}$, saving configurations for analysis every 0.1 ps. $\epsilon_{r,\text{solv}}$ and $A$ values for TIP3P water in Eq. (3.9) are shown in Table 3.6.

### 3.5.5 Solution Compositions

We calculated the solution equilibrium compositions using the thermodynamic model of Eqs. (3.5) and (3.6), with the $\mu_i^\dagger$ parameters obtained by the simulation methodology of Section 3.3. The conservation of mass constraints are expressed in terms of the quantities $\{N^0(\text{RNH}_2), N^0(\text{H}_2\text{O}), N^0(\text{CO}_2)\}$, which are in turn defined in terms of the weight fraction $\omega$ and $CO_2$ loading $L$ as follows:

$$N^0(\text{RNH}_2) = \left(\frac{\omega \text{M}_{\text{H}_2\text{O}}}{(1-\omega)\text{M}_{\text{RNH}_2}}\right) N^0(\text{H}_2\text{O}) \tag{3.38}$$

$$N^0(CO_2) = \left(\frac{\omega L \text{M}_{\text{H}_2\text{O}}}{(1-\omega)\text{M}_{\text{RNH}_2}}\right) N^0(\text{H}_2\text{O}) \tag{3.39}$$

where $N^0$ is a particle/mole number and M is a molecular weight (our simulations used $N^0(\mathrm{H_2O}) = 888$.)

We performed two sets of calculations, both implemented by means of a locally developed Python script: (1) based on the Henry–Law model of Eq. (3.1) in the case of an ideal solution ($\ln \gamma_i$) $\equiv 0$); and (2) using the Davies approximation[107] for the activity coefficients:

$$\ln(\gamma_i) = -z_i^2 A \left( \frac{\sqrt{I}}{1+\sqrt{I}} - 0.3I \right) \tag{3.40}$$

where $z_i$ is the valence and $I$ is the ionic strength. Numerical results for all systems studied are given in the Supporting Information.

Results obtained using the Davies approximation are shown in Fig. 3.2 at a range of temperatures and $CO_2$ loadings for a 30 weight % MEA/$H_2O$ solvent, where they are compared with experimental results from the literature. The combination MEA/$RNH_3^+$ is also shown because in some cases only this quantity is available experimentally. The inset in Subfigure (a) shows the minor species concentrations at the only state point for which experimental data exists. Numerical results for all species compositions are provided in the Supplementary Information, for both the Henry–Law ideal solution and the Davies approximation.

The methodology for the error bars on our simulation results (indicating one standard deviation) is discussed in Section 3.5.7. The scatter of the experimental results, particularly for $HCO_3^-$, indicate that it is problematic to experimentally determine the species compositions with high precision, particularly at mole fractions less than about 0.01. We conclude that our simulation results provide equilibrium compositions of similar quality to the experimental measurements; in addition, estimates of very small species compositions are available from our simulations, unlike the case for the experiments.

We now compare our results with those of the only previous simulation study of this system[103], who used a variant of the REMC algorithm[32, 98, 99]. We first remark that the REMC algorithm (in common with many other simulation algorithms) is intrinsically unsuited to calculations involving systems with species of very low concentrations. For example, using a simulation box with $N_{\mathrm{box}}$ particles, an equilibrium mole fraction of $z_i$ would require 1 particle of the species to be observed on average every $1/(N_{\mathrm{box}} z_i)$ reaction moves. In our simulations, a mole fraction $x_{\mathrm{CO_2}}$ of order $10^{-10}$ is not uncommon. To observe such a concentration, the REMC algorithm would require a $CO_2$ particle to be observed on average every 20 million reaction moves (and a reasonable uncertainty would require it to be observed multiple times) using the $N_{\mathrm{box}} \approx 500$ value of Balaji *et al.* [103], who displayed graphical results for $L \leq 0.7$ for the concentrations

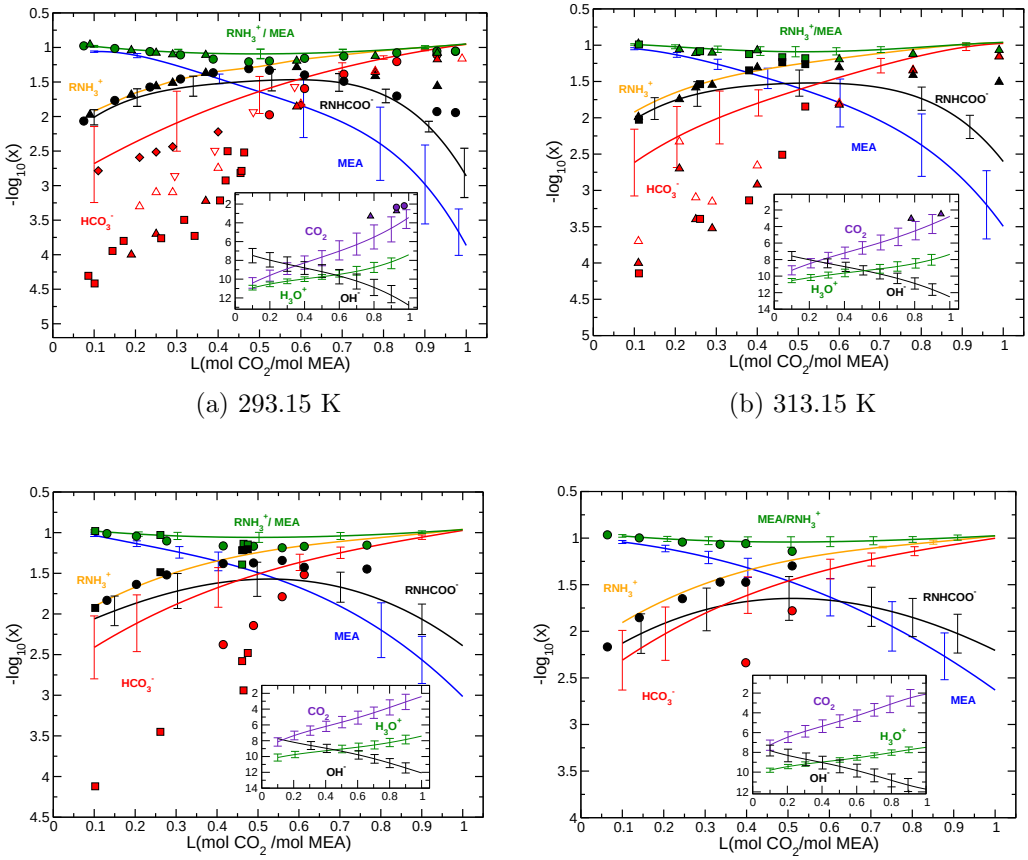


(a) 293.15 K (b) 313.15 K

(c) 333.15 K (d) 353.15 K

Figure 3.2: Mole fractions of the major solution species as a function of $CO_2$ loading, $L$, at the indicated temperatures and $P = 1$ bar for a 30 weight % aqueous MEA solution. Curves are our simulation results, with error bars indicating their uncertainties (one standard deviation). The main graphs show the major species and the insets show the minor species. Experimental data points, whose symbol colors match the corresponding curves, are as follows: filled diamonds: Matin *et al.* [90] (21°C); filled circles: Böttinger *et al.* [87]; open downward triangles: du Preez *et al.* [95]; filled upward triangles: Jakobsen *et al.* [86]; open upward triangles: Jakobsen *et al.* [86], 293.15 K and 313.15 K only, indicating the sum of the mole fractions of $HCO_3$ and $CO_3^{-2}$; filled squares: Hilliard[88], indicating the sum of the mole fractions of $HCO_3$ and $CO_3^{-2}$.

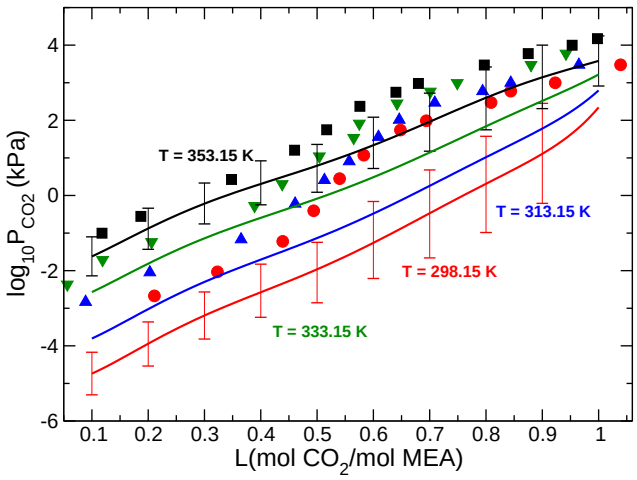


Figure 3.3: Partial pressure of $CO_2$ above the solution as a function of loading, $L$, at the indicated temperatures and $P = 1$ bar for a 30 weight % aqueous MEA solution. Curves are simulation results of this work, and points are experimental data from Jou *et al.* [84]. The error bars on the simulation curves at 298.15 K and 353.15 K indicate their uncertainties (one standard deviation); the error bars at the other temperatures are not shown, but are of similar magnitude.

of $\{\mathrm{MEA} + \mathrm{RNH_3^+}, \mathrm{RNHCOO^-}, \mathrm{HCO_3^-}\}$, and for $\mathrm{HCO_3^-}$ only at high loadings where its concentration is non–negligible.

We also note that in the work of Balaji *et al.* [103], the ideal–gas quantities $\Delta G_j(0)$ in Eq. (3.27) were erroneously omitted in the calculation of the values of $\Delta G_j(T; P^0)/RT$ in Table B.2; these quantities provide by far the largest contributions to $\Delta G_j(T; P^0)/RT$. Their study also modelled the system using a different species set than used here, omitting $\mathrm{OH^-}$ and including $\mathrm{CO_3^{2-}}$; however, since these species are present in very small amounts, they have only a minor effect on the concentrations of the remaining species. In addition, in our study different species force fields were used. Differences in our results could be due to any of these factors; it could also be due to the nonconvergence of their REMC simulations.

### 3.5.6 $\mathrm{CO_2}$ Partial Pressure

The partial pressure of $\mathrm{CO_2}$ in the vapour phase at a total pressure of 1 bar is determined from the equality of its solution and vapour phase chemical potentials. At the relatively low pressure considered here, the vapour phase may be treated as an ideal gas, which yields its partial pressure, $P_{\mathrm{CO_2}}$, as

$$\widetilde{P}_{\mathrm{CO_2}} = \left(\frac{RT}{100P^0}\right)\left(\frac{\overline{\rho}_{\mathrm{solv}}(T,\widetilde{P})}{1000}\right) m_{\mathrm{CO_2}} \exp\left(\frac{\mu_{\mathrm{CO_2}}^{\mathrm{res},NVT,\infty}(T,\rho(T,\widetilde{P})}{RT}\right) \tag{3.41}$$

We ignore the small pressure dependences of the quantities in this expression, and use our simulation values calculated at $P = 1$ bar.

The dependence of $P(\mathrm{CO_2})$ on loading at the temperatures considered is shown in Fig. 3.3. Error bars are shown at 298.15 K and 353.15 K, and those at the other temperatures are similar. The methodology used is described in the next Section.

### 3.5.7 Uncertainty Analysis

Although the propagation of uncertainties in the values of $\Delta\widetilde{G}_j$ in Table B.2 to the uncertainties $\Delta \ln(x_i^*)$ in the equilibrium species mole fractions and to the uncertainty $\Delta \ln(\widetilde{P}_{\mathrm{CO_2}})$ in the $\mathrm{CO_2}$ partial pressure can be performed using methodology similar to that of Morgan *et al.* [108], we take a simpler numerical approach here.

Since the equilibrium concentrations of $\mathrm{H_3O^+}$ and $\mathrm{OH^-}$ are very small, the equilibrium mole fractions $x_i^*$ are primarily determined by Reactions R1 and R3. We thus estimated the

uncertainties in the equilibrium compositions arising from the uncertainties in $\Delta\widetilde{G}_1/RT$ and $\Delta\widetilde{G}_3/RT$, by numerically calculating the compositional derivatives with respect to these quantities, and then using

$$\begin{aligned}\Delta \ln(x_i^*) &= \left\{ \left( \frac{\partial \ln(x_i^*)}{\partial(\Delta\widetilde{G}_1/RT)} \right)^2 (\Delta\Delta\widetilde{G}_1/RT)^2 \right. \\ &\quad \left. + \left( \frac{\partial \ln(x_i^*)}{\partial(\Delta\widetilde{G}_3/RT)} \right)^2 (\Delta\Delta\widetilde{G}_3/RT)^2 \right\}^{1/2}\end{aligned} \tag{3.43}$$

Applying the same approach for $P_{\mathrm{CO}_2}$ gives

$$\begin{aligned}\Delta \ln(\widetilde{P}_{\mathrm{CO}_2}) &= \left\{ \left( \frac{\partial \ln m_{\mathrm{CO}_2}^{\mathrm{soln}}(T,P;\boldsymbol{m}^*)}{(\Delta\widetilde{G}_1/RT)} \right)^2 (\Delta\Delta\widetilde{G}_1/RT)^2 \right. \\ &\quad \left. + \left( \frac{\partial \ln m_{\mathrm{CO}_2}^{\mathrm{soln}}(T,P;\boldsymbol{m}^*)}{(\Delta\widetilde{G}_3/RT)} \right)^2 (\Delta\Delta\widetilde{G}_3/RT)^2 + \left( \frac{\Delta\mu_{\mathrm{CO}_2}^{\mathrm{res}}}{RT} \right)^2 \right\}^{1/2}\end{aligned} \tag{3.45}$$

where the asterisk denotes the equilibrium composition.

## 3.6 Discussion

We have demonstrated that our simulation results are in good agreement with those of experiment when their mutual uncertainties are taken into account. We are investigating the application of our methodology to other solvents for $CO_2$ reactive absorption.

The accuracy of our predictions of the species solution concentrations and the $CO_2$ partial pressure above the solution, $P_{\mathrm{CO}_2}$, depends on the accuracies of three quantities:

1. the ideal–gas free energy changes for the reactions R1–R4, of which the most important are R1 and R3.
   Although our calculations of these quantities have relatively large uncertainties, we believe that they are reasonably accurate.

2. the hydration free energy changes for the reactions.
   Although these have relatively low uncertainties, they may not be sufficiently accurate due to inadequacies in the underlying force fields, and in current work, we are investigating improvements to the force fields

3. the species chemical potential model used to calculate reaction equilibrium.
   The Davies approximation for the activity coefficients in conjunction with the species Henry–law–based chemical potential model may not be sufficiently accurate, particularly at high $CO_2$ loading values. We are investigating the approach of dispensing with a particular algebraic form of chemical potential model, and instead employing the strategy of the ReMD algorithm[44], which recalculates species chemical potentials at a sequence of states calculated by ideal solution extrapolations.

## 3.7 Conclusions and Recommendations

1. We have developed a molecular–based simulation methodology to calculate all species concentrations undergoing chemical reaction equilibrium in electrolyte solutions; an important feature is and is its ability to treat species with very small concentrations. We have applied it to the benchmark MEA($RHN_2$)–$H_2O$–$CO_2$ reactive absorption system, which is a key system used in $CO_2$ capture. We have also calculated $P_{CO_2}$, the partial pressure of $CO_2$ above the solution. We have used no experimental data in our methodology. Our approach is readily extended to other electrolyte systems, including to other solvents candidates for $CO_2$ capture.

2. We compared our results and methodology with those of the only other group to have studied the MEA–$H_2O$–$CO_2$ system using molecular simulation methodology[103]. This group inadvertently omitted significant terms in the ideal–gas chemical potential contributions involved in their algorithm, and their simulation methodology did not permit the calculation of minor species concentrations and of $P_{CO_2}$.

3. Our predictions are accompanied by an Uncertainty Analysis based on propagating the uncertainties of the underlying parameters to those of the equilibrium species concentrations. This allows comparison with the literature results for the species

concentrations, which show mutual disagreement due to the experimental challenges involved. We thus believe that the quality of our predictive methodology is comparable to that of the experimental studies. We recommend that all theoretical and experimental predictions be accompanied by an Uncertainty Analysis.

4. We made contact with macroscopic thermodynamic modeling approaches by translating relevant molecular simulation quantities to the parameters of a Henry-Law–based thermodynamic model, which is then used to calculate the equilibrium compositions.

## 3.8 Acknowledgements

Support for this work was provided by the Natural Sciences and Engineering Research Council of Canada (Strategic Program Grant No. STPGP 479466-15), and by the SHARCNET (Shared Hierarchical Academic Research Computing Network) HPC consortium (www.sharcnet.ca) and Compute Canada (www.computecanada.ca)

# Chapter 4

# Accurate Prediction of Speciation in Aqueous Alkanolamine-$CO_2$ System Requiring No Solvent Experimental Data



## Abstract

We present a general atomistic simulation framework for efficient reactive equilibrium calculations in dilute solutions, and its application to $CO_2$ reactive absorption in aqueous alkanolamine solutions. No experimental data of any kind are required for the solvents, and no empirical adjustments are required for its implementation. This hybrid methodology calculates reaction equilibrium constants by combining high–level quantum chemical calculations of ideal–gas standard reaction Gibbs energies ($\Delta G^0$) with conventional solvation free energy calculations obtained from classical force field methodology. For

these quantities we use explicit solvent molecular dynamics simulations with the General AMBER Force Field (GAFF). The resulting equilibrium constants are then coupled with a macroscopic Henry–Law–based ideal solution model to calculate the solution speciation and the $CO_2$ partial pressure, $P_{CO_2}$. We show results for seven primary amines: monoethanolamine (MEA), 2–amino–2-methylpropanol (AMP), 1-amino-2-propanol (1–AP), 2–amino–2–methyl–1,3-propanediol (AMPD), 2–aminopropane–1,3-diol (SAPD), 2–(2–aminoethoxy)ethanol or diglycolamine (2–AEE or DGA, respectively), and 2–amino–1–propanol (2–AP). Experimental speciation and $P_{CO_2}$ data for some of these is available, with which we validate our methodology. We predict new results for others in cases when such data are unavailable, and provide explanations for the experimental inability to detect carbamate solution species in relevant cases. Our results for the $pK$ value of the carbamate reversion reaction are within the chemical accuracy limit of $218.546/T$ units (corresponding to 1 kcal·mol$^{-1}$ in the corresponding free energy change) in comparison with experimental results when such data exist, which at 298.15 K corresponds to 0.73 $pK$ units. The precision of our $pK$ predictions is comparable to that which can be obtained from conventional experimental methodologies for these quantities. Our results suggest that the presented molecular simulation methodology may provide a robust and cost–efficient tool for solvent screening in the design of post–combustion $CO_2$ capture processes.

## 4.1 Introduction

Increasing atmospheric concentrations of $CO_2$ and other greenhouse gases and their consequent environmental effects have prompted a large body of research probing the $CO_2$ capturing properties of adsorbing materials and absorbing chemical solvents. Carbon capture and storage (CCS) is considered to be one of the most viable short term options for reducing global carbon emissions[82, 83]. Chemical absorption using aqueous alkanolamine solutions currently being used in industry is considered one of the most mature options for large-scale $CO_2$ capture[140]. However, the capture process suffers from several drawbacks, including high solvent regeneration energy costs, both due to parasitic energy losses due to the high latent heat of the water co-solvent, and formation of the thermally stable carbamates, which also result in poor cyclic capacity[141]. In order to circumvent these problems, various alternative solvents, such as non-aqueous solvents[142], lipophilic amines[143] and phase changing compounds[144] have been recently considered. Unravelling the effects of different functional groups in the amine structures on their behaviour is crucial for the design of improved alkanolamine–based $CO_2$ solvents. For example, heavily hindered alkanolamines have been shown to reversibly absorb $CO_2$ in an equimolar ratio from which $CO_2$ can be completely desorbed at relatively low regeneration temperatures[145].

The $CO_2$ capturing properties of the absorbent are a consequence of the kinetic and chemical reaction equilibrium properties resulting from the $CO_2$ dissolution, and the equilibrium composition of $CO_2$ in the solvent is an important tool for solvent screening. In the case of primary and secondary amines, $CO_2$ is absorbed primarily in the solution in the form of the carbamate ($RNHCO_2^-$), bicarbonate ($HCO_3^-$) and carbonate ($CO_3^{-2}$) species, in coexistence with the neutral ($RNH_2$) and protonated ($RNH_3^+$) amine species, water and its ionization products, and free $CO_2$.

The set of linearly independent chemical equations used to model chemical reaction equilibrium is governed only by the requirement that their number is $R = N - \text{rank}(\mathbf{A})$, where $N$ is the number of species and $\mathbf{A}$ is the species formula matrix[111]. The actual set of reactions used need not be related to any postulated or actual reaction mechanics, and may be motivated by computational convenience. The following stoichiometry provides a convenient thermodynamic basis for describing the reaction equilibria of the indicated

species in the case of primary and secondary amines.

$$2RNH_2 + CO_2 = RNH_3^+ + RNHCO_2^- \quad \text{(R1)}$$
$$RNHCO_2^- + H_2O = RNH_2 + HCO_3^- \quad \text{(R2)}$$
$$H_2O + CO_2 = HCO_3^- + H^+ \quad \text{(R3)}$$
$$HCO_3^- = CO_3^{-2} + H^+ \quad \text{(R4)}$$
$$H_2O = H^+ + OH^- \quad \text{(R5)}$$
$$CO_2(aq) = CO_2(vap) \quad \text{(R6)}$$

Tertiary amines do not form carbamates, and for these reactions R1 and R2 can be replaced by their sum

$$CO_2 + RNH_2 + H_2O = HCO_3^- + RNH_3^+ \quad \text{(R7)}$$

The equilibrium constants (or equivalently, the $pK$ values) for reactions R3–R5 as functions of temperature are experimentally well–known. Their experimental determination for reactions R1 and R2 requires experimental data for each postulated solvent. Furthermore, the equilibrium constants can only be determined indirectly from such data, by fitting to the parameters of an empirically based chemical potential model.

$pK$ values have been determined in this way by fitting to potentiometric titration measurements for the carbamate reversion reaction R2[146], and for the amine protonation reaction[147, 148, 149, 150, 151, 146, 152], which is the linear combination R1+R2-R3.

$$RNH_2 + H^+ = RNH_2^+ \quad \text{(R8)}$$

$pK$ values have also been obtained by fitting thermodynamic models to experimental spectroscopically obtained speciation data of $CO_2$–loaded solutions[153, 154, 155, 156, 157]. In such experimental studies, the presence of the fast proton–exchanging species (*i.e*, the $CO_3^{-2}/HCO_3^-$ or $(RNH_3^+/RNH_2)$ pairs) complicates the data analysis, and usually only the total concentration of the carbonate/bicarbonate pair is available and can be used in the parameter fitting.

Finally, parameters of chemical potential models and/or equations of state have been fitted to reaction models of $CO_2$ solubility data[158]. In other cases, the reactions have been approximated by pseudo–reaction physical association models incorporated in the SAFT[159, 93, 160, 161] or the CPA[162, 163] approaches.

Experimental screening of the vast number of potential solvent candidates is prohibitively expensive and time consuming, and more predictive and less costly computational tools offer a promising alternative and complementary approach. The ability to accurately predict the equilibrium speciation and the associated $CO_2$ partial pressure for $CO_2$-loaded solutions of candidate solvents is one of the most important requirements, which is very challenging due to the complex chemical reaction and phase equilibria involved.

Three general approaches have been used toward this goal: combined Electronic Structure (ES) dielectric continuum solvent (DCS) models, *ab initio* Molecular dynamics (MD) methods, and classical force–field (CFF) methodologies. The first group includes methods based on the Conductor-like Screening Model for Realistic Solvents (COSMO–RS)[164] and Solvation Models based on Density (SMD)[165]. These have been used to study reaction mechanisms and the relative stability of the carbamate product species[][166, 167, 168, 169]. Alternative DCS methods such as the SMDx family of Cramer *et al.* [165], usually trained on hydration free energy data of neutral molecules at 298.15 K, may be potentially applied to such systems; however, their extension to ionic species and to higher temperatures has not been fully tested. Whereas the deficiencies of the continuum solvation models can be partially overcome by incorporating explicit solvent molecules in the first solvation shell[97], their application to flexible molecules is not straightforward[170].

In the second group, Nakai *et al.* [171, 172, 173] used density-functional tight-binding MD simulations to study reaction mechanisms in $CO_2$ chemical absorption and regeneration processes in aqueous amine solutions. While such approaches do not require *a priori* knowledge of the identities of the product species, they require detailed geometric criteria to dynamically evaluate their chemical identity and population at each step of the MD simulation. Moreover, such *ab initio* methods have only been carried out for relatively small system sizes and scale poorly with the system size, making them highly inefficient for the high throughput $CO_2$ solvent screening task. Other *ab initio* approaches based on first principles calculations have also been developed and used for speciation predictions in reactive systems[48], and they share the same disadvantages.

CFF methodologies have been employed by the groups of Vlugt *et al.* [103], Maginn *et al.* [102], and our group [174, 175]. Balaji *et al.* [103] used the Reaction Ensemble (REMC) algorithm[32, 99] (see also Johnson *et al.* [98]) in conjunction separately obtained ideal–gas electronic structure (ES) free energy calculations and fractional insertion of molecular species, in a preliminary study of reaction equilibria in the MEA-$CO_2$-$H_2O$ system. Although the REMC algorithm was incorrectly implemented (by omitting the atomization energies in the ideal–gas ES calculations[174]), it was fortuitously able to reasonably predict the most abundant species (but not those present is minor concentrations) in the system at low to moderate $CO_2$ loadings. Mullen *et al.* [102] applied the REMC algorithm

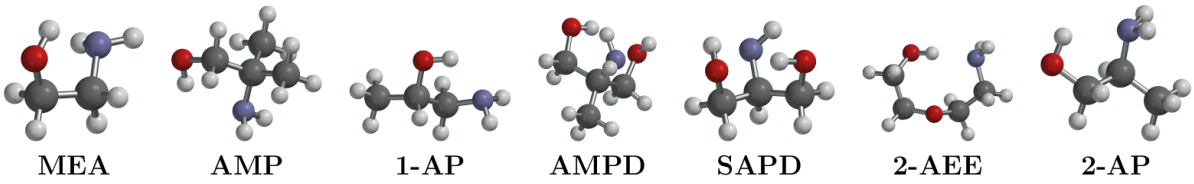


Figure 4.1: Molecular structures of the studied alkanolamines.

in conjunction with an enhanced Monte Carlo sampling approach for $CO_2$ absorption in a reactive ionic liquid. MC–based approaches for complex systems such as those involved in $CO_2$ reactive absorption generally suffer from the computational disadvantage in the case of even moderately complex molecules of requiring special system–specific sampling moves; they also require very long computation times and/or large system sizes to deal with the concentrations of species present in small amounts. These drawbacks make the REMC approach inefficient for their use in solvent screening.

Based on a recently developed reaction equilibrium algorithm requiring only straightforward conventional CFF–based MD free energy calculations, coupled with ES ideal–gas ES free energy calculations, we recently implemented[53] a general and computationally efficient reaction equilibrium algorithm to predict speciation concentrations (including for species present in very small concentrations) and $P_{CO_2}$ in a preliminary study in the case of the benchmark $CO_2$–MEA–$H_2O$ system.

The goal of this paper is to improve this CFF–based methodology and to illustrate its application to the accurate prediction of $CO_2$ reactive absorption speciation and $P_{CO_2}$ data as functions of loading, temperature and solvent composition, for aqueous MEA and for six additional primary alkanolamine systems, whose molecular structures are shown in Fig.4.1. Where experimental data are available, we compare our predictions with experimentally obtained $P_{CO_2}$ and solution speciation data in the literature. For situations in which experimental data are unavailable, our calculations provide predictions that await experimental verification.

## 4.2 Molecular–Based Thermodynamic Methodology

A major challenge in implementing reaction equilibrium calculations from molecular simulations is the expression of the macroscopic thermodynamic models involved in terms of molecular simulation quantities. These little known relationships are briefly described in this section.

The equilibrium composition of a closed chemically reacting system at specified $(T, P)$ can be obtained by minimizing its Gibbs free energy subject to the conservation of mass and electroneutrality constraints, and implemented by calculating the solution of the $R$ equations

$$\Delta G_j(T, P; \mathbf{x}) \equiv \sum_{i=1}^{N_s} \nu_{ij} \mu_i(T, P; \mathbf{x}) = 0; \quad j = 1, 2, \ldots, R \tag{4.1}$$

where $\nu_{ij}$ is the stoichiometric coefficient of species $i$ in reaction $j$ and $\mathbf{x}$ represents the system composition vector. The reaction equilibrium composition can be readily accomplished by a wide range of numerical algorithms[111] and chemical potential models, and we employ here a Henry–Law–based model. The chemical potentials (for both solutes and solvent) in this model are expressed as

$$\mu_i(T, P; \mathbf{m}) = \mu_i^{\dagger}(T; P) + RT \ln \left( \frac{m_i}{m^0} \right) + RT \ln \gamma_i(T, P; \mathbf{m}), i = 1, 2, \ldots, N_{\text{solu}} \tag{4.2}$$

where $T$ is the absolute temperature, $P$ is the pressure, $R$ is the universal gas constant, $m_i$ is the molality of species $i$, $\gamma_i$ is its Henry–Law activity coefficient, and $\mathbf{m}$ is the vector of species molalities. $m^0 = 1$ mol·kg$^{-1}$ solvent.

We have previously shown[114] that the standard chemical potential $\mu_i^{\dagger}(T; P)$ of solute species $i$ can be calculated in terms of molecular simulation quantities by

$$\mu_i^{\dagger}(T, P) = \mu_i^0(T; P^0) + RT \ln \left( \frac{RT M_{\text{solv}} m^0 \rho_{\text{solv}}^*(T, P)}{1000 P^0} \right) + \mu_i^{\text{res},NVT;\infty}[T, \rho_{\text{solv}}^*(T, P)] \tag{4.3}$$

where $P^0 = 1$ bar is the standard state pressure and $\mu_i^0(T; P^0)$ is the ideal gas chemical potential of species $i$, which can be calculated from the partition function of its ideal–gas molecule under the harmonic oscillator rigid rotor approximation[61, 176], $\rho_{\text{solv}}^*(T, P)$ is the density of the pure solvent (water in our case), $M_{\text{solv}}$ is its molecular weight, and $m^0 = 1$ mol·kg$^{-1}$ solvent. For a solute, $\mu_i^{\text{res},NVT;\infty}[T, \rho_{\text{solv}}^*(T, P)]$ is its residual chemical potential at infinite dilution in the solvent (also referred to as its intrinsic hydration free energy, $\Delta G_{\text{hyd}}(T, P)$), and the same quantity for the solvent is its self–solvation free energy; both are calculated by conventional MD simulations in the $NVT$ ensemble.

In the following, we restrict attention to the ideal solution approximation, $\gamma_i = 1$ (expressions for the nonideal case are given in our previous paper[174]). The solvent chemical potential is obtained from the Gibbs–Duhem equation as[174]

$$\mu_{\text{solv}}(T, P; \mathbf{m}) = \mu_{\text{solv}}^{\dagger}(T; P) + RT \ln \left( \frac{1000}{M_{\text{solv}} m^0} \right) - RT \left( \frac{1 - x_{\text{solv}}}{x_{\text{solv}}} \right) \tag{4.4}$$

We remark that for reactions in which the solvent (here water) participates, the solvent chemical potential is typically approximated in experimental studies by its Raoult Law form

$$\mu_{\rm solv}(T,P;\mathbf{m}) = \mu^*_{\rm solv}(T,P) + RT\ln(x_{\rm solv}) \tag{4.5}$$

where $\mu^*_{\rm solv}(T,P)$ is the pure solvent chemical potential and $x_{\rm solv}$ is its mole fraction. Substitution of Eqs. (4.2)–(4.4) in Eq. (4.1) yields the final working equations:

$$\frac{\Delta\widetilde{G}_j(T,P)}{RT} + \sum_{i=1}^{N_{\rm solu}} \nu_{ij}\ln\left(\frac{m_i}{m^0}\right) + \nu_{solv}\left(\frac{x_{\rm solv}-1}{x_{\rm solv}}\right) = 0; \quad j=1,2,\ldots,R \tag{4.6}$$

where $\nu_{{\rm solv},j}$ is the stoichiometric coefficient of the solvent in reaction $j$, and

$$\Delta\widetilde{G}_j(T,P) = \Delta G^0_j(T;P^0) + \Delta G^{{\rm res},NVT;\infty}_j(T,P) \tag{4.7}$$

$$+RT\overline{\nu}_j\ln\left(\frac{RTM_{\rm solv}m^0\rho^*_{\rm solv}(T,P)}{1000P^0}\right) + \nu_{{\rm solv},j}RT\ln\left(\frac{1000}{M_{\rm solv}m^0}\right) \tag{4.8}$$

where

$$\Delta G^0_j(T;P^0) = \sum_{i=1}^{N_s}\nu_{ij}\mu^0_i(T;P^0) \tag{4.9}$$

$$\Delta G^{{\rm res},NVT;\infty}_j(T,P) = \sum_{i=1}^{N_s}\nu_{ij}\mu^{{\rm res},NVT;\infty}_i(T;P) \tag{4.10}$$

$$\overline{\nu}_j = \sum_{i=1}^{N_s}\nu_{ij} \tag{4.11}$$

$\Delta\widetilde{G}_j(T,P)$ is commonly expressed in terms of the equilibrium constant $K_j$, via

$$pK_j(T,P) \equiv -\log_{10}K_j = \frac{\Delta\widetilde{G}_j(T,P)}{RT\ln(10)} \tag{4.12}$$

We remark that the third term in Eq. (4.8) can be separated into a temperature–dependent term (often referred to as the "standard state correction") and a density term, which is often mistakenly neglected in $pK$ calculations (see Noroozi and Smith[175]).

## 4.3 Simulation Details

### 4.3.1 Ideal Gas Reaction Free Energies

In order to find the most stable conformer of the molecular/ionic species, an extensive gas phase conformational search was first performed for the geometries of the protonated, carbamate and neutral forms of each amine using the Merck Molecular Mechanics Force Field (MMFF94) implemented in the Spartan v.18 Software package[127]. For each species, for each of the 10 lowest energy conformers obtained from this search we performed further geometry optimizations to find the lowest free energy conformers arising from five different high–level composite quantum chemical (QM) methods: G4, G3, G3B3, CBS-QB3 and CBS-APNO in Gaussian16[121]. We ensured that for each QM method, the conformer converged to a stable minimum of the potential energy surface with positive real vibrational frequencies. We then used the conformer with the lowest free energy/chemical potential for the subsequent ideal–gas reaction free energy calculations for each of the five QM methods. The combination of the results of these five methods is described in the Results and Discussion section.

### 4.3.2 Force Field Development and Hydration Free Energy Calculations

For the amine's neutral ($RNH_2$), protonated ($RNH_3^+$) and carbamate ($RNHCO_2^-$) forms, and for the bicarbonate ion ($HCO_3^-$), the Lennard-Jones (LJ) and intramolecular bonded (bond stretching, angle bending, and dihedral torsion) potential parameters of the force fields were modeled in a consistent manner using the General Amber Force Field[177] parameters within its default functional form by using the Antechamber package in AMBER tools[178], which employs an algorithm to assign the parameters based on the atom types. Carbon dioxide ($CO_2$) was modeled using the TraPPE potential of Pottof[122], and to be consistent with GAFF parametrization the solvent (water) was modeled with the TIP3P Force Field.

To calculate the partial charges, high–level QM methods are generally preferred to refine the geometry of the lowest–energy solute conformer as described in the previous section. However, to be consistent with the ideal–gas geometry of the force fields in the hydration free energy calculations, we used the lowest free energy conformer at the G4 level of the previous section as representative of the solute gas–phase geometry to calculate its electrostatic potential energy grid at the GAFF default HF/6-31G* level using the

Merz-Kollman scheme in Gaussian16. We also examined the effects of determining the partial charges from several different QM electron density determination methodologies (B3LYP/6-311++G(d,p), MP2/aug-cc pVTZ, and MP2/aug-cc pVTZ+PCM) on the resulting hydration free energies and the equilibrium constants, which is discussed in Section 4.4.3.

Finally, we used the two–step Restrained Electrostatic Surface Potential (RESP) fitting method[65] within the Antechamber software package to assign the partial charges. The Gromacs–formatted topologies were then generated using the acpype (version 2019) python interface[179].

MD simulations of the hydration free energies in Eq. (4.11) were performed using a single solute molecule solvated in a periodic box of 1500 water molecules using the Gromacs (version 2016.3) program[180], with initial configurations generated using the packmol software package[181]. A steepest–descent minimization was then performed to remove any bad contacts, followed by a short (100 ps) $NVT$ equilibration run followed by a 12 ns $NPT$ simulation with the first 2 ns discarded to determine the system density. Free energy simulations to decouple the solute molecule from its solvent environment were then initiated from the equilibrated configurations in an $NVT$ ensemble, with box size corresponding to the calculated density.

The equations of motion were integrated using the Gromacs stochastic Langevin scheme, with a friction constant of 1.0 $ps^{-1}$. The pressure was maintained using a Parrinello-Rahman pressure coupling constant of 2.0 ps. The Lennard–Jones short–range interactions were smoothly switched off between 12 and 12.5 Å and the electrostatic interactions were computed using the particle mesh Ewald (PME) method with a 12 Å real–space cutoff, 1.0 Å grid spacing, sixth–order spline interpolation, and accuracy of $10^{-6}$. The free energy of decoupling the solute molecule from its solvent environment was calculated using the Gromacs Bennett Acceptance Ratio (BAR) method (gmx bar). We employed six equally spaced $\lambda$ values and linear decoupling for the electrostatic interaction, followed by 20 equally spaced $\lambda$ values with $\Delta\lambda = 0.05$ to decouple the LJ interactions using the standard GROMACS soft-core potential function originally proposed by Beutler et al[182], with parameters (in GROMACS notation) *sc-alpha* = 0.5, *sc-power* = 1 and *sc-sigma* = 0.3. For each alchemical window, we used a 12.5 ns simulation with the first 2.5 ns discarded for equilibration.

## 4.4 Results and Discussion

### 4.4.1 Ideal–Gas Standard Reaction Free Energies

Tables S1 and S2 of the Supporting Information show our calculated ideal–gas standard reaction free energies $\Delta G_j^0(T;P^0)$ of Eq. (4.9) for reactions R1 and R2 at the four temperatures (298.15 K, 313.15 K, 333.15 K, 353.15 K) for the set of seven amines considered, using five different composite QM methods.

As noted by Somer *et al.* [183], improved predictions can arise from the use of combinations of several–high level methods, since methods such as G4 tend to over-estimate and methods such as CBS-QB3 tend to underestimate the reaction free energy. The variations in the different methods also enable us to infer the uncertainty rooted in the different chemical species of the same class of molecules. For example, in our previous work[175], we found that for the amine species, the ideal gas free energies vary significantly among the QM methods, depending on the size and flexibility of the molecules involved. Based on the Table S1 results, for most species the Gaussian-n theories (G4, G3, G3B3) tend to predict higher $\Delta G_j^0(T;P^0)$ values than those of the complete basis set (CBS-QB3, CBS-APNO) approaches. We note that the R2 values generally indicate slightly smaller standard deviations than those of R1, except for the species containing multiple hydroxyl groups (SAPD, AMPD, 2-AEE). For these species reaction R2 shows significant scatter among the QM methods.

For speciation calculations involving reactions R1 and R2, we used the average $\Delta G_j^0(T;P^0)$ values from the five methods in Tables S1 and S2. Tables S8–S12 show the raw Gaussian16[180] output for each species from which they were calculated. Their standard deviations are about 3 kJ·mol$^{-1}$, which we take as a surrogate measure of the uncertainty in the $\Delta G_j^0(T;P^0)$ values. This value is well within a "chemical precision standard" of 1 kcal·mol$^{-1}$.

### 4.4.2 Equilibrium Constants $pK_1$ and $pK_2$

Table 4.1 summarizes our $pK_1$ and $pK_2$ results for the seven alkanolamines studied at the indicated temperatures and $P = 1$ bar. The underlying data used for their calculation is given in the Supplementary Information as follows. Table S4 shows the simulated $\mu^{\mathrm{res},NVT;\infty}(T,P)$ values for the neutral ($RNH_2$), protonated ($RNH_3^+$) and carbamate ($RNHCO_2^-$) forms of the seven alkanolamines at the four temperatures of this study. Table S5 shows $\mu^{\mathrm{res},NVT;\infty}(T,P)$ values for $HCO_3^-$, for $CO_2$ using the Trappe FF[122], and for

Table 4.1: Predicted $pK$ values for reactions R1 and R2 from this work at the indicated temperatures and $P = 1$ bar.

| $T$ (K) | MEA | AMP | 1–AP | AMPD | SAPD | 2–AEE | 2–AP |
|---|---|---|---|---|---|---|---|
| | | | | Reaction R1 | | | |
| 298.15 | $-5.75_{0.56}$ | $-2.29_{0.58}$ | $-3.89_{0.66}$ | $-2.24_{0.52}$ | $-3.63_{0.62}$ | $-5.84_{0.50}$ | $-3.57_{0.49}$ |
| 313.15 | $-4.84_{0.54}$ | $-1.58_{0.55}$ | $-3.08_{0.63}$ | $-1.69_{0.51}$ | $-2.95_{0.59}$ | $-4.93_{0.49}$ | $-2.88_{0.46}$ |
| 333.15 | $-3.83_{0.49}$ | $-0.74_{0.52}$ | $-2.30_{0.60}$ | $-0.80_{0.50}$ | $-2.11_{0.55}$ | $-3.77_{0.48}$ | $-2.05_{0.44}$ |
| 353.15 | $-3.20_{0.50}$ | $-0.01_{0.49}$ | $-1.61_{0.58}$ | $-0.32_{0.49}$ | $-2.05_{0.51}$ | $-2.63_{0.48}$ | $-1.37_{0.41}$ |
| | | | | Reaction R2 | | | |
| 298.15 | $1.62_{0.42}$ | $-1.87_{0.50}$ | $0.61_{0.40}$ | $-1.02_{0.60}$ | $-0.095_{0.53}$ | $1.22_{0.66}$ | $-0.26_{0.48}$ |
| 313.15 | $1.38_{0.40}$ | $-1.93_{0.49}$ | $0.43_{0.39}$ | $-1.08_{0.59}$ | $-0.19_{0.51}$ | $0.90_{0.65}$ | $-0.34_{0.47}$ |
| 333.15 | $1.15_{0.39}$ | $-1.90_{0.47}$ | $0.30_{0.37}$ | $-1.16_{0.57}$ | $-0.28_{0.49}$ | $0.59_{0.63}$ | $-0.42_{0.45}$ |
| 353.15 | $1.15_{0.38}$ | $-1.90_{0.46}$ | $0.25_{0.36}$ | $-1.14_{0.55}$ | $-0.38_{0.48}$ | $0.18_{0.62}$ | $-0.47_{0.44}$ |

$H_2O$ using the TIP3P FF. The $\Delta\widetilde{G}_j(T,P)$ and $pK_j(T,P)$ values for reactions R1 and R2 used in the reaction equilibrium calculations listed in Tables S6 and S7.

The indicated uncertainties are one standard deviation, which are seen to be within a "chemical precision standard" of 1 kcal·mol$^{-1}$ for $\Delta\widetilde{G}_j(T,P)$ in Eq. (4.8). This translates to a precision in $pK$ units of

$$\Delta pK = \frac{4184}{2.303RT} = \frac{218.546}{T} \tag{4.13}$$

which at 298.15 K is 0.73 $pK$ units.

The dependence of the equilibrium constants on temperature is shown in Fig. 4.2, using regressions to the expression

$$pK = a + b/T + c\ln(T) \tag{4.14}$$

The values of the parameters $(a, b, c)$ are given in Table S3 of the SI. Interestingly, the right panel of Fig. 4.2 shows that in comparison with the carbamate forming amines (MEA, 1–AP, 2–AEE), the $pK_2$ values for the sterically hindered amines (AMP, AMPD, SAPD, 2–AP) show a weaker temperature dependence.

Figure 4.2: Temperature dependence of the equilibrium constants for reactions R1 and R2 for the seven amines studied.

Table 4.2: Comparison of GAFF predicted intrinsic hydration free energies, $\mu^{\mathrm{res},NVT;\infty}$ (in kJ· mol$^{-1}$) of the protonated, neutral and carbamate forms of MEA and AMP at $T = 298.15$ K using different sets of partial charges in conjunction with RESP.

| Species | MP2/aug-cc-pVTZ+PCM | HF/6-31G* | B3LYP/6-311++G(d,p) | MP2/aug-cc-pVTZ |
|---|---|---|---|---|
| | | monoethanolamine (MEA) | | |
| $RNH_2$ | $-32.89_{0.05}$ | $-30.23_{0.14}$ | $-26.94_{0.19}$ | $-23.30_{0.07}$ |
| $RNH_3^+$ | $-243.87_{0.09}$ | $-239.43_{0.10}$ | $-235.95_{0.1}$ | $-234.71_{0.13}$ |
| $RNHCOO^-$ | $-400.63_{0.08}$ | $-366.79_{0.19}$ | $-365.63_{0.15}$ | $-358.62_{0.27}$ |
| | | 2-amino-2-methylpropanol (AMP) | | |
| $RNH_2$ | $-38.53_{0.03}$ | $-34.35_{0.13}$ | $-31.68_{0.16}$ | $-27.50_{0.07}$ |
| $RNH_3^+$ | $-228.33_{0.06}$ | $-222.50_{0.11}$ | $-216.22_{0.13}$ | $-215.57_{0.12}$ |
| $RNHCOO^-$ | $-393.84_{0.06}$ | $-352.33_{0.10}$ | $-349.64_{0.12}$ | $-342.94_{0.04}$ |

### 4.4.3 Effects of Different Partial Charge Methods on the $pK$ Values

As described in Section 4.3, for the $pK$ calculations and the resulting equilibrium compositions we used the default HF/6-31G* partial charges based on each molecule's G4 optimized geometry, from which the electrostatic surface grid and the RESP atomic partial charges were obtained. Numerous studies[184, 185] have addressed the effects on the $\mu^{\mathrm{res},NVT;\infty}$ values of different QM approaches used to obtain the FF partial charges. To examine this effect for our systems, we considered representative $\mu^{\mathrm{res},NVT;\infty}$ values for MEA and for AMP at $T = 298.15$ K based on RESP partial charge assignment arising from several different QM methodologies: the default GAFF HF/6-31G* results from Table S3, B3LYP/6-311++G(d,p), MP2/aug-cc-pVTZ) in the gas phase and a MP2/aug-cc-pVTZ calculation in presence of polarizable continuum solvent (MP2/aug-cc-pVTZ+PCM, with a dielectric constant of 78.39). These are shown in Table 4.2.

The results show relatively small (3–8 kJ·mol$^{-1}$) differences from our default HF/6-31G* calculations in the cases of B3LYP/6-311++G(d,p) and MP2/aug-cc-pVTZ). However, when the polarizable continuum model (PCM) is included in the calculation of the electron density (MP2-aug-cc-pVTZ+PCM), the hydration free energy of the carbamate anion ($RNHCO_2^-$) becomes considerably more negative (by 30–40 kJ·mol$^{-1}$) compared

Table 4.3: Comparison of the predicted $pK$ values of reactions R1 and R2 for the MEA and AMP systems at $T = 298.15$ K using different sets of partial charges from Table 4.2, the $\Delta G^0$ values in Table S1 and S2, and the $\mu^{\mathrm{res},NVT;\infty}$ values for $H_2O$, $CO_2$ and $HCO_3^-$ in Table S4.

| Reaction | HF/6-31G* | B3LYP/6-311++G(d,p) | MP2/aug-cc-pVTZ |
|---|---|---|---|
| | | monoethanolamine (MEA) | |
| R1 | $-5.75_{0.56}$ | $-6.09_{0.56}$ | $-5.92_{0.56}$ |
| R2 | $1.62_{0.42}$ | $2.00_{0.41}$ | $1.41_{0.41}$ |
| | | 2-amino-2-methylpropanol (AMP) | |
| R1 | $-2.29_{0.58}$ | $-1.64_{0.58}$ | $-1.81_{0.58}$ |
| R2 | $-1.87_{0.50}$ | $-1.85_{0.50}$ | $-1.31_{0.50}$ |

to the unpolarized charge density (mp2-aug-cc-pVTZ) result. In contrast, the charges derived from the polarized electronic density causes the hydration free energy of the protonated amines ($RNH_3^+$) becomes more negative by only 5–6 kJ·mol$^{-1}$. Partial charges obtained from the RESP methodology already tend to overpolarize anions in the absence of PCM[186], and our results show that this becomes excessive in its presence.

Representative $pK$ values at 298.15 K for reactions R1 and R2 calculated from Eqs (4.8)–(4.12) using columns 3–5 of Table 4.2 and the data of Tables S1, S2 and S4 are shown in Table 4.3. Whereas the $\mu^{\mathrm{res},NVT;\infty}$ vary substantially across the QM levels in Table 4.2, the $pK$ values in Table 4.3 are not overly sensitive to the different partial charge methodologies. However, we note that our comparisons were obtained using GAFF Lennard–Jones force–field parameters, which are optimized to the HF/6-31G* partial charges. A more complete comparison of the effects of the different theories/levels on the hydration free energies would require re–optimization with respect to experiment of the Lennard–Jones force-field parameters for each theory/level. Since the partial charges tend to be the major contribution to the hydration free energy values, we do not expect such a re-optimization to produce a large effect. In any event, such a study is beyond the scope of this work, and would also contradict its purely predictive approach.

### 4.4.4 Carbamate Stability Constant, $K_2$

In this section we discuss our results for the equilibrium constant $K_2$ of the carbamate reversion reaction R2 (the inverse of the carbamate formation reaction equilibrium constant), in

comparison with those obtained from experiment at the representative temperature 298.15 K when such data are available.

In our approach, we directly predict $K_2(T, P)$ from simulation quantities using Eq. (4.12). $K_2(T, P)$ cannot be directly measured experimentally, but must be obtained indirectly using

$$\ln K_2(T, P) = \sum_{i=1}^{N_s} [\nu_{i2}[\ln m_i^* + \ln \gamma_i(T, P; \mathbf{m}^*)] \tag{4.15}$$

where the molalities and activity coefficients refer to an experimentally measured equilibrium composition, $\mathbf{m}^*$, and $\nu_{i2}$ is the reaction stoichiometric coefficient of species $i$ in reaction R2. One approach is by means of extrapolation to zero ionic strength of the experimentally measured species activity coefficients of Eq. (4.15), and another is by fitting the measured equilibrium data to the parameters of a thermodynamic model for the chemical potentials.

Our predicted $pK_2$ values at the representative temperature $T = 298.15$ K are shown in Table 4.4, where they are compared with experimental results from the literature. The major source of uncertainty in our $pK$ calculations is that of the ideal–gas $\Delta G_2^0$ term in Eq (4.9). For the experimental values, the sources of uncertainty/error in $pK_2$ are the uncertainties in any model used for the activity coefficients and the uncertainties in the experimental composition measurements. The latter is likely the greater contributor, since both the neutral and the protonated amine pair are present as is the case for the bicarbonate/carbonate pair, and it is very difficult to experimentally distinguish the individual species concentrations from NMR data.

We have already noted that our $pK$ uncertainties are within a "chemical precision standard" of 0.73 $pK$ units at 298.15 K. We remark that the precisions of experimental studies are often not provided in their publications (but we highlight the careful experimental work of the Tremaine group[156], which recently studied $pK_2$ values from 283.2–313.2 K for 2–methylpiperadine using NMR spectroscopy and reported precisions of 0.35–1.50 $pK$ units).

Table 4.4: Comparison with literature data of calculated $pK_2$ for the carbamate reversion reaction R2 at $T = 298.15$ K (unless indicated otherwise) and $P = 1$ bar .

| Amine | This work, Table 4.2 | Literature |
|---|---|---|
| MEA | $1.62_{0.42}$ | 1.71(291.15 K)[187],1.25[188],1.31[189],1.86[190] 1.81[191],1.46[137],1.60[192],$1.76_{0.02}$[154] |
| AMP | $-1.87_{0.50}$ | -2.15*, -1.66[193], <-0.70(303 K)[153], $< -1$[16], -1.0[194] |
| 1–AP | $0.61_{0.40}$ | $1.70_{0.2}$[195] |
| AMPD | $-1.02_{0.60}$ | sterically hindered |
| 2–AEE | $1.22_{0.66}$ | 1.75[196] |
| SAPD | $-0.09_{0.53}$ | no carbamate detected[195] |
| 2–AP | $-0.26_{0.48}$ | $0.6_{0.1}$[195], 0.98[154] |

* calculated from the mole-fraction-based apparent equilibrium constant of 0.47 from Ciftja *et al.* .[197]

$pK_2(T, P)$ for MEA has been the subject of numerous experimental studies [189, 192, 153, 154, 195], using the indicated approaches or variants thereof. For MEA at 298.15 K, our predictive methodology gives $pK_2 = 1.62 \pm 0.42$. The spread of the literature $pK$ values (1.25–1.86) is partly due to differences in the activity coefficient models used by the authors, and likely more importantly to the difficulty in the measurement of the concentrations of the proton exchanging species. The precision of our prediction is seen to be similar to that of the experimentally measured values. (See also Section 4.6.)

There are fewer experimental $pK_2$ results for the other alkanolamines. Several groups[16, 196, 194, 197, 193, 156] have reported an "apparent equilibrium constant" for $pK_2$ for a range of solvents based on the approximations that the activity of water is unity and that the activity coefficients for $RNHCO_2^-$ and $HCO_3^-$ are equal and hence cancel in the activity coefficient ratio at all concentrations. The latter behaviour (referred to herein as the iso–Colombic approximation, ICA) is based on the fact that the cancellation holds exactly in the Debye–Hückel activity coefficient model for the iso–Coulombic reaction R2 at all concentrations. $pK_2$ obtained from the ICA is referred to as an "apparent equilibrium constant". We can see mild supporting evidence for the ICA from the $\mu^{\mathrm{res},NVT;\infty}$ values for $RNHCO_2^-$ and $HCO_3^-$ in Tables S3 and S4 of the Supporting Information, where it is seen that they are of the same sign and similar magnitude. We also found (not shown) that simulations show that this behaviour continues to hold as the solution concentrations increase.

Our predicted AMP value is $pK_2 = -1.87 \pm -0.50$. McCann *et al.* [153] studied the AMP system using $^1$H NMR. They did not detect carbamate, but they noted that $pK_2 < -0.70$ at 303 K. Other authors reported apparent equilibrium constants based on

the ICA. Sartorl and Savage[16] reported $pK_2 < -1.0$ at 313 K in their $^{13}$C NMR study. Ciftja *et al.* [197] obtained a value of $pK_2 = -2.15$ and later[193] a value of $pK_2 = -1.66$, based on $^{13}$C NMR measurements. Yamada *et al.* [194] reported $pK_2 \approx -1.0$ for AMP from $^{13}$C NMR studies. The negative AMP $pK_2$ value compared to that of MEA indicates that AMP carbamate formation is thermodynamically less favoured, a consequence of the steric effect of the two methyl groups ($-CH_3$) on the $\alpha$ carbon connected to the amine nitrogen atom.

The addition of a $-CH_3$ group to the $\beta$ carbon of MEA gives 1–AP. For this molecule, we predict a carbamate formation constant of $pK_2 = 0.61 \pm 0.40$, which is smaller than that of MEA. This indicates a small steric effect, arising from the −CH3 group being further away from the amino group. The experimental study of Conway *et al.* [195] also noted significant carbamate formation in the 1–AP solution, and they reported $pK_2 = 1.7$.

We did not find any experimental carbamate/bicarbonate concentration data for AMPD. Similarly to AMP, it is a sterically hindered amine and we predict $pK_2 = -1.02 \pm 0.60$.

For 2–AEE, we predict $pK_2 = 1.21 \pm 0.66$ at 298.15 K; this system was experimentally studied by Al-Juaied *et al.* [196] using $^{13}$C NMR, who reported an apparent $pK_2 = 1.75$ for 17.7 M 2–AEE at relatively low $CO_2$ loading at 300 K. (See the iso–Coulombic discussion above.)

While Conway *et al.* [195] did not observe carbamate formation in SAPD, Bougie *et al.* [198] suggested carbamate formation in SAPD similar to that of unhindered amines based on the trend of the solubility data. For SAPD, we predict a value of $pK_2 = -0.09 \pm 0.53$ at 298.15 K, indicating that it is a mildly carbamate–forming amine.

Removing one of the $-CH_3$ groups from the $\alpha$ carbon of AMP gives 2–AP. For 2–AP, the predicted $pK_2$ value increases to $pK_2 = -0.26 \pm -0.48$, which lies between that of MEA and AMP. Fernandes *et al.* [154] reported a value of $pK_2 = 0.98$ at 298.15 K for 2–AP from their NMR study. In a more recent study by the same group[195], they obtained $pK_2 = 0.6 \pm 0.1$, which agrees with our predicted value within their mutual uncertainties.

Figs 4.3 and 4.4 of Section 4.4.6 show the decreasing carbamate concentrations for the solvents as their $pK_2$ value decreases. For AMP, the alkanolamine with the lowest $pK_2$ value, evidence of the experimental difficulty of observing carbamate is indicated in Fig. 4.3, where it is seen that its carbamate mole fraction becomes less than $10^{-4}$ at low and at high $CO_2$ loadings.

In general, comparison with the (often limited) experimental data shows that the molecular models employed here are able to capture qualitatively and to a reasonable quantitative accuracy, the observed trend in the steric effects on carbamate formation for the common primary amines used in the PCC process studied herein.

Table 4.5: Prediction of the amine protonation constant $pK_8$ independently of knowledge of the proton ($H^+$) hydration free energy at 298.15 K using $pK_8 = pK_1 + pK_2 - pK_3$, in conjunction with our results for $pK_1$ and $pK_2$ in Table 4.1 and the well–established experimental value $pK_3 = 6.30$[199] for the bicarbonate reaction R3.

| amine | -$pK_8$ (this work) | -$pK_8$ (expt) |
|---|---|---|
| MEA | $10.42_{0.50}$ | 9.51[200], 9.44[201], 9.50[202], $9.51_{0.01}$[203] $9.59_{0.19}$[204], 9.50[205], $9.44_{0.01}$[154] |
| AMP | $10.45_{0.52}$ | $9.67_{0.01}$[154] |
| 1–AP | $9.57_{0.56}$ | 9.50 |
| AMPD | $9.63_{0.44}$ | $8.84_{0.01}$[154] |
| SAPD | $10.07_{0.55}$ | 8.55 |
| 2-AEE | $10.97_{0.48}$ | 9.42 |
| 2-AP | $10.13_{0.52}$ | $9.52_{0.01}$[154], 9.40 |

### 4.4.5 Consistency Tests for the Amine Protonation Constants

For a wide range of amines, experimental data are available for the amine protonation reaction $pK_8$ of reaction R8[206]. Furthermore, the equilibrium constants for reactions R3–R5 are well studied, based on the $CO_2 - H_2O$ equilibria for a wide range of temperatures[199]. Since reaction R8 is the sum R1+R2-R3, this allows the prediction of any one of the equilibrium constants from those of the others. In particular, this approach allows the prediction of amine protonation $pK_8$values from molecular simulation that are independent of knowledge of the intrinsic hydration free energy of the proton, precise values of which remain unknown despite extensive experimental and theoretical efforts.

In Table B.2, we show predictions of $pK_8$ from our simulation results for the equilibrium constants of reactions R1 and R2 in conjunction with the experimental data of Edwards *et al.* [199] for the bicarbonate reaction R3. It is seen that the $pK_8$ values predicted in this way are generally within 1 $pK$ unit of the experimental values. Since we have previously seen that our $pK_2$ values agree well with the corresponding experimental values and the only species not appearing in both R1 and R2 is the protonated amine species, $RNH_3^+$, we conjecture that an improved treatment of this species would lead to better agreement with the experimental $pK_8$ values.

Figure 4.3: Speciation predictions (curves) for 30 wt% aqueous MEA and AMP solutions of $CO_2$ at $T = 298.15$ K and $P = 1$ bar, and their comparison with experimental data. For MEA/$MEAH^+$, all experimental data points are indistinguishable and fall on the predicted curve. For MEA carbamate, open green circles are data of Jakobsen *et al.* [207], filled green circles are data of Hilliard[88] and filled green squares are data of Böttinger *et al.* [191]). For the MEA $HCO_3^-/CO_2^{-2}$ data, open blue data points refer to the separately measured and subsequently combined data of Jakobsen *et al.* [207] (the separate concentrations are shown in the inset); filled data points refer to measurements of the combination only (filled blue circles of Hilliard[88] and filled blue squares of Böttinger *et al.* [191]). The data of Jakobsen*et al.* [207] and of Böttinger *et al.* [191] are at 293.15 K, and the data of Hilliard is at 300.15 K. Experimental data for AMP are from Ciftja *et al.* [193] at 298.15 K.

### 4.4.6 Speciation

Our species concentrations were calculated using the Henry–law based chemical potential model of Eq. (4.2), using our $pK_1$ and $pK_2$ values in conjunction with the well–known experimental $pK$ data for reactions R3–R5[199]. We first calculated compositions using the ideal solution form of the model ($\ln \gamma_i = 0$), and then performed preliminary calculations using the methodology of Smith and Qi[44] for extending the model to the nonideal case. We found that the equilibrium compositions resulting from the first iteration of this approach changed by very small amounts from those of the ideal solution, and our results presented here are those of the ideal solution form of the model.

Whereas there exists extensive $CO_2$ solubility data as a function of its partial pressure for a wide range of amines, only a few NMR–based studies have studied speciation data in the solvent[191, 193, 207, 88]. For the amines considered in this work, we only found NMR measurements for MEA and for AMP, which are shown in Fig. 4.3 along with our predictions.

For MEA (left panel of Fig. 4.3), our results are in excellent agreement with the experimental results at $CO_2$ loadings of 0.4 and greater, where the mole fractions are greater than about 0.005. There is significant scatter in the experimental data at low loadings for the $HCO_3^-/CO_2^{-2}$ pair, reflecting the experimental difficulty of accurately measuring such low concentrations. As already noted in Section 4.4.4, these difficulties can lead to significant scatter in the experimentally determined $pK_2$ value if such data are used for its estimation.

Jakobsen *et al.* [207] fitted a thermodynamic model to their NMR data to separate the

$HCO_3^-/CO_2^{-2}$ and considered low $CO_2$ loadings. Our results are in better agreement with their data (open blue circles) than those of Hilliard[88] (filled blue circles), which appear to under–predict the $HCO_3^-/CO_3^{-2}$ concentrations. The inset shows that the Jakobsen *et al.* [207] $HCO_3^-$ concentrations (open circles) agree well with our results, but their $CO_3^{-2}$ concentrations are higher than ours (although both are quite small) at high loadings. This is consistent with the suggestion of the Jakobsen group that their +NMR speciation data did not obey electroneutrality, which they attributed to possible over–estimation of the $CO_3^{-2}$ concentration. At higher loadings, our $HCO_3^-/CO_3^{-2}$ results are in excellent agreement with the data of both Böttinger *et al.* [191] and of Jakobsen *et al.* [207].

Finally, our results for the MEA carbamate species are in excellent agreement with those of results of both Böttinger *et al.* [191] (filled squares), Jakobsen *et al.* [207] (open circles) and Hilliard (filled circles) at loadings up to about 0.6. At higher loadings, our predictions are in agreement with the data of Böttinger *et al.* , who used a combination of $^{13}C$ and $^1H$ NMR procedures with the goal of obtaining more accurate carbamate concentrations. The Jakobsen *et al.* data are significantly higher.

In contrast to MEA, which is a carbamate forming species, AMP is a sterically hindered amine, and forms only very small amounts of carbamate due to ‘ the electronic effect of the methyl groups around the nitrogen. As shown in the right panel of Fig 4.3, this is well captured by our simulations. Our predicted concentration of the $HCO_3^-/CO_3^{-2}$ pair is in agreement with the Ciftja *et al.* measurements, whereas the AMP carbamate concentrations is significantly higher. The disagreement of $AMPCO_2^-$ concentration with the experimental NMR–based data of Ciftja *et al.* [193] can be justified in part by the fact that these concentrations are very small, and that the speciation fraction data reported by Ciftja *et al.* does not obey electroneutrality, resulting in the likelihood that the carbamate concentrations are subject to significant uncertainties.

Finally, Fig. 4.4 shows our predicted compositions for the other alkanolamines studied, for which no experimental data exists in the literature. If and when NMR experiments are performed for these solvents, we expect that species concentrations lower than about 0.005 will be either difficult to obtain accurately or undetectable. For example, for AMPD this is expected to be the case for the carbamate species, which will make the experimental determination of its $pK_2$ value very difficult.

### 4.4.7 $CO_2$ Solubility

The equilibrium solubility of $CO_2$ expressed in terms of its partial pressure, $P_{CO_2}$, in the vapor phase as a function of the total loading (both in its free and chemically bound

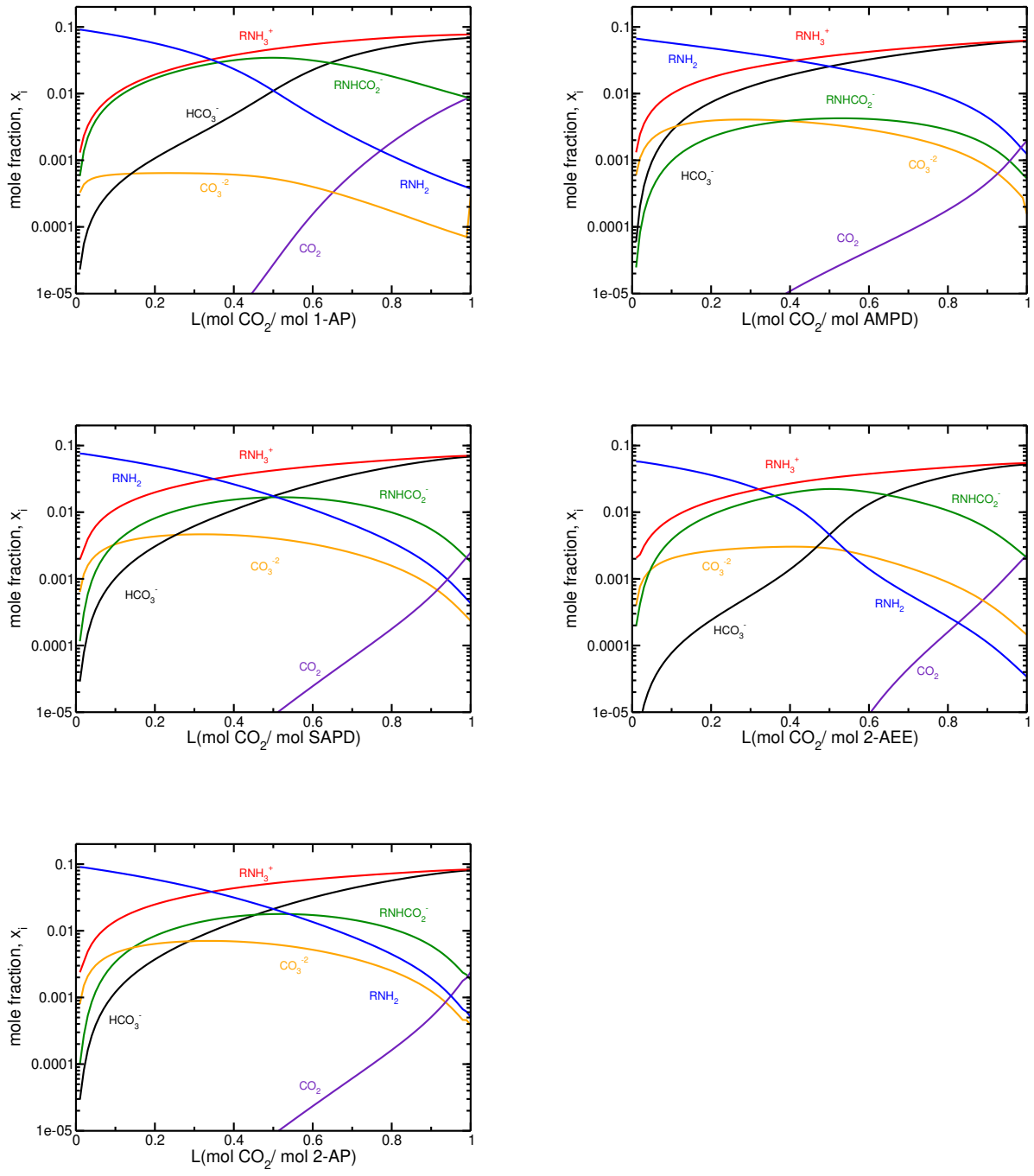


Figure 4.4: Speciation predictions (curves) for reactive absorption of $CO_2$ in 30 wt% amine aqueous solutions at $T = 298.15$ K and $P = 1$ bar. No experimental data exists for comparison.

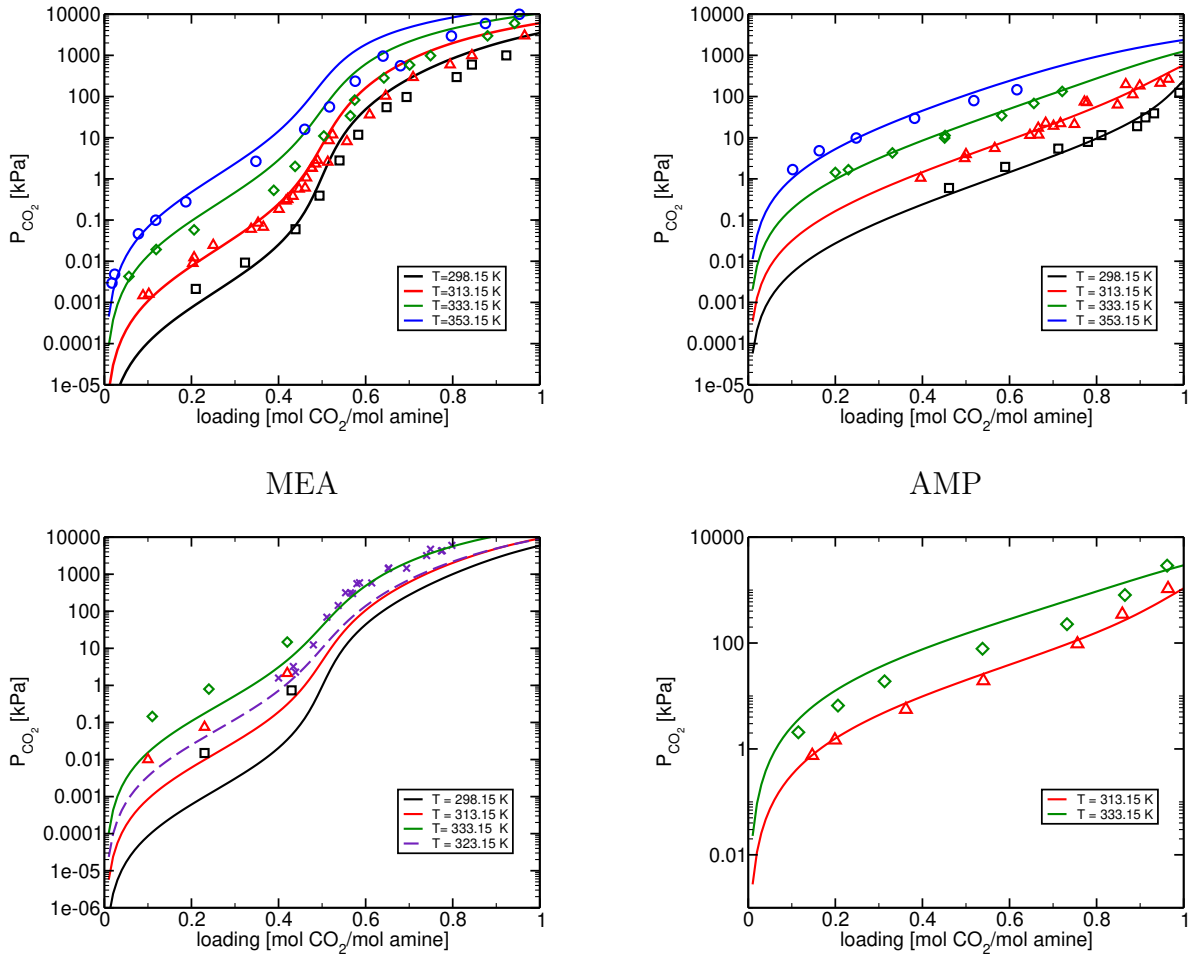


Figure 4.5: Comparison of the $CO_2$ partial pressures in 30 weight% MEA, AMP, AMPD and 60% 2–AEE aqueous solutions using the Henry–law–based ideal–solution model at different temperatures with experimental data [208, 209, 210, 211, 196]. In the case of 2–AEE, stars indicate the experimental data of Martin *et al.* [209] and the other symbols are data of Al-Juaied *et al.* [196](65 wt% 2-AEE).

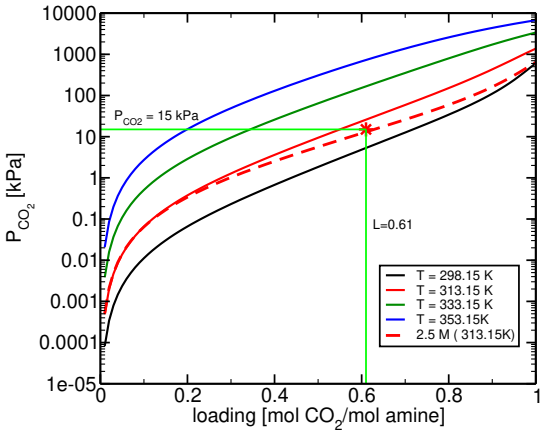


Figure 4.6: CO2 solubility in 30 wt% (solid lines) and 16 wt% (dashed red line) 2-AP.

solution forms) in the solution phase. It is determined from the equality of the chemical potentials of its free solution form and in the vapor phase in reaction R6. At the relatively low total pressures typically involved, the vapor phase may be treated as an ideal gas, which yields the following equation for the $P_{CO_2}$:

$$P_{CO_2} = \left(\frac{RT}{100P^0}\right)\left(\frac{\overline{\rho}_{solv}(T,\widetilde{P})}{1000}\right) m_{CO_2} \exp\left(\frac{\mu_{CO_2}^{res,NVT;\infty}(T,\rho(T,\widetilde{P})}{RT}\right) \tag{4.16}$$

The dependence of $P_{CO_2}$ on loading at several temperatures considered is shown and compared with available experimental data in Fig. 4.5 for 30 weight % MEA, AMP, AMPD and 60 weight % 2-(2-aminoethoxy)ethanol (2–AEE). For 2–AP shown in Fig. 4.6, we only found a single solubility measurement at 313.15 K, with a $CO_2$ partial pressure of 15 kPa over 2M (16 wt %) 2-AP aqueous solution[212]. It is seen that our predictions are in generally good agreement with the available experimental results.

## 4.5 Effect of Amine Concentration on $CO_2$ Solubility

Optimizing the amine concentration in the solvent is an important parameter for PCC system design. Our equilibrium model can be used to predict the effect of the amine concentration on the $CO_2$ solubility, and representative results are shown in Fig. 4.7. It can

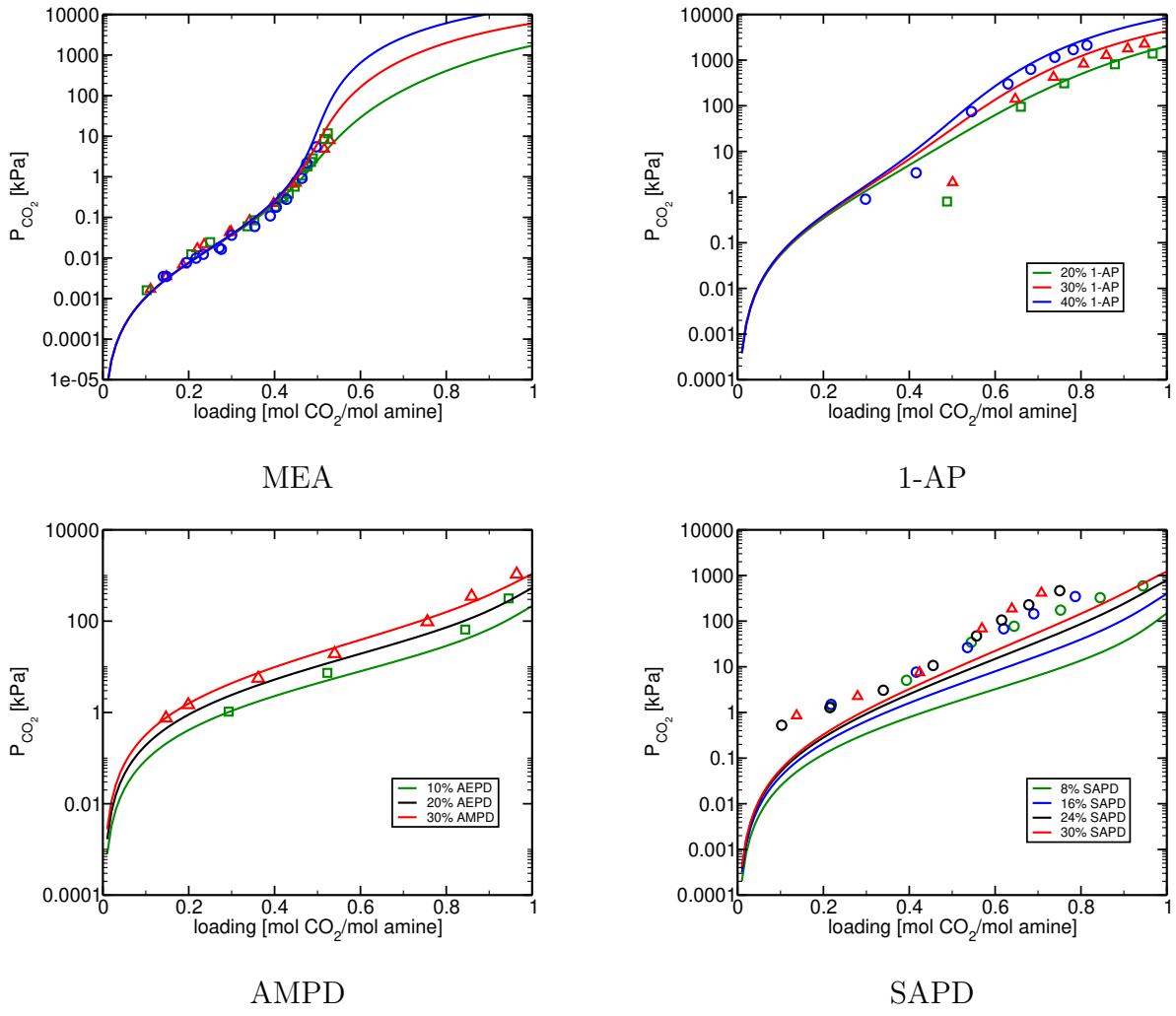


Figure 4.7: Effect of amine concentration on the $CO_2$ solubility of a) MEA, b) 1–AP c) AMPD, and d) SAPD at 313.15 K, in comparison with experimental data[213, 210, 214, 198].

be seen that for the carbamate forming amines (MEA, 1-AP, SAPD), the amine concentration has a small effect on the $CO_2$ solubility for loadings below 0.5. At higher loadings, amine solutions of lower concentration will have a higher CO $_2$ solubility, attributed to the change from carbamate formation to bicarbonate formation. This "salting out" effect is more pronounced for MEA, which is a strong carbamate forming species, whereas it is less pronounced for SAPD, which we found to be a mild carbamate forming molecule. Similar to MEA, 1–AP is a carbamate forming amine, and the concentration is predicted to have a small effect on the $CO_2$ solubility at low loadings, in qualitative accordance with the trend of the scattered experimental data points in that loading range.

## 4.6 Uncertainty Analysis

Consideration of the effects of uncertainties in input model parameters on its outputs is a generally important aspect of modelling[109, 110, 215, 216, 108]. Experimental studies often use regression models to determine fundamental thermodynamic parameters such as the $pK$ quantities shown in Table 4.1. These studies do not always provide uncertainty estimates for the $pK$ values, but when they are provided, it is in the context of a particular combination of experimental and modeling approaches. A more reasonable indication of the uncertainty of experimentally determined $pK$ values is the variation in the values obtained by different experimental groups using their different methodologies. In Section 4.4.2, we provided uncertainty estimates for our predictions.

Uncertainty analysis in the context of a nonlinear regression model of $CO_2$ reactive absorption has recently been considered by Morgan *et al.* [216, 108] by propagating the regressed model parameter uncertainties through the model to its $P_{CO_2}$ output value. Using a previous version of the molecular–based predictive methodology of this paper, our earlier MEA study[174] provided uncertainty estimates for both $P_{CO_2}$ and the solution compositions by propagating the $pK$ uncertainties to these output quantities. Although the latter are important quantities, we are unaware of any other uncertainty study involving them.

The primary quantities used in our methodology to predict $P_{CO_2}$ and speciation concentrations are the $pK_1$ and $pK_2$ values resulting from the ideal–gas free energy changes $\Delta G^0$ and the species hydration free energies $\mu_i^{\mathrm{res},NVT;\infty}(T;P)$ in Eqs. (4.9)–(4.12). We calculated uncertainty estimates by an empirical bootstrapping procedure by generating 1000 sets of $(pK_1, pK_2)$ values from independent normal distributions with means and variances given by the values in Table 4.1, and for each set we solved Eqs. (4.1) for the resulting solution equilibrium compositions and $P_{CO_2}$ as functions of the $CO_2$ loading. We then

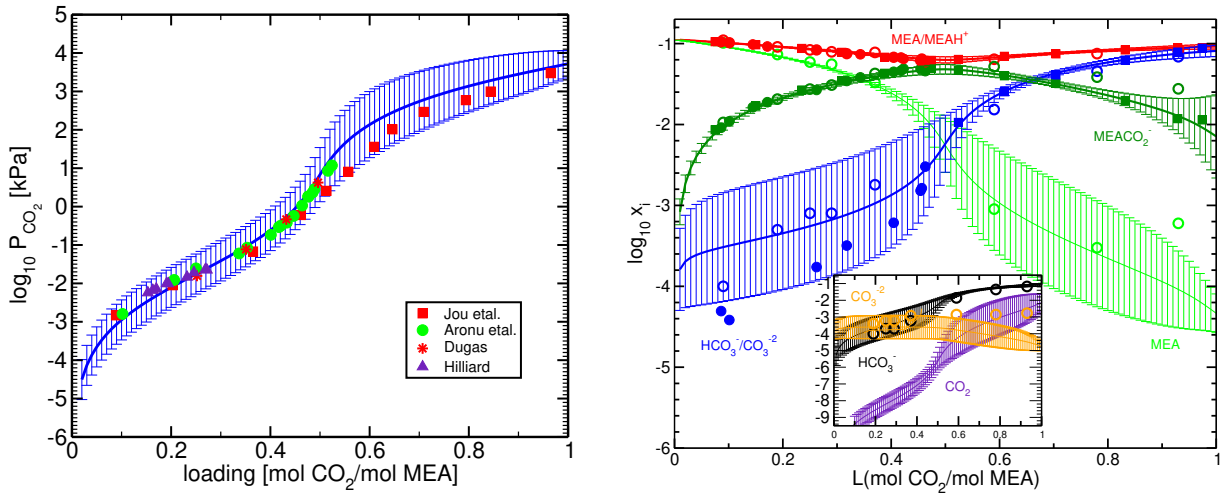


Figure 4.8: The left panel shows predicted values of $P_{CO_2}$ in 30 weight % MEA at 313.15 K and their uncertainty intervals corresponding to one standard deviation, and comparison with experimental data[213, 88, 208, 217]. The right panel shows the predicted solution concentrations and their one–standard–deviation uncertainty intervals for $CO_2$ in 30 with % MEA at 298.15 K, and comparison with the experimental data of Fig. 4.3.

calculated the means and standard deviations of these compositions and $P_{CO_2}$ values, and expressed our uncertainties as one standard deviation of the predicted results.

Figure 4.8 shows representative results for the uncertainties of our predictions for $P_{CO_2}$ for MEA at 313.15 K (left panel), and for the MEA solution compositions (right panel) at 298.15 K. We found no multiple sets of experimental $P_{CO_2}$ and solution compositions at any common set of conditions, but we believe that the slight variations in the experimental temperatures do not significantly affect the results shown in the figures. The figures indicate that our predictions and their precisions are compatible with the scatter of the experimental data. In the course of this study, we also found that $pK_1$ is the most important parameter at low loadings, and that $pK_2$ is the most important at loadings greater than 0.5, for both $P_{CO_2}$ and for the solution species concentrations. We conclude from these figures that our predictive approach for the calculation of $P_{CO_2}$ and the corresponding $CO_2$–loaded solution concentrations provides results of similar quality to those determined experimentally.

## 4.7 Summary and Conclusions

We have developed a purely predictive methodology that requires no experimental data of any kind for the amine solvent for predicting $P_{CO_2}$ and the corresponding $CO_2$–loaded solution concentrations for the reactive absorption of $CO_2$ in a range of primary alkanolamine solvents. Our methodology is able to predict species concentrations of arbitrarily small magnitude, which are either difficult to measure or inaccessible experimentally. Since the reaction scheme is irrelevant for calculating equilibrium thermodynamic properties, ours was chosen to avoid the use of $H^+$ as a species, which is notoriously difficult to treat theoretically, due to the requirement to know the value of the hydration free energy of the proton as a function of temperature, an experimentally and theoretically elusive quantity. We applied our methodology to seven alkanolamine solvents, and obtained excellent agreement with experimental results in cases when they are available, and made predictions in cases which have not yet been obtained.

Our algorithm entails the combination of the ideal–gas reaction standard free energies for the two reactions R1 and R2 using quantum mechanical methodology, and the calculation of hydration free energies for the solution species using classical force field methodology and standard molecular dynamics simulations. These quantities are appropriately translated to a macroscopically base thermodynamic model, from which $P_{CO_2}$ and the solution concentrations are calculated by a free energy minimization algorithm.

We also calculated uncertainties for our predicted values of the relevant equilibrium constants, and for $P_{CO_2}$ and the $CO_2$–loaded solution concentrations, by propagating the uncertainties in the ideal–gas quantities and hydration free energies through the equilibrium calculations to the final predicted quantities. We compared our predictions and their uncertainties with the corresponding experimental results obtained by different research groups (when these were available), and inferred the experimental uncertainties from the scatter of the data. For all quantities (with the possible slight exception of the value of $pK_1$), we conclude that our methodology provides predictions in mutual agreement with those obtained experimentally within their mutual uncertainties.

Potential improvements to our approach, which may be required for more complex solvents, would entail more accurate and precise estimates of the ideal–gas reaction free energies and of the species hydration free energies. The recently developed (on–the–fly–polarization) OTFP methodology for calculating hydration free energies is one possibilty[218, 219]. In addition, for more complex solutions it may be necessary to account for the non-ideal activity coefficient behaviour in the Henry–Law–based chemical potential model used in this paper. Although we have found this to be unnecessary for the solutions arising

in the systems considered here, these may be incorporated by means of the ideal–solution chemical potential extrapolation methodology of Smith and Qi[44].

We suggest that our algorithm provides a potentially cost-effective screening methodology for improved solvent selection, and current work is underway to apply it to other potential solvents and their mixtures.

## 4.8 Acknowledgements

Financial support was provided by the Natural Science and Engineering Council of Canada (NSERC) and the Agence Nationale de la Recherche (ANR) through the International Collaborative Strategic program between Canada and France (Grant NSERC STPGP 479466-15 and ANR-12-IS09-0001-01). We thank our industrial partner, Dr. John Carroll, Gas Liquids Engineering Ltd., for supporting this research and for helpful advice and encouragement. Computational facilities of the SHARCNET (Shared Hierarchical Academic Research Computing Network) HPC consortium (www.sharcnet.ca) and Compute Canada (www.computecanada.ca) are gratefully acknowledged.

## Associated Content

The Supporting Information provides ideal–gas standard reaction free energies for reactions R1 and R2, fitted equilibrium constant expressions for R1 and R2, species $\mu^{\mathrm{res},NVT;\infty}$ values at several temperatures, values of quantities contributing to the equilibrium constants of reactions R1 and R2, and raw Gaussian16 output for the neutral, protonated and carbamate forms of the alkanolamines studied, and for the small molecules.

# Chapter 5

# Prediction of Alkanolamine pKa Values by Combined Molecular Dynamics Free Energy Simulations and ab Initio Calculations



## Abstract

Knowledge of aqueous protonation constants ($pK_a$) of chemical species is of significant importance in $CO_2$ reactive absorption system design. Their theoretical prediction has mainly relied on implicit solvent models, and the performance of explicit solvent simulations based on classical force fields have rarely been studied. In this paper, we report the results of simulations in explicit TIP3P water with the General Amber Force Field (GAFF) and with the SMD continuum solvent method for the deprotonation $pK_a$ values of 29 conformationally diverse alkanolamine species commonly used in $CO_2$ capture. In both cases, we employ the Tissandier value for the hydration free energy of the proton (J. Phys. Chem. A, **1998**, 102, 7787). The ideal–gas reaction free energies and their uncertainties

were obtained from electronic structure calculations using five different compound methods (CBS–QB3, CBS–APNO, G3, G3B3, G4). The hydration free energies of the neutral and protonated forms of the amines were calculated using the semi–empirical AM1–BCC charge method, in addition to several partial atomic charge sets based on the RESP fitting method using electrostatic potentials computed at different ab initio theory/levels in the gas phase as well as in the presence of the solvent reaction field. We incorporated the Galvani surface potential of the ions in the ($pK_a$) calculations.

Although the individual species hydration free energies show significant sensitivity to the charge model, the resulting $pK_a$ values from different charge models are quite similar. Moreover, we found that the protonated amine hydration free energies show slightly less sensitivity to the partial charge method than in the case of the neutral amine. While the predicted $pK_a$ values based on the RESP charges yield reasonable agreement with the experimental data, they are prone to occasional disagreement for molecules of complex geometry. The best performance was achieved using the semi–empirical AM1–BCC charges, which showed a mean absolute error of less than 0.65 $pK_a$ units in comparison with experimental data. Our results suggest that the AM1–BCC charge method may be used to model electrolyte solutions encountered in the $CO_2$ reactive absorption process.

## 5.1 Introduction

Post–combustion capture (PCC) using aqueous amine solutions is one of the most mature technologies currently used for $CO_2$ capture from large point sources[140]. Knowledge of chemical reaction behaviour in the solvent is crucial for efficient solvent design of PCC technology.

The $pK_a$ values of the amine species is one of the fundamental quantities that affects reaction equilibria/kinetics, as well as the $CO_2$ absorption capacity and the heat of solvent regeneration[220, 221]. Theoretical prediction of this quantity has mainly relied on a thermodynamic–cycle–based approach utilizing the dielectric continuum solvation model (DCSM)[165, 222, 223], and its variant that includes a small number of explicit solvent molecules in the first solvation shell (a "cluster–continuum model") to account for hydrogen–bonding interactions[224, 225, 226, 227]. The DCSM approach has typically been tested on a limited set of small, rigid molecules, and its accuracy for large flexible molecules and ionic species has not yet been fully examined. While some DCSMs incorporate the effect of temperature on the solvation free energy (*e.g.*, SM8T[228] and COSMO-RS, most have been tested for a limited number of solvents at 298.15 K.

Typical DCSM simulations consider only the lowest energy conformer of the solute (usually in the ideal gas (IG) phase), and treat it as a rigid molecule in the estimation of its free energy of transfer to the solvent[229, 230]. As noted by Coote *et al.* [231], this implicitly assumes that the thermal contributions to the solute chemical potential (*i.e.*, those due to translational, rotational, and vibrational motions) are very similar in the IG and solution phases. While this may be a good approximation for the small rigid molecules that have been the target of most DCSM development, larger flexible molecules with more complex molecular geometries (such as amines and other hydrogen-bonding species) may undergo significant conformational and structural changes (*e.g.*, tautomerization) upon solvation, requiring the use of an ensemble of conformers for accurate solvation free energy estimation[170, 232]. Furthermore, the identification of the most stable conformation of a flexible molecule in solution is not a straightforward task, due to the fact that solution phase energies ($E_{\text{soln}}$), commonly used to rank the conformer relative stabilities may not be a proper metric, and estimated solution phase Gibbs energies ($G_{\text{soln}}$) should instead be used in order to identify the most stable conformers. Recently, Haworth *et al.* [170] showed that ignoring these effects can lead to erroneous p$K_a$ estimation for flexible molecules. Explicit solvent models, on the other hand, have the advantage that solvent effects on the solute conformations are inherently taken into account.

In spite of these shortcomings, DCSM simulations have been quite successful in predicting p$K_a$ values for a wide range of species, typically by employing strategies such as changing the level of quantum theory or using different optimal scaling factors to modify the original parameterization of the model to account for polarization in the solvent phase[233].

The SMx family of continuum solvation models of Cramer and Truhlar[165] are widely used for p$K_a$ predictions[230, 234, 57, 235]. Pliego *et al.* [230] assessed the performance of the SMD and the SM8 model for the estimation of p$K_a$ of diverse chemical species in methanol. They found RMS error values with respect to experiment of 3.6 and 2.7 p$K_a$ units for 23 amine species. Svendsen *et al.* [235] reported an average absolute error of 1.65 p$K_a$ units for 25 amines in water using SM8T. Although these models have shown an overall good performance for certain classes of chemicals[227], they are unsuitable for systems involving explicit solute–solvent(water) interaction, especially involving ionic species and molecules forming intramolecular hydrogen bonds, which is difficult to describe accurately by a DCSM.

While DCSM simulations have been extensively used for p$K_a$ estimation, there are only a handful of studies using classical force–field (FF) methodology[236]. This alternative approach uses explicit solvent molecular dynamics (MD) free energy simulation to model the complex intra- and intermolecular interactions using an underlying FF

model. This methodology captures conformational effects when the solute is being annihilated/decoupled from its molecular environment by sampling its multiple conformations.

In a notable work, Brooks *et al.* [236] used molecular dynamics simulations with empirical force field in conjunction with a DFT calculation of the IG free energy of deprotonation to predict the p$K_a$ values of drug–like molecules in a SAMPL6 challenge with an overall RMSE of 2.4 p$K_a$ units. For ionic species, the solvation calculation requires both the bulk phase (intrinsic hydration free energy) and the air–water surface potential contribution (*i.e.*, the Galvani potential)[237]; however, this study omitted the surface contribution. Moreover, the value of the proton hydration free energy used in their work (-1106.7 kJ·mol$^{-1}$) refers to a standard state of 1 atm in the gas phase and 1 molar in solution, whereas the conventional hydration free energies calculated using the thermodynamic integration (TI) approach refer to a standard state of 1 molar in both gas and solution phases.

To the best of our knowledge there has been no systematic study using the classical force–field (CFF) approach to calculate either the solvation free energies (especially for the charged species) of complex molecular species involved in a protonation reaction or its p$K_a$ value. Although experimental solvation free energies exist for many neutral species involved in such a reaction, this is not the case for the charged species. The goal of the present study is to investigate the use of the CFF approach for a test set of 29 amine species comprising 13 primary amines, 10 secondary amines, and 6 tertiary amines using FFs generated using the General Amber Force Field (GAFF) approach with semi–empirical AM1–BCC charges and partial charges obtained from several different quantum chemical calculations of the molecular electron density computed using Hartree-Fock (HF), density functional theory (DFT) and the second-order Møller-Plesset theory (MP2). We calculated species solvation free energies and p$K_a$ values, and compared results with those of a popular implicit solvent method. We also compared our results with available experimental results to assess the quality of the methodologies and the employed force fields (FF)

The paper is organized as follows. The next section reviews the thermodynamic background for translating the relevant simulation quantities to the experimental p$K_a$ values. The subsequent section gives the details of our simulations, followed by a section presenting our results and their discussion. We conclude with a summary and conclusions section.

## 5.2 Thermodynamic Background

Whereas the chemical potential may be defined relative to different reference, standard states and concentration variables, the Henry-law-based (HL) chemical potential model

using the infinite dilution reference state, the standard state as that of a hypothetical ideal solution of unit concentration, and the molality concentration variable $m_i$ (in mol $kg^{-1}$ solvent) is commonly used in macroscopic theoretical and experimental studies of electrolyte solutions. In contrast, molecular simulation results are most readily available using the ideal gas (IG) standard state and the density composition variable, $\rho_i$ (in mol $V^{-1}$, where $V$ is the system volume). The translation between the two forms of chemical potential expressions leading to the expression of $pK_a$ in terms of molecular simulation quantities is not straightforward, since it involves a careful consideration of standard state quantities. We thus first give a brief overview of the translation, and clarify some potential points of confusion regarding $pK_a$ simulations that have appeared in the literature.

We consider $pK_a$, the equilibrium constant for the deprotonation reaction

$$\mathrm{RNH_3^+} = \mathrm{RNH_2} + \mathrm{H^+} \tag{5.1}$$

where $RNH_2$ is a primary, secondary or tertiary alkanolamine.

For generality, we first derive an expression for $pK_a$ in terms of molecular simulation quantities for the general case of a reaction that also involves $H_2O$. This permits, for example, consideration of $pK_a$ for the reaction

$$\mathrm{RNH_3^+} + \mathrm{H_2O} = \mathrm{RNH_2} + \mathrm{H_3O^+} \tag{5.2}$$

Solute chemical potentials in the HL model using the molality concentration variable are expressed as:

$$\mu_i(T,P;\boldsymbol{m}) = \mu_i^\dagger(T;P) + RT\ln\left(\frac{m_i}{m^0}\right) + RT\ln\gamma_i(T,P;\boldsymbol{m}) \tag{5.3}$$

where $\boldsymbol{m}$ denotes the system molality vector, $\gamma_i \to 1$ as $m_i \to 0$, and $\mu_i^\dagger(T;P)$ is the standard state chemical potential of solute species $i$ in a hypothetical ideal solution of $m^0 = 1$ molal. For the solvent, the Lewis–Randall (LR) chemical potential model using the pure solvent standard state and the mole fraction concentration variable is commonly adopted, and the solvent chemical potential is given by

$$\mu_{\mathrm{solv}}(T,P) = \mu_{\mathrm{solv}}^*(T,P) + RT\ln a_{\mathrm{solv}}(T,P;\boldsymbol{x}) \tag{5.4}$$

where $\boldsymbol{x}$ denotes the system mole fraction vector, $a_{\mathrm{solv}}$ is the activity of the solvent, and $\mu_{\mathrm{solv}}^*(T,P)$ is the chemical potential of the pure solvent. In this model, $a_{solv} \to 1$ as $x_i \to 1$, or equivalently as the molality $m_{\mathrm{solv}} \to 1000/M_{\mathrm{solv}}$, where $M_{\mathrm{solv}}$ is the solvent molecular

weight.

It is most convenient to express all concentration variables in terms of the molality composition variable, which may be achieved by expressing $\mu^*_{\rm solv}(T,P)$ as

$$\mu^*_{\rm solv}(T,P) = \mu^\dagger_{\rm solv}(T,P) + RT\ln\left(\frac{1000}{M_{\rm solv}}\right) \tag{5.5}$$

and Eq. (5.4) then becomes

$$\mu_{\rm solv}(T,P) = \mu^\dagger_{\rm solv}(T,P) + RT\ln\left(\frac{1000}{M_{\rm solv}}\right) + RT\ln a_{solv}(T,P;\boldsymbol{m}) \tag{5.6}$$

$\mu^\dagger_i(T,P)$ (for both solutes and the solvent) is related to the intrinsic solvation free energy, $\mu_i^{{\rm res},NVT;\infty}[T,\rho(T,P)]$, by[114, 53]

$$\mu^\dagger_i(T,P) = \mu^0_i(T;P^0) + RT\ln\left(\frac{RT}{100P^0}\right) + RT\ln\left(\frac{\overline{\rho}_{\rm solv}(T,P)}{1000}\right) + \mu_i^{{\rm res},NVT;\infty}[T,\rho_{\rm solv}(T,P)] \tag{5.7}$$

where $\mu^0_i(T;P^0)$ is the species ideal–gas (IG) chemical potential at $T$ and standard state pressure $P^0$ (expressed in bar) and $\rho_{\rm solv}$ is the density of the pure solvent. ($\overline{\rho}_{\rm solv}$ denotes its expression in kg m$^{-3}$).

The second and third terms in Eq. (5.7) bring the IG from its density at the standard state $T$ and standard state pressure $P^0 = 1$ bar to that of an ideal solution density of unit molality, and we refer to $\mu_i^{{\rm res},NVT;\infty}[T,\rho_{\rm solv}(T,P)]$ as the solute *intrinsic solvation free energy*. It is the molar free energy change when a solute molecule is transferred from the ideal gas phase to the pure solvent and both phases are at the same density. For a solvent, this quantity is equivalent to its intrinsic self–solvation free energy. $\mu_i^{{\rm res},NVT;\infty}[T,\rho_{\rm solv}(T,P)]$ is readily obtained by means of conventional free energy calculations in an MD simulation software package such as GROMACS[180].

The equilibrium condition for a chemical reaction $j$ is

$$\Delta G_j \equiv \sum_{i=1}^{N_s} \nu_{ij}\mu_i = 0 \tag{5.8}$$

where $N_s$ is the total number of species and $\nu_{ij}$ is the stoichiometric coefficient of species $i$ in reaction $j$ (conventionally positive for products and negative for reactants). Using Eqs. (5.3) and (5.6), Eq. (5.8) becomes

$$\sum_{i=1}^{N_s} \nu_{ij}\mu_i^{\dagger}(T,P) + RT\nu_{\mathrm{solv},j}\ln\left(\frac{1000}{M_{\mathrm{solv}}}\right) + RT\sum_{\mathrm{solutes}}\nu_{ij}\ln\left(\frac{m_i\gamma_i(T,P;\boldsymbol{m})}{m^0}\right) + RT\left(\nu_{\mathrm{solv},j}\ln[a_{solv}(T,P;\boldsymbol{m})]\right) = 0 \tag{5.9}$$

Finally, $pK$ is obtained from the concentration–independent terms of Eq. (5.9) via:

$$pK_j = \frac{\Delta G_j^*}{RT\ln(10)} \tag{5.10}$$

where (using Eq. (5.7))

$$\Delta G_j^*(T,P) = \sum_{i=1}^{N_s}\nu_{ij}\mu_i^{\dagger}(T;P) + RT\nu_{\mathrm{solv},j}\ln\left(\frac{1000}{M_{\mathrm{solv}}}\right) \tag{5.11}$$

$$= \sum_{i=1}^{N_s}\nu_{ij}\mu_i^{0}(T;P^0) + RT\overline{\nu}_j\ln\left(\frac{RT}{100P^0}\right) + RT\overline{\nu}_j\ln\left(\frac{\overline{\rho}_{\mathrm{solv}}(T,P)}{1000}\right) + RT\nu_{\mathrm{solv},j}\ln\left(\frac{1000}{M_{\mathrm{solv}}}\right) + \sum_{i=1}^{N_s}\nu_{i,j}\mu_i^{\mathrm{res},NVT;\infty}[T,\rho(T,P)] \tag{5.12}$$

and $\bar{\nu}_j = \sum\nu_{ij}$.

Eq. (5.12) is a general expression for the equilibrium constant of any reaction $j$ when the HL model using the molality concentration variable is used. For the deprotonation reaction of Eq. (5.1), with $\bar{\nu}_j = 1$ and $\nu_{\mathrm{solv},j} = 0$, the following well-known expression for $\Delta G_j^*$ is obtained:

$$\Delta G_j^*(T,P) = \Delta G_j^0(T;P^0) + RT\ln\left(\frac{RT}{100P^0}\right) + RT\ln\left(\frac{\overline{\rho}_{\mathrm{solv}}(T,P)}{1000}\right) + \sum_{i=1}^{N_s}\nu_{i,j}\mu_i^{\mathrm{res},NVT;\infty}[T,\rho(T,P)] \tag{5.13}$$

where

$$\Delta G^0(T;P^0) = \sum_{i=1}^{N_s} \nu_{ij}\mu_i^0(T;P^0) \tag{5.14}$$

In the literature, the term involving the density in Eqs. (5.12) and Eq. (5.13) is sometimes omitted. At $P = 298.15$ K and $P = 1$ bar, for reactions with $\bar{\nu}_j \neq 0$ and water as solvent, the density is very near 1000 kg m$^{-3}$, and the term is negligible. However, when the solvent density is far from 1000 kg $m^{-3}$, omission of this term can result in significant error for the p$K_a$ value. The term has been thusly mistakenly omitted in the literature for aqueous amine p$K_a$ calculations at higher temperatures[58], and for non-aqueous solvents such as ionic liquids and dimethyl sulfoxide (MDSO) at ambient conditions[238]. For example, for methanol solvent at 298.15K and 1 bar ($\rho$ = 765.8 kg m$^{-3}$) its omission introduces an error of 0.26 p$K_a$ units.

Another important point is that for an ionic species, Eq. (5.7) omits the contribution to $\mu_i^{\text{res}}$ due to its crossing of the vacuum–solvent interface (*i.e.*, the solvent's Galvani potential, $\phi_G$, which arises from surface polarization[239]). Hence, the solvent–specific Galvani potential must be added to the intrinsic solvation free energy to obtain the absolute/real solvation free energy of an ion according to [240, 241]

$$\mu_i^{res,ion} = \mu_i^{\text{res},NVT}[T,\rho(T,P)] + z_i\phi_G \tag{5.15}$$

where $z_i$ is the ion's valence.

Although the Galvani contributions cancel in a charge–balanced reaction, it must be included when an individual ion is of interest. In this study, we calculate p$K_a$ for the deprotonation reaction of Eq. (5.1) and use the value of the hydration free energy of $H^+$ in water from Tissandier *et al.* [242]. As noted by Palmer *et al.* [240], numerous studies suggest that the Tissandier result is the absolute value, which incorporates the Galvani potential[243, 244, 245]. Hence, when the Tissandier value for $H^+$ is used, the Galvani potential must be added to the intrinsic hydration free energy of $RNH_3^+$ to obtain the correct p$K_a$ value for reaction (5.1). This has mistakenly been ignored in the SAMPL6 challenge study of Brooks *et al.* [236].

## 5.3 Simulation Details

### 5.3.1 Conformational Search and Ideal Gas Reaction Free Energies

Initially, all possible molecular conformations were constructed for the 29 amine species studied and their protonated forms using the Spartan18 software package[127]. The resulting geometries were then further optimized using the fast semi–empirical PM6 model implemented in Spartan. When the conformational space was very large (more than 25 conformers), only the first 25 with the lowest PM6 energies were submitted for further optimization and frequency calculations using five compound model chemistries using the Gaussian program[121]: CBS–QB3, CBS-APNO, G3B3, G3 and G4. For each compound method, the conformer with the lowest Gibbs free energy (and no negative imaginary frequency) was used for the IG reaction free energy calculations at the standard state of $T = 298.15$ K and $P = 1$ bar and using standard expressions for the partition function under the harmonic oscillator rigid rotor approximation.

### 5.3.2 Partial Charges and Intrinsic Hydration Free Energy Calculations

All amine species were modeled using the General Amber Force Field (GAFF) [177] with partial charges derived from RESP charge fitting[65], in addition to the semi–empirical AM1–BCC[246] charge model in TIP3P water. The molecular structures of the amines in the test set are shown in Fig.5.1. For each molecule, starting with the PM6 optimized geometries of its conformers as described in the previous section, they were further optimized at the MP2–cc–pVTZ level to find the conformer with the lowest energy in the gas phase. Single-point calculations were then performed on this conformer using the HF/6–31G(d) and B3LYP/6–311++G(d,p) levels of theory. The electron density based on these two levels is widely used in conjunction with the GAFF intramolecular parameters [247, 248, 249], since they tend to overestimate the solute dipole moments in the gas phase and implicitly incorporate the polarization effect in the solution. Additionally, the electron density was calculated using the more sophisticated second–order Møller–Plesset theory employing the cc–pVTZ basis set in the presence of a solvent reaction field mimicked using the polarizable continuum model (PCM[222]) with a dielectric constant of 78.39. For the latter, we allowed the MP2–cc–pVTZ gas phase minimum conformer geometry to further relax in the solution. All partial charge assignments were performed with the Antechamber package

(version 17.3) of Ambertools, and Gromacs topologies were generated using the acpype (version 2019) python interface[179].

All MD simulations were performed with the GROMACS 2018.3 program[180] in a cubic box of one solute molecule solvated in 888 TIP3P water molecules using packmol[181]. The resulting structure was then minimized to remove any bad contacts, and a short $NVT$ run was followed by a 12 ns $NPT$ simulation. The free energy simulations were then started from these equilibrated structures in an $NVT$ ensemble with box size corresponding to the TIP3P density at the standard state of $T = 298.15$ K and $P = 1$ bar. The equations of motion were integrated using the stochastic Langevin scheme, with a friction constant of 1.0 ps $^{-1}$. Lennard-Jones short–range interactions were smoothly switched off between 12 and 12.5 Å, and the electrostatic interactions were computed using the particle mesh Ewald (PME) method with a 12 Å real space cutoff, 1.0 Å grid spacing, 6th–order spline interpolation, and accuracy of $10^{-6}$.

For the constant pressure simulations, a Parrinello–Rahman pressure coupling constant of 2.0 ps was used. The free energy of decoupling the solute in the solvent environment was calculated using the statistically optimal Multi-state Bennett Acceptance Ratio (MBAR) method[124] with the Hamiltonian difference between the neighbouring states saved every 0.2 ps. We employed 6 equally spaced $\lambda$ values and linear decoupling of the electrostatics interaction, followed by 20 $\lambda$ values with equal spacing of $\Delta\lambda = 0.05$ to decouple the LJ interactions using the standard GROMACS soft-core potential function originally proposed by Beutler *et al.* [182] with parameters (in GROMACS notation) *sc-alpha* = 0.5, *sc-power*= 1 and *sc-sigma*=0.3. Each $\lambda$ window was subjected to a 12.5 ns simulation with the first 2.5 ns discarded for equilibration.

## 5.4 Results and Discussion

Various data used in our calculations are summarized in Table 5.1.

### 5.4.1 Intrinsic Hydration Free Energies of Amine Species

Since experimental free energies of solvation are not available for the species in this study, in Fig.5.2 we compare our GAFF results against the SMD solvation model of Truhlar *et al.* [252], which is parameterized with the goal of reproducing experimental solvation free energies at 298.15 K. The SMD simulations were performed using a Gaussian16 implementation similar to that of Cox*et al.* [229]. Starting with the gas phase cc–pVTZ optimized

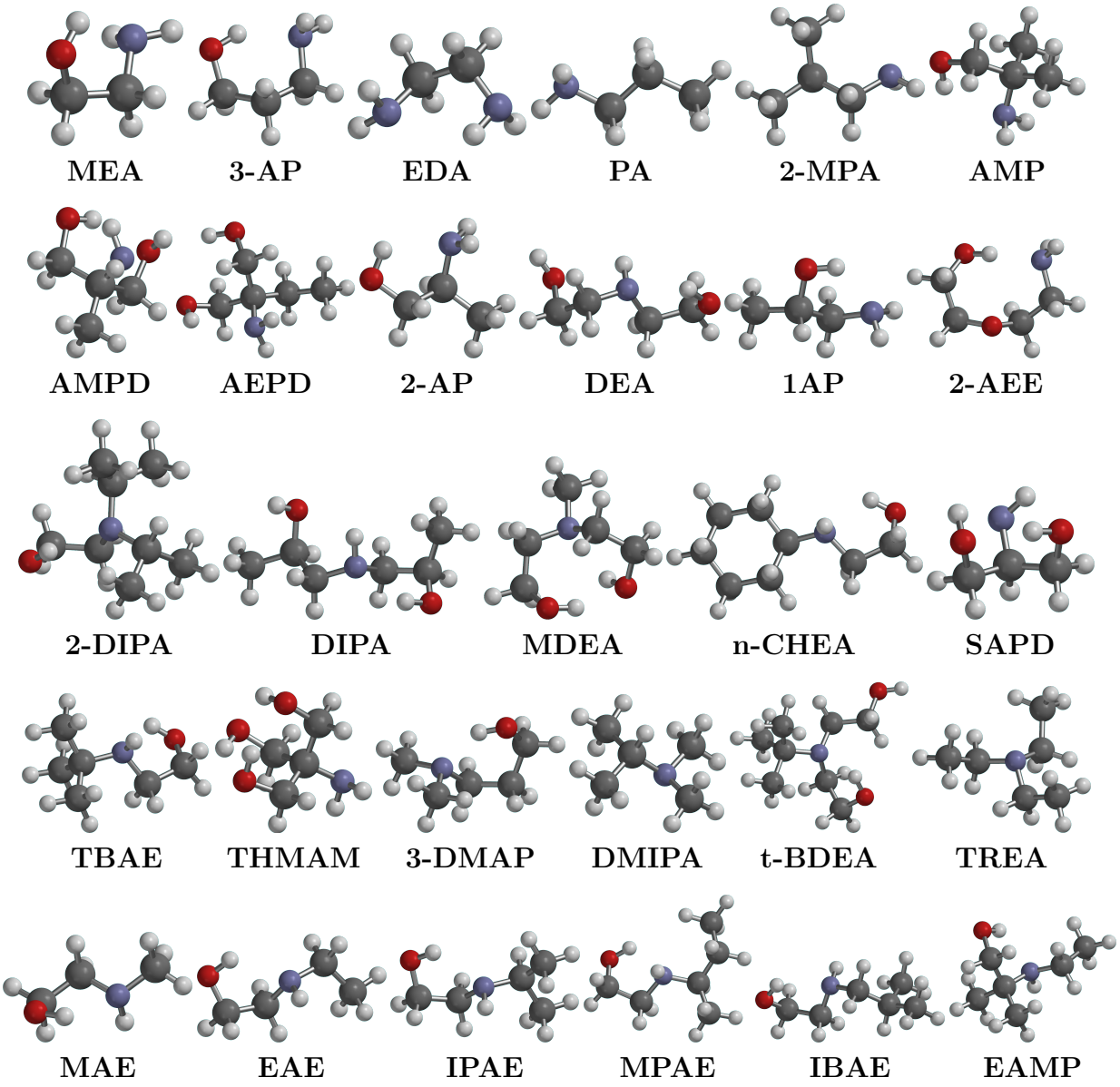


Figure 5.1: Molecular Structures of the 29 alkanolamines investigated in this work.

Table 5.1: Thermodynamic data used in this study. All values are at $T = 298.15$ K, $P = 1$ bar. $\mu^0_{H^+}$ is based on the standard equations of thermodynamics for the ideal gas enthalpy and entropy of a monatomic classical ideal gas based on the Sackur–Tetrode equation[250], and $\overline{\rho}_{H_2O}$ and $\phi_G$ refer to the TIP3P water model. $\mu^{res,NVT;\infty}_{H^+}$ refers to a 1M molar concentration in the ideal gas and a 1M ideal solution.

| Property | Value | Source |
|---|---|---|
| $\mu^0_{H^+}$ | -26.2 kJ·mol$^{-1}$ | McQuarrie[250] |
| $\overline{\rho}_{H_2O}$ | 987.4 kg· m$^{-3}$ | This work |
| $\phi_G$ | -48.24 kJ·mol$^{-1}$ | [241, 251] |
| $\mu^{res,NVT;\infty}_{H^+}$ | -1112.5 kJ·mol$^{-1}$ | Tissandier *et al.* [242] |

minimum energy conformer geometries, the solute structures were further optimized at the M06–2X/c–pVTZ level in vacuum, followed by a single–point energy calculations at the M06–2X/6–31G(d)level. Second single–point energy calculations were performed on the vacuum geometry in the presence of the SMD water model to obtain the solute infinite dilution residual chemical potential and its absolute solvation free energy. The raw intrinsic hydration free energies from all the charge methods and from SMD are tabulated in the Supporting Information.

As shown in Fig.5.2, there is reasonable agreement (+/- 5 kJ·mol$^{-1}$) between the RESP–derived hydration free energies and those of the SMD model. However, for heavily sterically hindered amines with multiple hydroxyl group (each enclosed by an ellipse), the hydration free energies based on RESP charges deviate from the corresponding SMD values. RESP assigns charges to atoms based on a grid of electrostatic potential points, and is quite sensitive to the conformer geometry; the presence of strong intramolecular electrostatic interactions may thus lead to unreasonably distorted partial charges for the atoms involved in such interactions. To alleviate this, multiple conformation RESP fitting may be used[253]. The AM1–BCC results (shown by blue circles) are in the best agreement with the SMD results for all solutes. A possible explanation for this is that AM1–BBC derives partial charges from the AM1 semi–empirical quantum mechanical calculation, after which empirical bond–charge corrections (BCCs) are applied to the partial charges. This makes the AM1–BCC charges less sensitive to the conformation and to steric clashes. Previously, AM1–BCC has been shown to give superior performance for hydration free energy predictions of species in the FreeSolv Database[254, 255].

While there exist numerous studies addressing the effects of the charge model for neutral species on the resulting hydration free energies[184, 185], this has been rarely studied for

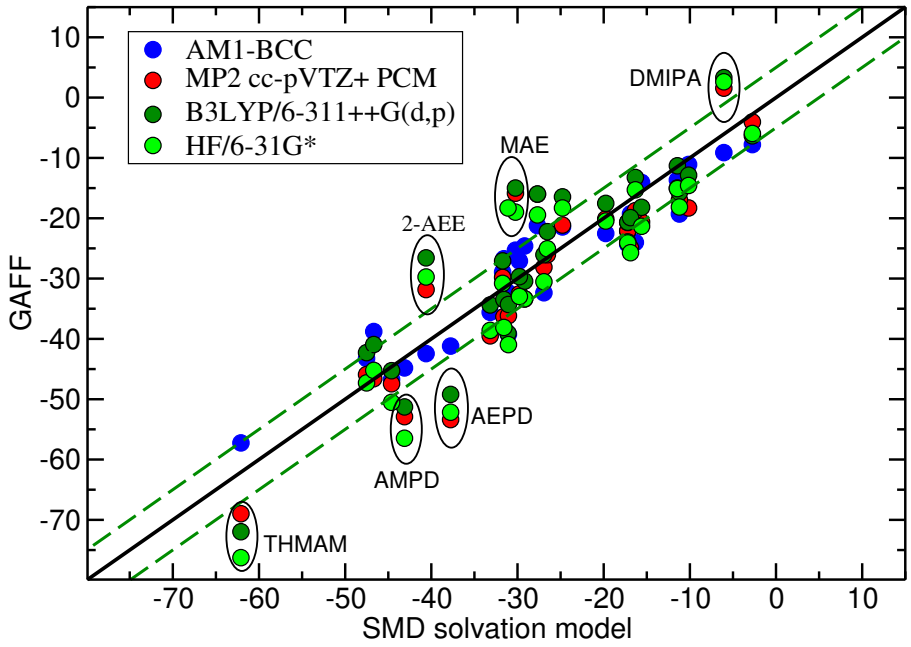


Figure 5.2: Parity plot comparison of the neutral amine hydration free energies (in kJ·mol$^{-1}$) against the corresponding SMD results. The black line shows the y=x parity line and the dotted green lines show y=x +/- 5 kJ·mol$^{-1}$.

ionized species. A main reason is that such data for ionized species are generally inaccessible experimentally. However, we have seen that AM1–BCC performs well for neutral species with respect to SMD, which is considered to perform well with respect to experiment for such species. We will thus test both methods against experimental results for p$K_a$ values and use the results to infer the quality of the AM1–BCC and SMD predictions for the ions.

We first benchmark different charge methods against the AM1–BCC approach. For a charged solute, the intrinsic hydration free energy obtained from an atomistic simulations with periodic boundary conditions and Ewald summation differs from the absolute/real solvation free energy, which includes the contribution from the solvent Galvani surface potential, whereas a continuum solvent model (including SMD), inherently includes this contribution. To obtain the absolute hydration values for the protonated amines, the Galvani potential value for the TIP3P water model was added to the raw intrinsic values from GROMACS MBAR simulations. The resulting absolute hydration free energies obtained using RESP charges and using the SMD model are benchmarked against the AM1–BCC results in Fig. 5.3. Clearly, for protonated amines, the hydration free energy from different RESP charge sets agrees well with the AM1–BCC result, whereas for species with multiple hydroxyl groups, the SMD values (orange circles) show significant deviations. This could be attributed to the inability of SMD to describe complex hydrogen bonding interactions in these molecular species.

### 5.4.2 *p*K$_a$ Calculations

The gas–phase protonation reaction free energies or basicities for Eq. (5.1) at $T = 298.15$ K and $P = 1$ bar are summarized in Table 5.2 using five composite methods: CBS–QB3, CBS–APNO, G3B3, G3 and G4. The final column gives the average value from the methods, which we use in our calculations, and the standard deviation, which we use as the uncertainty. Only the free energies of the neutral amine and its protonated form were calculated from the molecular partition function and frequency calculations. For the species in our list, we found experimental reaction free energies (all in kJ·mol$^{-1}$) for MEA (896.8), 3–AP (917.3), EDA (912.5), PA (883.9) and 2-MPA (890.8) from a literature database[256]. Given that the experimental basicity may be subject to an uncertainty of several kJ, the agreement between the calculated and experimental values is considered to be reasonable.

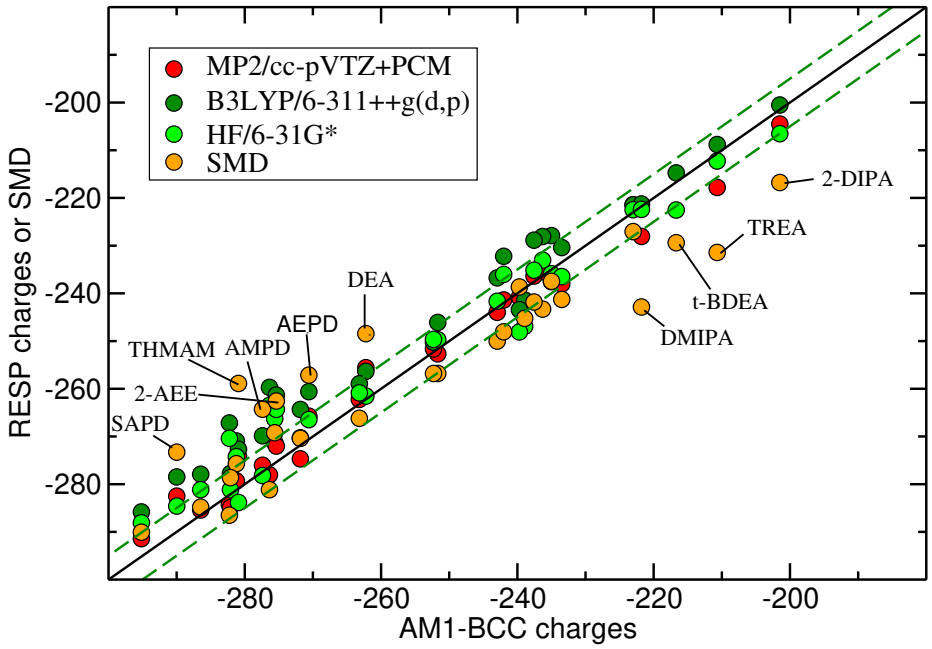


Figure 5.3: Parity plot comparison of the amine cation hydration free energies (in kJ·mol$^{-1}$) against the corresponding semi–empirical AM1–BCC results. The black line shows the y=x parity line and the dotted green lines show y=x +/- 5 kJ·mol$^{-1}$.

Table 5.2: $\Delta G^0$ in Eq. (5.14) of the reaction $RNH_3^+ = RNH_2 + H^+$ for 29 amines in kJ·mol$^{-1}$ at $T = 298.15$ K and $P = 1$ bar considered in this work. Subscripts in the final column denote the standard deviation of the indicated value. A superscript indicates the type of amine: $p$, $s$ and $t$ respectively denote a primary, secondary and tertiary alkanolamine.

| Amine | abbreviation | CBS–QB3 | CBS–APNO | G3B3 | G3 | G4 | Average |
|---|---|---|---|---|---|---|---|
| monoethanolamine$^p$ | MEA | 888.9 | 888.5 | 891.0 | 889.4 | 891.0 | $889.76_{1.17}$ |
| 3-amino-1-propanol$^p$ | 3-AP | 916.9 | 919.2 | 919.9 | 920.0 | 919.6 | $919.12_{1.28}$ |
| ethylenediamine$^p$ | EDA | 914.2 | 917.1 | 915.9 | 916.8 | 915.5 | $915.90_{1.15}$ |
| propanamine$^p$ | PA | 885.9 | 888.4 | 887.8 | 888.4 | 888.0 | $887.70_{1.03}$ |
| 2-methyl-1-propanamine$^p$ | 2-MPA | 890.9 | 893.5 | 892.5 | 893.2 | 892.6 | $892.54_{1.00}$ |
| 2-amino-2-methylpropanol$^p$ | AMP | 909.3 | 911.1 | 911.4 | 911.5 | 911.4 | $910.94_{0.92}$ |
| 2-amino-2-methyl-1,3-propanediol$^p$ | AMPD | 921.3 | 922.6 | 923.8 | 923.7 | 920.3 | $922.34_{1.52}$ |
| 2-amino-2-ethyl-1,3-propanediol$^p$ | AEPD | 924.5 | 926.3 | 929.6 | 930.1 | 929.4 | $927.98_{2.45}$ |
| 2-amino-1-propanol$^p$ | 2-AP | 900.5 | 902.5 | 902.7 | 902.9 | 902.6 | $902.24_{0.98}$ |
| diethanolamine$^s$ | DEA | 942.0 | 944.7 | 945.8 | 945.6 | 945.3 | $944.68_{1.55}$ |
| 2-(2-aminoethoxy)ethanol$^p$ | 2-AEE | 928.7 | 926.5 | 933.0 | 932.6 | 932.5 | $930.66_{2.90}$ |
| 2-(diisopropylamino)ethanol$^t$ | 2-DIPA | 965.4 | 969.6 | 969.0 | 969.3 | 969.5 | $968.56_{1.78}$ |
| diisopropanolamin$^s$ | DIPA | 958.2 | 958.6 | 961.3 | 960.8 | 961.5 | $960.08_{1.56}$ |
| methyldiethanolamine$^t$ | MDEA | 961.7 | 960.6 | 967.8 | 961.2 | 966.3 | $963.52_{3.28}$ |
| n-cyclohexylethanolamine$^s$ | n-CHEA | 944.2 | 947.0 | 946.7 | 947.2 | 948.5 | $946.72_{1.56}$ |
| serinol(2-aminopropane-1,3-diol)$^p$ | SAPD | 913.1 | 914.4 | 913.9 | 916.0 | 915.8 | $914.64_{1.24}$ |
| 2-(tert-butylamino)ethanol$^s$ | TBAE | 942.0 | 945.0 | 945.0 | 945.0 | 945.5 | $944.50_{1.41}$ |
| tris(hydroxymethyl)aminomethane$^p$ | THMAM | 919.6 | 920.9 | 922.0 | 923.4 | 924.2 | $922.02_{2.14}$ |
| 3-dimethylamino-1-propanol$^t$ | 3-DMAP | 955.2 | 958.3 | 960.0 | 960.4 | 959.6 | $958.70_{2.1}$ |
| N,N-dimethylisopropanolamine$^t$ | DMIPA | 935.8 | 939.9 | 939.9 | 940.7 | 939.8 | $939.22_{1.94}$ |
| tert-butyldiethanolamine$^t$ | t-BDEA | 971.1 | 976.0 | 973.6 | 976.4 | 976.6 | $974.74_{2.36}$ |
| triethylamine$^t$ | TREA | 949.4 | 950.6 | 947.6 | 950.0 | 950.2 | $949.56_{1.17}$ |
| 1-amino-2-propanol$^p$ | 1-AP | 895.2 | 894.6 | 897.2 | 895.5 | 893.1 | $895.12_{1.48}$ |
| 2-(methylamino)ethanol$^s$ | MAE | 916.8 | 919.2 | 919.9 | 920.3 | 920.0 | $919.24_{1.42}$ |
| 2-(ethylamino)ethanol$^s$ | EAE | 930.2 | 932.6 | 933.2 | 933.0 | 933.4 | $932.48_{1.30}$ |
| 2-(isopropylamino)ethanol$^s$ | IPAE | 935.0 | 937.9 | 938.0 | 938.0 | 938.3 | $937.44_{1.37}$ |
| 2-((1-methylpropyl)amino)ethanol$^s$ | MPAE | 939.1 | 942.8 | 942.0 | 942.6 | 941.7 | $941.46_{1.48}$ |
| 2-(isobutylamino)ethanol$^s$ | IBAE | 936.6 | 939.4 | 939.2 | 939.2 | 939.3 | $938.74_{1.20}$ |
| 2-(ethylamino)-2-methyl-1-propanol$^s$ | EAMP | 944.3 | 946.9 | 947.5 | 947.6 | 947.3 | $946.73_{1.39}$ |

For our p$K_a$ calculations, we used the average gas–phase values of Table 5.2 and the data in Table 5.1.

Our predicted p$K_a$ values for each charge model are compared with the SMD predictions and with available experimental results in Table 5.3. We ascribe the p$K_a$ uncertainties in Eq. (5.10) to those of the corresponding ideal–gas contributions of Table 5.2. (This

excludes any uncertainty in the Tissandier proton hydration free energy, and the relatively small uncertainties of the simulation results for the intrinsic hydration free energies.)

All our raw simulation results are given in the Supplementary Information, and the quality of the agreement with experiment of the results of different approaches can be assessed by various statistical measures. We note in passing that the Pearson $R^2$ value is not a useful statistic for assessing the ability of a method to accurately predict experimental data, due to its well–known deficiencies. For example, $R^2$ measures the quality of a linear regression of $y$(predicted) on $y$(experiment), whereas the question at hand is whether or not that the quantities are equal. We consider here the two alternative measures of the Average Absolute Deviation (AAD) and the confidence interval arising from the Student t–test for the hypothesis that the predicted and experimental values are equal. Based on the AAD values alone, Table 5.3 indicates that the AM1–BCC charges are in the best agreement with the experimental data for the test set of species considered.

The validity of the Student t–test approach is based on the assumption that the predicted and experimental values each independently follow a normal distribution, which is not an unreasonable assumption. The results comparing each of the AM1–BCC and SMD methodologies by this approach are shown in Table 5.4. For the entire set of 26 species, the 95% confidence intervals for corresponding differences of the predicted minus the experimental values for both approaches enclose the zero value, indicating that there is insufficient information to reject the hypothesis that either approach adequately predicts the experimental results. Notwithstanding, the combination of its lower AAD value and tighter confidence interval suggests that the AM1–BCC method is slightly superior. When the same analysis is applied to the different types of alkanolamines are considered, the results of Table 5.4 suggest that the AM1–BCC approach is satisfactory for each type of alkanolamine, whereas the SMD approach performs poorly for the primary and tertiary alkanolamines.

A parity plot comparing the AM1–BCC results against the experimental values is shown in Fig. 5.4. For only 4 of the 29 molecules studied (propanamine(PA), 2-methyl-1-propanamine(2-MPA), diethanolamine(DEA) and methyldiethanolamine(MDEA)), is the error appreciably larger than 1.0 p$K_a$ units. The fact that DEA and MDEA, in addition to the PA and 2-MPA pair, differ only in a methyl group, suggests a common source of this discrepancy. The largest error in the predicted value is associated with MDEA, and its gas phase reaction free energy also shows significant uncertainty. Although less pronounced for the AM1–BCC charges, possibly due to *ad hoc* bond–charge corrections, the significant

Table 5.3: p$K_a$ values for the reaction $RNH_3^+ = RNH_2 + H^+$ using different charge models and from SMD continuum solvent simulations at $T = 298.15$ K and $P = 1$ bar.

| amine | RESP | | | SMD | AM1–BCC | p$K_a$(expt)[10, 257, 258, 259, 194] |
|---|---|---|---|---|---|---|
| | HF/6–31G* | B3LYP/ 6–311++G(d,p) | MP2–cc–pVTZ+PCM | | | |
| MEA | 7.42 | 7.67 | 8.19 | 7.62 | 9.00 | 9.47 |
| 3-AP | 8.79 | 9.26 | 10.09 | 9.95 | 10.12 | 10.00 |
| EDA | 8.20 | 8.36 | 8.95 | 9.43 | 9.97 | 9.90 |
| PA | 5.61 | 5.59 | 8.18 | 9.46 | 8.98 | 10.60 |
| 2-MPA | 6.34 | 6.34 | 8.93 | 10.10 | 8.87 | 10.50 |
| AMP | 7.56 | 7.02 | 8.34 | 8.33 | 9.39 | 9.70 |
| AMPD | 6.89 | 6.34 | 7.16 | 6.81 | 8.81 | 8.80 |
| AEPD | 6.58 | 6.06 | 6.26 | 7.49 | 9.24 | 8.80 |
| 2-AP | 7.16 | 7.38 | 8.15 | 7.89 | 9.35 | 9.40 |
| DEA | 9.49 | 9.46 | 8.71 | 7.18 | 10.34 | 9.00 |
| 2AEE | 10.60 | 10.6 | 11.61 | 8.41 | 10.33 | 9.42 |
| 2DIPA | 9.50 | 8.75 | 8.51 | 12.09 | 9.25 | 9.42 |
| DIPA | 9.99 | 9.79 | 8.81 | 9.46 | 9.74 | 8.88 |
| MDEA | 11.55 | 11.90 | 11.14 | 11.65 | 10.41 | 8.57 |
| n-CHEA | 9.25 | 8.35 | 9.39 | 9.29 | 9.09 | 10.10 |
| SAPD | 7.70 | 7.55 | 7.90 | 6.78 | 9.34 | 8.55 |
| TBAE | 9.55 | 9.00 | 9.50 | 10.24 | 9.59 | 9.70 |
| THMAM | 4.34 | 3.14 | 3.95 | 2.48 | 7.19 | 8.08 |
| 3-DMAP | 10.72 | 10.90 | 9.94 | 11.36 | 9.30 | 9.27 |
| DMIPA | 10.42 | 10.35 | 11.26 | 12.51 | 8.28 | 9.47 |
| t-BDEA | 8.53 | 8.00 | 11.52 | 11.99 | 9.55 | 9.03 |
| TREA | 8.96 | 8.28 | 10.29 | 12.90 | 8.38 | 10.70 |
| 1AP | 6.76 | 6.76 | 7.60 | 7.98 | 8.74 | 9.50 |
| MAE | 9.85 | 10.21 | 10.66 | 8.83 | 9.17 | 9.80 |
| EAE | 9.34 | 9.71 | 10.06 | 11.82 | 9.79 | 9.99 |
| IPAE | 9.44 | 9.10 | 9.93 | 11.05 | 9.33 | 9.93 |
| MPAE | 9.41 | 8.73 | 9.86 | 11.82 | 9.66 | -[a] |
| IBAE | 8.86 | 8.80 | 10.42 | 9.55 | 9.62 | -[a] |
| EAMP | 9.24 | 9.20 | 9.68 | 11.65 | 9.87 | -[a] |
| AAD[b] | 1.58 | 1.77 | 1.29 | 1.67 | 0.65 | |

[a] No experimental data found

[b] Average absolute deviation

Table 5.4: Comparisons with experiment of $pK_a$ values for the reaction $RNH_3^+ = RNH_2 + H^+$ using AM1–BCC and SMD continuum solvent simulations at $T = 298.15$ K and $P = 1$ bar. AAD is the average absolute deviation of the predicted from the experimental results, , AD is the average deviation of the predicted minus the experimental values of the indicated method, RMSD is its root–mean–square value, 95% Confidence Interval is computed from the student t distribution at the 95% level as described in the text, and the final column indicates whether or not the hypothesis that the predicted and experimental values are equal can be rejected at this confidence level.

| Method | AAD | AD | RMSD | 95% Confidence Interval | Hypothesis: Mean Value= 0 |
|---|---|---|---|---|---|
| Entire Data Set (26 species) | | | | | |
| AM1–BCC | 0.65 | 0.18 | | $(-0.20, 0.56)$ | Do not reject |
| SMD | 1.67 | 0.13 | | $(-0.82, 1.08)$ | Do not reject |
| Primary Alkanolamines (13 species) | | | | | |
| AM1–BCC | | 0.25 | | $(-0.37, 0.87)$ | Do not reject |
| SMD | | 1.54 | | $(0.37, 2.71)$ | Reject |
| Secondary Alkanolamines (7 species) | | | | | |
| AM1–BCC | | 0.04 | | $(-0.50, 0.58)$ | Do not reject |
| SMD | | 0.07 | | $(-1.25, 1.39)$ | Do not reject |
| Tertiary Alkanolamines (6 species) | | | | | |
| AM1–BCC | | 0.15 | | $(-0.80, 1.4)$ | Do not reject |
| SMD | | 2.70 | | $(1.87, 3.53)$ | Reject |

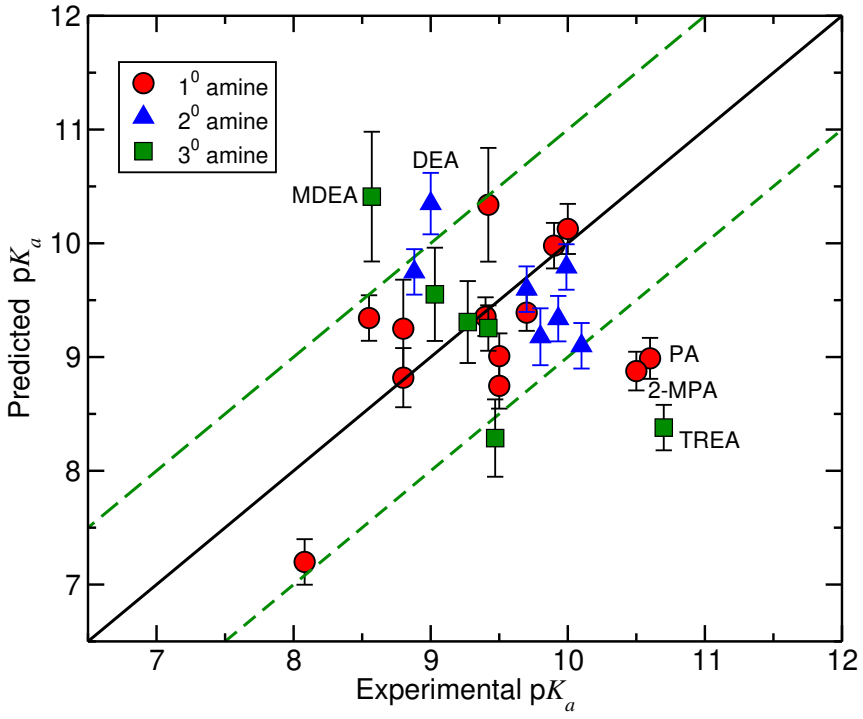


Figure 5.4: AM1–BCC calculated versus experimental p$K_a$ values for the 29 alkanolamine species considered in this work. Red denotes primary amines, blue denotes secondary amines and green denotes tertiary amines. The vertical error bars are obtained by propagating the uncertainty (horizontal error bars for the experimental data are not shown) in the ideal gas reaction free energy and the dashed line indicates a tolerance of 1.0 $pKa$ unit.

deviations of the PA and 2–MPA values using HF/6–31G* and B3LYP/6–311++G(d,p) charges suggest that partial charges based on the gas phase electron density might be unsuitable for these two molecules. This is further supported by the fact that the inclusion of implicit polarization using MP2–cc–pVTZ+PCM or SMD significantly improves the prediction of their p$K_a$ values.

HF/6–31G* and B3LYP/6–311++G(d,p) gas phase charge methods yield very similar results, and both generally tend to underestimate the experimental p$K_a$ values. MP2–cc–PVTZ+PCM performs significantly better than the gas phase HF and B3LYP charge methods, indicating the importance of polarization effects in the solvation calculation. All methods based on RESP charges tend to perform poorly for the heavily hindered amines with multiple hydroxyl groups, possibly due to effects such as local over–polarization or steric clashes.

For three of the studied alkanolamines (*i.e*, 2-((1-methylpropyl)amino)ethanol (MPAE), 2-(isobutylamino)ethanol(IBAE) and 2-(ethylamino)-2-methyl-1-propanol(EAMP)), we were unable to locate experimentally measured p$K_a$ values. However, we note that the AM1–BCC predicted value of 9.66 for IBAE is very close to the experimentally measured value of 9.92 for that of its isomer 2-(butylamino)ethanol (BAE)[194]. The corresponding AM1–BCC predicted value for EAMP (9.87) is higher that of AMP(9.39), suggesting that steric hindrance by the addition of an alkyl group to the nitrogen atom of AMP increases its p$K_a$ value. Similarly, based on the AM1–BCC predictions, the p$K_a$ values of EAE (9.79), MPAE(9.66), IBAE(9.62), TBAE (9.59), IPAE(9.33) are higher than that of MEA(9.00), further indicating that the addition of alkyl chains to the nitrogen atom of MEA increases the p$K_a$ value. This trend was also observed in the recent experimental study of Narku–Tetteh *et al.* [260], who found that the longer alkyl chain lengths of secondary alkanolamines resulted in higher equilibrium $CO_2$ loading and p$K_a$ values.

Since the AM1–BCC p$K_a$ results agree well with experiment and the AM1–BCC results for neutral species agree well with the SMD resulst, we conclude that the AM1–BCC results for the charged species are also accurate. In general, we believe that AM1–BCC is a very promising approach for predicting alkanolamine p$K_a$ values and for studying the effects of different functional groups on their potential $CO_2$ capturing abilities.

## 5.5 Summary and Recommendations

We have implemented molecular simulation methodology for calculating p$K_a$ values at ambient conditions ($T = 298.15$ K and $P = 1$ bar) for the deprotonation reaction of Eq. (5.1) for 29 potential $CO_2$ solvents involving primary, secondary, and tertiary alkanolamines.

We used the ideal–gas (IG) free energy of -26.28 kJ·mol$^{-1}$ for $H^+$ relative to 0 Kelvin, and calculated the free energy of each amine and its protonated form. We investigated the use of five composition methods: CBS–QB3, neutral CBS–APNO, G3B3 and G4. We used TIP3P water as the solvent model and calculated the neutral and protonated amine force fields using GAFF in conjunction with both RESP and AM1–BCC charges. We calculated the solution phase hydration free energies of the amines and their protonated forms, and used the value of Tissandier *et al.* for the $H^+$ hydration free energy. Since this incorporates the hydration Galvani surface potential, we also incorporated it in our calculations for the cations, using the TIP3P value of -48.25 kJ·mol$^{-1}$[261, 251].

For the hydration free energies of the neutral molecules, we found that the AM1–BCC results agree more closely with the SMD values than those of the RESP methods. The different charge methods generally agree; however, for species with multiple hydroxyl groups, the RESP hydration free energies significantly differ from the AM1–BCC results. For the ions, the agreement of the RESP and AM1–BCC models is better than in the case of the neutral molecules. A possible explanation is that for the ions, the intermolecular interaction with the solute is dominated by the total Coulombic charge, and the effects of the intramolecular interactions on the electronic density are less pronounced than for the neutral molecules.

We found that the AM1–BCC charge method yielded the best overall AAD for the experimental p$K_a$ of 0.65 p$K_a$ units. Based on these results, we suggest that AM1–BCC also gives the best results for the ions. We also considered a statistical analysis of our data by calculating the 95% confidence interval for the mean difference between the predicted and experimental p$K_a$ values, based on the use of the Student t distribution, an approach based only on the reasonable assumption that the predicted and experimental data are normally distributed. We applied this approach to our AM1–BCC and our SMD data sets, and found that the hypothesis that the predicted and experimental values are equal could be rejected only for the SMD p$K_a$ predictions of the primary and tertiary alkanolamines.

We conclude that larger test sets of data are required to better distinguish between the abilities of different approaches to adequately predict experimental p$K_a$ data.

The accuracy of the predictions may be improved by using various method/basis set combinations to overcome the limitation of the RESP derived charges (*i.e*, its reliance on the on the gas phase HF/6-31G* calculations to derive the condensed phase charges). Developing fixed charge force fields to calculate the phase transfer properties such as hydration free energy is the subject of ongoing research[255, 262]. For example, the physically motivated IPolQ partial charge method of Cerutti and *et al.* [263] uses the average partial charges of the gas phase and liquid phase to implicitly include the effect of the solute po-

larization upon transfer between the phases. Finally, we believe that the p$K_a$ prediction using fixed charge explicit solvent can be further improved with optimization of the GAFF LJ parameter which originally designed to work with the HF/6-31G* based partial charges.

Our approach can be extended to consider the temperature dependence of p$K_a$ in both aqueous and nonaqueous solvents (*e.g.*, methanol). Using our recent reaction equilibrium simulation approach[53], the p$K_a$ results of this paper can be used to predict $CO_2$ solubility for a range of tertiary amines.

## 5.6 Acknowledgements

Support for this work was provided by the Natural Sciences and Engineering Research Council of Canada (Strategic Program Grant No. STPGP 479466-15), and by the SHARCNET (Shared Hierarchical Academic Research Computing Network) HPC consortium (www.sharcnet.ca) and Compute Canada (www.computecanada.ca)

# Chapter 6

# Force–Field–Based Computational Study of the Thermodynamics of a Large Set of Aqueous Alkanolamine Solvents for Post–Combustion $CO_2$ Capture



## Abstract

The ability to predict the thermodynamic properties of amine species in $CO_2$-loaded aqueous solutions, including their deprotonation ($pK_a$) and carbamate to bicarbonate reversion ($pK_c$) equilibrium constants and their corresponding standard reaction enthalpies, is of critical importance for the design of improved carbon capture solvents. In this study, we used isocoulombic forms of both reactions to determine these quantities for a large set

of aqueous alkanolamine solvent systems. Our hybrid approach involves using classical molecular dynamics simulations with the General Amber Force Field (GAFF) and semi–empirical AM1–BCC charges (GAFF/AM1–BCC) in the solution phase, combined with high level composite quantum chemical ideal-gas calculations.

We first determined a new force–field (FF) for the hydronium ion ($H_3O^+$) by matching to the single experimental (p$K_a$) data point for the well–known MEA system at 298.15 K. We then used this FF to predict the p$K_a$ values for 76 other amines at 298.15 K and for all 77 amines at elevated temperatures. Additionally, we indirectly relate the $H_3O^+$ hydration free energy to that of $H^+$, and provide expressions for intrinsic hydration free energy and enthalpy of the proton.

Using the derived $H_3O^+$ FF, we predicted the (p$K_a$) values of a diverse set of alkanolamines with an overall AAD of less than 0.72 p$K_a$ units. Furthermore, the derived $H_3O^+$ force field is able to predict the protonation enthalpy of these amines when used with the GAFF. We also predicted the carbamate reversion constants of the primary and secondary amine species in the data set and their corresponding standard heats of reaction, which we compared with their scarcely available experimental data, which are often subject to significant uncertainty. Finally, we also described the influence of electronic and steric of different molecular fragments/groups on the stabilities of the carbamates.

## 6.1 Introduction

The combined absorption–stripping process using aqueous amine solvents is considered to be the dominant near–term technology for large–scale $CO_2$ capture from point sources, such as coal-fired power plants, and cement and steel plants[264]. $CO_2$ is primarily absorbed in the form of carbamate and bicarbonate ions, and stripped off in a later stage of the process by supplying heat to reverse the reaction and release the absorbed $CO_2$[265].

There is continuing interest in discovering $CO_2$ solvents that show improvements over the traditional monoethanolamine (MEA) base case, and the solvent's equilibrium $CO_2$ solubility is a property of primary importance. This is governed by the equilibrium constants and their temperature dependence for the involved underlying reactions, which may

be represented by the following set:

$$\begin{aligned} RNH_3^+ + H_2O &= RNH_2 + H_3O^+ && \text{(R1)} \\ RNHCO_2^- + H_2O &= RNH_2 + HCO_3^- && \text{(R2)} \\ CO_2 + 2H_2O &= HCO_3^- + H_3O^+ && \text{(R3)} \\ H_2O + HCO_3^- &= CO_3^{-2} + H_3O^+ && \text{(R4)} \\ 2H_2O &= H_3O^+ + OH^- && \text{(R5)} \\ CO_2 &= CO_2(\text{vap}) && \text{(R6)} \end{aligned}$$

All species are in the aqueous solution phase unless indicated otherwise; $RNH_2$, $RNH_3^+$ and $RNHCO_2^-$ denote the neutral, protonated and carbamate forms of the amine solvent respectively. Tertiary amines do not form carbamates, resulting in the omission of reaction R2 for these compounds.

A main concern associated with the $CO_2$ capture process is the high energy demand for solvent regeneration, due to the relatively stable $CO_2$-containing solution species, coupled with the high latent heat of the water co-solvent. This is particularly acute for primary amines, which tend to form more stable carbamates than is the case for secondary and sterically hindered amines, but they have the advantage of exhibiting faster reaction kinetics than the latter group of compounds[16]. On the other hand, tertiary amines have the advantage that $CO_2$ reacts in an overall 1:1 stoichiometric ratio with respect to the amine solvent (the combination R3−R1 of the above reaction set), whereas primary and secondary amines react in only an overall 1:2 stoichiometric ratio (the combination R3 − R1 − R2). However, this advantage of tertiary amines is offset by their slower reaction kinetics.

The equilibrium constants (expressed in terms of their p$K$ values) are commonly obtained experimentally from concentration measurements in relatively dilute equilibrium solutions or by their extrapolation to zero ionic strength, typically in conjunction with a Debye-Hückel-related equation to model the species activity coefficients [154, 189, 266]. Whereas the p$K_a$ of the amine deprotonation reaction R1 can be measured relatively accurately by means of potentiometric titration or by spectroscopic concentration measurements in a $CO_2$-free solution[267, 268], accurate determination of p$K_c$ for the carbamate reversion reaction R2 is more challenging[192] due to the presence in a $CO_2$-loaded solution of the coexisting species involved in the indicated set of reactions. In addition, due to the rapid proton exchange, NMR techniques cannot distinguish between the bicarbonate/carbonate species peaks or the amine/protonated amine species peaks, and only the sums of the relevant individual species concentrations in each pair can be determined. This has resulted in the use of different approaches to unravel the individual species concentrations from the

NMR data[207, 193, 269]. By relating the intensity of the two–species compound peak to the individual species peaks and their concentrations in the solution, amine and its protonated form may be distinguished by interpolation of the NMR chemical shifts at low and high pH values or by measuring the spectra of solutions that contain only the individual species [193]. In addition, species at concentrations less than about $10^{-4}$ molal are undetectable by the analysis of NMR data. These experimental challenges typically result in a significant uncertainty in the resulting carbamate reversion constant values, even for the well–studied monoethanolamine (MEA)[192] system.

A common theoretical approach to determine p$K$ values uses ideal-gas electronic structure (ES) calculations in conjunction with conductor–like polarizable continuum models (CPCM), universal solvation models (SMD, SM8), or their explicit solvent variants (the inclusion of explicit solvent molecules in the first solvation shell)[270, 233]. The calculation of solvation free energy using such models requires five temperature–dependent solvent–based parameters based on experimental data: dielectric constant, bulk surface tension, refractive index, and acidity and basicity parameters. The accuracy of these models is often unsatisfactory, in part because their development and application has generally been limited to small rigid molecules; furthermore, the models have only been parameterized at 298.15 K. Their static nature also hampers extensions to flexible molecules in solution, in which the contribution of different molecular conformers to the solvation free energy are non-negligible. In a notable study, Coote *et al.* [170] demonstrated different criteria for obtaining the most stable conformer in the solution phase, and showed how an erroneous result may be obtained if the commonly used gas–phase geometry is adopted for the solution phase solvation free energy calculation in the case of larger flexible amine molecules.

Since the pioneering study of da Silva and Svendsen[271], numerous studies have used a similar thermodynamic-cycle-based approach[272] to investigate the deprotonation reaction p$K_a$ value, whereas similar studies for the carbamate reversion equilibrium constant p$K_c$ are extremely limited[271]. While some studies show reasonable accuracy (a mean absolute deviation from experiment below 0.5 pK unit), they usually require a particular combination of gas–phase quantum chemical theory/basis set and solvation model that is often different from the original quantum chemical method used for the solvation model development, questioning the transferability of such approaches to different classes of compounds[233, 230].

More rigorous direct *ab initio* simulation of the free-energy profile of the dissociation reaction taking place in the condensed phase has been shown to be a promising route for p$K_a$ estimation[273]. However, apart from being extremely computationally demanding, such simulations may require advanced sampling techniques to escape from local free energy

minima, inhibiting their wide-spread use for rapid solvent screening[274].

In a recent paper[275], we developed a molecular–based framework for reactive absorption in $CO_2$-amine-water systems without any amine-specific experimental data or experimental proton hydration free energy data only using the p$K_c$ and the equilibrium constant of the following *isoelectric* reaction (one with the same total numbers of positive and negative charges on the reactant and product side), which is the reaction combination R3-R1-R2 of the above reaction set:

$$RNH_2 + 2CO_2 \quad = \quad RNH_3^+ + RNHCO_2^- \tag{R7}$$

We combined these equilibrium constants with a Henry-law-based thermodynamic model and the experimentally well-known p$K$ values for the binary $CO_2$-$H_2O$ system to predict the speciation and other quantities of interest for a set of 7 $CO_2$–loaded primary and secondary alkanolamine solvents.

In this paper, we refine our methodology by focusing on the deprotonation reaction R1 and the carbamate reversion reaction R2, both of which are *isocoulombic* (with the same number of like-charged species on the reactant and the product side). Use of an isocoulombic reaction has been shown to provide a better estimate of the temperature trend for its equilibrium constant[276]. Furthermore, such reactions have the advantage that for activity coefficient models based on the Debye-Huckel approximation (*e.g.*, the Davies model), the ionic contributions to the reaction free energy change cancel. We test this approach for the equilibrium constants (p$K_a$ and p$K_c$) for a much larger set of 77 primary, secondary and tertiary amines, Our approach combines ideal-gas calculations with explicit solvent MD simulations in TIP3P water using the fast AM1-BCC partial charge assignment method for the amine molecules and their protonated and carbamate forms, which we have previously shown to be superior to the RESP-based charges for p$K_a$ prediction used in our previous work[175].

To enable the use of the isocoulombic reaction R1, we develop a new GAFF-compatible force field for $H_3O^+$ to be used in conjunction with TIP3P water by matching the well—known experimental MEA deprotonation equilibrium constant at 298.15 K. This enables the $H_3O^+$ FF to be used to calculate the p$K_a$ of reaction R1 as a function of temperature, both for MEA and all other alkanolamines. We further validate the $H_3O^+$ FF by comparing its indirect prediction of proton hydration free energy with the well-established literature value at 298.15 K[60], and also use it to calculate the intrinsic proton solvation free energy as a function of temperature.

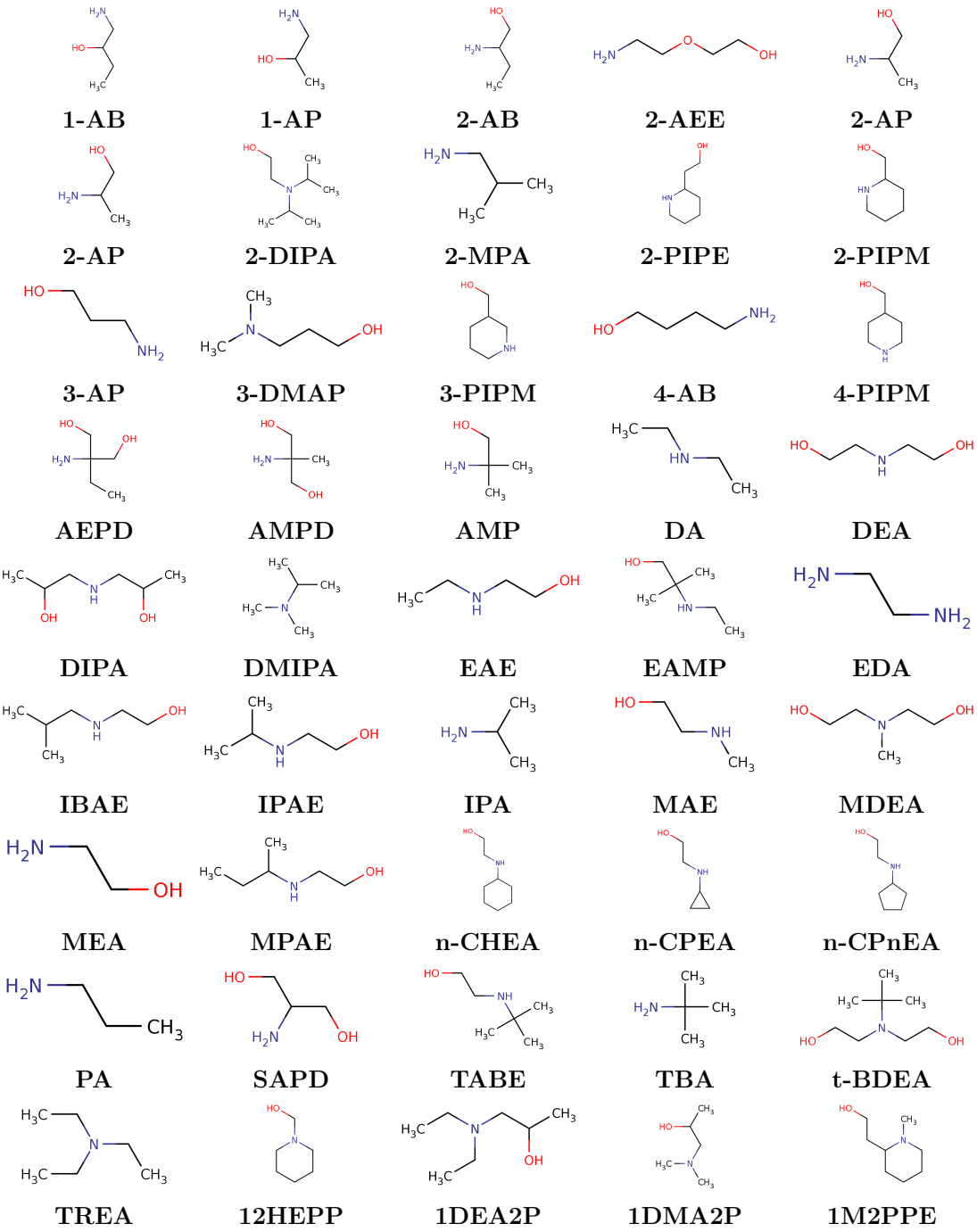


Figure 6.1: Molecular Structures of the alkanolamines considered in this work.

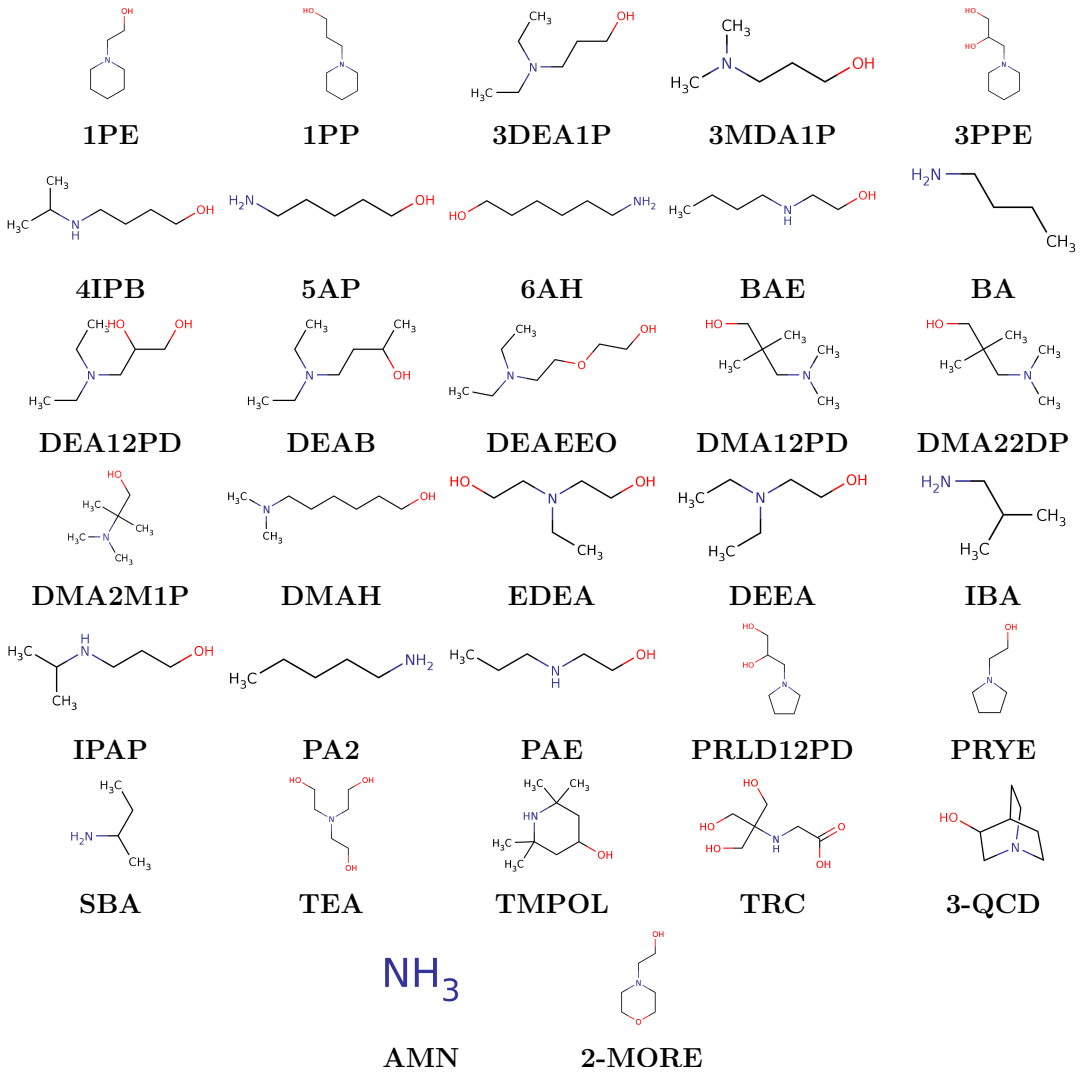


Figure 6.2: Molecular Structures of the alkanolamines considered in this work (continued).

## 6.2 Thermodynamic Background

### 6.2.1 Molecular–Based Framework for the Calculation of p$K_a$ and p$K_c$

Our framework for predicting p$K_a$ and p$K_c$ without the need for experimental data is described in detail in our previous papers[174, 175, 275], and only a brief summary is provided here.

The Henry-Law-based standard chemical potential using the molality concentration variable, $\mu_i^\dagger(T,P)$, may be defined for both solutes and the solvent, and is related to the infinite dilution *intrinsic solvation free energy* (self solvation free energy in the case of the solvent), $\mu_i^{\mathrm{res},NVT;\infty}[T,\rho(T,P)]$, by

$$\mu_i^\dagger(T,P) = \mu_i^0(T;P^0) + RT\ln\left(\frac{RT}{100P^0}\right) + RT\ln\left(\frac{\overline{\rho}_{\mathrm{solv}}(T,P)}{1000}\right) + \mu_i^{\mathrm{res},NVT;\infty}[T,\rho_{\mathrm{solv}}(T,P)] \tag{6.1}$$

where $\mu_i^0(T;P^0)$ is the species ideal–gas (IG) chemical potential at $T$ and reference state pressure $P^0 = 1$ bar, $P$ is expressed in bar, and $\rho_{\mathrm{solv}}$ is the density of the pure solvent. ($\overline{\rho}_{\mathrm{solv}}$ denotes its expression in kg m$^{-3}$). $\mu_i^\dagger(T,P)$ is numerically equal to the chemical potential in a hypothetical ideal solution of unit molality.

The p$K$ value for a reaction $j$ is obtained from the concentration-independent quantity $\Delta G_j^*(T,P)$, via

$$pK_j(T,P) = \frac{\Delta G_j^*(T,P)}{RT\ln(10)} \tag{6.2}$$

where $\Delta G_j^*(T,P)$ is the standard Gibbs energy change of the reaction in the solvent, given by

$$\begin{aligned}
\Delta G_j^*(T,P) &= \sum_{i=1}^{N_s} \nu_{ij}\mu_i^\dagger(T;P) + RT\nu_{\mathrm{solv},j}\ln\left(\frac{1000}{M_{\mathrm{solv}}}\right) \\
&= \Delta G_j^0(T;P^0) + RT\overline{\nu}_j\ln\left(\frac{RT}{100P^0}\right) + RT\overline{\nu}_j\ln\left(\frac{\overline{\rho}_{\mathrm{solv}}(T,P)}{1000}\right) \\
&\quad + RT\nu_{\mathrm{solv},j}\ln\left(\frac{1000}{M_{\mathrm{solv}}}\right) + \Delta G^{\mathrm{res},NVT;\infty}(T,P)
\end{aligned} \tag{6.3}$$

where

$$\begin{aligned} \Delta G_j^0(T;P^0) &= \sum_{i=1}^{N_s} \nu_{ij}\mu_i^0(T;P^0) \\ \Delta G_j^{\mathrm{res},NVT;\infty}(T,P) &= \sum_{i=1}^{N_s} \nu_{i,j}\mu_i^{\mathrm{res},NVT;\infty}[T,\rho(T,P)] \end{aligned} \tag{6.4}$$

$N_s$ is the number of species involved in the reaction, $\nu_{ij}$ is the stoichiometric coefficient of species $i$ in reaction $j$ (conventionally positive for products and negative for reactants), $\bar{\nu}_j = \sum_i \nu_{ij}$ and $M_{\mathrm{solv}}$ is the solvent (water in this case) molecular weight.

For the deprotonation and carbamate reversion reactions in this study (reactions R1 and R2, respectively, $\bar{\nu}_j = 0$ and $\nu_{\mathrm{solv},j} = -1$, and the following expression for $\Delta G_j^*$ is obtained for both reactions:

$$\Delta G_j^*(T,P) = \Delta G_j^0(T;P^0) + \Delta G^{\mathrm{res},NVT;\infty}[T,\rho(T,P)] - RT\ln\left(\frac{1000}{M_{\mathrm{solv}}}\right) \tag{6.5}$$

$$= \Delta G_j^\dagger(T,P) - RT\ln\left(\frac{1000}{M_{\mathrm{solv}}}\right) \tag{6.6}$$

Finally, the temperature dependence of p$K$ for the deprotonation and carbamate reversion reactions is obtained by application of the Gibbs-Helmholtz equation to Eqs. (6.5) and (6.2), resulting in :

$$\begin{aligned} \left(-\frac{\partial \ln K_j}{\partial T}\right) = \left(\frac{\partial \Delta G^\dagger[T,P]/RT}{\partial T}\right) &= \frac{\partial(\Delta G_j^0[T;P]/RT)}{\partial T} + \frac{\partial(\Delta G^{\mathrm{res},NVT;\infty}/RT)}{\partial T} \\ &= -\frac{\Delta H^0(T,P)}{RT^2} - \frac{\Delta H^{\mathrm{res},NVT;\infty}[T,\rho(T,P)]}{RT^2} \\ &= -\frac{\Delta H^\dagger(T,P)}{RT^2} \end{aligned} \tag{6.7}$$

Assuming a linear temperature dependence of the enthalpy quantities in each term (equivalent to assuming constant reaction $\Delta C_p$ values) gives an expression at the pressure of interest of the form

$$-\ln K_j = A_j^0 + \frac{B_j^0}{T} + C_j^0\ln(T) + A_j^{\mathrm{res}} + \frac{B_j^{\mathrm{res}}}{T} + C_j^{\mathrm{res}}\ln(T) \tag{6.8}$$

### 6.2.2 $H_3O^+$ FF Determination and the Proton Hydration Free Energy

Replacing $H_3O^+$ in reaction R1 by $H^+$ would yield the alternative reaction equation

$$RNH_3^+ = RNH_2 + H^+ \tag{R8}$$

The reaction combination R1-R8 gives the reaction

$$H_2O + H^+ = H_3O^+ \tag{R9}$$

Since by convention, in water solvent $\Delta G^*$ for reaction R5 and for the following reaction are identical:

$$H_2O \;=\; H^+ + OH^- \tag{R10}$$

this means that $\Delta G^*$ for reaction R9=R5-R10 must vanish. Hence the p$K$ values for reactions R1 and R8 must also be identical. Eqs. (6.2) and (6.3) for reaction R8 give

$$\begin{aligned} RT\ln(10)pK_{R8} \;=\; & \Delta G^0_{R8}(T;P^0) + \mu^{\mathrm{res},NVT;\infty}_{H^+}(T,P) + \mu^{\mathrm{res},NVT;\infty}_{RNH_2}(T,P) \\ & -\mu^{\mathrm{res},NVT;\infty}_{RNH_3^+}(T,P) + RT\ln\left(\frac{\overline{\rho}_{\mathrm{solv}}(T,P)}{1000}\right) + RT\ln\left(\frac{RT}{100P^0}\right) \end{aligned} \tag{6.9}$$

The proton intrinsic hydration free energy, $\mu^{\mathrm{res},NVT;\infty}_{H^+}$, is then given by

$$\begin{aligned} \mu^{\mathrm{res},NVT;\infty}_{H^+} \;=\; & RT\ln(10)pK_{R8}(T,P) - \Delta G^0_{R8}(T;P^0) - \mu^{\mathrm{res},NVT;\infty}_{RNH_2}(T,P) \\ & +\mu^{\mathrm{res},NVT;\infty}_{RNH_3^+}(T,P) - RT\ln\left(\frac{\overline{\rho}_{\mathrm{solv}}(T,P)}{1000}\right) - RT\ln\left(\frac{RT}{100P^0}\right) \end{aligned} \tag{6.10}$$

Eq. (6.10) is the conventional means by which $\mu^{\mathrm{res},NVT;\infty}_{H^+}$ is determined from experimental p$K_a$ data for a variety of species (*e.g.*, Malloum *et al.* [277]), typically by means of continuum solvent calculations to obtain $\mu^{\mathrm{res},NVT;\infty}$ for the neutral and protonated species. (We note in passing that the term in Eq. (6.10) involving the solvent density is often omitted from such calculations; this is a reasonable approximation at 298.15 K for water solvent, where this term is small; however at higher temperatures and for solvents other than water, this may not be the case.) Also, since Eq. (6.10) requires experimental data at each temperature, such calculations have mostly been limited to 298.15 K, at which temperature data for many species is available.

In our work, we use reaction R1, whose $pK_a$ value is identical to that of reaction R8, and for which Eqs. (6.2) and (6.3) give

$$\begin{aligned}\mu^{\mathrm{res},NVT;\infty}_{\mathrm{H_3O^+}}(T,P) &= RT\ln(10)pK_1(T,P) - \Delta G^0_{R1}(T;P^0) - \mu^{\mathrm{res},NVT;\infty}_{\mathrm{RNH_2}}(T,P) \\ &\quad + \mu^{\mathrm{res},NVT;\infty}_{\mathrm{H_2O}}(T,P) + \mu^{\mathrm{res},NVT;\infty}_{\mathrm{RNH_3^+}}(T,P) + RT\ln\left(\frac{1000}{M_{solv}}\right) \quad (6.11)\end{aligned}$$

We have adjusted the $H_3O^+$ FF to match the well-known experimental $pK_1$ value for MEA at 298.15 K and 1 bar, using FFs predicted value of hydration free energy for MEA and $MEAH^+$ obtained from the GAFF/AM1–BCC and quantum chemical calculations of $\Delta G^0_{R1}(T;P^0)$. The availability of the $H_3O^+$ FF then allows $pK_a$ calculations to be performed at any temperature.

We can test the resulting $H_3O^+$ FF by applying the same procedure to reaction R9, whose $\Delta G^*$ value is zero and for which Eq. (6.3) gives the intrinsic solvation free energy of the proton in terms of the readily calculated hydronium ion solvation value:

$$\begin{aligned}\mu^{\mathrm{res},NVT;\infty}_{\mathrm{H^+}} &= \mu^{\mathrm{res},NVT;\infty}_{\mathrm{H_3O^+}}(T,P) - \mu^{\mathrm{res};\infty}_{\mathrm{H_2O}}(T,P) + \Delta G^0_{R9}(T,P^0) \\ &\quad - RT\ln\left(\frac{\overline{\rho}_{\mathrm{solv}}(T,P)}{1000}\right) - RT\ln\left(\frac{RT}{100P^0}\right) - RT\ln\left(\frac{1000}{M_{\mathrm{solv}}}\right) \quad (6.12)\end{aligned}$$

where

$$\Delta G^0_{R9}(T,P^0) = \mu^0_{\mathrm{H_3O^+}}(T,P^0) - \mu^0_{\mathrm{H_2O}}(T,P^0) - \mu^0_{\mathrm{H^+}}(T,P^0) \quad (6.13)$$

This calculation is not limited to 298.15 K and 1 bar and allows $\mu^{\mathrm{res},NVT;\infty}_{\mathrm{H^+}}(T,P)$ to be readily obtained as a function of temperature and pressure.

Finally, the absolute solvation free energies of the proton and the hydronium ion may be obtained by adding the Galvani contribution, $z_i\xi_{\mathrm{G}}(T,P)$, to their respective intrinsic values, where $z_i$ is the ion valence (+1 for $H^+$ ), and $\xi_{\mathrm{G}}(T,P)$ is the solvent Galvani potential.

## 6.3 Computational Details

All intramolecular parameters (bond stretching, angle bending, and torsional constants) and LJ parameters($\sigma$, $\epsilon$) of the bicarbonate ion ($HCO_3^-$), the neutral ($RNH_2$), protonated ($RNH_3^+$) and carbamate ($RNHCO_2^-$) form of the amines were taken from the General Amber Force Field (GAFF)[177] with its default functional form using the Antechamber package in

AMBER tools[178], which assigns the parameters based on atom typing rules. Carbon dioxide ($CO_2$) was modeled using the Transferable Potential for Phase Equilibrium (TraPPE) model of Potoff[122] and the solvent (water) was modeled by the TIP3P FF which is the default water model for the GAFF. We used the lowest-free-energy conformer at the G4 level as an initial structure input for calculation of partial charges. For the bicarbonate ion, we used electrostatic potential energy grid calculations at the GAFF default HF/6-31G* level using the Merz-Kollman scheme in Gaussian16 with the two-step Restrained Electrostatic Surface Potential (RESP) fitting method[65] within the Antechamber software package to assign the partial charges. For neutral ($RNH_2$), protonated ($RNH_3^+$) and carbamate ($RNHCO_2^-$), partial charges were assigned using the Antechamber software package based on the fast semi-empirical AM1-BCC method using the G4 ideal-gas geometry. The GROMACS–formatted force field input files were then generated using the acpype (version 2019) python interface[179]. Default GAFF 1-4 interactions were used for all molecules, except for the bicarbonate ion, for which the H–O electrostatic 1-4 interactions were scaled by 0.5 due to excessive 1-4 electrostatic interaction between these pairs.

The initial configurations for a single solute molecule solvated in a periodic box of 1500 water molecules generated using the packmol software package[181]. All MD simulations were performed using using the GROMACS (version 2016.3) program[180]. Initially, A steepest–descent minimization was performed to relax the system and remove any bad contacts, followed by a short (100 ps) $NVT$ equilibration run followed by a 12 ns long $NPT$ simulation with the first 2 ns discarded to determine the system density . Alchemical free energy simulations to decouple the solute molecule from its solvent environment were then started from the previously equilibrated configurations in an $NVT$ ensemble, with simulation box size based on the calculated $NPT$ density.

The classical equations of motion were integrated using the GROMACS stochastic Langevin algorithm, with a friction constant of 1.0 $ps^{-1}$ and time step of 2.0 $fs^{-1}$. The pressure was maintained using a Parrinello-Rahman pressure coupling constant of 2.0 ps. The Lennard–Jones short–range interactions were smoothly switched off between 12 and 12.5Å and the electrostatic interactions were computed using the particle mesh Ewald (PME) method with a 12 Å real–space cutoff, 1.0 Å grid spacing, sixth–order spline interpolation, and accuracy of $10^{-6}$. The free energy of decoupling the solute molecule from its solvent environment was calculated using the GROMACS implementation of the Bennett Acceptance Ratio (BAR) method (gmx bar). We employed a linear decoupling for the electrostatic interaction with six equally spaced $\lambda$ values (0, 0.2, 0.4, 0.6, 0.8, 1.0) followed by 20 equally spaced $\lambda$ values (0.0, 0.05, ..., 1.0) with $\Delta\lambda = 0.05$ to decouple the LJ interactions using the standard GROMACS soft-core potential function originally proposed by Beutler et al[182], with parameters (in GROMACS notation) *sc-alpha* = 0.5, *sc-power* =

1 and *sc-sigma* = 0.3. For each alchemical window, we used a 12.5 ns simulation with the first 2.5 ns discarded for equilibration.

### 6.3.1 Ideal–Gas Reaction Free Energies and Conformational Search

Initial conformations of the neutral, protonated and carbamate forms of the amines were generated using the Spartan v.18 software package with the default Merck Molecular Force Field (MMFF94). The 10 lowest energy conformers of each solute at the MMFF94 level were further optimized using the Gaussian 16 package, followed by frequency calculations using high–level composite methods (G4, G3, CBS-QB3 and CBS-APNO) to find the lowest-free-energy conformer for each QM method at 298.15 K. For a given QM method, the free energies of the most stable conformers were then used to calculate the ideal–gas reaction free energies at $T$ = 298.15 K; to save computational time, the effect of temperature on the reaction free energy was implemented only using G4 calculations over the temperature range of 283.15–373.15 K according to:

$$\Delta G_j^0(T;P^0) = \Delta G_j^0(298.15;P^0)^{avg} + [\Delta G_j^0(T;P^0) - \Delta G_j^0(298.15;P^0)]^{\mathrm{G4}} \tag{6.14}$$

where $\Delta G_j^0(298.15;P^0)^{avg}$ is the average value of the reaction free energy using G4, G3, CBS-QB3 and CBS-APNO calculations and $[\Delta G_j^0(T;P^0) - \Delta G_j^0(298.15;P^0)]^{\mathrm{G4}}$ is that of G4 calculations. We have previously shown[278] that the second term, which accounts for the effect of temperature on the ideal–gas free energy, is insensitive to the QM method/theory level; however, the absolute ideal–gas free energy of the species (the first term) can vary substantially across different QM methods. As noted previously[174], improved predictions can arise from the use of the combination of several high–level QM methods for the calculation of this term. We therefore used the average value of $\Delta G_j^0(298.15;P^0)$ obtained from the G4, G3, CBS-QB3 and CBS-APNO calculations and the standard deviation was taken as a surrogate measure of the uncertainty of the $\Delta G_j^0(T;P^0)$ values.

## 6.4 Results and Discussion

### 6.4.1 Ideal-Gas Reaction Free Energy Changes, $\Delta G_j^0(T;P^0)$

Ideal-gas reaction free energy values $\Delta G_j^0(T,P)$ in Eq. (6.3) were obtained at $T$ = 283.15, 293.15, 298.15, 303.15, 313.15, 323.15, 343.15, 353.15, 363.15 and 373.15K according to

Eq. (6.14). We then expressed the temperature dependence of the amine deprotonation and carbamate reversion ideal-gas reaction free energies in the form

$$\frac{\Delta G_j^0(T,P^0)}{RT} = A_j^0 + \frac{B_j^0}{T} + C_j^0 \ln(T) \tag{6.15}$$

The coefficients of Eq. (6.15) for the reactions R1 and R1 are provided in Tables S1 and S2 of the Supporting Information. Fig. 6.3 shows the dimensionless ideal–gas reaction free energies of deprotonation (filled symbols) and for the carbamate reversion reaction (open symbols) for a primary (MEA), secondary (DEA), tertiary (TEA) and sterically hindered amine (AMP). As indicated by the $R^2$ values in the Supplementary Information, the data are well represented by the fitted functions. Generally, the deprotonation reaction free energy change shows more sensitivity to temperature than does that of the carbamate reversion reaction.

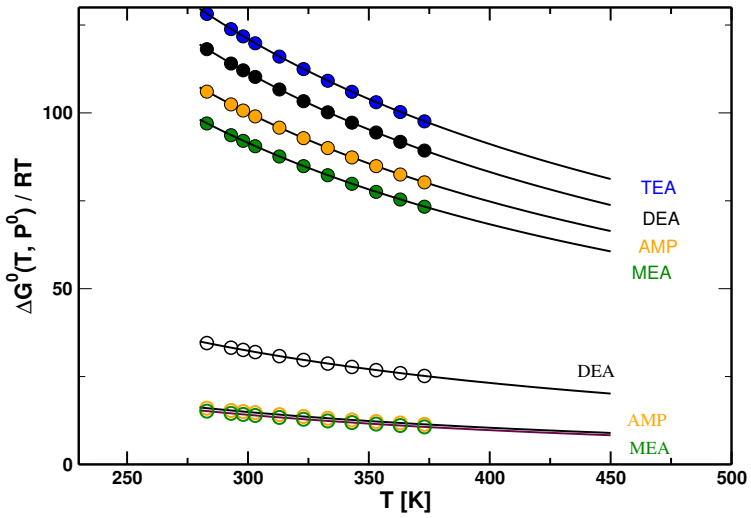


Figure 6.3: Ideal–gas reaction free energy change of the deprotonation reaction R1 (filled symbols) and the carbamate reversion reaction R2 (open symbols) for the indicated amines. The curves are regressions to Eq. (6.15).

### 6.4.2 Residual Reaction Free Energy Changes, $\Delta G_j^{\mathrm{res},NVT;\infty}(T,P)$

Calculation of the residual contribution to the reaction free energy $\Delta G_j^{\mathrm{res},NVT;\infty}(T,P)$ in Eq. (6.4) requires individual species $\mu_i^{\mathrm{res};\infty}(T,P)$ values as functions of temperature.

While QM ideal-gas chemical potential calculations exhibit no imprecision apart from the use of different quantum theory levels, residual chemical potentials obtained from MD simulations are subject to inherent stochastic uncertainties. We have thus smoothed the individual species $\mu_i^{\mathrm{res};\infty}(T,P)$ values by regression to the functional form:

$$\frac{\mu_i^{\mathrm{res},NVT;\infty}[T,\rho(T,P)]}{RT} = a_i^{\mathrm{res}} + \frac{b_i^{\mathrm{res}}}{T} + c_i^{\mathrm{res}}\ln(T) \tag{6.16}$$

The coefficients $a_i^{\mathrm{res}}, b_i^{\mathrm{res}}, c_i^{\mathrm{res}}$ for all species, including the small molecules ($H_2O$, $CO_2$, $HCO_3^-$, $H_3O^+$), are provided in Tables S3–S6 of the Supplementary Information. The coefficients $A_j^{\mathrm{res}}, B_j^{\mathrm{res}}, C_j^{\mathrm{res}}$ in Eq. (6.8) for reaction $j$ are then obtained from

$$A_j^{\mathrm{res}} = \sum_{i=1}^{N_s} \nu_{i,j} a_i^{\mathrm{res}} \tag{6.17}$$

$$B_j^{\mathrm{res}} = \sum_{i=1}^{N_s} \nu_{i,j} b_i^{\mathrm{res}} \tag{6.18}$$

$$C_j^{\mathrm{res}} = \sum_{i=1}^{N_s} \nu_{i,j} c_i^{\mathrm{res}} \tag{6.19}$$

For the majority of solutes considered in this work, the $\mu_i^{\mathrm{res}}$ regressions are of good quality, as indicated by their $R^2$ values. However, larger flexible molecules with multiple conformers in the solution exhibit somewhat scattered $\mu_i^{\mathrm{res}}/RT$ values. For these molecules, we performed five independent replicate simulations (each using different random–number seeds to generate the initial configuration and the initial atomic velocity assignment), and we used the resulting average $\mu_i^{\mathrm{res}}/RT$ values in the regression. We show a typical result for such a larger molecule in Fig. 6.4.

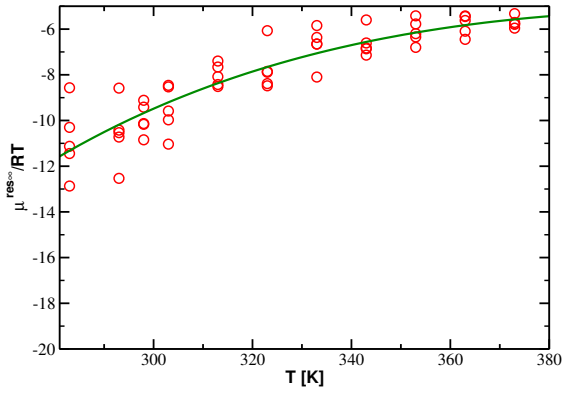


Figure 6.4: Infinite dilution residual chemical potential of the neutral 4IPB as a function of temperature from five replicate simulations at each temperature. The curve is the result of fitting Eq. (6.16) to the simulation data using the average value at each temperature.

### 6.4.3 Deprotonation Constant, p$K_a$

A parity plot of predicted versus experimental p$K_a$ data is shown in Fig. 6.5. The dashed line indicates a tolerance of 1.0 $pK_a$ unit, and for most of the considered amines the error is less than 1.0 $pK_a$ unit, equivalent to an error of $\approx$ 5.7 kJ·mol$^{-1}$ in the reaction free energy at T=298.15 K.

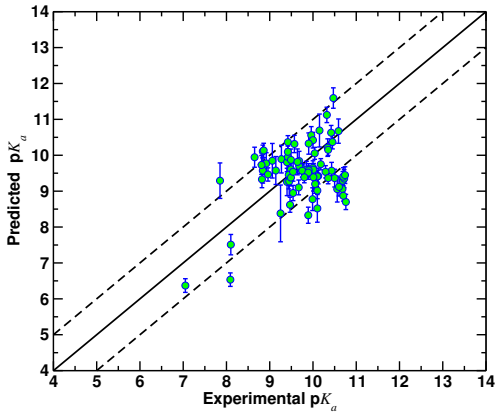


Figure 6.5: Calculated versus experimental p$K_a$ values for the 77 alkanolamine species considered in this work. The vertical error bars are obtained by propagating the uncertainty in the ideal–gas reaction free energy (horizontal error bars for the experimental data are not shown) and the dashed line indicates a tolerance of 1.0 p$K_a$ unit.

Table 6.1 summarizes the numerical values of the protonation constant of the 77 studied amine at 298.15 K, along with the carbamate formation constant of the primary and secondary amines obtained in this work. The experimental p$K_a$ data were taken from the literature[279, 280, 281, 266, 282, 268, 283, 284, 267, 10, 285]. Using the developed $H_3O^+$ FF, we found an average absolute deviation (AAD) of 0.72 $pK_a$ units for a set of 77 amines. Our results show that the $pK_a$ values of amines with multiple hydroxyl groups are underestimated and those of alkyamines (amines with no hydroxyl group) are overestimated.

Table 6.1: Protonation and carbamate formation constants of the studied amines at $T = 298.15$ K. The uncertainty in the simulation values is based on the uncertainty in the ideal gas contribution to the reaction free energy, since that of the residual part is negligible. The uncertainty in the experimental p$K_a$ data is typically smaller than 0.1 p$K$ unit and that for the carbamate formation is inferred to be around the MEA value of ≈ 0.25 p$K_a$ unit. $t$ indicates tertiary amines, which do not form carbamate.

| | p$K_a$ | | p$K_c$ | |
|---|---|---|---|---|
| **Amine** | this work | literature | this work | literature |
| 1AB | $9.26_{0.38}$ | 9.4 | $1.62_{0.27}$ | |
| 1AP | $9.27_{0.40}$ | 9.45 | $1.53_{0.28}$ | 1.70[195] |
| 2AB | $9.89_{0.39}$ | 9.27 | $1.32_{0.30}$ | |
| 2AEE | $10.36_{0.18}$ | 9.42 | $3.78_{0.34}$ | |

*Continued on next page*

Table 6.1 – *Continued from previous page*

| | p$K_a$ | | p$K_c$ | |
|---|---|---|---|---|
| **Amine** | this work | literature | this work | literature |
| 2AP | $9.81_{0.26}$ | 9.4 | $0.75_{0.15}$ | 0.60[195], 0.98 [154] |
| 2DIPA | $9.95_{0.20}$ | 9.42 | t | |
| 2MPA | $9.36_{0.25}$ | 10.5 | $1.28_{0.11}$ | |
| 2PIPE | $10.63_{0.20}$ | 10.42 | $-0.19_{0.40}$ | no carbamate detected[154] |
| 2PIPM | $9.42_{0.22}$ | 10.12 | $-0.06_{0.32}$ | no carbamate detected[154] |
| 3AP | $10.56_{0.24}$ | 9.96 | $2.07_{0.15}$ | 1.83[195] |
| 3DMAP | $9.61_{0.26}$ | 9.49 | t | |
| 3PIPM | $9.20_{0.26}$ | 10.05 | $4.23_{0.33}$ | |
| 4AB | $11.12_{0.21}$ | 10.32 | $1.87_{0.35}$ | |
| 4PIPM | $9.06_{0.36}$ | 10.56 | $1.88_{0.33}$ | 1.39[154] |
| AEPD | $9.33_{0.23}$ | 8.82 | $-0.39_{0.38}$ | |
| AMPD | $9.57_{0.35}$ | 8.84 | $0.98_{0.32}$ | no carbamate detected[154] |
| AMP | $9.84_{0.27}$ | 9.68 | $0.16_{0.21}$ | no carbamate detected[154] |
| DA | $8.70_{0.21}$ | 10.76 | $1.10_{0.75}$ | |
| DEA | $9.77_{0.30}$ | 8.92 | $1.57_{0.46}$ | 0.92[154] |
| DIPA | $10.11_{0.17}$ | 8.84 | $1.91_{0.40}$ | |
| DMIPA | $8.62_{0.21}$ | 9.47 | t | |
| EAE | $9.65_{0.19}$ | 10 | $1.53_{0.32}$ | |
| EAMP | $10.42_{0.22}$ | 10 | $-1.57_{0.57}$ | |
| EDA | $10.33_{0.30}$ | 9.9 | $0.42_{0.29}$ | |
| IBAE | $9.60_{0.16}$ | 10.01 | $2.93_{0.24}$ | |
| IPAE | $9.61_{0.15}$ | 9.78 | $0.16_{0.28}$ | |
| IPA | $9.06_{0.23}$ | 10.68 | $-0.30_{0.10}$ | |
| MAE | $9.60_{0.23}$ | 9.85 | $2.42_{0.60}$ | |
| MDEA | $9.95_{0.28}$ | 8.65 | t | |
| MEA | $9.46_{0.39}$ | 9.44 | $1.61_{0.25}$ | 1.6, 1.81, 1.76, 1.31, 1.25[192, 191, 154, 189, 188] |
| MPAE | $10.10_{0.16}$ | 9.42 | $1.13_{0.36}$ | |
| nCHEA | $9.41_{0.16}$ | 10.1 | $-0.21_{0.26}$ | |
| nCPEA | $6.53_{0.19}$ | 8.09 | $-0.30_{0.54}$ | |
| nCPnEA | $9.02_{0.23}$ | 10.1 | $-1.01_{0.28}$ | |
| PA | $9.12_{0.25}$ | 10.6 | $0.81_{0.10}$ | 2.20[195] |
| SAPD | $9.73_{0.24}$ | 8.55 | $1.05_{0.25}$ | no carbamate detected[154] |
| TBAE | $10.05_{0.16}$ | 10.04 | $-2.61_{0.63}$ | |
| TBA | $9.57_{0.23}$ | 10.43 | $-0.77_{0.66}$ | |
| tBDEA | $9.85_{0.48}$ | 9.06 | t | |
| TREA | $8.87_{0.14}$ | 10.7 | t | |
| 12HEPP | $10.31_{0.24}$ | 9.57 | t | |
| 1DEA2P | $9.75_{0.15}$ | 10.18 | t | |
| 1DMA2P | $9.10_{0.20}$ | 9.67 | t | |
| 1M2PPE | $8.33_{0.22}$ | 9.89 | t | |
| 1PE | $9.46_{0.18}$ | 8.96 | t | |
| 1PP | $9.38_{0.23}$ | 9.49 | t | |
| 3DEA1P | $9.54_{0.17}$ | 10.29 | t | |
| 3MDA1P | $9.54_{.25}$ | 9.54 | t | |
| 3PPE | $9.87_{0.30}$ | 9.49 | t | |

*Continued on next page*

Table 6.1 – *Continued from previous page*

| | p$K_a$ | | p$K_c$ | |
|---|---|---|---|---|
| **Amine** | this work | literature | this work | literature |
| 4IPB | $10.37_{0.19}$ | 10.45 | $-0.34_{0.38}$ | |
| 5AP | $11.59_{0.28}$ | 10.47 | $3.17_{0.40}$ | |
| 6AH | $10.67_{0.33}$ | 10.59 | $5.35_{0.36}$ | |
| BAE | $9.58_{0.18}$ | 9.9 | $1.54_{0.32}$ | |
| BA | $9.29_{0.25}$ | 10.69 | $0.85_{0.11}$ | 1.7[195] |
| DEA12PD | $9.70_{0.20}$ | 9.68 | t | |
| DEAB | $9.36_{0.15}$ | 10.35 | t | |
| DEAEEO | $10.69_{0.46}$ | 10.15 | t | |
| DMA12PD | $9.57_{0.38}$ | 9.14 | t | |
| DMA22DP | $8.95_{0.21}$ | 9.54 | t | |
| DMA2M1P | $10.21_{0.24}$ | 10.34 | t | |
| DMAH | $9.39_{0.38}$ | 10.01 | t | |
| EDEA | $10.13_{0.20}$ | 8.86 | t | |
| DEEA | $9.57_{0.17}$ | 9.75 | t | |
| IBA | $9.35_{0.25}$ | 10.72 | $1.34_{0.11}$ | 1.98 [195] |
| IPAP | $10.15_{0.15}$ | 10.35 | $0.48_{0.31}$ | |
| PA2 | $9.40_{0.25}$ | 10.7 | $1.01_{0.11}$ | |
| PAE | $9.52_{0.18}$ | 9.89 | $2.73_{0.31}$ | |
| PRLD12PD | $9.82_{0.36}$ | 9.64 | t | |
| PRYE | $9.39_{0.15}$ | 9.8 | t | |
| SBA | $9.45_{0.23}$ | 10.74 | $0.13_{0.08}$ | 1.32 [195] |
| TEA | $9.29_{0.50}$ | 7.85 | t | |
| TMPOL | $8.78_{0.31}$ | 9.99 | $-6.48_{0.70}$ | |
| TRC | $7.51_{0.28}$ | 8.1 | $-0.90_{0.80}$ | |
| 3QCD | $8.52_{0.38}$ | 10.1 | t | |
| AMN | $8.38_{0.79}$ | 9.25 | $1.2_{1.03}$ | |
| 2MORE | $6.37_{0.20}$ | 7.05 | t | |

### 6.4.4 Temperature Dependence of p$K_a$ and the Deprotonation Standard Reaction Enthalpy

Figs. 6.6 and Fig.6.7 show the temperature dependence of the MEA p$K_a$ and of the amines for which we found experimental temperature dependent p$K_a$ data, namely AMP, 1-AP, DEEA, MAE, 2DIPA, 2AP, 3DMA1P employing our $H_3O^+$ FF. The data shows that the developed $H_3O^+$ FF is able to accurately predict the temperature trend despite the fact that only the p$K_a$ of MEA at $T = 298.15$ K was used to train it.

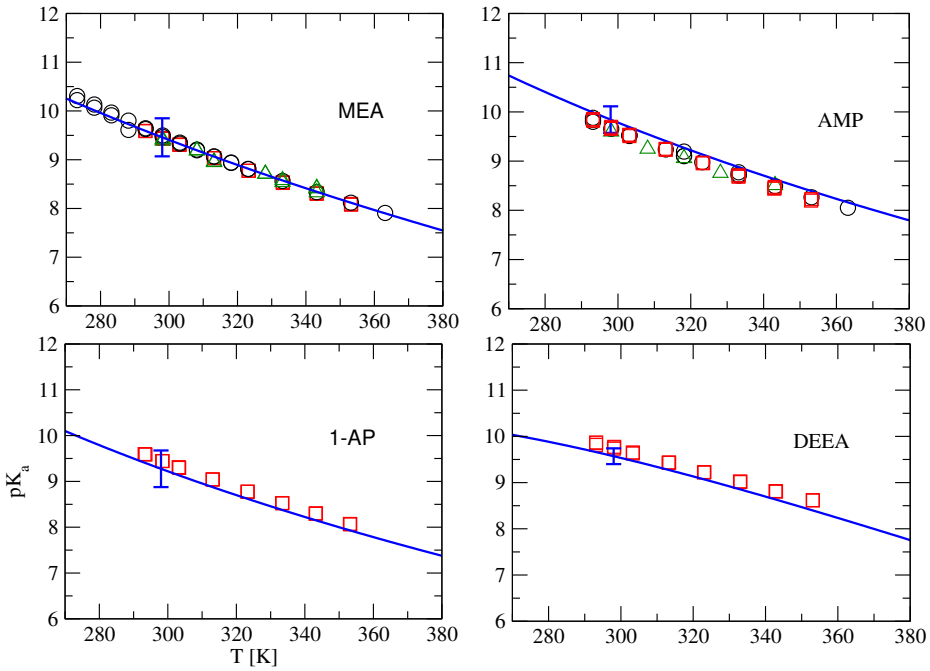


Figure 6.6: Deprotonation constants of monoethanolamine(MEA), 2-amino-2-methyl-1-propanol (AMP), 1-amino-2-propanol (1-AP) and diethylethanolamine (DEEA) as functions of temperature. Experimental data is shown by a circle[281], square[266] and triangle up[284], and the curves are our simulation results. The error bars indicate the uncertainty at 298.15 K indicated in the caption to Table 6.1.

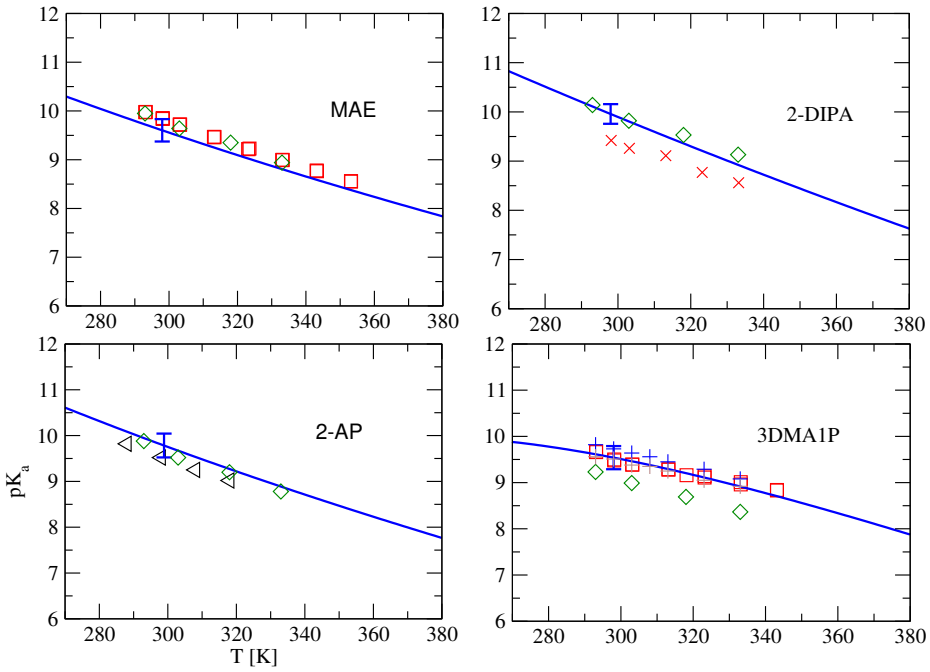


Figure 6.7: Deprotonation constants of methylaminoethanol(MAE), 2-(diisopropylamino)ethanol (2-DIPA), 2-amino-1-propanol (2-AP) and 3-dimethylamino-1-propanol (3DMA1P) as functions of temperature. Experiemental data are shown by a square[266], diamon[282], triangle left [268] plus[279] and star[280], and the curves are our simulation results. The error bar indicates the uncertainty at 298.15 K indicated in the caption to Table 6.1.

As shown in Figs. 6.8–6.9, for the molecules with multiple hydroxyl groups, namely TBAE, 2AEE, EAE, AEPD, AMPD, DEA, SAPD, the p$K_a$ simulations overestimate the experimental results. Since the ideal gas and the residual chemical potentials both contribute to the resulting p$K_a$ values, we are not able to pinpoint the source of the error, and it could be due to the well-known issue with the amine hydroxyl parameters of the GAFF and its hydration free energy prediction[286], or due to the error in the ideal gas QM prediction for species with multiple oxygen atoms, which are subjected to relatively larger uncertainty, as in the case of TEA with three hydroxyl groups.

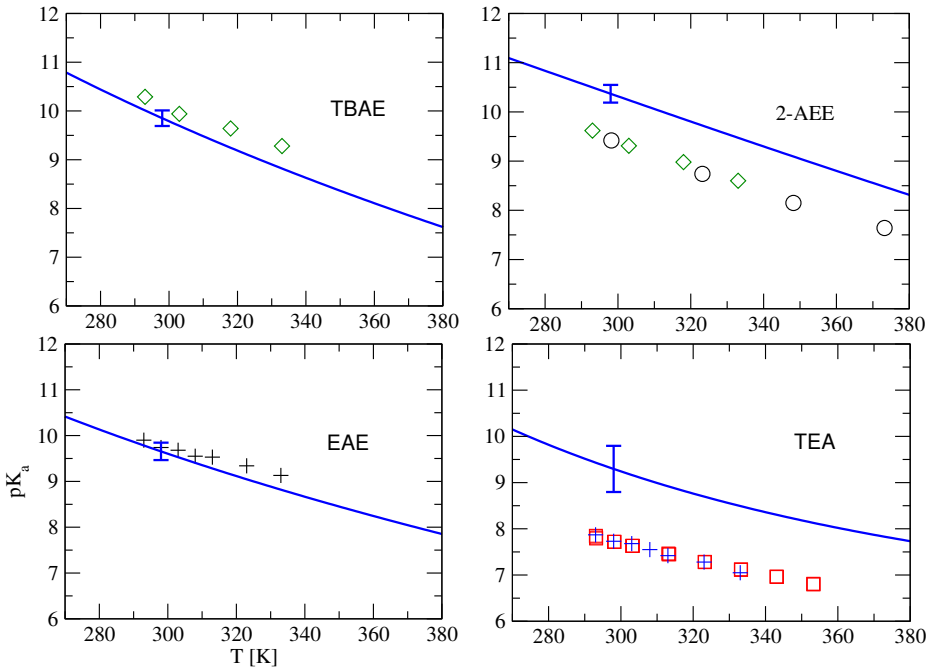


Figure 6.8: Deprotonation constant of 2-(tert-butylamino)ethanol (TBAE), 2-(2-aminoethoxy)ethanol (2-AEE),2-(ethylamino)ethanol (EAE) and triethanolamine (TEA) as function of temperature. Experimental data is shown by square[266], diamon[282], triangle left [268] plus[279] and star[280], and the curves are our simulation results. The error bar indicates the uncertainty at 298.15 K from the caption to Table 6.1.

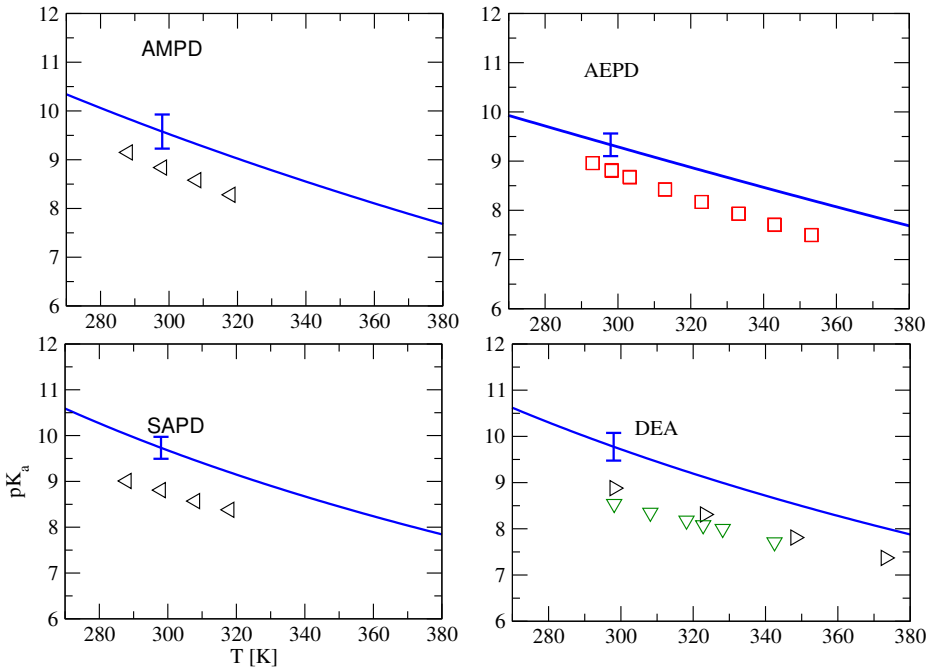


Figure 6.9: Deprotonation constant of 2-amino-2-ethyl-1,3-propanediol (AEPD), 2-amino-2-methyl-1,3-propanediol (AMPD),diethanolamine (DEA) and serinol(2-aminopropane-1,3-diol) (SAPD) as function of temperature. Experimental data is shown by square[266], diamond[282], triangle left [268] plus[279] and star[280], and the curves are our simulation results. The error bar indicates the simulation uncertainty at 298.15 K from the caption to Table 6.1.

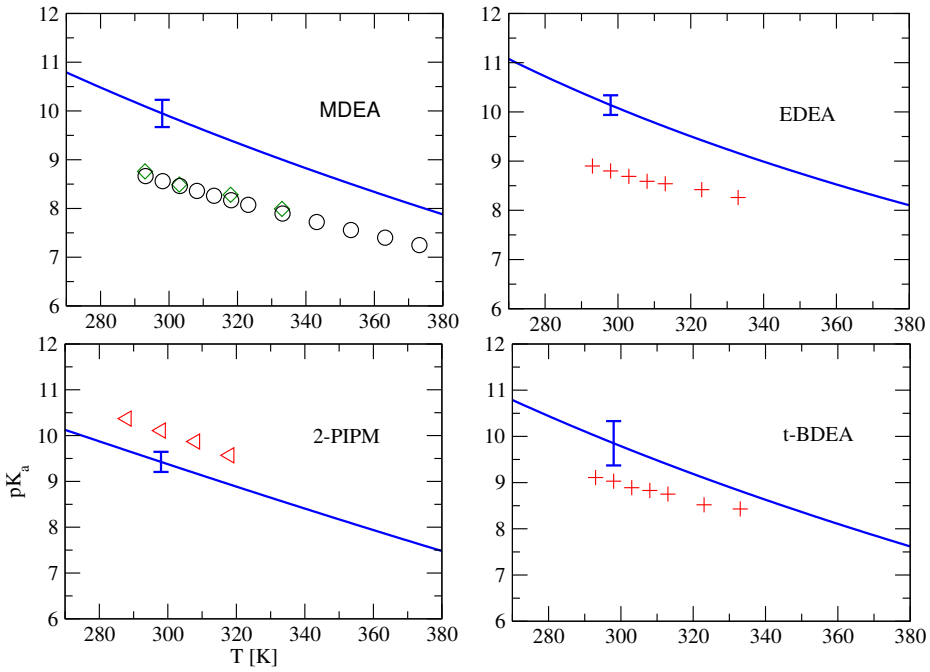


Figure 6.10: Deprotonation constant of methyldiethanolamine (MDEA), n-ethyldiethanolamine (EDEA),2-piperidinemethanol (2PIPM) and tert-butyldiethanolamine (t-BDEA) as function of temperature. Experimental data is shown by square[266], diamond[282], triangle left [268] plus[279] and star[280], and the curves are our simulation results. The error bar indicates the uncertainty at 298.15 K from the caption to Table 6.1.

The Gibbs–Helmholtz (G–H) equation relates the equilibrium constant of the reaction to its standard reaction enthalpy, via.

$$-\Delta H_j^{\dagger}(T,P) \;=\; -RT^2\left(\frac{\partial \ln K_j}{\partial T}\right) = R[-(B_j^0 + B^{\mathrm{res}}) + (C_j^0 + C_j^{\mathrm{res}})T] \qquad (6.20)$$

The coefficients of $-\ln K_j$ and $-\Delta H_j^{\dagger}(T,P)$ of the deprotonation reaction obtained from the coefficients of the ideal gas free energy function ($A_j^0$, $B_j^0$, $C_j^0$ ) and the residual free energy function ($A^{res}$, $B^{res}$, $C^{res}$) of the corresponding reaction according to Eq. (6.8) and Eq. (6.20) are given in Tables S7. The reaction enthalpy data at a typical absorption

temperature ($T = 313.15$ K) is given in Table S9.

We remark that most literature studies have measured the equilibrium constant over a narrow temperature range around $T = 298.15$ K and assumed a constant reaction enthalpy, obtained from van't Hoff–type equation of $\ln K$ against 1/T data[139]. This is only valid over the small temperature range at which experimental $\ln K$ measured and should be compared to our values at $T = 298.15$ K.

We previously have shown that the uncertainty in the IG reaction enthalpies is very similar to that of the IG reaction free energies[278], for which we used the standard deviation of the IG results from G4, G3, CBS-QB2 and CBS-APNO calculations as a surrogate uncertainty measure. The data in Table 6.1 indicate that the IG contribution to the uncertainty in the deprotonation reaction enthalpies at 298.15 K is smaller than 0.5 p$K_a$ unit ($\approx$ 2.85 kJ) in all cases. Table 6.2 compares the simulation values of the de-protonation reaction enthalpy of the amines for which there is experimental data. Due to the sensitivity of the reaction enthalpy to the $\ln K$ data (which is subject to experimental uncertainty) there is significant scatter in the experimental reaction enthalpy data, however, our simulation values are in reasonable agreement with the available experimental data.

Table 6.2: Enthalpy of deprotonation of amines ($\Delta H^{deprot}$/kJ.mol$^{-1}$) in aqueous solution at 298.15 and 313.15 K. The uncertainty in the simulation values are smaller than ≈ 2.85 kJ in all cases.

| Amine | T=298.15 K | | T=313.15 K |
|---|---|---|---|
| | This work | Literature | This work |
| MEA | 45.64 | 48.6[266] 43.0[267] 41.0[268] 50.5[287] 50.89[284] | 47.60 |
| AMP | 50.70 | 52.2[266] 46.6 [268] 40.61[267] 53.99[288] | 52.07 |
| AMPD | 44.33 | 47.2[268] 49.85[289] | 46.65 |
| AEPD | 35.81 | 47.5[266] | 38.90 |
| 3-AP | 52.92 | 53.6[266] | 53.57 |
| MAE | 40.50 | 44.4[266] | 42.97 |
| 1-AP | 46.72 | 48.8[266] | 48.11 |
| 2-AEE | 43.95 | 50.2[266] | 48.09 |
| DEA | 47.46 | 42.4[266] 37.5[268] 38.71[267] 42.4[290] | 48.54 |
| DIPA | 50.40 | 39.2[266] | 52.48 |
| 2-DIPA | 51.73 | 46.50[280] | 55.67 |
| 2-AP | 45.49 | 47.0 [268] | 48.90 |
| 3DMA1P | 25.78 | 28.07[267] 30.81[279] | 33.06 |
| EAE | 43.50 | 33.86[279] | 45.15 |
| SAPD | 47.94 | 37.8 | 48.74 |
| DEEA | 31.76 | 36.2[266] 34.22[279] | 38.25 |
| DMIPA | 34.84 | 36.99[279] | 36.56 |
| TEA | 45.40 | 31.3[266] 32.0[268] 34.0[291] 31.59[267] | -43.77 |
| MDEA | 48.70 | 34.9[266] 36.0[268] 33.37[267] | 51.11 |
| EDEA | 52.17 | 28.97[279] | 52.83 |
| TREA | 54.14 | 45.60[279] 44.4[266] | 49.16 |
| t-BDEA | 53.60 | 33.02[279] | 55.77 |
| 2-PIPM | 42.12 | 46.0[268] | 45.84 |
| 3-PIPM | 41.60 | 40.3[268] | 41.91 |
| 4-PIPM | 28.22 | 34.0[268] | 33.78 |
| 2-PIPE | 36.81 | 37.0[268]53.8 [292] | 48.08 |

### 6.4.5 Carbamate Reversion Constant, (p$K_c$)

Carbamate reversion into bicarbonate is one of the major chemical reactions involving $CO_2$ absorption occurring in primary and secondary amine based solutions. The results for the

carbamate reversion reaction p$K$ R2 (the negative of the carbamate formation reaction value) for the primary and secondary amines are summarized in Table 6.1, and compared with scarcely available experimental determinations at 298.15 K. We remark that the equilibrium constant is composition-independent quantity which may be directly predicted from simulation quantities at infinite dilution. On the other hand, this quantity cannot be directly measured experimentally, but must be obtained indirectly from concentration measurements at finite compositions $\mathbf{m}^*$, governed by

$$\ln K_j(T,P) \quad = \quad \sum_{i=1}^{N_s}[\nu_{ij}[\ln m_i^* + \ln \gamma_i(T,P;\mathbf{m}^*)] \tag{6.21}$$

which requires the use of an activity coefficient model. Unlike the case for the deprotonation reaction, it is problematic to extrapolate results obtained for the carbamate reaction using Eq. (6.21) to infinite dilution, since in $CO_2$-loaded aqueous amine solutions, the carbamate reversion reaction cannot be isolated and the bicarbonate and carbamate ions co-exist with other ions (i.e, $OH^-$ , $H_3O^+$, $CO_3^{-2}$ etc). At relatively low $CO_2$ loadings (low ionic strength), the activity coefficients of the bicarbonate and carbamate ions approach unity and at low amine weight fractions, only the activity coefficient data of binary amine/water system (at relatively low amine weight fraction, where only amine infinite dilution activity coefficients are required) along with the equilibrium composition maybe used in the Eq. (6.21) to estimate the equilibrium constant. An approximation often made for isocoulombic reactions (with ions on each side of the reaction having the same charge, which is the case for the carbamate reversion reaction) is to assume that the activity of water is unity and the activity coefficients of $RNHCO_2^-$ and $HCO_3^-$ are equal (as is the case for the Debye-Hückel; and other simple activity coefficient models). In this case, the activity coefficient terms in Eq. (6.21) cancel at all concentrations.

Another approach is to fit the experimental VLE data ($CO_2$ partial pressure and speciation data) to the parameters of a thermodynamic model for the chemical potentials to obtain the equilibrium constant. As a result of the different approximation approaches, the spread of the literature values is partly due to differences in the activity coefficient models used by the authors, and more likely due to the difficulty in the experimental NMR measurement of the concentrations of the bicarbonate ion and neutral amine species, which is difficult to distinguish from the protonated and carbonate ion in the NMR peaks. The experimental carbamate formation constant data are limited and likely subject to significant uncertainty. For example, carbamate formation constants of MEA have been measured using various experimental methodology including NaOH titration of the carbamate solution[189], fitting thermodynamic models to vapour-liquid-equilibrium (VLE)

data of $CO_2$-loaded solutions, and to $CO_2$ partial pressure data [208, 191, 293], NMR titrations[207], calorimetric studies and H-NMR Spectroscopy[154], giving values ranging from 1.31[189]-1.85[154]. We compare our predicted values with the scarcely available experimental data in Table 6.1. Given the lack of the p$K_c$ data from different measurement, based on the MEA data, we infer the uncertainty in the experimental to be $\approx$ 0.25 p$K$ unit comparable to that of the simulation data. Lack of comprehensive and accurate experimental p$K_c$ data complicates fair comparison with the simulations data. Overall, our predictions are in reasonable agreement with the available experimental data.

### 6.4.6 Effect of Structural Features on Carbamate Reversion

The effect of structural feature modifications with respect to those of MEA on the extent of carbamate formation may be explained, allowing us to identify structural factors of alkanolamine molecules that influence the $CO_2$ absorption properties. The increasing trend in the carbamate reversion constants of MEA (p$K_c$= 1.61± 0.25), 3-AP (p$K_c$= 2.07± 0.15), 4-AB (p$K_c$= 1.87± 0.35), 5AP (p$K_c$= 3.17±0.40) and 6-AH (p$K_c$= 5.35±0.36) indicates that increasing the chain length promotes carbamate formation. The addition of a -$CH_3$ and -$C_2H_5$ group on the $\beta$ carbon of MEA gives 1-AP (p$K_c$= 1.53 ±0.28) and 1AB (p$K_c$= 1.62 ±0.27) respectively, with a carbamate reversion constant similar to that of MEA, indicating that the steric effect of the $\beta$ carbon is not significant. However, addition of the same -$CH_3$, -$C_2H_5$ and -$CH_2$(OH) groups on the $\beta$ carbon of MEA gives 2-AP (p$K_c$= 0.75 ±0.15) and 2-AB (p$K_c$= 1.32 ±0.30) and SAPD (p$K_c$= 1.05 ±0.25), respectively, significantly lowering their tendency to form carbamate. AMP (p$K_c$= 0.16 ±0.21), AMPD (p$K_c$= 0.98 ±0.32) and AEPD (p$K_c$= -0.39 ±0.38) are heavily hindered derivatives of MEA, and all show little or no tendency to form carbamate as predicted by the molecular models.

The addition of various alky chain groups on the nitrogen atom of MEA gives the primary amines MAE (pK$_c$=2.42 ±0.60), EAE (p$K_c$= 1.53 ±0.32), BAE (p$K_c$= 1.54 ±0.32), IPAE (p$K_c$= 0.16 ±0.28) and TBAE (p$K_c$= -2.61 ±0.63), clearly indicating that the longer and more branched the alkane chain, the more unstable is the amine carbamate (p$K_c$ becomes more negative). Compared to EAE, EAMP (p$K_c$= -1.57±0.57) has two additional $CH_3$ groups in the $\alpha$ carbon, significantly lowering its p$K_c$.

n-CHEA (p$K_c$= -0.21±0.26), nCPEA (p$K_c$= -0.30±0.54) and nCPnEA (p$K_c$= -1.01±0.28) are obtained by a adding a six-, five- and three-membered ring structure to the amine group of MEA. They all show a negative carbamate reversion constant, indicating that the addition of the ring group makes the carbamate formation extremely unstable.

In the case of the primary alkyamines, PA (p$K_c$= 0.81 ± 0.10), BA (p$K_c$= 0.85 ±0.11), PA2 (p$K_c$= 1.01 ±0.11), IBA (p$K_c$= 1.34 ± 0.11), SBA (p$K_c$= 0.13 ±0.08), IPA (p$K_c$= -0.30± 0.10) and TBA (p$K_c$= -0.77 ± 0.66), the effect of the steric hindrance of the methyl group is in line with the decreasing p$K_c$.

For the cyclic amine 2PIPM (p$K_c$= -0.06± 0.32), 2PIPE (p$K_c$= -0.19± 0.40), due to proximity of the amino and hydroxyl group, it chemically easier to form intra-molecular hydrogen bonds, and this has been shown to reduce the stability of carbamate formation[294] by formation of stable ring structure that maximize internal hydrogen bonding , consistent with their predicted negative p$K_c$ values. This is also in agreement with the H-NMR spectroscopy measurements of Fernandes*et al.* , who did not detect carbamate formation in aqueous 2PIPM and 2PIPE. However, in case of 4PIPM (p$K_c$= 1.88 ± 0.33), the amino group is located far from the hydroxyl and results in a higher p$K_c$, in excellent agreement with the Fernandes*et al.* measured value of 1.39. Overally, we believe the molecular models employed in this work is able to predict the trend in the carbamate formation tendency of amines.

### 6.4.7 Temperature Dependence of p$K_c$ and the Carbamate Reversion Standard Reaction Enthalpy ($\Delta H^{carb}$)

Given the complications associated with the accurate experimental measurement of the carbamate reversion (inverse of carbamate formation reaction) constant, the experimental carbamate reversion enthalpy ($\Delta H^{carb}$), which obtained from the temperature derivative of its equilibrium constant, expected to have much larger errors associated with them. For example, the literature value of MEA experimental $\Delta H^{carb}$/kJ·mol$^{-1}$ obtained from Van't Hoff analysis of the equilibrium constant data over a narrow temperature range ranges from 12.84[189]kJ·mol$^{-1}$ to 29.7[192] kJ·mol$^{-1}$. Similarly for DEA, different analysis methods for the experimental measurements[192, 191, 154] give values ranging from 13.64[191] kJ·mol$^{-1}$ to 23.7[192] kJ·mol$^{-1}$. Fig.6.11 shows the temperature dependence of the MEA p$K_c$ from our simulations (red curve) and its comparison with the most recent studies of Fernandes [154](circles) and Böttinger[191](blue curve). Our predictions agree well with the experimental data from other sources[192, 295, 293] shown by different symbols. While the most literature studies assume constant ($\Delta H^{carb}$), our simulation indicate slight temperature dependency for $\Delta H^{carb}$ (change of ≈ 2.0 kJ over T change of ≈ 100 K).

The ideal gas contribution to the uncertainty of $\Delta H^{carb}$ is much larger than the deprotonation reaction($\Delta H^{deprot}$) as indicated in Table 6.1 ranging from 0.1-1.0 p$K$ unit or ≈ 0.57-5.7 kJ at T=298.15 K. The coefficients of $-\ln K_c$ and $\Delta H^{carb}$ obtained from

the coefficients of the ideal gas free energy function ($A_j^0$, $B_j^0$, $C_j^0$ ) and the residual free energy function ($A^{res}$, $B^{res}$, $C^{res}$) of the reversion reaction according to Eq. (6.8) and Eq. (6.20) are given in Tables S8 of Supplementary Information. The reaction enthalpy data at a typical absorption temperature ($T$ = 313.15 K) is given in Table S9. The $\Delta H^{carb}$ and $\Delta H^{deprot}$ data maybe used in conjunction with the readily available enthalpy data of reactions R3-R6 to estimate overall heat of $CO_2$ absorption in these amines.

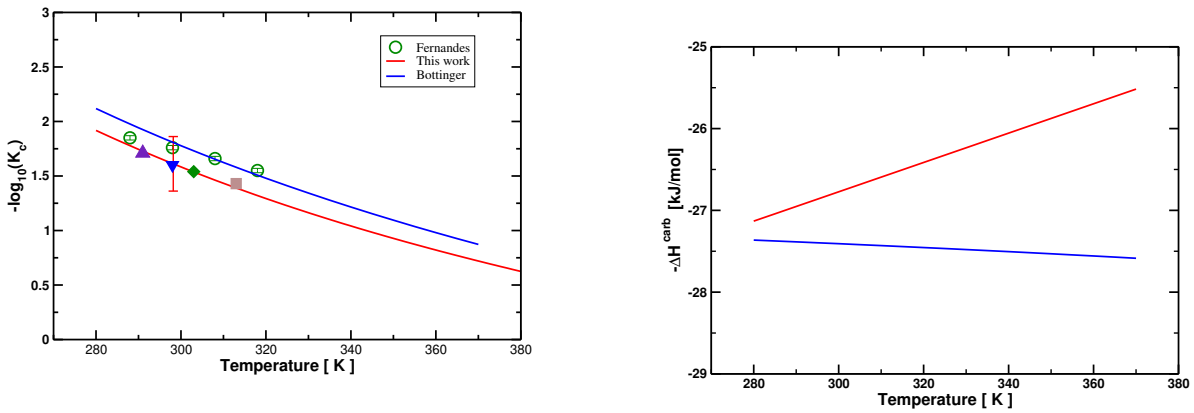


(a) (b)

Figure 6.11: (a) Comparison of the equilibrium constant of the MEA carbamate reversion reaction (R2) of this work (red curve ) with the experimental data of Bottinger [191] (blue curve), fernandes [154] (open green circles) and other symbols are from [192, 295, 293] . (b) the corresponding reaction enthalpies of carbamate reversion reaction R2.

Table 6.3: Enthalpy of carbamate reversion ($\Delta H^{carb}$/kJ·mol$^{-1}$) of amines in aqueous solution at 298.15 (subscripts indicates the uncertainty of ideal gas contribution to reaction enthalpy) and 313.15 K.

| Amine | T=298.15 K | | T=313.15 K |
|---|---|---|---|
| | This work | Literature | This work |
| MEA | $26.80_{1.40}$ | 29.7[192]18.0[154] 27.40[191] 12.84 [189] | 26.53 |
| 2-AP | $16.86_{0.85}$ | 27[154] | 17.60 |
| DEA | $14.28_{2.62}$ | 18.0[154] 13.64[191] 23.7[192] | 15.51 |

### 6.4.8 Validation of the $H_3O^+$ Force Field Using its Prediction of the Proton Hydration Free Energy

Most p$K_a$ studies in the literature are restricted to $T = 298.15$ K, where a theoretically obtained literature value for the proton hydration free energy (*e.g.*, that of Tissandier *et al.* [60]) is typically used to predict the p$K_a$. However, a classical FF for the $H_3O^+$ ion allows the prediction of this quantity over a temperature range, including the elevated temperatures of interest to carbon capture processes. Other studies have calculated p$K_a$ at $T = 298.15$ K with respect to a reference acid and then used the experimental temperature dependence of the reference acid to accomplish this task. However, the reference acid experimental data at high temperatures might not be readily available or one might want to look at different solvents, requiring reference acid temperature–dependent p$K_a$ data for each solvent.

In our study, we have developed an $H_3O^+$ force field to reproduce the well-known experimental p$K_a$ value of $9.44 \pm 0.05$ for MEA (in water solvent) at 298.15 K. This allows the calculation of the temperature dependence of its hydration free energy. We first calculated its theoretical ideal–gas deprotonation reaction free energy value of $228.21 \pm 2.24$ kJ·mol$^{-1}$ (taken as the average of CBS-QB3, G4, G3 and CBS-APNO calculations), the MEA and $MEAH^+$ AM1–BCC hydration free energy values ($-28.56 \pm 0.10$ and $-246.25 \pm -0.250$ kJ·mol$^{-1}$, respectively), and the TIP3P $H_2O$ self–solvation free energy (-26.82 $\pm$ 0.08 kJ·mol$^{-1}$). From this data, Eqs. (6.2)-(6.6) yield an $H_3O^+$ intrinsic hydration free energy of -408.84$\pm$ 2.3 kJ·mol$^{-1}$. Finally, using the TIP3P LJ parameters of water and the non-bonded parameters of Váchaet *al.* [296] for the $H_3O^+$ FF, we adjusted its oxygen partial charge to reproduce this value. The details of the resulting $H_3O^+$ FF are given in the Supplementary Information.

We validated our $H_3O^+$ FF by comparing several of its intrinsic hydration free energy with the literature results. Using the values from CBS-APNO, CBS-QB3, G3 and G4 calculations of the water basicity $-\Delta G^0_{R9}(T, P^0)$ in Eq. (6.12) (662.83, 657.76, 661.40 and 662.98 kJ·mol$^{-1}$), we obtained an average value of $\Delta G^0_{R9}(T, P^0) = -661.24 \pm 2.43$ kJ·mol$^{-1}$. This agrees well with the Hunter and Lias[256] value of -660 kJ·mol$^{-1}$ recommended by the NIST Chemistry Webbook[297], *ab initio* values of -662.74 kJ·mol$^{-1}$ obtained by Palascak and Shields[298] and a "best estimate" of -658.14 kJ·mol$^{-1}$ by Zhan and Dixon[299].

Using the TIP3P water simulation properties of density ($\rho$ = 987.562 kg·m$^{-3}$), its self-solvation free energy ($\mu^{\mathrm{res},NVT;\infty}_{H_2O}$ =-26.82$\pm$ 0.08 (which is close to the experimental value of -26.44 kJ·mol$^{-1}$ given by Camaioni[300]), and the Galvani potential value of $\xi_G$ = -48.24 kJ·mol$^{-1}$[261, 251], Eq. (6.12) gives the value $\mu^{\mathrm{res},NVT;\infty}_{H^+}(298.15\ \mathrm{K}, 1.0\ \mathrm{bar}) = -1109.38 \pm 2.43$ kJ·mol$^{-1}$ for the proton absolute hydration free energy. This agrees well

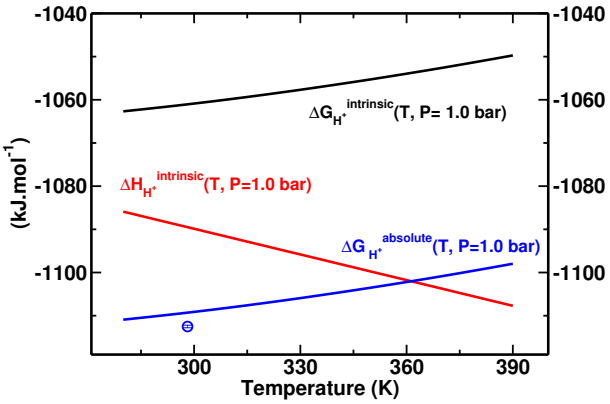


Figure 6.12: Intrinsic hydration free energy (black curve), intrinsic hydration enthalpy (red curve) and absolute hydration free energy of the proton (blue curve) as functions of temperature, assuming that that the water Galvani potential of the water is invariant with temperature. The filled blue circle indicates the value of Tissandier *et al.* [60].

with the most well–established experimental value of $-1112.5$ kJ·mol$^{-1}$ of Tissandier*et al.* [60].

Assuming that the Galvani potential is invariant with respect to temperature, Fig. 6.12 shows the intrinsic and absolute values of the proton solvation free energies and enthalpies as functions of temperature.

Table 6.4: Coefficients of the function $A + B/T + C\ln(T)$ fitted to $\Delta G^0_{R9}(T, P^0)/RT$, $\ln\left(\frac{\overline{\rho}_{\rm solv}(T,P)RT}{100P^0 M_{solv}}\right)$, $\mu^{res,\infty}_{H_2O}/RT$ , $\mu^{res,\infty}_{HCO_3^-}/RT$, $\mu^{res,\infty}_{H_3O^+}/RT$ $\mu^{res,\infty}_{H^+}/RT$ terms in Eq.6.12 .

| **molecule/ion** | **A** | **B** | **C** | $R^2$ |
|---|---|---|---|---|
| $\Delta G^0_{R9}(T, P^0)/RT$ | -235.09 | -70902.4 | 36.1984 | 0.001 |
| $\ln\left(\frac{\overline{\rho}_{\rm solv}(T,P)RT}{100P^0 M_{solv}}\right)$ | 9.85008 | -305.675 | -0.282471 | 0.008 |
| $\mu^{res,\infty}_{H_2O}/RT$ | 27.2591 | -5988.09 | -3.15944 | 0.0013 |
| $\mu^{res,\infty}_{HCO_3^-}/RT$ | -99.6984 | -48119.3 | 17.9077 | 0.0337 |
| $\mu^{res,\infty}_{H_3O^+}/RT$ | 124.002 | -59320.3 | -15.7999 | 0.0330 |
| $\mu^{res,\infty}_{H^+}/RT$ | -148.19718 | -123928.935 | 23.840411 | - |

## 6.5 Conclusions and Recommendations for Future Work

We have refined our previously developed[275] general framework for prediction of the equilibrium constants of chemical reactions in solution applied to $CO_2$–loaded aqueous amine solutions. The primary aspect of the refinement is the use of *isocoulombic* reactions to predict the deprotonation and carbamate reversion equilibrium constants and their temperature dependence; this use of such reactions is in concordance with the recent finding that such reactions enable improved estimates of the temperature trend of equilibrium constants[276].

This approach requires the development of a new $H_3O^+$ (hydronium) force field (FF) for the deprotonation reaction. We developed this FF by matching the well-known monethanolamine deprotonation equilibrium constant value at 298.15 K, which involved adjusting the GAFF oxygen atom partial charge. We are thereby able to predict the p$K_a$ of a diverse set of 77 amines at 298.15 K and all other temperatures by the appropriate combination of ideal-gas and residual chemical potential values for the deprotonation reactions. The predictions at 298.15 K show an absolute average deviation (AAD) with respect to experimental values of less than 0.72 p$K_a$ unit (our previous study[175] on 29 amines incorporating the Tissandier value of the proton hydration free energy achieved an AAD of 0.73 p$K_a$ units at 298.15 K). This is equivalent to an absolute error of $\approx$ 4 kJ in the reaction free energy at 298.15 K, which is within so-called "chemical accuracy" of 1 kcal·mol$^{-1}$.

Our approach can be viewed as a methodology for accurately "bootstrapping" knowledge of the single well-studied MEA p$K_a$ data point at 298.15 K to predict p$K_a$ data both for MEA at higher temperatures and for other amines at all temperatures, requiring only the calculation of the reaction ideal–gas values and their solvation free energies.

Whereas the predicted p$K_a$ values compare well with the experimental data, the intrinsic uncertainties in the experimental p$K_c$ determinations complicate the direct comparison of such data with simulation values. However, we showed that our simulations of p$K_c$ agree well with the scarcely available experimental data taking into account their mutual uncertainty; moreover, the molecular models are able to capture the trend in the carbamate formation and the effect of steric hindrance on the p$K_c$.

We have provided temperature–dependent functions for the protonation and carbamate formation constants of the studied amines based on our methodology. These determine the corresponding standard reaction enthalpies as functions of temperature. Based on the same approach as followed in our recent purely predictive study for a set of 7 primary amines[275], the simulation data/methodology provided here can be combined with the

readily available experimental equilibrium constant data of the $CO_2$-$H_2O$ binary system to give improved predictions for the speciation and equilibrium $CO_2$ loading of $CO_2$ in aqueous amine solutions.

In future work, equilibrium compositions calculated from our equilibrium constant predictions may be used in conjunction with the individual reaction enthalpies obtained in this work to predict both integral and differential overall heat (physical absorption + chemical reaction) of $CO_2$ absorption in the amine-water system, which is a fundamentally important quantity for solvent selection in the PCC process. For such calculations, isocoulombic reactions have the intrinsic advantage that the ionic activity coefficient contributions to the reaction free energy change cancel for simple models such as the Davies extension of the Debye-Hückel model, which become numerically equivalent to an ideal solution model.

Finally, the new $H_3O^+$ force field allows us to predict the solvation free energy of the proton, $H^+$, as a function of temperature. This provided a validation of the force field by showing that the proton solvation free energy at 298.15 K agrees well with the literature value. Furthermore, our calculations of the intrinsic proton solvation free energy can in principle be combined with temperature–dependent calculations of the Galvani potential to determine its absolute value as a function of temperature. This would enable the estimation of standard chemical potential and enthalpy data for all the ionic species considered in this study, which would be useful in the application of macroscopic thermodynamic models of aqueous solutions containing them.

# Acknowledgements

Financial support was provided by the Natural Science and Engineering Council of Canada (NSERC) and the Agence Nationale de la Recherche (ANR) through the International Collaborative Strategic program between Canada and France (Grant NSERC STPGP 479466-15 and ANR-12-IS09-0001-01). We thank our industrial partner, Dr. John Carroll, Gas Liquids Engineering Ltd., for supporting this research and for helpful advice and encouragement. Computational facilities of the SHARCNET (Shared Hierarchical Academic Research Computing Network) HPC consortium (www.sharcnet.ca) and Compute Canada (www.computecanada.ca) are gratefully acknowledged.

# Associated Content

The Supporting Information provides (1) coefficients for the temperature-dependent functions fitted to the dimensionless individual species infinite dilution chemical potentials $\frac{\mu_i^{res,\infty}}{RT}$, the protonation (R1) and carbamate formation reaction (R2) value of $\frac{\Delta G^0(T,p^0)}{RT}$, equilibrium constants, $\ln K$ and the reaction enthalpies of reactions R1 ($\Delta H^{deprot}$) and R2 ($\Delta H^{carb}$).(2) The GROMACS formatted force field parameters of all species.

# Chapter 7

# Conclusions and Recommendations

## 7.1 Summary

This research has been aimed at developing and implementing new algorithms for molecular-based simulation of chemical and phase equilibria in complex chemical systems containing electrolyte species, with particular applications to $CO_2$ reactive absorption in aqueous amine solutions. Our approach has been based on the integration of macroscopic-based principles of electrolyte thermodynamics into the simulation methodology. Although such principles are generally well-known to experimental researchers in other fields (particularly in geochemistry) involved with such systems, they are not widely appreciated or well-known within the molecular simulation community. Our papers published in high-quality scientific journals have demonstrated the success of our approach.

In the past, the principle tool for the simulation of such systems has been the Reaction Ensemble algorithm[32] and its variants, which involve molecular exchanges among species and between the phases. Despite the advances in algorithm development, such as configurational or force biased methods to speed up such simulations, the complexity and computational cost of such approaches has hindered their widespread use for complex systems of industrial importance such as those studied herein. Our goal was to propose an alternative algorithm to the REMC approach that can be straightforwardly implemented and that entails reasonable computational times for systems of any complexity. The proposed approach is particularly advantageous for systems with species present in very small concentrations, which require extremely long simulation times and/or large system sizes for conventional REMC simulation to converge. In addition, we used a standard Molecular Dynamics (MD) simulation algorithm as the underlying computational engine, utilizing its

inherent parallelization capability to further accelerate such simulations. Such parallelization is problematic for MC-based approaches.

In our first study[53] we proposed a hybrid computational approach to calculate the solute standard state chemical potential $\mu^{\dagger}(T, P)$ in the Henry-based chemical potential model, based on the combination of (1) the solute ideal-gas IG) chemical potential calculated from the IG partition function for its most stable conformer; and (2) the explicit simulation of the solute's solvation free energy. In this chemical potential model, when the solute species is present in minor concentration and/or solute-solute interactions are negligible, the ideal form of the model allows the easy calculation of the system's equilibrium composition. This is achieved by the solution of a simple set of nonlinear equations without the need for any further molecular simulation. In this publication[53], we also proposed the use of the Davies equation, a thermodynamic extension of the Debye-Hückel activity coefficient model, for ionic solutes in concentrated solution. This effectively couples the simulation quantity $\mu^{\dagger}$ with a classical thermodynamic model, thereby obviating the need for computationally expensive simulations in concentrated solutions. In the Supplementary Information section of the paper, we also derived an expression for the direct calculation of activity coefficients in the Henry-based chemical potential model by the use of molecular simulations. However, we conjecture that the accuracy of such calculations would be challenging for the conventional force fields, since they have generally been parameterized with respect to solute-water interactions rather than solute-solute interactions. We applied our approach to $CO_2$ reactive absorption in a 30 wt% aqueous solution of monoethanolamine (MEA) to predict speciation and $CO_2$ equilibrium partial pressure as functions of the solvent loading.

Our second study[175] focused on the assessment of the General Amber Force Field (GAFF) for the prediction of the protonation constant $pK_a$ of alkanolamines at 298.15 K. $pK_a$, often referred to as acid dissociation constant, is a key parameter for solvent selection for post-combustion carbon capture processes (PCC), since it correlates with the amine absorption capacity, reaction kinetics and heat of absorption. For a selection of protonated amines, we showed how the intrinsic hydration free energy obtained from MD simulations is used in conjunction with the surface potential (Galvani potential) of the solvent model (TIP3P in our case) to convert the solute's intrinsic solvation free energy to its absolute hydration free energy. This can be used with the literature value of the absolute hydration free energy of the proton, which is challenging to model classically, to calculate the protonation reaction free energy change and hence its $pK_a$. In this study, we also addressed the effects of the atomic partial charge calculations for the force field on the resulting $pK_a$ values, and showed that the fast semi-empirical AM1-BCC method charge calculation methodology outperforms the commonly used RESP approach based on

MP2-cc-pVTZ, HF/6-31G(d) and B3LYP/6-311++G(d,p) electron density calculations. We also compared our result with the widely used continuum solvent simulations using the Universal Solvation Model Based on Solute Electron Density (SMD), which incorporates multiple experimentally fitted parameters. We showed that AM1-BCC approach generally outperforms such SMD calculations. Finally, for the ideal-gas calculations, we showed that using a combination of high-level composite quantum chemical calculations using G4, G3, CBS-APNO and CBS-QB3 in tandem generally provides improved prediction of ideal-gas reaction free energy.

Our third publication[301] incorporated readily available experimental equilibrium-constant data of the binary $CO_2$-$H_2O$ system in conjunction with molecular simulation calculations of the amine protonation and carbamate formation equilibrium constanta to make improved predictions of speciation and equilibrium loading in several primary amine aqueous solvents: 2-amino-2-methylpropanol (AMP), 1-amino-2-propanol (1-AP), 2-amino-2-methyl-1,3-propanediol (AMPD), 2-aminopropane- 1,3-diol (SAPD), 2-(2-aminoethoxy) ethanol or diglycolamine (2-AEE or DGA, respectively), and 2-amino-1-propanol (2-AP). In this work, we showed that the Henry-law-based ideal solution model accurately predicts the behaviour of such systems. We showed that the accuracy of our purely predictive calculations is competitive with the typical experimental approach using complicated activity coefficient models with multiple adjustable parameters to fit experimentally obtained data.

Building on the success of the semi-emprical AM1-BCC charge methodology in our previous works, in our final work, we applied this method to the prediction of the p$K_a$ temperature dependence for a comprehensive set of 75 amines. We calculated reaction equilibrium constants for protonation and carbamate formation reactions. We also developed a force field for the hydronium ion $H_3O^+$, based on the monoethanolamine p$K_a$ value at 298.15 K, and used this to calculate the p$K_a$ values at elevated temperatures. We showed that this model can predict p$K_a$ at 298.15 K with an absolute average deviation of less than 0.72 p$K_a$, a significant improvement over commonly used SMD simulations. Furthermore, the model is able to correctly predict the p$K_a$ temperature dependence, enabling the accurate prediction of standard state reaction enthalpies, which we performed for the carbamate formation reaction for the primary and secondary amines. We also discussed the effect of different functional groups on the tendency of amines to form carbamate, an important factor influencing their $CO_2$ absorption capacity.

## 7.2 Recommendations for Future Work

The following topics are recommended for the future study:

1. **Extensions to amine blends and other solvents such as ionic liquids (ILs):**

   The methodology presented in this work is a general framework that can be applied to amine mixtures, with the goal of optimizing the weight fraction of each amine. Such mixtures offer solvent tunability in terms of their reaction kinetics and absorption capacity. Our methodology can also be used to predict the absorption capacity of reactive ionic liquids, which are considered to be promising alternative solvents for $CO_2$ capture.

2. **Force-field improvements:**

   Optimized force field parameters can potentially significantly improve the prediction of solvation free energies, which in turn can improve the prediction of the reaction equilibrium constants of interest in this work. Our research group has shown that employing the effect of molecular polarization substantially improves the prediction of such quantities[302]. It would be interesting to see how the incorporation of this approach can improve the equilibrium constants.

   Another important area is testing the new generation of partial atomic charge methods used in our research group, such as minimal basis iterative Stockholder (MBIS) and recent improvements in the AM1-BCC charge assignment method[303]. We have noted that the LJ parameters of the GAFF should be re–optimized if alternative charge methods other than the default partial charge method (i.e, AM1-BCC or HF/6-31G*) are adopted.

3. **Prediction of the overall heat duty of the $CO_2$ reactive absorption process:**

   The overall heat duty of the $CO_2$ absorption process is obtained from the heat of solution at a lower temperature such as 298 K, the heat required to raise the temperature of the $CO_2$ loaded solution to a higher temperature such as 313 K, and its heat of vaporization at the upper temperature. The individual reaction enthalpies obtained in this work may be used in conjunction with the ideal–solution model to predict these quantities.

4. **Prediction of the absolute solvation free energy and solvation enthalpy of the proton as functions of temperature in water and in other solvents:**

   Our current work has allowed the prediction of the intrinsic solvation free energy and the corresponding enthalpy of the proton in water (and potentially in other solvents) as functions of temperature for solutes in conjunction with the TIP3P water force field. Separate determination of the Galvani potential as a function of temperature would enable the calculation of the absolute solvation free energy and enthalpy of this

experimentally inaccessible quantity. Similar calculations could also be performed for other solvents.

5. **Prediction of standard state chemical potential ($\mu^\dagger$) and standard state enthalpy ($h^\dagger$) data:** The expressions provided in this thesis for $\mu^\dagger$ and $h^\dagger$ allow these quantities to be calculated for the individual species. For the ideal-gas part of the $\mu^\dagger$ expression, it requires calculation of either the atomization energy (in this case chemical potentials are expressed relative to the separated atoms of the molecule) or the formation free energy of the species (in this case the chemical potential is expressed relative to the standard state of the usual form of the constituent atoms of the species) to obtain an absolute value for the ideal gas chemical potentials $\mu_i^0(T; P^0)$ . Individual $\mu^\dagger$ and $h^\dagger$ values may thereby be tabulated and available for use in the thermodynamic modelling of systems involving these species.

# References


[1] Mai Bui, Claire S Adjiman, André Bardow, Edward J Anthony, Andy Boston, Solomon Brown, Paul S Fennell, Sabine Fuss, Amparo Galindo, Leigh A Hackett, et al. Carbon capture and storage (CCS): The way forward. Energy & Environmental Science, 11(5):1062–1176, 2018.

[2] Mark Z Jacobson. Review of solutions to global warming, air pollution, and energy security. Energy & Environmental Science, 2(2):148–173, 2009.

[3] José D Figueroa, Timothy Fout, Sean Plasynski, Howard McIlvried, and Rameshwar D Srivastava. Advances in $CO_2$ capture technology–the US Department of Energy's Carbon Sequestration Program. International Journal of Greenhouse Gas Control, 2(1):9–20, 2008.

[4] B Metz, O Davidson, H de Coninck, M Loos, and L Meyer. IPCC (Intergovernmental Panel on Climate Change) special report on carbon dioxide capture and storage. 2005.

[5] Deanna M D'Alessandro, Berend Smit, and Jeffrey R Long. Carbon dioxide capture: prospects for new materials. Angewandte Chemie International Edition, 49(35):6058–6082, 2010.

[6] Bingyun Li, Yuhua Duan, David Luebke, and Bryan Morreale. Advances in $CO_2$ capture technology: A patent review. Applied Energy, 102:1439–1447, 2013.

[7] Noorlisa Harun, Thanita Nittaya, Peter L Douglas, Eric Croiset, and Luis A Ricardez-Sandoval. Dynamic simulation of MEA absorption process for $CO_2$ capture from power plants. International Journal of Greenhouse Gas Control, 10:295–309, 2012.

[8] Thanita Nittaya, Peter L Douglas, Eric Croiset, and Luis A Ricardez-Sandoval. Dynamic modelling and control of MEA absorption processes for $CO_2$ capture from power plants. Fuel, 116:672–691, 2014.

[9] Xavier Rozanska, Erich Wimmer, and Frédérick de Meyer. Quantitative kinetic model of $CO_2$ absorption in aqueous tertiary amine solvents. Journal of Chemical Information and Modeling, 61(4):1814–1824, 2021.

[10] Graeme Puxty, Robert Rowland, Andrew Allport, Qi Yang, Mark Bown, Robert Burns, Marcel Maeder, and Moetaz Attalla. Carbon dioxide post–combustion capture: A novel screening study of the carbon dioxide absorption performance of 76 amines. Environmental Science & Technology, 43(16):6427–6433, 2009.

[11] Meihong Wang, Adekola Lawal, Peter Stephenson, J Sidders, and C Ramshaw. Post-combustion $CO_2$ capture with chemical absorption: A state-of-the-art review. Chemical Engineering Research and Design, 89(9):1609–1624, 2011.

[12] Chao Chen, Jun Kim, and Wha-Seung Ahn. $CO_2$ capture by amine-functionalized nanoporous materials: A review. Korean Journal of Chemical Engineering, 31(11):1919–1934, 2014.

[13] Adisorn Aroonwilas and Amornvadee Veawab. Integration of $CO_2$ capture unit using single-and blended-amines into supercritical coal-fired power plants: Implications for emission and energy management. International Journal of Greenhouse Gas Control, 1(2):143–150, 2007.

[14] Takuya Hirata, Hiromitsu Nagayasu, Takahito Yonekawa, Masayuki Inui, Takashi Kamijo, Yasuo Kubota, Tatsuya Tsujiuchi, Daisuke Shimada, Todd Wall, and Jerrad Thomas. Current status of MHI $CO_2$ capture plant technology, 500 TPD CCS demonstration of test results and reliable technologies applied to coal fired flue gas. Energy Procedia, 63:6120–6128, 2014.

[15] Koji Kadono, Asao Suzuki, Masaki Iijima, Tsuyoshi Ohishi, Hiroshi Tanaka, Takuya Hirata, and Masami Kondo. New energy efficient processes and newly developed absorbents for flue gas $CO_2$ capture. Energy Procedia, 37:1785–1792, 2013.

[16] Guido Sartori and David W. Savage. Sterically hindered amines for carbon dioxide removal from gases. Industrial & Engineering Chemistry Fundamentals, 22(2):239–249, 1983.

[17] Yuting Tan, Worrada Nookuea, Hailong Li, Eva Thorin, and Jinyue Yan. Property impacts on carbon capture and storage (CCS) processes: A review. Energy Conversion and Management, 118:204–222, 2016.

[18] Joan F Brennecke and Edward J Maginn. Ionic liquids: Innovative fluids for chemical processing. AIChE Journal, 47(11):2384–2389, 2001.

[19] Darinel Valencia-Marquez, Antonio Flores-Tlacuahuac, and Luis Ricardez-Sandoval. A controllability analysis of a pilot-scale $CO_2$ capture plant using ionic liquids. AIChE Journal, 62(9):3298–3309, 2016.

[20] Congmin Wang, Xiaoyan Luo, Huimin Luo, De-en Jiang, Haoran Li, and Sheng Dai. Tuning the basicity of ionic liquids for equimolar $CO_2$ capture. Angewandte Chemie, 123(21):5020–5024, 2011.

[21] Alireza Shariati and Cor J Peters. High-pressure phase behavior of systems with ionic liquids: Measurements and modeling of the binary system fluoroform+ 1-ethyl-3-methylimidazolium hexafluorophosphate. The Journal of Supercritical Fluids, 25(2):109–117, 2003.

[22] Luís MC Pereira and Lourdes F Vega. A systematic approach for the thermodynamic modelling of $CO_2$-amine absorption process using molecular-based models. Applied Energy, 232:273–291, 2018.

[23] Luís MC Pereira, Fèlix Llovell, and Lourdes F Vega. Thermodynamic characterisation of aqueous alkanolamine and amine solutions for acid gas processing by transferable molecular models. Applied Energy, 222:687–703, 2018.

[24] Edward J Maginn. From discovery to data: What must happen for molecular simulation to become a mainstream chemical engineering tool. AIChE Journal, 55(6):1304–1310, 2009.

[25] Berk Hess, Carsten Kutzner, David Van Der Spoel, and Erik Lindahl. GROMACS 4: Algorithms for highly efficient, load-balanced, and scalable molecular simulation. Journal of Chemical Theory and Computation, 4(3):435–447, 2008.

[26] Adri CT Van Duin, Siddharth Dasgupta, Francois Lorant, and William A Goddard. ReaxFF: A reactive force field for hydrocarbons. The Journal of Physical Chemistry A, 105(41):9396–9409, 2001.

[27] Niko Prasetyo and Thomas S Hofer. Structure, dynamics, and hydration free energy of carbon dioxide in aqueous solution: A quantum mechanical/molecular mechanics molecular dynamics thermodynamic integration (QM/MM MD TI) simulation study. Journal of Chemical Theory and Computation, 14(12):6472–6483, 2018.

[28] Marcus G Martin and J Ilja Siepmann. Transferable potentials for phase equilibria. 1. United-atom description of n-alkanes. The Journal of Physical Chemistry B, 102(14):2569–2577, 1998.

[29] Sayee Prasaad Balaji, Satesh Gangarapu, Mahinder Ramdin, Ariana Torres-Knoop, Han Zuilhof, Earl LV Goetheer, David Dubbeldam, and Thijs JH Vlugt. Simulating the reactions of $CO_2$ in aqueous monoethanolamine solution by Reaction Ensemble Monte Carlo using the Continuous Fractional Compontent method. Journal of Chemical Theory and Computation, 11(6):2661–2669, 2015.

[30] Ryan Gotchy Mullen, Steven A Corcelli, and Edward J Maginn. Reaction Ensemble Monte Carlo simulations of $CO_2$ absorption in the reactive ionic liquid triethyl (octyl) phosphonium 2-cyanopyrrolide. The Journal of Physical Chemistry Letters, 9(18):5213–5218, 2018.

[31] Q. R. Sheridan, R. G. Mullen, T. B. Lee, E. J. Maginn, and W. F. Schneider. Hybrid computational strategy for predicting $CO_2$ solubilities in reactive ionic liquids. The Journal of Physical Chemistry C, 122:14213–14221, 2018.

[32] W. R. Smith and B. Tríska. The Reaction Ensemble method for the computer simulation of chemical and phase equilibria. I. Theory and basic examples. The Journal of Chemical Physics., 100(4):3019–3027, 1994.

[33] Thomas W Rosch and Edward J Maginn. Reaction Ensemble Monte Carlo simulation of complex molecular systems. Journal of Chemical Theory and Computation, 7(2):269–279, 2011.

[34] Hongjun Liu, Sheng Dai, and De-en Jiang. Solubility of gases in a common ionic liquid from molecular dynamics based free energy calculations. The Journal of Physical Chemistry B, 118(10):2719–2725, 2014.

[35] Erik E Santiso and Keith E Gubbins. Multi-scale molecular modeling of chemical reactivity. Molecular Simulation, 30(11-12):699–748, 2004.

[36] J Karl Johnson, Athanassios Z Panagiotopoulos, and Keith E Gubbins. Reactive canonical Monte Carlo: A new simulation technique for reacting or associating fluids. Molecular Physics, 81(3):717–733, 1994.

[37] E. E. Santiso and K. E. Gubbins. Multi-scale molecular modeling of chemical reactivity. Molecular Simulation, 30(11-12):699–748, 2004.

[38] Niels Hansen, Sven Jakobtorweihen, and Frerich J Keil. Reactive Monte Carlo and grand-canonical Monte Carlo simulations of the propene metathesis reaction system. The Journal of Chemical Physics, 122(16):164705, 2005.

[39] Martin Lísal, John K Brennan, and William R Smith. Mesoscale simulation of polymer reaction equilibrium: Combining dissipative particle dynamics with Reaction Ensemble Monte Carlo. II. Supramolecular diblock copolymers. The Journal of Chemical Physics, 130(10):104902, 2009.

[40] Martin Lísal, John K Brennan, and William R Smith. Mesoscale simulation of polymer reaction equilibrium: Combining dissipative particle dynamics with Reaction Ensemble Monte Carlo. I. Polydispersed polymer systems. The Journal of Chemical Physics, 125(16):164905, 2006.

[41] Martin Lısal, Ivo Nezbeda, and William R Smith. The Reaction Ensemble method for the computer simulation of chemical and phase equilibria. II. The $Br_2$ + $Cl_2$+ BrCl system. The Journal of Chemical Physics, 110(17):8597–8604, 1999.

[42] Ryan Gotchy Mullen and Edward J Maginn. Reaction Ensemble Monte Carlo simulation of xylene isomerization in bulk phases and under confinement. Journal of Chemical Theory and Computation, 13(9):4054–4062, 2017.

[43] Ali Poursaeidesfahani, Remco Hens, Ahmadreza Rahbari, Mahinder Ramdin, David Dubbeldam, and Thijs JH Vlugt. Efficient application of Continuous Fractional Compontent Monte Carlo in the Reaction Ensemble. Journal of Chemical Theory and Computation, 13(9):4452–4466, 2017.

[44] William R. Smith and Weikai Qi. Molecular simulation of chemical reaction equilibrium by computationally efficient free energy minimization. ACS Central Science, 4:1185–1193, 2018.

[45] John K Brennan, Martin Lísal, Keith E Gubbins, and Betsy M Rice. Reaction Ensemble molecular dynamics: Direct simulation of the dynamic equilibrium properties of chemically reacting mixtures. Physical Review E, 70(6):061103, 2004.

[46] C Heath Turner, J Karl Johnson, and Keith E Gubbins. Effect of confinement on chemical reaction equilibria: The reactions $2NO \leftrightarrow (NO)_2$ and $N_2+3H_2 \leftrightarrow 2NH_3$ in carbon micropores. The Journal of Chemical Physics, 114(4):1851–1859, 2001.

[47] Martin Lísal, Paolo Cosoli, William R Smith, Surendra K Jain, and Keith E Gubbins. Molecular-level simulations of chemical reaction equilibrium for nitric oxide

dimerization reaction in disordered nanoporous carbons. Fluid Phase Equilibria, 272(1-2):18–31, 2008.

[48] Evgenii O Fetisov, I-Feng William Kuo, Chris Knight, Joost VandeVondele, Troy Van Voorhis, and J Ilja Siepmann. First-principles Monte Carlo simulations of reaction equilibria in compressed vapors. ACS Central Science, 2(6):409–415, 2016.

[49] Chao Wu, Thomas P Senftle, and William F Schneider. First-principles-guided design of ionic liquids for $CO_2$ capture. Physical Chemistry Chemical Physics, 14(38):13163–13170, 2012.

[50] Congmin Wang, Huimin Luo, Haoran Li, Xiang Zhu, Bo Yu, and Sheng Dai. Tuning the physicochemical properties of diverse phenolic ionic liquids for equimolar $CO_2$ capture by the substituent on the anion. Chemistry–A European Journal, 18(7):2153–2160, 2012.

[51] Mahinder Ramdin, Sayee Prasaad Balaji, José Manuel Vicent-Luna, Ariana Torres-Knoop, Qu Chen, David Dubbeldam, Sofía Calero, Theo W de Loos, and Thijs JH Vlugt. Computing bubble-points of $CO_2/CH_4$ gas mixtures in ionic liquids from Monte Carlo simulations. Fluid Phase Equilibria, 418:100–107, 2016.

[52] Quintin R Sheridan, Ryan G Mullen, Tae Bum Lee, Edward J Maginn, and William F Schneider. Hybrid computational strategy for predicting $CO_2$ solubilities in reactive ionic liquids. The Journal of Physical Chemistry C, 122(25):14213–14221, 2018.

[53] Javad Noroozi and William R Smith. An efficient molecular simulation methodology for chemical reaction equilibria in electrolyte solutions: Application to $CO_2$ reactive absorption. Journal of Physical Chemistry A, 123(18):4074–4086, 2019.

[54] Bo Han, Chenggang Zhou, Jinping Wu, Daniel J Tempel, and Hansong Cheng. Understanding $CO_2$ capture mechanisms in aqueous monoethanolamine via first principles simulations. The Journal of Physical Chemistry Letters, 2(6):522–526, 2011.

[55] Xin Yang, Robert J Rees, William Conway, Graeme Puxty, Qi Yang, and David A Winkler. Computational modeling and simulation of $CO_2$ capture by aqueous amines. Chemical reviews, 117(14):9524–9593, 2017.

[56] Ciro A Guido, Fabio Pietrucci, Gregoire A Gallet, and Wanda Andreoni. The fate of a zwitterion in water from ab initio molecular dynamics: Monoethanolamine (MEA)-$CO_2$. Journal of Chemical Theory and Computation, 9(1):28–32, 2012.

[57] Mayuri Gupta, Eirik F da Silva, and Hallvard F Svendsen. Explicit solvation shell model and continuum solvation models for solvation energy and $pK_a$ determination of amino acids. Journal of Chemical Theory & Computation, 9(11):5021–5037, 2013.

[58] Mayuri Gupta, Eirik F da Silva, and Hallvard F Svendsen. Modeling temperature dependency of amine basicity using PCM and SM8T implicit solvation models. Journal of Physical Chemistry B, 116(6):1865–1875, 2012.

[59] Mayuri Gupta, Eirik F da Silva, Ardi Hartono, and Hallvard F Svendsen. Theoretical study of differential enthalpy of absorption of $CO_2$ with MEA and MDEA as a function of temperature. The Journal of Physical Chemistry B, 117(32):9457–9468, 2013.

[60] M. D. Tissandier, K. A. Cowen, W. Y. Feng, E. Gundlach, M. H. Cohen, A. D. Earhart, J. V. Coe, and T. R. Tuttle. The proton's absolute aqueous enthalpy and Gibbs Free Energy of solvation from cluster–ion solvation data. Journal of Physical Chemistry A, 102(40):7787–7794, 1998.

[61] Donald A. McQuarrie. Statistical Mechanics. University Science Books, Sausalito, California, 2000.

[62] Daan Frenkel and Berend Smit. Understanding Molecular Simulation: From Algorithms to Applications. Volume 1, Elsevier, 2001.

[63] Michael P Allen and Dominic J Tildesley. Computer Simulation of Liquids. Oxford University Press, 2017.

[64] Dennis C Rapaport and Dennis C Rapaport Rapaport. The Art of Molecular Dynamics Simulation. Cambridge University Press, 2004.

[65] Christopher I Bayly, Piotr Cieplak, Wendy Cornell, and Peter A Kollman. A well-behaved electrostatic potential based method using charge restraints for deriving atomic charges: The RESP model. The Journal of Physical Chemistry, 97(40):10269–10280, 1993.

[66] Eirik F da Silva, Tatyana Kuznetsova, Bjørn Kvamme, and Kenneth M Merz. Molecular dynamics study of ethanolamine as a pure liquid and in aqueous solution. The Journal of Physical Chemistry B, 111(14):3695–3703, 2007.

[67] Junmei Wang, Romain M Wolf, James W Caldwell, Peter A Kollman, and David A Case. Development and testing of a General Amber Force Field. Journal of Computational Chemistry, 25(9):1157–1174, 2004.

[68] Kenno Vanommeslaeghe, Elizabeth Hatcher, Chayan Acharya, Sibsankar Kundu, Shijun Zhong, Jihyun Shim, Eva Darian, Olgun Guvench, P Lopes, Igor Vorobyov, et al. CHARMM general force field: A force field for drug-like molecules compatible with the CHARMM all-atom additive biological force fields. Journal of Computational Chemistry, 31(4):671–690, 2010.

[69] Chris Oostenbrink, Alessandra Villa, Alan E Mark, and Wilfred F Van Gunsteren. A biomolecular force field based on the free enthalpy of hydration and solvation: the GROMOS force-field parameter sets 53A5 and 53A6. Journal of Computational Chemistry, 25(13):1656–1676, 2004.

[70] Stephen L Mayo, Barry D Olafson, and William A Goddard. Dreiding: A generic force field for molecular simulations. Journal of Physical Chemistry, 94(26):8897–8909, 1990.

[71] Filip Moučka, Ivo Nezbeda, and William R Smith. Computationally efficient Monte Carlo simulations for polarisable models: Multi-particle move method for water and aqueous electrolytes. Molecular Simulation, 39(14-15):1125–1134, 2013.

[72] Jörn Ilja Siepmann and Daan Frenkel. Configurational Bias Monte Carlo: a new sampling scheme for flexible chains. Molecular Physics, 75(1):59–70, 1992.

[73] Younes Nejahi, Mohammad Soroush Barhaghi, Jason Mick, Brock Jackman, Kamel Rushaidat, Yuanzhe Li, Loren Schwiebert, and Jeffrey Potoff. GOMC: GPU optimized Monte Carlo for the simulation of phase equilibria and physical properties of complex fluids. SoftwareX, 9:20–27, 2019.

[74] Jindal K Shah, Eliseo Marin-Rimoldi, Ryan Gotchy Mullen, Brian P Keene, Sandip Khan, Andrew S Paluch, Neeraj Rai, Lucienne L Romanielo, Thomas W Rosch, Brian Yoo, et al. Cassandra: An open source Monte Carlo package for molecular simulation. Journal of Computational Chemistry, 38(19):1727–1739, 2017.

[75] John M Prausnitz, Rudiger N Lichtenthaler, and Edmundo Gomes de Azevedo. Molecular Thermodynamics of Fluid-Phase Equilibria. Pearson Education, 1998.

[76] Donald Allan McQuarrie and John D Simon. Molecular Thermodynamics. Volume 63, University Science Books Sausalito, CA, 1999.

[77] G.N. Lewis and M. Randall. Thermodynamics and the Free Energy of Chemical Substances. McGraw-Hill, 1923.

[78] D. D. Wagman, W. H. Evans, V. B. Parker, R. H. Schumm, I. Halow, S. M. Bailey, K. L. Churney, and R. L. Nuttall. The NBS tables of chemical thermodynamic properties: Selected values for inorganic and $C_1$ and $C_2$ organic substances in SI units. Journal of Physical & Chemical Reference Data, 11(Supplement No. 2), 1982.

[79] M.W Chase, Jr. L Curnutt, A.T Hu, H Prophet, A.N Syverud, and L.C Walker. JANAF thermochemical tables, 1974 supplement. Journal of Physical and Chemical Reference Data, 3(2):311–480, 1974.

[80] R. A. Robinson and R. H. Stokes. Electrolyte Solutions. Dover Publications, New York, 2002.

[81] G. M. Kontogeorgis, B. Maribo-Mogensen, and K. Thomsen. The Debye-Hückel theory and its importance in modeling electrolyte solutions. Fluid Phase Equilibria, 462:130–152, 2018.

[82] A. C. Kumoro, A. Raksajati, M. Ho, D. Wiley, Hadiyanto, S. A. Roces, L. Yung, X. Rong, A. W. Lothongkum, M. T. Phong, M. A. Hussain, W. R. W. Daud, and P. T. S. Nam. Solvent development for post-combustion $CO_2$ capture: Recent development and opportunities. MATEC Web of Conferences, 156:03015, 2018.

[83] C. Song, Q. Liu, N. Ji, S. Deng, J. Zhao, Y. Li, Y. Song, and H. Li. Alternative pathways for efficient $CO_2$ capture by hybrid processes—a review. Renewable and Sustainable Energy Reviews, 82:215–231, 2018.

[84] F. Y. Jou, A. E. Mather, and F. D. Otto. The solubility of $CO_2$ in a 30 mass percent monoethanolamine solution. Canadian Journal of Chemical Engineering, 73:140–147, 1995.

[85] J. Gabrielsen, M. L. Michelsen, E. H. Stenby, and G. M. Kontogeorgis. A model for estimating $CO_2$ solubility in aqueous alkanolamines. Industrial & Engineering Chemistry Research, 44:3348–3354, 2005.

[86] J. P. Jakobsen, J. Krane, and H. F. Svendsen. Liquid–phase composition determination in $CO_2$–$H_2O$–alkanolamine systems: An NMR study. Industrial & Engineering Chemistry Research, 44(26):9894–9903, 2005.

[87] W. Böttinger, M. Maiwald, and H. Hasse. Online NMR spectroscopic study of species distribution in MEA–$H_2O$–$CO_2$ and DEA–$H_2O$–$CO_2$. Fluid Phase Equilibria, 263(2):131–143, 2008.

[88] M. D. Hilliard. A Predictive Thermodynamic Model for an Aqueous Blend of Potassium Carbonate, Piperazine, and Monoethanolamine for Carbon Dioxide Capture from Flue Gas. PhD Thesis, Un. of Texas Austin, 2008.

[89] H. Arcis, K. Ballerat-Busserolles, L. Rodier, and J. Y. Coxam. Enthalpy of solution of carbon dioxide in aqueous solutions of monoethanolamine at temperatures of 322.5 K and 372.9 K and pressures up to 5 MPa. Journal of Chemical Engineering Data, 56(8):3351–3362, 2011.

[90] N. S. Matin, J. E. Remias, J. K. Neathery, and K. Liu. Facile method for determination of amine speciation in $CO_2$ capture solutions. Industrial & Engineering Chemistry Research, 51(19):6613–6618, 2012.

[91] G. Puxty and M. Maeder. A simple chemical model to represent $CO_2$–amine–$H_2O$ vapour–liquid–equilibria. International Journal of Greenhouse Gas Control, 17:215–224, 2013.

[92] H. Arcis, Y. Coulier, K. Ballerat-Busserolles, L. Rodier, and J.-Y. Coxam. Enthalpy of solution of $CO_2$ in aqueous solutions of primary alkanolamines: A comparative study of hindered and nonhindered amine-based solvents. Industrial & Engineering Chemistry Research, 53:10876–10885, 2014.

[93] J. O. Lloret, L. F. Vega, and F. Llovell. A consistent and transferable thermodynamic model to accurately describe $CO_2$ capture with monoethanolamine. Journal of $CO_2$ Utilization, 21:521–533, 2017.

[94] A. Plakia, G. Pappa, and E. Voutsas. Modeling of $CO_2$ solubility in aqueous alkanolamine solutions with an extended UMR-PRU model. Fluid Phase Equilibria, 478:134–144, 2018.

[95] L. J. du Preez, N. Motang, L. H. Callanan, and A. J. Burger. Determining the liquid phase equilibrium speciation of the $CO_2$–MEA–$H_2O$ system using a simplified in situ fourier transform infrared method. Industrial & Engineering Chemistry Research, 58:469–478, 2019.

[96] M. Gupta, E. F. da Silva, and H. F. Svendsen. Computational study of equilibrium constants for amines and amino acids for $CO_2$ capture solvents. Energy Procedia, 37:1720–1727, 2013.

[97] Kei Teranishi, Atsushi Ishikawa, Hiroshi Sato, and Hiromi Nakai. Systematic investigation of the thermodynamic properties of amine solvents for $CO_2$ chemical

absorption using the cluster-continuum model. Bulletin of the Chemical Society of Japan, 90(4):451–460, 2017.

[98] Karl. J Johnson, Z. Panagiotopoulos, A., and Keith E. Gubbins. A new simulation technique for reacting or associating fluids. Molecular Physics, 81(3):717–733, 1994.

[99] C Heath. Turner, John K. Brennan, Martin Lísal, William R. Smith, J. Karl Johnson, and Keith E. Gubbins. Simulation of chemical reaction equilibria by the Reaction Ensemble Monte Carlo method: A review. Molecular Simulation, 34(2):119–146, 2008.

[100] M. Lísal, W. R. Smith, M. Bureš, V. Vacek, and J. Navrátil. REMC computer simulations of the thermodynamic properties of argon and air plasmas. Molecular Physics, 100(15):2487–2497, 2002.

[101] M. Tuttafesta, A. D'Angola, A. Laricchiuta, P. Minelli, M. Capitelli, and G. Colonna. GPU and multi–core based Reaction Ensemble Monte Carlo method for non-ideal thermodynamic systems. Computer Physics Communications, 185(2):540–549, 2014.

[102] R. G. Mullen, S. A. Corcelli, and E. J. Maginn. Reaction Ensemble Monte Carlo simulations of $CO_2$ absorption in the reactive ionic liquid triethyl(octyl)phosphonium 2-cyanopyrrolide. The Journal of Physical Chemistry Letters, 9:5213–5218, 2018.

[103] S. P. Balaji, S. Gangarapu, M. Ramdin, A. Torres-Knoop, H. Zuilhof, E. L. Goetheer, D. Dubbeldam, and T. J. Vlugt. Simulating the reactions of $CO_2$ in aqueous monoethanolamine solution by Reaction Ensemble Monte Carlo using the Continuous Fractional Compontent method. Journal of Chemical Theory & Computation, 11(6):2661–2669, 2015.

[104] W. Shi and E. J. Maginn. Improvement in molecule exchange efficiency in Gibbs ensemble Monte Carlo: Development and implementation of the Continuous Fractional Compontent move. Journal of Computational Chemistry, 29(15):2520–2530, 2008.

[105] T. W. Rosch and E. J. Maginn. Reaction Ensemble Monte Carlo simulation of complex molecular systems. Journal of Chemical Theory & Computation, 7(2):269–279, 2011.

[106] A. Poursaeidesfahani, R. Hens, A. Rahbari, M. Ramdin, D. Dubbeldam, and T. J. H. Vlugt. Efficient application of Continuous Fractional Compontent Monte Carlo in the Reaction Ensemble. Journal of Chemical Theory & Computation, 13:4452–4466, 2017.

[107] C. W. Davies. The extent of dissociation of salts in water. Part VIII. An equation for the mean ionic activity coefficient of an electrolyte in water, and a revision of the dissociation constants of some sulphates. Journal of the Chemical Society, pages 2093–2098, 1938.

[108] J. C. Morgan, A. S. Chinen, B. Omell, D. Bhattacharyya, C. Tong, and D. C. Miller. Thermodynamic modeling and uncertainty quantification of $CO_2$–loaded aqueous MEA solutions. Chemical Engineering Science, 168:309–324, 2017.

[109] William R. Smith and Ronald W. Missen. Sensitivity analysis in ChE education. Part 1. Introduction and Application to explicit models. Journal of Chemical Engineering Education, 37(2):222–227, 2003.

[110] William R. Smith and Ronald W. Missen. Sensitivity analysis in ChE education. Part 2. Application to implict models. Journal of Chemical Engineering Education, 37(3):254–260, 2003.

[111] W. R. Smith and R. W. Missen. Chemical Reaction Equilibrium Analysis: Theory and Algorithms. Krieger Publishing Co.; Reprint of same title, Willey-Interscience, 1982, Malabar, Florida, 1991.

[112] W. J. Hamer and Y.-C. Wu. Osmotic coefficients and mean activity coefficients of uni-univalent electrolytes in water at 25° C. The Journal of Physical Chemistry Ref. Data, 1(4), 1972.

[113] W. R. Smith, I. Nezbeda, J. Kolafa, and F. Moučka. Recent progress in the molecular simulation of thermodynamic properties of aqueous electrolyte solutions. Fluid Phase Equilibria, 466:19–30, 2018.

[114] Ivo Nezbeda, Filip Moučka, and William R. Smith. Recent progress in molecular simulation of aqueous electrolytes: force fields, chemical potentials and solubility. Molecular Physics, 114(11):1665–1690, 2016.

[115] H. Zhang, Y. Jiang, H. Yan, C. Yin, T. Tan, and D. van der Spoel. Free-energy calculations of ionic hydration consistent with the experimental hydration free energy of the proton. The Journal of Physical Chemistry Letters, 8(12):2705–2712, 2017.

[116] T. S. Hofer and P. H. Hünenberger. Absolute proton hydration free energy, surface potential of water, and redox potential of the hydrogen electrode from first principles: QM/MM MD free-energy simulations of sodium and potassium hydration. The Journal of Chemical Physics, 148(22):222814, 2018.

[117] F. Y. Lin, P. E. Lopes, E. D. Harder, B. Roux, and A. D. MacKerell. Polarizable force field for molecular ions based on the classical Drude oscillator. Journal of Chemical Information & Modeling, 2018.

[118] V. Majer, J. Sedlbauer, and R. H. Wood. Calculation of Standard Thermodynamic Properties of Aqueous Electrolytes and Nonelectrolytes, book section 4. Elsevier Academic Press, Amsterdam, 2004.

[119] D. A. Perlman, D. A. Case, J. W. Caldwell, W. S. Ross, T. E. Cheatham III, S. DeBolt, D. ferguson, G. Seibel, and P. Kollman. Amber, a package of computer programs for applying molecular mechanics, normal mode analysis, molecular dynamics and free energy calculations to simulate the structural and energetic properties of molecules. Computer Physics Communications, 91:1–41, 1995.

[120] Y. Zhang, Y. Zhang, M. J. McCready, and E. J. Maginn. Evaluation and refinement of the General Amber Force Field for nineteen pure organic electrolyte solvents. Journal of Chemical Engineering Data, 63:3488–3502, 2018.

[121] M. J. Frisch, G. W. Trucks, H. B. Schlegel, G. E. Scuseria, M. A. Robb, J. R. Cheeseman, G. Scalmani, V. Barone, B. Mennucci, G. A. Petersson, H. Nakatsuji, M. Caricato, X. Li, H. P. Hratchian, A. F. Izmaylov, J. Bloino, G. Zheng, J. L. Sonnenberg, M. Hada, M. Ehara, K. Toyota, R. Fukuda, J. Hasegawa, M. Ishida, T. Nakajima, Y. Honda, O. Kitao, H. Nakai, T. Vreven, J. A. M. Jr, J. E. Peralta, F. Ogliaro, M. Bearpark, J. J. Heyd, E. Brothers, K. N. Kudin, V. N. Staroverov, R. Kobayashi, J. Normand, K. Raghavachari, A. Rendell, J. C. Burant, S. S. Iyengar, J. Tomasi, M. Cossi, N. Rega, J. M. Millam, M. Klene, J. E. Knox, J. B. Cross, V. Bakken, C. Adamo, J. Jaramillo, R. Gomperts, R. E. Stratmann, O. Yazyev, A. J. Austin, R. Cammi, C. Pomelli, J. W. Ochterski, R. L. Martin, K. Morokuma, V. G. Zakrzewski, G. A. Voth, P. Salvador, J. J. Dannenberg, S. Dapprich, A. D. Daniels, O. Farkas, J. B. Foresman, J. V. Ortiz, J. Cioslowski, and D. J. Fox. Gaussian 09, revision E.01. Gaussian Inc., Wallingford CT, 2009.

[122] J. J. Potoff and J. I. Siepmann. Vapor-liquid equilibria of mixtures containing alkanes, carbon dioxide, and nitrogen. AIChE J., 47(7):1676–1682, 2001.

[123] S. Roy and L. X. Dang. Water exchange dynamics around $H_3O^+$ and $OH^-$ ions. Chemical Physics Letters, 628(1):30–34, 2015.

[124] C. H. Bennett. Efficient estimation of free energy differences from Monte Carlo data. Journal of Computational Physics, 22:245–268, 1976.

[125] M. R. Shirts and J. D. Chodera. Statistically optimal analysis of samples from multiple equilibrium states. The Journal of Chemical Physics, 129(12):124105, 2008.

[126] I. S. Joung and T. E. Cheatham III. Determination of alkali and halide monovalent ion parameters for use in explicitly solvated biomolecular simulations. Journal of Physical Chemistry B, 112(30):9020–9041, 2008.

[127] Spartan18, Wavefunction Inc., Irvine CA, 2018.

[128] Chase, M. W., Jr. Thermochemical Tables, Fourth Edition, Parts I and II. The Journal of Physical Chemistry Ref. Data, Monograph #9,, Am. Chem. Society and Am. Physical Society, 1998.

[129] C. H. Turner, J. K. Brennan, and M. Lísal. Replica Exchange for reactive Monte Carlo simulations. The Journal of Physical Chemistry C, 111:15706–15715, 2007.

[130] M. Gupta, E. F. da Silva, and H. F. Svendsen. Modeling temperature dependency of amine basicity using PCM and SM8T implicit solvation models. Journal of Physical Chemistry B, 116(6):1865–1875, 2012.

[131] M. Gupta, E. F. d. Silva, and H. F. Svendsen. Comparison of equilibrium constants of various reactions involved in amines and amino acid solvents for $CO_2$ absorption. Energy Procedia, 51:161–168, 2014.

[132] M. Gupta, E. F. da Silva, and H. F. Svendsen. Post–combustion $CO_2$ capture solvent characterization employing the explicit solvation shell model and continuum solvation models. Journal of Physical Chemistry B, 120(34):9034–9050, 2016.

[133] W. R. Smith and R. W. Missen. The effect of isomerization on chemical equilibrium. Canadian Journal of Chemical Engineering, 52(2):280–282, 1974.

[134] J. Ho, M. L. Coote, C. J. Cramer, and D. G. Truhlar. Theoretical Calculation of Reduction Potentials, book section 4, pages 229–259. CRC Press, Boca Raton, FL, 2016.

[135] H. B. Xie, C. Li, N. He, C. Wang, S. Zhang, and J. Chen. Atmospheric chemical reactions of monoethanolamine initiated by oh radical: mechanistic and kinetic study. Environmental Science & Technology, 48(3):1700–1706, 2014.

[136] Y. V. Novakovskaya and M. N. Rodnikova. Ethanolamine: conformational diversity. Structural Chemistry, 26(1):177–187, 2014.

[137] I. Kim, K. A. Hoff, E. T. Hessen, T. Haug-Warberg, and H. F. Svendsen. Enthalpy of absorption of $CO_2$ with alkanolamine solutions predicted from reaction equilibrium constants. Chemical Engineering Science, 64(9):2027–2038, 2009.

[138] N. McCann, M. Maeder, and H. Hasse. A calorimetric study of carbamate formation. Journal of Chemical Thermodynamics, 43(5):664–669, 2011.

[139] Debra Fernandes, William Conway, Xiaoguang Wang, Robert Burns, Geoffrey Lawrance, Marcel Maeder, and Graeme Puxty. Protonation constants and thermodynamic properties of amines for post combustion capture of $CO_2$. Journal of Chemical Thermodynamics, 51:97–102, 2012.

[140] Bryce Dutcher, Maohong Fan, and Armistead G Russell. Amine–based $CO_2$ capture technology development from the beginning of 2013: A review. ACS Applied Materials & Interfaces, 7(4):2137–2148, 2015.

[141] Ardi Hartono, Solrun Johanne Vevelstad, Arlinda Ciftja, and Hanna K Knuutila. Screening of strong bicarbonate forming solvents for $CO_2$ capture. International Journal of Greenhouse Gas Control, 58:201–211, 2017.

[142] Francesco Barzagli, Fabrizio Mani, and Maurizio Peruzzini. Efficient $CO_2$ absorption and low temperature desorption with non-aqueous solvents based on 2-amino-2-methyl-1-propanol (AMP). International Journal of Greenhouse Gas Control, 16:217–223, 2013.

[143] Jiafei Zhang, Yu Qiao, and David W Agar. Improvement of lipophilic-amine-based thermomorphic biphasic solvent for energy-efficient carbon capture. Energy Procedia, 23:92–101, 2012.

[144] Diego DD Pinto, Syed AH Zaidy, Ardi Hartono, and Hallvard F Svendsen. Evaluation of a phase change solvent for $CO_2$ capture: Absorption and desorption tests. International Journal of Greenhouse Gas Control, 28:318–327, 2014.

[145] Young-Seop Choi, Jinkyu Im, Jun Kyo Jeong, Sung Yun Hong, Ho Gyeom Jang, Minserk Cheong, Je Seung Lee, and Hoon Sik Kim. $CO_2$ absorption and desorption in an aqueous solution of heavily hindered alkanolamine: Structural elucidation of $CO_2$-containing species. Environmental Science & Technology, 48(7):4163–4170, 2014.

[146] Nafis Mahmud, Abdelbaki Benamor, Mustafa S. Nasser, and Paitoon Tontiwachwuthikul. Carbamate formation and amine protonation constants in 2-amino-1-butanol–$CO_2$–$H_2O$ system and their temperature dependences. Journal of Solution Chemistry, 47(2):262–277, 2018.

[147] Alvaro Perez-Salado Kamps and Gerd Maurer. Dissociation constant of n-methyldiethanolamine in aqueous solution at temperatures from 278 K to 368 K. Journal of Chemical Engineering Data, 41:1505–1513, 1996.

[148] Aravind V. Rayer, Kazi Z. Sumon, Laila Jaffari, and Amr Henni. Dissociation constants ($pK_a$) of tertiary and cyclic amines: Structural and temperature dependences. Journal of Chemical & Engineering Data, 59(11):3805–3813, 2014.

[149] Ali Tagiuri, Mohanned Mohamedali, and Amr Henni. Dissociation constant ($pK_a$) and thermodynamic properties of some tertiary and cyclic amines from (298 to 333) K. Journal of Chemical & Engineering Data, 61(1):247–254, 2016.

[150] Sholeh Ma'mun, Kamariah, Sukirman, Desi Kurniawan, Eleonora Amelia, Vitro Rahmat, Deasy R. Alwani, S. Ismadji, T. E. Agustina, I. Yani, L. N. Komariah, and S. Hasyim. Experimental determination of monoethanolamine protonation constant and its temperature dependency. MATEC Web of Conferences, 101:02001, 2017.

[151] Ida M. Bernhardsen, Iris R. T. Krokvik, Cristina Perinu, Diego D. D. Pinto, Klaus J. Jens, and Hanna K. Knuutila. Influence of $pK_a$ on solvent performance of mapa promoted tertiary amines. International Journal of Greenhouse Gas Control, 68:68–76, 2018.

[152] William Hoang Chi Hieu Nguyen and Amr Henni. Dissociation constant ($pK_a$) and thermodynamic properties of 1,4-bis(3-aminopropyl) piperazine, 1,3-bis(aminomethyl) cyclohexane, tris(2-aminoethyl) amine, and 1-amino-4-methyl piperazine: Study of the protonation mechanism using the density function theory. Journal of Chemical & Engineering Data, 2020.

[153] Nichola McCann, Duong Phan, Debra Fernandes, and Marcel Maeder. A systematic investigation of carbamate stability constants by $^1$H NMR. International Journal of Greenhouse Gas Control, 5(3):396–400, 2011.

[154] Debra Fernandes, William Conway, Robert Burns, Geoffrey Lawrance, Marcel Maeder, and Graeme Puxty. Investigations of primary and secondary amine carbamate stability by $^1$H NMR spectroscopy for post combustion capture of carbon dioxide. Journal of Chemical Thermodynamics, 54:183–191, 2012.

[155] Gilles Richner and Graeme Puxty. Assessing the chemical speciation during $CO_2$ absorption by aqueous amines using in situ FTIR. Industrial & Engineering Chemistry Research, 51(44):14317–14324, 2012.

[156] C. McGregor, M. S. Al-Abdul-Wahid, V. Robertson, J. S. Cox, and P. R. Tremaine. Formation constants and conformational analysis of carbamates in aqueous solutions of 2-methylpiperidine and $CO_2$ from 283 to 313 k by NMR spectroscopy. Journal of Physical Chemistry B, 122:9178–9190, 2018.

[157] Sujin Na, Sung June Hwang, Hoonsik Kim, Il-Hyun Baek, and Kwang Soon Lee. Modeling of $CO_2$ solubility of an aqueous polyamine solvent for $CO_2$ capture. Chemical Engineering Science, 204:140–150, 2019.

[158] R. D. Deshmukh and A. E. Mather. A mathematical model for equilibrium solubility of hydrogen sulfide and carbon dioxide in aqueous alkanolamine solutions. Chemical Engineering Science, 36:355–362, 1981.

[159] Azam Najafloo, Farzaneh Feyzi, and Ali T. Zoghi. Modeling solubility of $CO_2$ in aqueous MDEA solution using electrolyte SAFT-HR EoS. Journal of the Taiwan Institute of Chemical Engineers, 58:381–390, 2016.

[160] Luís M. C. Pereira and Lourdes F. Vega. A systematic approach for the thermodynamic modelling of $CO_2$-amine absorption process using molecular-based models. Applied Energy, 232:273–291, 2018.

[161] Anton Wangler, Georg Sieder, Thomas Ingram, Manfred Heilig, and Christoph Held. Prediction of $CO_2$ and $H_2S$ solubility and enthalpy of absorption in reacting n-methyldiethanolamine /water systems with epc-saft. Fluid Phase Equilibria, 461:15–27, 2018.

[162] Tianyuan Wang, Elise El Ahmar, Christophe Coquelet, and Georgios M. Kontogeorgis. Improvement of the PR-CPA equation of state for modelling of acid gases solubilities in aqueous alkanolamine solutions. Fluid Phase Equilibria, 471:74–87, 2018.

[163] Tianyuan Wang, Philippe Guittard, Christophe Coquelet, Elise El Ahmar, Olivier Baudouin, and Georgios M. Kontogeorgis. Improvement of the PR-CPA equation of state for modelling of acid gases solubilities in aqueous alkanolamine solutions. Fluid Phase Equilibria, 485:126–127, 2019.

[164] Thomas Gerlach, Simon Müller, and Irina Smirnova. Development of a COSMO-RS based model for the calculation of phase equilibria in electrolyte systems. AIChE J., 64(1):272–285, 2018.

[165] Aleksandr V. Marenich, Christopher J. Cramer, and Donald G. Truhlar. Universal solvation model based on solute electron density and on a continuum model of the solvent defined by the bulk dielectric constant and atomic surface tensions. Journal of Physical Chemistry B, 113(18):6378–6396, 2009.

[166] Satesh Gangarapu, Antonius TM Marcelis, and Han Zuilhof. Carbamate stabilities of sterically hindered amines from quantum chemical methods: Relevance for $CO_2$ capture. ChemPhysChem, 14(17):3936–3943, 2013.

[167] Hong-Bin Xie, Ning He, Zhiquan Song, Jingwen Chen, and Xuehua Li. Theoretical investigation on the different reaction mechanisms of aqueous 2-amino-2-methyl-1-propanol and monoethanolamine with $CO_2$. Industrial & Engineering Chemistry Research, 53(8):3363–3372, 2014.

[168] Thomas Gerlach, Thomas Ingram, Georg Sieder, and Irina Smirnova. Modeling the solubility of $CO_2$ in aqueous methyl diethanolamine solutions with an electrolyte model based on COSMO-RS. Fluid Phase Equilibria, 461:39–50, 2018.

[169] Mayuri Gupta and Hallvard F. Svendsen. Modeling temperature dependent and absolute carbamate stability constants of amines for $CO_2$ capture. International Journal of Greenhouse Gas Control, 98, 2020.

[170] Naomi L Haworth, Qinrui Wang, and Michelle L Coote. Modeling flexible molecules in solution: A $pK_a$ case study. Journal of Physical Chemistry A, 121(27):5217–5225, 2017.

[171] Hiromi Nakai, Yoshifumi Nishimura, Takeaki Kaiho, Takahito Kubota, and Hiroshi Sato. Contrasting mechanisms for $CO_2$ absorption and regeneration processes in aqueous amine solutions: Insights from density-functional tight-binding molecular dynamics simulations. Chemical Physics Letters, 647:127–131, 2016.

[172] A. W. Sakti, Y. Nishimura, and H. Nakai. Rigorous $pK_a$ estimation of amine species using density-functional tight-binding-based metadynamics simulations. Journal of Chemical Theory & Computation, 14:351–356, 2017.

[173] Aditya Wibawa Sakti, Yoshifumi Nishimura, Hiroshi Sato, and Hiromi Nakai. Divide-and-conquer density-functional tight-binding molecular dynamics study on the formation of carbamate ions during $CO_2$ chemical absorption in aqueous amine solution. Bulletin of the Chemical Society of Japan, 90(11):1230–1235, 2017.

[174] Javad Noroozi and William R Smith. An efficient molecular simulation methodology for chemical reaction equilibria in electrolyte solutions: Application to $CO_2$ reactive absorption. The Journal of Physical Chemistry A, 123(18):4074–4086, 2019.

[175] Javad Noroozi and William R Smith. Prediction of alkanolamine $pK_a$ values by combined molecular dynamics free energy simulations and ab initio calculations. Journal of Chemical & Engineering Data, 2019.

[176] Joseph W Ochterski. Thermochemistry in Gaussian. Gaussian Inc, 1:19, 2000.

[177] J. Wang, R. M. Wolf, J. W. Caldwell, P. A. Kollman, and D. A. Case. Development and testing of a General Amber Force Field. Journal of Computational Chemistry, 25(9):1157–1174, 2001.

[178] Junmei Wang, Wei Wang, Peter A Kollman, and David A Case. Automatic atom type and bond type perception in molecular mechanical calculations. Journal of Molecular Graphics and Modelling, 25(2):247–260, 2006.

[179] Alan W Sousa da Silva and Wim F Vranken. Acpype-antechamber python parser interface. BMC research notes, 5(1):367, 2012.

[180] S. Pronk, S. Pall, R. Schulz, P. Larsson, P. Bjelkmar, R. Apostolov, M. R. Shirts, J. C. Smith, P. M. Kasson, D. van der Spoel, B. Hess, and E. Lindahl. GROMACS 4.5: A high–throughput and highly parallel open source molecular simulation toolkit. Bioinformatics, 29(7):845–854, 2013.

[181] L. Martinez, R. Andrade, E. G. Birgin, and J. M. Martinez. PACKMOL: A package for building initial configurations for molecular dynamics simulations. Journal of Computational Chemistry, 30(13):2157–2164, 2009.

[182] Thomas C Beutler, Alan E Mark, René C van Schaik, Paul R Gerber, and Wilfred F Van Gunsteren. Avoiding singularities and numerical instabilities in free energy calculations based on molecular simulations. Chemical Physics Letters, 222(6):529–539, 1994.

[183] John M Simmie and Kieran P Somers. Benchmarking compound methods (CBS-QB3, CBS-APNO, G3, G4, W1BD) against the Active Thermochemical Tables: A litmus test for cost-effective molecular formation enthalpies. The Journal of Physical Chemistry A, 119(28):7235–7246, 2015.

[184] David L Mobley, Elise Dumont, John D Chodera, and Ken A Dill. Comparison of charge models for fixed-charge force fields: Small-molecule hydration free energies in explicit solvent. The Journal of Physical Chemistry B, 111(9):2242–2254, 2007.

[185] Joakim PM Jämbeck, Francesca Mocci, Alexander P Lyubartsev, and Aatto Laaksonen. Partial atomic charges and their impact on the free energy of solvation. Journal of Computational Chemistry, 34(3):187–197, 2013.

[186] O. Kroutil, M. Predota, and M. Kabelac. Force field parametrization of hydrogenoxalate and oxalate anions with scaled charges. Journal of Molecular Modeling, 23(11):327, 2017.

[187] M. B. Jensen, E. Jorgensen, and C. Faurholt. Reactions between carbon dioxide and amino alcohols. I. Monoethanoamine and diethanolamine. Acta Chemica Scandinavica, 8:1137–1140, 1954.

[188] D. M. Austgen, G. T. Rochelle, X. Peng, and C. C. Chen. Model of vapor liquid equilibria for aqueous acid gas alkanolamine systems using the electrolyte NRTL equation. Industrial & Engineering Chemistry Research, 28(7):1060–1073, 1989.

[189] Mohammed Kheireddine Aroua, Abdelbaki Benamor, and Mohd Zaki Haji-Sulaiman. Equilibrium constant for carbamate formation from monoethanolamine and its relationship with temperature. Journal of Chemical Engineering Data, 44:887–891, 1999.

[190] William Conway, Xiaoguang Wang, Debra Fernandes, Robert Burns, Geoffrey Lawrance, Graeme Puxty, and Marcel Maeder. Comprehensive kinetic and thermodynamic study of the reactions of $CO_2$ (aq) and $HCO_3^-$–with monoethanolamine (MEA) in aqueous solution. The Journal of Physical Chemistry A, 115(50):14340–14349, 2011.

[191] Wolfram Böttinger, Michael Maiwald, and Hans Hasse. Online NMR spectroscopic study of species distribution in MEA–$H_2O$–$CO_2$ and DEA–$H_2O$–$CO_2$. Fluid Phase Equilibria, 263(2):131–143, 2008.

[192] Nichola McCann, Marcel Maeder, and Hans Hasse. A calorimetric study of carbamate formation. The Journal of Chemical Thermodynamics, 43(5):664–669, 2011.

[193] Arlinda F Ciftja, Ardi Hartono, and Hallvard F Svendsen. Experimental study on carbamate formation in the AMP–$CO_2$–$H_2O$ system at different temperatures. Chemical Engineering Science, 107:317–327, 2014.

[194] Hidetaka Yamada, Shinkichi Shimizu, Hiromichi Okabe, Yoichi Matsuzaki, Firoz A Chowdhury, and Yuichi Fujioka. Prediction of the basicity of aqueous amine solutions and the species distribution in the amine- $H_2O$- $CO_2$ system using the COSMO-RS method. Industrial & Engineering Chemistry Research, 49(5):2449–2455, 2010.

[195] William Conway, Xiaoguang Wang, Debra Fernandes, Robert Burns, Geoffrey Lawrance, Graeme Puxty, and Marcel Maeder. Toward the understanding of chemical absorption processes for post-combustion capture of carbon dioxide: Electronic and steric considerations from the kinetics of reactions of $CO_2$ (aq) with sterically hindered amines. Environmental Science & Technology, 47(2):1163–1169, 2013.

[196] Mohammed Al-Juaied and Gary T Rochelle. Thermodynamics and equilibrium solubility of carbon dioxide in diglycolamine/morpholine/water. Journal of Chemical & Engineering Data, 51(2):708–717, 2006.

[197] Arlinda F Ciftja, Ardi Hartono, Eirik F da Silva, and Hallvard F Svendsen. Study on carbamate stability in the AMP/$CO_2$/$H_2O$ system from 13C-NMR spectroscopy. Energy Procedia, 4:614–620, 2011.

[198] Francis Bougie and Maria C Iliuta. Solubility of $CO_2$ in and density, viscosity, and surface tension of aqueous 2-amino-1, 3-propanediol (serinol) solutions. Journal of Chemical & Engineering Data, 59(2):355–361, 2014.

[199] TJ Edwards, Gerd Maurer, John Newman, and JM Prausnitz. Vapor-liquid equilibria in multicomponent aqueous solutions of volatile weak electrolytes. AIChE Journal, 24(6):966–976, 1978.

[200] Sen Liu, Hongxia Gao, Chuan He, and Zhiwu Liang. Experimental evaluation of highly efficient primary and secondary amines with lower energy by a novel method for post-combustion $CO_2$ capture. Applied Energy, 233–234:443–452, 2019.

[201] Espen S. Hamborg and Geert F. Versteeg. Dissociation constants and thermodynamic properties of amines and alkanolamines from (293 to 353) K. Journal of Chemical & Engineering Data, 54:1318–1328, 2009.

[202] R.G. Bates and G. D. Pinching. Acidic dissociation constant and related thermodynamic quantities for monoethanolammonium ion in water from 0 to 500 C. Journal of Research of the National Bureau of Standards, 46:349–352, 1951.

[203] Jin-Ho Kim, Celina Dobrogowska, and Loren G. Hepler. Thermodynamics of ionization of aqueous alkanolamines. Canadian Journal of Chemical Engineering, 65:1726–1728, 1987.

[204] Juan M. Antelo, Florencio Arce, Julio Casado, Manuel Sastre, and Angel Varela. Protonation constants of mono-, di-, and triethanolamine. Influence of the ionic composition of the medium. Journal of Chemical & Engineering Data, 29:10–11, 1984.

[205] S. P. Datta and A. K. Grzybowski. Acid dissociation constants of the ammonium group in 2-aminoethanol, 2-aminoethyl phosphate, and 2-aminoethyl sulphate. Journal of the Chemical Society, 568:3068–3077, 1962.

[206] Graeme Puxty, Robert Rowland, Andrew Allport, Mark Borwn, Robert Burns, Marcel Maeder, and Moetaz Attalla. Carbon dioxide post–combustion capture: A novel screening study of the carbon dioxide absorption performance of 76 amines. Environmental Science & Technology, 43:6427–6433, 2009.

[207] Jana Poplsteinova Jakobsen, Jostein Krane, and Hallvard F Svendsen. Liquid-phase composition determination in $CO_2$-$H_2O$-alkanolamine systems: An NMR study. Industrial & Engineering Chemistry Research, 44(26):9894–9903, 2005.

[208] Fang-Yuan Jou, Alan E Mather, and Frederick D Otto. The solubility of $CO_2$ in a 30 mass percent monoethanolamine solution. Canadian Journal of Chemical Engineering, 73(1):140–147, 1995.

[209] Joel L Martin, Frederick D. Otto, and Alan E. Mather. Solubility of hydrogen sulfide and carbon dioxide in a diglycolamine solution. Journal of Chemical & Engineering Data, 23(2):163–164.

[210] Jeom-In Baek and Ji-Ho Yoon. Solubility of carbon dioxide in aqueous solutions of 2-amino-2-methyl-1, 3-propanediol. Journal of Chemical & Engineering Data, 43(4):635–637, 1998.

[211] Danlu Tong, JP Martin Trusler, Geoffrey C Maitland, Jon Gibbins, and Paul S Fennell. Solubility of carbon dioxide in aqueous solution of monoethanolamine or 2-amino-2-methyl-1-propanol: Experimental measurements and modelling. International Journal of Greenhouse Gas Control, 6:37–47, 2012.

[212] Sen Liu, Hao Ling, Hongxia Gao, Paitoon Tontiwachwuthikul, Zhiwu Liang, and Haiyan Zhang. Kinetics and new Brønsted correlations study of $CO_2$ absorption into

primary and secondary alkanolamine with and without steric-hindrance. Separation and Purification Technology, 233:115998, 2020.

[213] Ugochukwu E Aronu, Shahla Gondal, Erik T Hessen, Tore Haug-Warberg, Ardi Hartono, Karl A Hoff, and Hallvard F Svendsen. Solubility of $CO_2$ in 15, 30, 45 and 60 mass% MEA from 40 to 120 C and model representation using the extended UNIQUAC framework. Chemical Engineering Science, 66(24):6393–6406, 2011.

[214] Miguel Ángel Rebolledo-Morales, María Esther Rebolledo-Libreros, and Arturo Trejo. Equilibrium solubility of $CO_2$ in aqueous solutions of 1-amino-2-propanol as function of concentration, temperature, and pressure. The Journal of Chemical Thermodynamics, 43(5):690–695, 2011.

[215] Paul M. Mathias and John P. Gilmartin. Quantitative evaluation of the effect of uncertainty in property models on the simulated performance of solvent-based $CO_2$ capture. Energy Procedia, 63:1171–1185, 2014.

[216] Joshua C. Morgan, Debangsu Bhattacharyya, Charles Tong, and David C. Miller. Uncertainty quantification of property models: Methodology and its application to $CO_2$ -loaded aqueous MEA solutions. AIChE Journal, 61(6):1822–1839, 2015.

[217] Ross E Dugas and Gary T Rochelle. $CO_2$ absorption rate into concentrated aqueous monoethanolamine and piperazine. Journal of Chemical & Engineering Data, 56(5):2187–2195, 2011.

[218] Braden Kelly and William Robert Smith. Alchemical hydration free-energy calculations using molecular dynamics with explicit polarization and induced polarity decoupling: An on-the-fly polarization approach. Journal of Chemical Theory & Computation, 16:1146–1161, 2020.

[219] Braden D Kelly and William R Smith. A simple method for including polarization effects in solvation free energy calculations when using fixed-charge force fields: Alchemically polarized charges. ACS Omega, 5(28):17170–17181, 2020.

[220] Min Xiao, Helei Liu, Raphael Idem, Paitoon Tontiwachwuthikul, and Zhiwu Liang. A study of structure–activity relationships of commercial tertiary amines for post–combustion $CO_2$ capture. Applied Energy, 184:219–229, 2016.

[221] Ida M Bernhardsen and Hanna K Knuutila. A review of potential amine solvents for $CO_2$ absorption process: Absorption capacity, cyclic capacity and $pK_a$. International Journal of Greenhouse Gas Control, 61:27–48, 2017.

[222] Jacopo Tomasi, Benedetta Mennucci, and Roberto Cammi. Quantum mechanical continuum solvation models. Chemical Reviews, 105(8):2999–3094, 2005.

[223] Andreas Klamt. Conductor–like screening model for real solvents: A new approach to the quantitative calculation of solvation phenomena. The Journal of Physical Chemistry, 99(7):2224–2235, 1995.

[224] Casey P. Kelly, Christopher J. Cramer, and Donald G. Truhlar. Adding explicit solvent molecules to continuum solvent calculations for the calculation of aqueous acid dissociation constants. Journal of Physical Chemistry A, 110(7):2493–2499, 2006.

[225] Josefredo R Pliego and José M Riveros. Theoretical calculation of $pK_a$ using the cluster–continuum model. Journal of Physical Chemistry A, 106(32):7434–7439, 2002.

[226] Josefredo R Pliego and José M Riveros. The cluster–continuum model for the calculation of the solvation free energy of ionic species. Journal of Physical Chemistry A, 105(30):7241–7247, 2001.

[227] Shuming Zhang. A reliable and efficient first principles–based method for predicting $pK_a$ values. III. Adding explicit water molecules: Can the theoretical slope be reproduced and $pK_a$ values predicted more accurately? Journal of Computational Chemistry, 33(5):517–526, 2012.

[228] Adam C Chamberlin, Christopher J Cramer, and Donald G Truhlar. Extension of a temperature-dependent aqueous solvation model to compounds containing nitrogen, fluorine, chlorine, bromine, and sulfur. Journal of Physical Chemistry B, 112(10):3024–3039, 2008.

[229] Courtney E Cox, Jeremy R Phifer, Larissa Ferreira Da Silva, Gabriel Goncalves Nogueira, Ryan T Ley, Elizabeth J O'Loughlin, Ana Karolyne Pereira Barbosa, Brett T Rygelski, and Andrew S Paluch. Combining MOSCED with molecular simulation free energy calculations or electronic structure calculations to develop an efficient tool for solvent formulation and selection. Journal of Computer-Aided Molecular Design, 31(2):183–199, 2017.

[230] Elizabeth LM Miguel, Poliana L Silva, and Josefredo R Pliego. Theoretical prediction of $pK_a$ in methanol: Testing SM8 and SMD models for carboxylic acids, phenols, and amines. Journal of Physical Chemistry B, 118(21):5730–5739, 2014.

[231] Junming Ho, Andreas Klamt, and Michelle L Coote. Comment on the correct use of continuum solvent models. Journal of Physical Chemistry A, 114(51):13442–13444, 2010.

[232] Art D Bochevarov, Mark A Watson, Jeremy R Greenwood, and Dean M Philipp. Multiconformation, density functional theory–based $pK_a$ prediction in application to large, flexible organic molecules with diverse functional groups. Journal of Chemical Theory & Computation, 12(12):6001–6019, 2016.

[233] Longkun Xu and Michelle L Coote. Improving the accuracy of PCM-UAHF and PCM-UAKS calculations using optimized electrostatic scaling factors. Journal of Chemical Theory & Computation, 2019.

[234] Catherine CR Sutton, George V Franks, and Gabriel da Silva. First principles $pK_a$ calculations on carboxylic acids using the SMD solvation model: Effect of thermodynamic cycle, model chemistry, and explicit solvent molecules. Journal of Physical Chemistry B, 116(39):11999–12006, 2012.

[235] Mayuri Gupta, Eirik F da Silva, and Hallvard F Svendsen. Post–combustion $CO_2$ capture solvent characterization employing the explicit solvation shell model and continuum solvation models. Journal of Physical Chemistry B, 120(34):9034–9050, 2016.

[236] Samarjeet Prasad, Jing Huang, Qiao Zeng, and Bernard R Brooks. An explicit–solvent hybrid QM and MM approach for predicting $pK_a$ of small molecules in sampl6 challenge. Journal of Computer-Aided Molecular Design, 32(10):1191–1201, 2018.

[237] Kevin Leung. Surface potential at the air- water interface computed using density functional theory. The Journal of Physical Chemistry Lett., 1(2):496–499, 2009.

[238] Xiao-Song Xue, Ya Wang, Chen Yang, Pengju Ji, and Jin-Pei Cheng. Toward prediction of the chemistry in ionic liquids: An accurate computation of absolute $pK_a$ values of benzoic acids and benzenethiols. Journal of Organic Chemistry, 80(18):8997–9006, 2015.

[239] Edward Harder and Benoît Roux. On the origin of the electrostatic potential difference at a liquid–vacuum interface. The Journal of Chemical Physics., 129(23), 2008.

[240] Maksim Misin, Maxim V Fedorov, and David S Palmer. Hydration free energies of molecular ions from theory and simulation. Journal of Physical Chemistry B, 120(5):975–983, 2016.

[241] Haiyang Zhang, Yang Jiang, Hai Yan, Ziheng Cui, and Chunhua Yin. Comparative assessment of computational methods for free energy calculations of ionic hydration. Journal of Chemical Information and Modeling, 57(11):2763–2775, 2017.

[242] Michael D Tissandier, Kenneth A Cowen, Wan Yong Feng, Ellen Gundlach, Michael H Cohen, Alan D Earhart, James V Coe, and Thomas R Tuttle. The proton's absolute aqueous enthalpy and Gibbs free energy of solvation from cluster–ion solvation data. Journal of Physical Chemistry A, 102(40):7787–7794, 1998.

[243] Casey P. Kelly, Christopher J. Cramer, and Donald G. Truhlar. Aqueous solvation free energies of ions and ion–water clusters based on an accurate value for the absolute aqueous solvation free energy of the proton. Journal of Physical Chemistry B, 110(32):16066–16081, 2006.

[244] Thomas L Beck. The influence of water interfacial potentials on ion hydration in bulk water and near interfaces. Chemical Physics Letters, 561:1–13, 2013.

[245] D Asthagiri, Lawrence R Pratt, and HS Ashbaugh. Absolute hydration free energies of ions, ion–water clusters, and quasichemical theory. The Journal of Chemical Physics., 119(5):2702–2708, 2003.

[246] Araz Jakalian, David B Jack, and Christopher I Bayly. Fast, efficient generation of high-quality atomic charges. AM1-BCC model: II. Parameterization and validation. Journal of Computational Chemistry, 23(16):1623–1641, 2002.

[247] Yushan Zhang, Yong Zhang, Mark J McCready, and Edward J Maginn. Evaluation and refinement of the general AMBER Force Field for nineteen pure organic electrolyte solvents. Journal of Chemical Engineering Data, 63(9):3488–3502, 2018.

[248] Nathalia SV Barbosa, Yong Zhang, Eduardo RA Lima, Frederico W Tavares, and Edward J Maginn. Development of an AMBER–compatible transferable force field for poly (ethylene glycol) ethers (glymes). Journal of Molecular Modeling, 23(6):194, 2017.

[249] David L Mobley, Christopher I Bayly, Matthew D Cooper, Michael R Shirts, and Ken A Dill. Small molecule hydration free energies in explicit solvent: an extensive test of fixed-charge atomistic simulations. Journal of Chemical Theory & Computation, 5(2):350–358, 2009.

[250] DA McQuarrie. Statistical Mechanics University Science Books. Sausalito, CA, 2000.

[251] Guillaume Lamoureux and Benoît Roux. Absolute hydration free energy scale for alkali and halide ions established from simulations with a polarizable force field. Journal of Physical Chemistry B, 110(7):3308–3322, 2006.

[252] Aleksandr V. Marenich, Christopher J. Cramer, and Donald G. Truhlar. Performance of SM6, SM8, and SMD on the SAMPL1 test set for the prediction of small–molecule solvation free energies. Journal of Physical Chemistry B, 113(14):4538–4543, 2009.

[253] Piotr Cieplak, Wendy D Cornell, Christopher Bayly, and Peter A Kollman. Application of the multimolecule and multiconformational resp methodology to biopolymers: Charge derivation for DNA, RNA, and proteins. Journal of Computational Chemistry, 16(11):1357–1377, 1995.

[254] David L. Mobley and J. Peter Guthrie. Freesolv: A database of experimental and calculated hydration free energies, with input files. Journal of Computer-Aided Molecular Design, 28(7):711–720, 2014.

[255] Maximiliano Riquelme, Alejandro Lara, David L Mobley, Toon Verstraelen, Adelio R Matamala, and Esteban Vöhringer-Martinez. Hydration free energies in the FreeSolv Database calculated with polarized iterative Hirshfeld charges. Journal of Chemical Information and Modeling, 58(9):1779–1797, 2018.

[256] Edward PL Hunter and Sharon G Lias. Evaluated gas phase basicities and proton affinities of molecules: An update. The Journal of Physical Chemistry Ref. Data, 27(3):413–656, 1998.

[257] Aravind V Rayer, Kazi Z Sumon, Laila Jaffari, and Amr Henni. Dissociation constants ($pK_a$) of tertiary and cyclic amines: Structural and temperature dependences. Journal of Chemical Engineering Data, 59(11):3805–3813, 2014.

[258] Ali Tagiuri, Mohanned Mohamedali, and Amr Henni. Dissociation constant ($pK_a$) and thermodynamic properties of some tertiary and cyclic amines from (298 to 333) K. Journal of Chemical Engineering Data, 61(1):247–254, 2015.

[259] Espen S Hamborg and Geert F Versteeg. Dissociation constants and thermodynamic properties of amines and alkanolamines from (293 to 353) K. Journal of Chemical Engineering Data, 54(4):1318–1328, 2009.

[260] Jessica Narku-Tetteh, Pailin Muchan, and Raphael Idem. Effect of alkanol chain length of primary alkanolamines and alkyl chain length of secondary and tertiary alkanolamines on their $CO_2$ capture activities. Separation and Purification Technology, 187:453–467, 2017.

[261] Haiyang Zhang, Yang Jiang, Hai Yan, Chunhua Yin, Tianwei Tan, and David van der Spoel. Free-energy calculations of ionic hydration consistent with the experimental hydration free energy of the proton. The Journal of Physical Chemistry Lett., 8(12):2705–2712, 2017.

[262] A. Mecklenfeld and G. Raabe. Efficient solvation free energy simulations: Impact of soft-core potential and a new adaptive $\lambda$–spacing method. Molecular Physics, 115(9-12):1322–1334, 2017.

[263] David S Cerutti, Julia E Rice, William C Swope, and David A Case. Derivation of fixed partial charges for amino acids accommodating a specific water model and implicit polarization. Journal of Physical Chemistry B, 117(8):2328–2338, 2013.

[264] Claus J Nielsen, Hartmut Herrmann, and Christian Weller. Atmospheric chemistry and environmental impact of the use of amines in carbon capture and storage (CCS). Chemical Society Reviews, 41(19):6684–6704, 2012.

[265] Gary T Rochelle. Amine scrubbing for $CO_2$ capture. Science, 325(5948):1652–1654, 2009.

[266] Espen S Hamborg and Geert F Versteeg. Dissociation constants and thermodynamic properties of amines and alkanolamines from (293 to 353) K. Journal of Chemical & Engineering Data, 54(4):1318–1328, 2009.

[267] Mickaël R. Simond, Karine Ballerat-Busserolles, Yohann Coulier, Laurence Rodier, and J-Y Coxam. Dissociation constants of protonated amines in water at temperatures from 293.15 K to 343.15 K. Journal of Solution Chemistry, 41(1):130–142, 2012.

[268] Debra Fernandes, William Conway, Xiaoguang Wang, Robert Burns, Geoffrey Lawrance, Marcel Maeder, and Graeme Puxty. Protonation constants and thermodynamic properties of amines for post combustion capture of $CO_2$. The Journal of Chemical Thermodynamics, 51:97–102, 2012.

[269] Naser S Matin, Joseph E Remias, James K Neathery, and Kunlei Liu. Facile method for determination of amine speciation in $CO_2$ capture solutions. Industrial & Engineering Chemistry Research, 51(19):6613–6618, 2012.

[270] Junming Ho and Michelle L Coote. A universal approach for continuum solvent $pK_a$ calculations: Are we there yet? Theoretical Chemistry Accounts, 125(1):3–21, 2010.

[271] Eirik F da Silva and Hallvard F Svendsen. Study of the carbamate stability of amines using ab initio methods and free-energy perturbations. Industrial & Engineering Chemistry Research, 45(8):2497–2504, 2006.

[272] Josefredo R Pliego Jr. Thermodynamic cycles and the calculation of $pK_a$. Chemical Physics Letters, 367(1-2):145–149, 2003.

[273] Aditya Wibawa Sakti, Yoshifumi Nishimura, and Hiromi Nakai. Rigorous $pK_a$ estimation of amine species using density-functional tight-binding-based metadynamics simulations. Journal of Chemical Theory and Computation, 14(1):351–356, 2018.

[274] Anil Kumar Tummanapelli and Sukumaran Vasudevan. Estimating successive $pK_a$ values of polyprotic acids from ab initio molecular dynamics using metadynamics: The dissociation of phthalic acid and its isomers. Physical Chemistry Chemical Physics, 17(9):6383–6388, 2015.

[275] Javad Noroozi and William R Smith. Accurately predicting $CO_2$ reactive absorption properties in aqueous alkanolamine solutions by molecular simulation requiring no solvent experimental data. Industrial & Engineering Chemistry Research, 59(40):18254–18268, 2020.

[276] George D Miron, Dmitrii A Kulik, and Tres Thoenen. Generating isocoulombic reactions as a tool for systematic evaluation of temperature trends of thermodynamic properties: Application to aquocomplexes of lanthanides and actinides. Geochimica et Cosmochimica Acta, 286:119–142, 2020.

[277] Alhadji Malloum, Jean Jules Fifen, and Jeanet Conradie. Determination of the absolute solvation free energy and enthalpy of the proton in solutions. Journal of Molecular Liquids, page 114919, 2020.

[278] Nayyereh Hatefi and William R Smith. Ideal-gas thermochemical properties for alkanolamine and related species involved in carbon-capture applications. Journal of Chemical & Engineering Data, 66(4):1592–1599, 2021.

[279] Aravind V Rayer, Kazi Z Sumon, Laila Jaffari, and Amr Henni. Dissociation constants ($pK_a$) of tertiary and cyclic amines: Structural and temperature dependences. Journal of Chemical & Engineering Data, 59(11):3805–3813, 2014.

[280] Ali Tagiuri, Mohanned Mohamedali, and Amr Henni. Dissociation constant ($pK_a$) and thermodynamic properties of some tertiary and cyclic amines from (298 to 333) K. Journal of Chemical & Engineering Data, 61(1):247–254, 2016.

[281] Inna Kim, Christian M Jens, Andreas Grimstvedt, and Hallvard F Svendsen. Thermodynamics of protonation of amines in aqueous solutions at elevated temperatures. The Journal of Chemical Thermodynamics, 43(11):1754–1762, 2011.

[282] Rob J Littel, Martinus Bos, and Gerdine J Knoop. Dissociation constants of some alkanolamines at 293, 303, 318, and 333 K. Journal of Chemical and Engineering Data, 35(3):276–277, 1990.

[283] JL Oscarson, G Wu, PW Faux, RM Izatt, and JJ Christensen. Thermodynamics of protonation of alkanolamines in aqueous solution to 325 C. Thermochimica acta, 154(1):119–127, 1989.

[284] Roger G Bates and Gladys D Pinching. Acidic dissociation constant and related thermodynamic quantities for monoethanolammonium ion in water from 0 to 50 C. Journal of Research of the National Bureau of Standards, 46(5):349352, 1951.

[285] Debra Fernandes, William Conway, Xiaoguang Wang, Robert Burns, Geoffrey Lawrance, Marcel Maeder, and Graeme Puxty. Protonation constants and thermodynamic properties of amines for post combustion capture of $CO_2$. The Journal of Chemical Thermodynamics, 51:97–102, 2012.

[286] Christopher J Fennell, Karisa L Wymer, and David L Mobley. A fixed-charge model for alcohol polarization in the condensed phase, and its role in small molecule hydration. The Journal of Physical Chemistry B, 118(24):6438–6446, 2014.

[287] SP Datta and AK Grzybowski. Acid dissociation constants of the ammonium group in 2-aminoethanol, 2-aminoethyl phosphate, and 2-aminoethyl sulphate. Journal of the Chemical Society (Resumed), pages 3068–3077, 1962.

[288] BA Timimi and DH Everett. The thermodynamics of the acid dissociation of some amino-alcohols in water. Journal of the Chemical Society B: Physical Organic, pages 1380–1386, 1968.

[289] Hannah B Hetzer and Roger G Bates. Dissociation constant of 2-ammonium-2-methyl-1, 3-propanediol in water from 0 to 50°C and related thermodynamic quantities. The Journal of Physical Chemistry, 66(2):308–311, 1962.

[290] Vincent E Bower, Robert A Robinson, and Roger G Bates. Acidic dissociation constant and related thermodynamic quantities for diethanolammonium ion in water from 0 to 50 °C. Journal of Research of the National Bureau of Standards, 66:71–75, 1962.

[291] Jin-Ho Kim, Celina Dobrogowska, and Loren G Hepler. Thermodynamics of ionization of aqueous alkanolamines. Canadian Journal of Chemistry, 65(8):1726–1728, 1987.

[292] Shuo Xu, Yiwei Wang, Frederick D Otto, and Alan E Mather. Physicochemical properties of 2-piperidineethanol and its aqueous solutions. Journal of Chemical and Engineering Data, 37(4):407–411, 1992.

[293] Sang Hyun Park, Ki Bong Lee, Jae Chun Hyun, and Sung Hyun Kim. Correlation and prediction of the solubility of carbon dioxide in aqueous alkanolamine and mixed alkanolamine solutions. Industrial & Engineering Chemistry Research, 41(6):1658–1665, 2002.

[294] Deepika Malhotra, David C Cantu, Phillip K Koech, David J Heldebrant, Abhijeet Karkamkar, Feng Zheng, Mark D Bearden, Roger Rousseau, and Vassiliki-Alexandra Glezakou. Directed hydrogen bond placement: Low viscosity amine solvents for $CO_2$ capture. ACS Sustainable Chemistry & Engineering, 7(8):7535–7542, 2019.

[295] Mogens Ballund Jensen, Erik Jorgensen, and Carl Faurholt. Reactions between carbon dioxide and amino alcohols. 1. monoethanolamine and diethanolamine. Acta Chemica Scandinavica, 8(7):1137–1140, 1954.

[296] Robert Vácha, Victoria Buch, Anne Milet, J Paul Devlin, and Pavel Jungwirth. Autoionization at the surface of neat water: Is the top layer pH neutral, basic, or acidic? Physical Chemistry Chemical Physics, 9(34):4736–4747, 2007.

[297] Peter J Linstrom and William G Mallard. The NIST Chemistry WebBook: A chemical data resource on the internet. Journal of Chemical & Engineering Data, 46(5):1059–1063, 2001.

[298] Matthew W Palascak and George C Shields. Accurate experimental values for the free energies of hydration of $H^+$, $OH^-$, and $H_3O^+$. The Journal of Physical Chemistry A, 108(16):3692–3694, 2004.

[299] Chang-Guo Zhan and David A Dixon. Absolute hydration free energy of the proton from first-principles electronic structure calculations. The Journal of Physical Chemistry A, 105(51):11534–11540, 2001.

[300] Donald M Camaioni and Christine A Schwerdtfeger. Comment on "accurate experimental values for the free energies of hydration of $H^+$, $OH^-$, and $H_3O^+$". The Journal of Physical Chemistry A, 109(47):10795–10797, 2005.

[301] Javad Noroozi and William R Smith. Accurately predicting $CO_2$ reactive absorption properties in aqueous alkanolamine solutions by molecular simulation requiring no solvent experimental data. Industrial & Engineering Chemistry Research, 59(40):18254–18268, 2020.

[302] Braden D Kelly and William R Smith. Alchemical hydration free-energy calculations using molecular dynamics with explicit polarization and induced polarity decoupling: An on–the–fly polarization approach. Journal of Chemical Theory and Computation, 16(2):1146–1161, 2020.

[303] Braden D Kelly and William R Smith. A simple method for including polarization effects in solvation free energy calculations when using fixed-charge force fields: Alchemically polarized charges. ACS Omega, 5(28):17170–17181, 2020.

# Appendix A

# Supporting Information:An Efficient Molecular Simulation Methodology for Chemical Reaction Equilibria In Electrolyte Solutions: Application to $CO_2$ Reactive Absorption

## A.1 Ideal–Gas Standard Chemical Potentials

The ideal–gas chemical potential per particle of a species $i$ at $T$ and the standard state pressure $P^0$ relative to its atomic species at 0 K is calculated from its total partition function $q^0(T,V)$ using

$$\beta\mu_i^0(T,P^0) = -\ln[q_i^0(T,V)] \tag{A.1}$$

$q_i^0(T,V)$ maybe factored to its translational, rotational, vibrational and electronic contributions,

$$q_i^0(T,V) = q_{\text{trans}}q_{\text{rot}}q_{\text{vib}}q_{\text{elect}} = q_{\text{trans}}q_{\text{int}} \tag{A.2}$$

where

$$q_{\text{trans}} = \frac{V}{\Lambda_i^3} = V\left(\frac{2\pi M_i k_B T}{h^2}\right)^{3/2} \tag{A.3}$$

$$q_{\text{rot}} = \frac{\pi^{1/2}}{\sigma}\frac{T^{3/2}}{(\phi_{r,x}\phi_{r,y}\phi_{r,z})^{1/2}} \tag{A.4}$$

$$q_{\text{vib}} = \prod_{j=1}^{3n-6}\frac{1}{1-\exp(\frac{-\phi_{vib,j}}{T})} \tag{A.5}$$

$$q_{\text{elect}} = \omega\exp(-\beta D_i) \tag{A.6}$$

where $D_i$ is the ground state energy level, and $\omega$ is its degeneracy. Defining

$$\hat{q}_i(T) = \frac{q_{\text{int}}(T)}{\Lambda_i^3} = \frac{q^0(T,V)}{V} \tag{A.7}$$

and using the ideal–gas law, $P^0V/kT = 1$, the ideal-gas chemical potential per particle relative to the molecule's atoms at 0 K may be expressed as:

$$\beta\mu_i^0(T;P^0) = -\ln[\hat{q}_i(T)] - \ln\left(\frac{RT}{P^0}\right) + \beta D_i \tag{A.8}$$

The sum of the first two terms gives the chemical potential with respect to the ground state of molecule $i$ at 0 K. When chemical reactions are considered, all $\mu_i$ must be measured with respect to a common energy level (taken as zero). $D_i$ may thus be measured with respect the molecule's isolated atoms (in which case, it is referred to the atomization energy, $\Delta H_a(0)$) or alternatively, with respect to the elements in their conventional standard states (the negative of which is referred to as the formation enthalpy, $\Delta H_f(0)$). In the context of chemical reactions, these terms are a major contribution to $\mu_i$. We remark that, in an early implementation of their Rx/CFC algorithm for the reactive $CO_2$–MEA–$H_2O$ system[103], Vlugt *et al. et al.* omitted these terms, but they included them in a subsequent study on different systems[106]. Values of $[G(T) - H(298.15)]/RT$ are shown in Table S1.

Table A.1: Dimensionless species Gibbs energy functions, $[G_i(T) - H_i(0)]/RT$, at $P^0 = 1$ bar, calculated in this work at the temperatures considered in this study for the species involved in the MEA-$CO_2$-$H_2O$ system.

| Species | 293.15 | 298.15 | 313.15 | 333.15 | 353.15 |
|---|---|---|---|---|---|
| $H_2O$ | -18.630 | -18.699 | -18.895 | -19.142 | -19.376 |
| $CO_2$ | -21.866 | -21.930 | -22.116 | -22.354 | -22.580 |
| $OH^-$ | -17.170 | -17.230 | -17.401 | -17.618 | -17.822 |
| $H_3O^+$ | -19.121 | -19.190 | -19.392 | -19.647 | -19.888 |
| $RNH_2$ | -28.754 | -28.862 | -29.177 | -29.587 | -29.987 |
| $RNH_3^+$ | -28.973 | -29.085 | -29.413 | -29.839 | -30.254 |
| $RNHCOO^-$ | -33.070 | -33.210 | -33.618 | -34.152 | -34.674 |
| $HCO_3^-$ | -27.248 | -27.328 | -27.565 | -27.869 | -28.166 |

Table A.3: $RNH_3^+$ bond parameters

| bond | $r_0$(nm) | $K_r(kJmol^{-1}nm^{-2})$ |
|---|---|---|
| O - H | 9.7300e-02 | 3.1079e+05 |
| O-C | 1.4233e-01 | 2.6501e+05 |
| C - H1 | 1.0969e-01 | 2.7665e+05 |
| C - H2 | 1.0969e-01 | 2.7665e+05 |
| C - CA | 1.5375e-01 | 2.5179e+05 |
| CA - HA1 | 1.0910e-01 | 2.8342e+05 |
| CA - HA2 | 1.0910e-01 | 2.8342e+05 |
| CA - N | 1.5110e-01 | 2.3707e+05 |
| N - H4 | 1.0304e-01 | 3.1229e+05 |
| N - H5 | 1.0304e-01 | 3.1229e+05 |
| N - H3 | 1.0304e-01 | 3.1229e+05 |

## A.2 Force Field Parameters

Table A.2: $RNH_3$ non-bonded parameters

| no. | type | name | charge | mass | $\sigma$(nm) | $\epsilon$(kJ mol$^{-1}$) |
|---|---|---|---|---|---|---|
| 1 | oh | O | -0.663324 | 16.00000 | 3.06647e-01 | 8.80314e-01 |
| 2 | ho | H | 0.477583 | 1.00800 | 0.00000e+00 | 0.00000e+00 |
| 3 | c3 | C | 0.113132 | 12.01000 | 3.39967e-01 | 4.57730e-01 |
| 4 | h1 | H1 | 0.072304 | 1.00800 | 2.47135e-01 | 6.56888e-02 |
| 5 | h1 | H2 | 0.101301 | 1.00800 | 2.47135e-01 | 6.56888e-02 |
| 6 | c3 | CA | 0.007298 | 12.01000 | 3.39967e-01 | 4.57730e-01 |
| 7 | hx | HA1 | 0.095795 | 1.00800 | 1.95998e-01 | 6.56888e-02 |
| 8 | hx | HA2 | 0.135457 | 1.00800 | 1.95998e-01 | 6.56888e-02 |
| 9 | n4 | N | -0.301825 | 14.01000 | 3.25000e-01 | 7.11280e-01 |
| 10 | hn | H4 | 0.320759 | 1.00800 | 1.06908e-01 | 6.56888e-02 |
| 11 | hn | H5 | 0.320759 | 1.00800 | 1.06908e-01 | 6.56888e-02 |
| 12 | hn | H3 | 0.320759 | 1.00800 | 1.06908e-01 | 6.56888e-02 |

Table A.4: $RNH_3^+$ angle parameters

| angle | $\theta_0$(deg) | $K_\theta(kJmol^{-1}rad^{-2})$ |
|---|---|---|
| O - C - H1 | 1.1026e+02 | 4.2593e+02 |
| O - C - H2 | 1.1026e+02 | 4.2593e+02 |
| O - C - CA | 1.1019e+02 | 5.6484e+02 |
| H - O - C | 1.0726e+02 | 3.9664e+02 |
| C - CA - HA1 | 1.1056e+02 | 3.8660e+02 |
| C - CA - HA2 | 1.1056e+02 | 3.8660e+02 |
| C - CA - N | 1.1421e+02 | 5.3723e+02 |
| H1 - C - H2 | 1.0846e+02 | 3.2803e+02 |
| H1 - C - CA | 1.0956e+02 | 3.8828e+02 |
| H2 - C - CA | 1.0956e+02 | 3.8828e+02 |
| CA - N - H4 | 1.1011e+02 | 3.8409e+02 |
| CA - N - H5 | 1.1011e+02 | 3.8409e+02 |
| CA - N - H3 | 1.1011e+02 | 3.8409e+02 |
| HA1 - CA - HA2 | 1.0975e+02 | 3.2803e+02 |
| HA1 - CA - N | 1.0801e+02 | 4.0668e+02 |
| HA2 - CA - N | 1.0801e+02 | 4.0668e+02 |
| H4 - N - H5 | 1.0830e+02 | 3.3974e+02 |
| H4 - N - H3 | 1.0830e+02 | 3.3974e+02 |
| H5 - N - H3 | 1.0830e+02 | 3.3974e+02 |

Table A.5: $RNH_3^+$ dihedral parameters

| dihedral | $C_0$ | $C_1$ | $C_2$ | $C_3$ | $C_4$ | $C_5$ |
|---|---|---|---|---|---|---|
| O- C- CA- HA1 | 0.65084 | 1.95253 | 0.00000 | -2.60338 | 0.00000 | 0.00000 |
| O- C- CA- HA2 | 0.65084 | 1.95253 | 0.00000 | -2.60338 | 0.00000 | 0.00000 |
| O- C- CA- N | 0.60250 | 1.80749 | 10.87840 | -2.40998 | 0.00000 | 0.00000 |
| H- O- C- H1 | 0.69733 | 2.09200 | 0.00000 | -2.78933 | 0.00000 | 0.00000 |
| H- O- C- H2 | 0.69733 | 2.09200 | 0.00000 | -2.78933 | 0.00000 | 0.00000 |
| H- O- C- CA | 1.71544 | 0.96232 | 0.00000 | -2.67776 | 0.00000 | 0.00000 |
| C- CA- N- H4 | 0.65084 | 1.95253 | 0.00000 | -2.60338 | 0.00000 | 0.00000 |
| C- CA- N- H5 | 0.65084 | 1.95253 | 0.00000 | -2.60338 | 0.00000 | 0.00000 |
| C- CA- N- H3 | 0.65084 | 1.95253 | 0.00000 | -2.60338 | 0.00000 | 0.00000 |
| H1- C- CA- HA1 | 0.65084 | 1.95253 | 0.00000 | -2.60338 | 0.00000 | 0.00000 |
| H1- C- CA- HA2 | 0.65084 | 1.95253 | 0.00000 | -2.60338 | 0.00000 | 0.00000 |
| H1- C- CA- N | 0.65084 | 1.95253 | 0.00000 | -2.60338 | 0.00000 | 0.00000 |
| H2- C- CA- HA1 | 0.65084 | 1.95253 | 0.00000 | -2.60338 | 0.00000 | 0.00000 |
| H2- C- CA- HA2 | 0.65084 | 1.95253 | 0.00000 | -2.60338 | 0.00000 | 0.00000 |
| H2- C- CA- N | 0.65084 | 1.95253 | 0.00000 | -2.60338 | 0.00000 | 0.00000 |
| HA1- CA- N- H4 | 0.65084 | 1.95253 | 0.00000 | -2.60338 | 0.00000 | 0.00000 |
| HA1- CA- N- H5 | 0.65084 | 1.95253 | 0.00000 | -2.60338 | 0.00000 | 0.00000 |
| HA1- CA- N- H3 | 0.65084 | 1.95253 | 0.00000 | -2.60338 | 0.00000 | 0.00000 |
| HA2- CA- N- H4 | 0.65084 | 1.95253 | 0.00000 | -2.60338 | 0.00000 | 0.00000 |
| HA2- CA- N- H5 | 0.65084 | 1.95253 | 0.00000 | -2.60338 | 0.00000 | 0.00000 |
| HA2- CA- N- H3 | 0.65084 | 1.95253 | 0.00000 | -2.60338 | 0.00000 | 0.00000 |

Table A.6: $RNHCOO^-$ non-bonded parameters

| no. | type | name | charge | mass | $\sigma$(nm) | $\epsilon$(kJ mol$^{-1}$) |
|---|---|---|---|---|---|---|
| 1 | oh | O1 | -0.728086 | 16.00000 | 3.06647e-01 | 8.80314e-01 |
| 2 | ho | H1 | 0.448184 | 1.00800 | 0.00000e+00 | 0.00000e+00 |
| 3 | c3 | C1 | 0.345507 | 12.01000 | 3.39967e-01 | 4.57730e-01 |
| 4 | h1 | H2 | -0.028072 | 1.00800 | 2.47135e-01 | 6.56888e-02 |
| 5 | h1 | H3 | -0.081747 | 1.00800 | 2.47135e-01 | 6.56888e-02 |
| 6 | c3 | C2 | 0.386149 | 12.01000 | 3.39967e-01 | 4.57730e-01 |
| 7 | h1 | H4 | -0.127592 | 1.00800 | 2.47135e-01 | 6.56888e-02 |
| 8 | h1 | H5 | -0.044848 | 1.00800 | 2.47135e-01 | 6.56888e-02 |
| 9 | n | N1 | -0.963181 | 14.01000 | 3.25000e-01 | 7.11280e-01 |
| 10 | hn | H6 | 0.357279 | 1.00800 | 1.06908e-01 | 6.56888e-02 |
| 11 | c | C3 | 1.145413 | 12.01000 | 3.39967e-01 | 3.59824e-01 |
| 12 | o | O2 | -0.854504 | 16.00000 | 2.95992e-01 | 8.78640e-01 |
| 13 | o | O3 | -0.854504 | 16.00000 | 2.95992e-01 | 8.78640e-01 |

Table A.7: $RNHCOO^-$ bond parameters

| bond | $r_0$(nm) | $K_r(kJmol^{-1}nm^{-2})$ |
|---|---|---|
| O1 - H1 | 9.7300e-02 | 3.1079e+05 |
| O1 - C1 | 1.4233e-01 | 2.6501e+05 |
| C1 - H2 | 1.0969e-01 | 2.7665e+05 |
| C1 - H3 | 1.0969e-01 | 2.7665e+05 |
| C1 - C2 | 1.5375e-01 | 2.5179e+05 |
| C2 - H4 | 1.0969e-01 | 2.7665e+05 |
| C2 - H5 | 1.0969e-01 | 2.7665e+05 |
| C2 - N1 | 1.4619e-01 | 2.7506e+05 |
| N1 - H6 | 1.0129e-01 | 3.3740e+05 |
| N1 - C3 | 1.3789e-01 | 3.5782e+05 |
| C3 - O2 | 1.2183e-01 | 5.3363e+05 |
| C3 - O3 | 1.2183e-01 | 5.3363e+05 |

Table A.8: $RNHCOO^-$ angle parameters

| angle | $\theta_0$(deg) | $K_\theta(kJmol^{-1}rad^{-2})$ |
|---|---|---|
| O1 - C1 - H2 | 1.1026e+02 | 4.2593e+02 |
| O1 - C1 - H3 | 1.1026e+02 | 4.2593e+02 |
| O1 - C1 - C2 | 1.1019e+02 | 5.6484e+02 |
| H1 - O1 - C1 | 1.0726e+02 | 3.9664e+02 |
| C1 - C2 - H4 | 1.0956e+02 | 3.8828e+02 |
| C1 - C2 - H5 | 1.0956e+02 | 3.8828e+02 |
| C1 - C2 - N1 | 1.1161e+02 | 5.5145e+02 |
| H2 - C1 - H3 | 1.0846e+02 | 3.2803e+02 |
| H2 - C1 - C2 | 1.0956e+02 | 3.8828e+02 |
| H3 - C1 - C2 | 1.0956e+02 | 3.8828e+02 |
| C2 - N1 - H6 | 1.1768e+02 | 3.8325e+02 |
| C2 - N1 - C3 | 1.2069e+02 | 5.3053e+02 |
| H4 - C2 - H5 | 1.0846e+02 | 3.2803e+02 |
| H4 - C2 - N1 | 1.0888e+02 | 4.1673e+02 |
| H5 - C2 - N1 | 1.0888e+02 | 4.1673e+02 |
| N1 - C3 - O2 | 1.2305e+02 | 6.2091e+02 |
| N1 - C3 - O3 | 1.2305e+02 | 6.2091e+02 |
| H6 - N1 - C3 | 1.1755e+02 | 4.0417e+02 |
| O2 - C3 - O3 | 1.3025e+02 | 6.5187e+02 |

Table A.9: $RNCOO^-$ dihedral parameters

| dihedral | $C_0$ | $C_1$ | $C_2$ | $C_3$ | $C_4$ | $C_5$ |
|---|---|---|---|---|---|---|
| O1- C1- C2- H4 | 1.04600 | -1.04600 | 0.00000 | 0.00000 | 0.00000 | 0.00000 |
| O1- C1- C2- H5 | 1.04600 | -1.04600 | 0.00000 | 0.00000 | 0.00000 | 0.00000 |
| O1- C1- C2- N1 | 0.65084 | 1.95253 | 0.00000 | -2.60338 | 0.00000 | 0.00000 |
| H1- O1- C1- H2 | 0.69733 | 2.09200 | 0.00000 | -2.78933 | 0.00000 | 0.00000 |
| H1- O1- C1- H3 | 0.69733 | 2.09200 | 0.00000 | -2.78933 | 0.00000 | 0.00000 |
| H1- O1- C1- C2 | 1.71544 | 0.96232 | 0.00000 | -2.67776 | 0.00000 | 0.00000 |
| C1- C2- N1- H6 | 0.00000 | 0.00000 | 0.00000 | 0.00000 | 0.00000 | 0.00000 |
| C1- C2- N1- C3 | 2.84512 | -4.10032 | 16.73600 | 2.51040 | -16.73600 | 6.73600 |
| H2- C1- C2- H4 | 0.65084 | 1.95253 | 0.00000 | -2.60338 | 0.00000 | 0.00000 |
| H2- C1- C2- H5 | 0.65084 | 1.95253 | 0.00000 | -2.60338 | 0.00000 | 0.00000 |
| H2- C1- C2- N1 | 0.65084 | 1.95253 | 0.00000 | -2.60338 | 0.00000 | 0.00000 |
| H3- C1- C2- H4 | 0.65084 | 1.95253 | 0.00000 | -2.60338 | 0.00000 | 0.00000 |
| H3- C1- C2- H5 | 0.65084 | 1.95253 | 0.00000 | -2.60338 | 0.00000 | 0.00000 |
| H3- C1- C2- N1 | 0.65084 | 1.95253 | 0.00000 | -2.60338 | 0.00000 | 0.00000 |
| C2- N1- C3- O2 | 20.92000 | 0.00000 | -20.92000 | 0.00000 | 0.00000 | 0.00000 |
| C2- N1- C3- O3 | 20.92000 | 0.00000 | -20.92000 | 0.00000 | 0.00000 | 0.00000 |
| H4- C2- N1- H6 | 0.00000 | 0.00000 | 0.00000 | 0.00000 | 0.00000 | 0.00000 |
| H4- C2- N1- C3 | 0.00000 | 0.00000 | 0.00000 | 0.00000 | 0.00000 | 0.00000 |
| H5- C2- N1- H6 | 0.00000 | 0.00000 | 0.00000 | 0.00000 | 0.00000 | 0.00000 |
| H5- C2- N1- C3 | 0.00000 | 0.00000 | 0.00000 | 0.00000 | 0.00000 | 0.00000 |
| H6- N1- C3- O2 | 29.28800 | -8.36800 | -20.92000 | 0.00000 | 0.00000 | 0.00000 |
| H6- N1- C3- O3 | 29.28800 | -8.36800 | -20.92000 | 0.00000 | 0.00000 | 0.00000 |

Table A.10: $RNH_2$ non-bonded parameters

| no. | type | name | charge | mass | $\sigma$(nm) | $\epsilon$(kJ mol$^{-1}$) |
|---|---|---|---|---|---|---|
| 1 | oh | O | -0.615643 | 16.00000 | 3.06647e-01 | 8.80314e-01 |
| 2 | ho | H | 0.361512 | 1.00800 | 0.00000e+00 | 0.00000e+00 |
| 3 | c3 | C | 0.197602 | 12.01000 | 3.39967e-01 | 4.57730e-01 |
| 4 | h1 | H1 | 0.021988 | 1.00800 | 2.47135e-01 | 6.56888e-02 |
| 5 | h1 | H2 | 0.021930 | 1.00800 | 2.47135e-01 | 6.56888e-02 |
| 6 | c3 | CA | 0.240250 | 12.01000 | 3.39967e-01 | 4.57730e-01 |
| 7 | h1 | HA1 | -0.055756 | 1.00800 | 2.47135e-01 | 6.56888e-02 |
| 8 | h1 | HA2 | 0.043363 | 1.00800 | 2.47135e-01 | 6.56888e-02 |
| 9 | n3 | N | -0.905880 | 14.01000 | 3.25000e-01 | 7.11280e-01 |
| 10 | hn | H3 | 0.345316 | 1.00800 | 1.06908e-01 | 6.56888e-02 |
| 11 | hn | H4 | 0.345316 | 1.00800 | 1.06908e-01 | 6.56888e-02 |

Table A.11: $RNH_2$ bond parameters

| bond | $r_0$(nm) | $K_r(kJmol^{-1}nm^{-2})$ |
|---|---|---|
| O - H | 9.7300e-02 | 3.1079e+05 |
| O - C | 1.4233e-01 | 2.6501e+05 |
| C - H1 | 1.0969e-01 | 2.7665e+05 |
| C - H2 | 1.0969e-01 | 2.7665e+05 |
| C - CA | 1.5375e-01 | 2.5179e+05 |
| CA - HA1 | 1.0969e-01 | 2.7665e+05 |
| CA - HA2 | 1.0969e-01 | 2.7665e+05 |
| CA - N | 1.4647e-01 | 2.7271e+05 |
| N - H3 | 1.0190e-01 | 3.2836e+05 |
| N - H4 | 1.0190e-01 | 3.2836e+05 |

Table A.12: $RNH_2$ angle parameters

| angle | $\theta_0$(deg) | $K_\theta(kJmol^{-1}rad^{-2})$ |
|---|---|---|
| O - C - H1 | 1.1026e+02 | 4.2593e+02 |
| O - C - H2 | 1.1026e+02 | 4.2593e+02 |
| O - C - CA | 1.1019e+02 | 5.6484e+02 |
| H - O - C | 1.0726e+02 | 3.9664e+02 |
| C - CA - HA1 | 1.0956e+02 | 3.8828e+02 |
| C - CA - HA2 | 1.0956e+02 | 3.8828e+02 |
| C - CA - N | 1.1104e+02 | 5.5229e+02 |
| H1 - C - H2 | 1.0846e+02 | 3.2803e+02 |
| H1 - C - CA | 1.0956e+02 | 3.8828e+02 |
| H2 - C - CA | 1.0956e+02 | 3.8828e+02 |
| CA - N - H3 | 1.0929e+02 | 3.9664e+02 |
| CA - N - H4 | 1.0929e+02 | 3.9664e+02 |
| HA1 - CA - HA2 | 1.0846e+02 | 3.2803e+02 |
| HA1 - CA - N | 1.0988e+02 | 4.1422e+02 |
| HA2 - CA - N | 1.0988e+02 | 4.1422e+02 |
| H3 - N - H4 | 1.0640e+02 | 3.4644e+02 |

Table A.13: $RNH_2$ dihedral parameters

| dihedral | $C_0$ | $C_1$ | $C_2$ | $C_3$ | $C_4$ | $C_5$ |
|---|---|---|---|---|---|---|
| O- C- CA- HA1 | 1.04600 | -1.04600 | 0.00000 | 0.00000 | 0.00000 | 0.00000 |
| O- C- CA- HA2 | 1.04600 | -1.04600 | 0.00000 | 0.00000 | 0.00000 | 0.00000 |
| O- C- CA- N | 0.65084 | 1.95253 | 0.00000 | -2.60338 | 0.00000 | 0.00000 |
| H- O- C- H1 | 0.69733 | 2.09200 | 0.00000 | -2.78933 | 0.00000 | 0.00000 |
| H- O- C- H2 | 0.69733 | 2.09200 | 0.00000 | -2.78933 | 0.00000 | 0.00000 |
| H- O- C- CA | 1.71544 | 0.96232 | 0.00000 | -2.67776 | 0.00000 | 0.00000 |
| C- CA- N- H3 | 1.25520 | 3.76560 | 0.00000 | -5.02080 | 0.00000 | 0.00000 |
| C- CA- N- H4 | 1.25520 | 3.76560 | 0.00000 | -5.02080 | 0.00000 | 0.00000 |
| H1- C- CA- HA1 | 0.65084 | 1.95253 | 0.00000 | -2.60338 | 0.00000 | 0.00000 |
| H1- C- CA- HA2 | 0.65084 | 1.95253 | 0.00000 | -2.60338 | 0.00000 | 0.00000 |
| H1- C- CA- N | 0.65084 | 1.95253 | 0.00000 | -2.60338 | 0.00000 | 0.00000 |
| H2- C- CA- HA1 | 0.65084 | 1.95253 | 0.00000 | -2.60338 | 0.00000 | 0.00000 |
| H2- C- CA- HA2 | 0.65084 | 1.95253 | 0.00000 | -2.60338 | 0.00000 | 0.00000 |
| H2- C- CA- N | 0.65084 | 1.95253 | 0.00000 | -2.60338 | 0.00000 | 0.00000 |
| HA1- CA- N- H3 | 1.25520 | 3.76560 | 0.00000 | -5.02080 | 0.00000 | 0.00000 |
| HA1- CA- N- H4 | 1.25520 | 3.76560 | 0.00000 | -5.02080 | 0.00000 | 0.00000 |
| HA2- CA- N- H3 | 1.25520 | 3.76560 | 0.00000 | -5.02080 | 0.00000 | 0.00000 |
| HA2- CA- N- H4 | 1.25520 | 3.76560 | 0.00000 | -5.02080 | 0.00000 | 0.00000 |

Table A.14: $HCO_3^-$ non-bonded parameters

| no. | type | name | charge | mass | $\sigma$(nm) | $\epsilon$(kJ mol$^{-1}$) |
|---|---|---|---|---|---|---|
| 1 | oh | O | -0.728558 | 16.00000 | 3.06647e-01 | 8.80314e-01 |
| 2 | o | O1 | -0.826268 | 16.00000 | 2.95992e-01 | 8.78640e-01 |
| 3 | o | O2 | -0.826268 | 16.00000 | 2.95992e-01 | 8.78640e-01 |
| 4 | c | C | 1.057315 | 12.01000 | 3.39967e-01 | 3.59824e-01 |
| 5 | ho | H | 0.323778 | 1.00800 | 0.00000e+00 | 0.00000e+00 |

Table A.15: $HCO_3^-$ bond parameters

| bond | $r_0$(nm) | $K_r(kJmol^{-1}nm^{-2})$ |
|---|---|---|
| O - C | 1.3513e-01 | 3.3480e+05 |
| O - H | 9.7300e-02 | 3.1079e+05 |
| O1 - C | 1.2183e-01 | 5.3363e+05 |
| O2 - C | 1.2183e-01 | 5.3363e+05 |

Table A.16: $HCO_3^-$ angle parameters

| angle | $\theta_0$(deg) | $K_\theta(kJmol^{-1}rad^{-2})$ |
|---|---|---|
| O - C - O1 | 1.2210e+02 | 6.3513e+02 |
| O - C - O2 | 1.2210e+02 | 6.3513e+02 |
| O1 - C - O2 | 1.3025e+02 | 6.5187e+02 |
| C - O - H | 1.0655e+02 | 4.1756e+02 |

Table A.17: $HCO_3^-$ dihedral parameters

| dihedral | $C_0$ | $C_1$ | $C_2$ | $C_3$ | $C_4$ | $C_5$ |
|---|---|---|---|---|---|---|
| H- O- C- O1 | 27.19600 | -7.94960 | -19.24640 | 0.00000 | 0.00000 | 0.00000 |
| H- O- C- O2 | 27.19600 | -7.94960 | -19.24640 | 0.00000 | 0.00000 | 0.00000 |

Table A.18: $H_3O^+$ and $OH^-$ non-bonded parameters

| no. | name | charge | mass | $\sigma$(nm) | $\epsilon$(kJ mol$^{-1}$) |
|---|---|---|---|---|---|
| 1 | O(H3O) | -0.4166 | 15.99940 | 2.42e-01 | 0.300000 |
| 2 | H1(H3O) | 0.4722 | 1.00800 | 1.00e-01 | 0.008314 |
| 3 | H2(H3O) | 0.4722 | 1.00800 | 1.00e-01 | 0.008314 |
| 4 | H3(H3O) | 0.4722 | 1.00800 | 1.00e-01 | 0.008314 |
| 5 | O(OH) | -1.20 | 15.99940 | 3.35e-01 | 0.763580 |
| 6 | H(OH) | 0.20 | 1.008000 | 1.00e-01 | 0.008314 |

* O–H distance constrained to 0.098 nm and 0.1 nm for $H_3O^+$ and $OH^-$ respectively. For $H_3O^+$, H–O–H angle of 112.5 degrees implemented by constraining the H–H distance to 0.163 nm .

# Appendix B

# Supporting Information:Accurately Predicting $CO_2$ Reactive Absorption Properties in Aqueous Alkanolamine Solutions by Molecular Simulation Requiring No Solvent Experimental Data

Table B.1: Constants of the equation $\ln K_1 = A + \frac{B}{T} + C \ln T$.

| amine | A | B | C |
|---|---|---|---|
| MEA | -857.349 | 51103.3 | -122.721 |
| AMP | -81.2367 | 12575.7 | -7.78077 |
| 1–AP | -419.364 | 28824.9 | -58.2029 |
| AMPD | -318.81 | 22804.1 | -43.4493 |
| SAPD | -1693.36 | 87427.4 | -247.224 |
| 2-AEE | 403.862 | -6781.68 | 64.5314 |
| 2-AP | -152.481 | 15845.9 | -18.8785 |

Table B.2: Constants of the equation $\ln K_2 = A + \frac{B}{T} + C \ln T$.

| amine | A | B | C |
|---|---|---|---|
| MEA | 638.849 | -32494.7 | 93.6555 |
| AMP | 149.869 | -7012.08 | 21.4173 |
| 1–AP | 347.043 | -17969.4 | 50.5784 |
| AMPD | 217.334 | -10754.1 | 31.4043 |
| SAPD | 2.07136 | -1125.76 | -0.338594 |
| 2-AEE | -179.977 | 4697.4 | -28.3349 |
| 2-AP | 89.2047 | -5012.15 | 12.6011 |

Table B.3: BAR predicted residual chemical potential (kJ/mol) of neutral ($RNH_2$), protonated ($RNH_3^+$) and carbamate forms ($RNHCO_2^-$) of the seven alkanolamines in TIP3P water at P=1.0 bar and T=298.15-353.15K. Subscripts indicate uncertainty obtained from the block averaging.

| form | MEA | AMP | 1AP | AMPD | SAPD | 2AEE | 2AP |
|---|---|---|---|---|---|---|---|
| | | | | T=298.15 K | | | |
| $RNH_2$ | -30.23 $_{0.14}$ | -34.35 $_{0.18}$ | -33.14 $_{0.07}$ | -57.48 $_{0.12}$ | -51.98 $_{0.13}$ | -41.63 $_{0.07}$ | -37.23 $_{0.13}$ |
| $RNH_3^+$ | -239.43 $_{0.10}$ | -222.50 $_{0.16}$ | -232.10 $_{0.14}$ | -228.14 $_{0.23}$ | -234.82 $_{0.22}$ | -215.89 $_{0.43}$ | -232.25 $_{0.22}$ |
| $RNHCO_2^-$ | -366.79 $_{0.19}$ | -352.33 $_{0.09}$ | -363.16 $_{0.11}$ | -360.12 $_{0.40}$ | -362.55 $_{0.31}$ | -373.19 $_{0.24}$ | -362.34 $_{0.16}$ |
| | | | | T=313.15 K | | | |
| $RNH_2$ | -29.17 $_{0.06}$ | -32.94 $_{0.13}$ | -31.69 $_{0.24}$ | -55.43 $_{0.12}$ | -50.03 $_{0.18}$ | -39.64 $_{0.06}$ | -35.58 $_{0.10}$ |
| $RNH_3^+$ | -237.70 $_{0.18}$ | -220.50 $_{0.11}$ | -230.04 $_{0.09}$ | -226.27 $_{0.16}$ | -232.63 $_{0.20}$ | -214.24 $_{0.11}$ | -230.13 $_{0.22}$ |
| $RNHCO_2^-$ | -363.90 $_{0.25}$ | -349.21 $_{0.08}$ | -359.96 $_{0.15}$ | -356.70 $_{0.43}$ | -359.25 $_{0.22}$ | -369.28 $_{0.20}$ | -359.27 $_{0.12}$ |
| | | | | T=333.15 K | | | |
| $RNH_2$ | -27.45 $_{0.06}$ | -30.67 $_{0.13}$ | -29.52 $_{0.10}$ | -52.74 $_{0.06}$ | -48.05 $_{0.08}$ | -35.15 $_{0.10}$ | -33.50 $_{0.08}$ |
| $RNH_3^+$ | -235.80 $_{0.08}$ | -217.39 $_{0.08}$ | -228.16 $_{0.18}$ | -222.82 $_{0.27}$ | -232.13 $_{0.07}$ | -209.79 $_{0.13}$ | -227.88 $_{0.25}$ |
| $RNHCO_2^-$ | -359.78 $_{0.16}$ | -344.97 $_{0.05}$ | -355.67 $_{0.19}$ | -351.85 $_{0.18}$ | -359.12 $_{0.12}$ | -359.08 $_{0.28}$ | -354.96 $_{0.04}$ |
| | | | | T=353.15 K | | | |
| $RNH_2$ | -26.63 $_{0.10}$ | -28.92 $_{0.10}$ | -27.55 $_{0.08}$ | -50.06 $_{0.13}$ | -45.87 $_{0.07}$ | -37.13 $_{0.05}$ | -31.43 $_{0.10}$ |
| $RNH_3^+$ | -235.05 $_{0.04}$ | -215.07 $_{0.14}$ | -226.02 $_{0.08}$ | -221.01 $_{0.18}$ | -228.15 $_{0.11}$ | -211.71 $_{0.18}$ | -225.79 $_{0.17}$ |
| $RNHCO_2^-$ | -358.13 $_{0.08}$ | -341.10 $_{0.12}$ | -352.19 $_{0.15}$ | -347.68 $_{0.21}$ | -350.94 $_{0.14}$ | -364.63 $_{0.17}$ | -351.00 $_{0.32}$ |

Table B.4: BAR predicted residual chemical potential (kJ/mol) of the small molecules ($CO_2$, $H_2O$, HCO3$^-$ in TIP3P water at P=1.0 bar and T=298.15-353.15K. Subscripts indicate uncertainty obtained from the block averaging. Numbers in inside the paranthesis are the density (kg/m3) of the solvent.

| T (Kelvin) | $CO_2$ | $H_2O$ | $HCO_3^-$ |
|---|---|---|---|
| 298.15 ($\rho_s$=987.425) | $1.11_{0.06}$ | $-26.76_{0.04}$ | $-382.89_{0.09}$ |
| 313.15 ($\rho_s$=974.125) | $1.67_{0.04}$ | $-26.11_{0.06}$ | $-380.52_{0.09}$ |
| 333.15 ($\rho_s$=954.257) | $2.24_{0.01}$ | $-25.06_{0.06}$ | $-376.9_{0.09}$ |
| 353.15 ($\rho_s$=932.802) | $2.74_{0.06}$ | $-24.16_{0.02}$ | $-373.53_{0.13}$ |

Table B.5: Ideal gas reaction free energy of the main reaction (R1 : $CO_2 + 2RNH_2 = RNHCO_2^- + RNH_3^+$) from different QM methods.

| QM method | MEA | AMP | 1AP | AMPD | SAPD | 2AEE | 2AP |
|---|---|---|---|---|---|---|---|
| | | | | T=298.15 K | | | |
| G4 | 521.69 | 504.67 | 518.80 | 472.86 | 484.47 | 483.95 | 510.51 |
| CBS-QB3 | 517.33 | 499.36 | 510.21 | 467.31 | 478.75 | 480.95 | 505.95 |
| CBS-APNO | 521.74 | 497.76 | 514.78 | 465.85 | 477.16 | 477.27 | 505.57 |
| G3B3 | 522.89 | 504.41 | 515.65 | 471.94 | 484.88 | 484.45 | 510.83 |
| G3 | 526.26 | 504.5 | 519.75 | 469.88 | 483.58 | 481.21 | 511.06 |
| avg | 521.98 | 502.14 | 515.84 | 469.57 | 481.77 | 481.57 | 508.79 |
| std | 3.20 | 3.32 | 3.77 | 2.98 | 3.56 | 2.87 | 2.77 |
| | | | | T=313.15 K | | | |
| G4 | 524.07 | 507.05 | 521.17 | 475.48 | 486.93 | 487.29 | 512.85 |
| CBS-QB3 | 519.67 | 501.73 | 512.57 | 469.89 | 481.18 | 484.31 | 508.27 |
| CBS-APNO | 524.27 | 500.13 | 517.34 | 468.23 | 479.71 | 480.34 | 507.86 |
| G3B3 | 525.24 | 506.77 | 518.00 | 474.54 | 487.36 | 487.65 | 513.14 |
| G3 | 528.76 | 506.84 | 522.27 | 472.48 | 485.98 | 484.28 | 513.35 |
| avg | 524.4 | 504.51 | 518.27 | 472.12 | 484.23 | 484.77 | 511.09 |
| std | 3.25 | 3.32 | 3.80 | 3.06 | 3.53 | 2.95 | 2.77 |
| | | | | T=333.15 K | | | |
| G4 | 527.22 | 510.24 | 524.34 | 478.98 | 490.2 | 491.75 | 515.96 |
| CBS-QB3 | 522.82 | 504.88 | 515.71 | 473.35 | 484.42 | 488.79 | 511.36 |
| CBS-APNO | 527.65 | 503.29 | 520.78 | 471.4 | 483.11 | 484.44 | 510.91 |
| G3B3 | 528.38 | 509.93 | 521.14 | 478.01 | 490.67 | 491.92 | 516.22 |
| G3 | 532.1 | 509.98 | 525.64 | 475.97 | 489.16 | 488.37 | 516.40 |
| avg | 527.64 | 507.67 | 521.52 | 475.54 | 487.51 | 489.06 | 514.17 |
| std | 3.31 | 3.32 | 3.85 | 3.17 | 3.49 | 3.06 | 2.78 |
| | | | | T=353.15 K | | | |
| G4 | 530.39 | 513.43 | 527.52 | 482.49 | 493.49 | 496.23 | 519.09 |
| CBS-QB3 | 525.97 | 508.04 | 518.86 | 476.80 | 487.66 | 493.30 | 514.46 |
| CBS-APNO | 531.05 | 506.46 | 524.21 | 474.57 | 486.53 | 488.54 | 513.97 |
| G3B3 | 531.52 | 513.09 | 524.28 | 481.50 | 493.99 | 496.37 | 519.32 |
| G3 | 535.46 | 513.12 | 529.01 | 479.46 | 492.34 | 492.47 | 519.46 |
| avg | 530.88 | 510.83 | 524.77 | 478.96 | 490.80 | 493.38 | 517.26 |
| std | 3.38 | 3.32 | 3.91 | 3.28 | 3.46 | 3.21 | 2.79 |

Table B.6: Ideal gas reaction free energy of the carbamate reversion reaction (R2 : $RNHCO_2^- + H_2O = RNH_2 + HCO_3^-$) from different QM methods.

| method | MEA | AMP | 1AP | AMPD | SAPD | 2AEE | 2AP |
|---|---|---|---|---|---|---|---|
| | | | | T=298.15 K | | | |
| G4 | 37.16 | 33.95 | 37.94 | 53.22 | 51.37 | 37.48 | 36.76 |
| CBS-QB3 | 38.70 | 36.28 | 39.56 | 56.34 | 54.10 | 39.96 | 38.45 |
| CBS-APNO | 36.11 | 37.36 | 36.94 | 57.88 | 54.80 | 40.93 | 38.24 |
| G3B3 | 39.76 | 37.78 | 40.77 | 57.87 | 54.86 | 41.27 | 40.09 |
| G3 | 42.23 | 41.86 | 42.68 | 62.78 | 59.75 | 47.68 | 43.96 |
| avg | 38.79 | 37.45 | 39.58 | 57.62 | 54.98 | 41.46 | 39.50 |
| std | 2.38 | 2.88 | 2.28 | 3.45 | 3.02 | 3.78 | 2.76 |
| | | | | T=313.15 K | | | |
| G4 | 36.78 | 33.52 | 37.54 | 52.63 | 50.95 | 36.55 | 36.40 |
| CBS-QB3 | 38.33 | 35.86 | 39.18 | 55.76 | 53.68 | 39.02 | 38.10 |
| CBS-APNO | 35.67 | 36.95 | 36.47 | 57.52 | 54.27 | 40.17 | 37.92 |
| G3B3 | 39.47 | 37.45 | 40.47 | 57.37 | 54.49 | 40.50 | 39.83 |
| G3 | 41.90 | 41.57 | 42.33 | 62.36 | 59.44 | 47.01 | 43.73 |
| avg | 38.43 | 37.07 | 39.20 | 57.13 | 54.57 | 40.65 | 39.20 |
| std | 2.42 | 2.94 | 2.33 | 3.52 | 3.07 | 3.88 | 2.81 |
| | | | | T=333.15 K | | | |
| G4 | 36.27 | 32.95 | 37.02 | 51.84 | 50.38 | 35.31 | 35.92 |
| CBS-QB3 | 37.83 | 35.31 | 38.68 | 55.00 | 53.14 | 37.77 | 37.65 |
| CBS-APNO | 35.08 | 36.41 | 35.84 | 57.04 | 53.58 | 39.15 | 37.51 |
| G3B3 | 39.10 | 37.02 | 40.09 | 56.71 | 54.00 | 39.48 | 39.49 |
| G3 | 41.45 | 41.18 | 41.86 | 61.80 | 59.07 | 46.13 | 43.44 |
| avg | 37.95 | 36.57 | 38.70 | 56.48 | 54.03 | 39.57 | 38.80 |
| std | 2.48 | 3.01 | 2.39 | 3.62 | 3.15 | 4.02 | 2.88 |
| | | | | T=353.15 K | | | |
| G4 | 35.77 | 32.39 | 36.52 | 51.06 | 49.82 | 34.08 | 35.45 |
| CBS-QB3 | 37.35 | 34.77 | 38.19 | 54.26 | 52.60 | 36.53 | 37.20 |
| CBS-APNO | 34.49 | 35.88 | 35.23 | 56.57 | 52.89 | 38.15 | 37.10 |
| G3B3 | 38.74 | 36.59 | 39.72 | 56.06 | 53.51 | 38.38 | 39.16 |
| G3 | 41.02 | 40.80 | 41.40 | 61.25 | 58.70 | 45.25 | 43.15 |
| avg | 37.47 | 36.09 | 38.21 | 55.84 | 53.51 | 38.48 | 38.41 |
| std | 2.55 | 3.08 | 2.46 | 3.72 | 3.23 | 4.16 | 2.96 |

Table B.7: Quantities contributing to the equilibrium constant of the main reaction (R1 : $CO_2 + 2RNH_2 = RNHCO_2^- + RNH_3^+$). $\Delta G^0(T, P^0)$ is average ideal gas reaction free energy from Table. B.5 and $\Delta G^{res,\infty}(T, P)$ is the infinte dilution residual chemical potential change of the reaction in TIP3P water.

| T | $\Delta G^0(T, P^0)$ | $\Delta G^* = \Delta G^0 + \Delta nRT \ln(RT/P^0)$ | $\Delta G^{res,\infty}(T, P)$ | $\Delta G^\dagger$ | $\Delta \tilde{G}(T, P)$ | $pK_a$ |
|---|---|---|---|---|---|---|
| | | | MEA | | | |
| 298.15 | 521.981359424184 | 514.022862016923 | -546.87 | -32.8344832486188 | -32.8344832486188 | -5.75235440188678 |
| 313.15 | 524.399969692071 | 515.913275476776 | -544.93 | -29.0040697887656 | -29.0040697887656 | -4.83789889942046 |
| 333.15 | 527.635635447790 | 518.435430369241 | -542.92 | -24.4377473789792 | -24.4377473789792 | -3.83152458395972 |
| 353.15 | 530.878652602496 | 520.954947813168 | -542.66 | -21.6354898675257 | -21.6354898675257 | -3.20005752434263 |
| | | | AMP | | | |
| 298.15 | 502.138883348923 | 494.180385941662 | -507.24 | -13.0469593238797 | -13.0469593238797 | -2.28572910161802 |
| 313.15 | 504.506033823886 | 496.019339608591 | -505.50 | -9.45420450015613 | -9.45420450015613 | -1.5769678489712 |
| 323.15 | 507.665034990057 | 498.464829911508 | -503.26 | -4.74834783671269 | -4.74834783671269 | -0.744479889550139 |
| 353.15 | 510.828762055642 | 500.905057266314 | -501.07 | -0.095380414379803 | -0.095380414379803 | -0.014107506443343 |
| | | | 1-AP | | | |
| 298.15 | 515.837690267762 | 507.879192860501 | -530.09 | -22.1981524050408 | -22.1981524050408 | -3.88894927122879 |
| 313.15 | 518.268902933946 | 509.782208718651 | -528.29 | -18.4813877559819 | -18.4813877559819 | -3.08270825906853 |
| 333.15 | 521.520846787448 | 512.320641708899 | -527.03 | -14.6625360393213 | -14.6625360393213 | -2.29889712937206 |
| 353.15 | 524.774891040553 | 514.851186251225 | -525.85 | -10.9292514294691 | -10.9292514294691 | -1.61652144168921 |
| | | | AMPD | | | |
| 298.15 | 469.568510121229 | 461.610012713968 | -474.41 | -12.7873325515738 | -12.7873325515738 | -2.24024444467326 |
| 313.15 | 472.124171470308 | 463.637477255013 | -473.78 | -10.1161192196197 | -10.1161192196197 | -1.68737568194519 |
| 333.15 | 475.540996701142 | 466.340791622593 | -471.43 | -5.04238612562726 | -5.04238612562726 | -0.790581312694022 |
| 353.15 | 478.962547831330 | 469.038843042002 | -471.31 | -2.20159463869220 | -2.20159463869220 | -0.325633000788859 |
| | | | SAPD | | | |
| 298.15 | 481.767631646112 | 473.809134238851 | -494.52 | -20.6982110266908 | -20.6982110266908 | -3.62617082806 |
| 313.15 | 484.228775008110 | 475.742080792815 | -493.49 | -17.7215156818177 | -17.7215156818177 | -2.95596107158509 |
| 333.15 | 487.512224857356 | 478.312019778806 | -491.84 | -13.4811579694142 | -13.4811579694142 | -2.11367223742095 |
| 353.15 | 490.801450805690 | 480.877746016362 | -494.81 | -13.8626916643318 | -13.8626916643318 | -2.0504001083272 |
| | | | 2-AEE | | | |
| 298.15 | 481.568618773524 | 473.610121366263 | -506.93 | -33.3072238992787 | -33.3072238992787 | -5.83517500674247 |
| 313.15 | 484.771728333617 | 476.285034118322 | -505.91 | -29.5985623563107 | -29.5985623563107 | -4.93706067082656 |
| 333.15 | 489.055493545367 | 479.855288466818 | -503.97 | -24.0678892814022 | -24.0678892814022 | -3.7735355896606 |
| 353.15 | 493.381266751496 | 483.457561962168 | -501.31 | -17.7828757185262 | -17.7828757185262 | -2.63022587405955 |
| | | | 2-AP | | | |
| 298.15 | 508.785598236164 | 500.827100828903 | -521.24 | -20.4002444366387 | -20.4002444366387 | -3.57396932353431 |
| 313.15 | 511.091837119496 | 502.605142904201 | -519.91 | -17.2784535704317 | -17.2784535704317 | -2.88205800499271 |
| 333.15 | 514.171023096798 | 504.970818018249 | -518.08 | -13.0623597299711 | -13.0623597299711 | -2.04801005811855 |
| 353.15 | 517.257035372863 | 507.333330583535 | -516.67 | -9.26710709715911 | -9.26710709715911 | -1.37067734434175 |

Table B.8: Quantities contributing to the equilibrium constant of the carbamate reversion reaction (R2 : $RNHCO_2^- + H_2O = RNH_2 + HCO_3^-$). $\Delta G^0(T, P^0)$ is average ideal gas reaction free energy from Table. B.6 and $\Delta G^{res,\infty}(T, P)$ is the infinte dilution residual chemical potential change of the reaction in TIP3P water.

| T | $\Delta G^0(T, P^0)$ | $\Delta G^* = \Delta G^0 + \Delta n RT \ln(RT/P^0)$ | $\Delta G^{res,\infty}(T, P)$ | $\Delta G^\dagger$ | $\Delta \tilde{G}(T, P)$ | $pK_a$ |
|---|---|---|---|---|---|---|
| | | | MEA | | | |
| 298.15 | 38.7933324730883 | 38.7933324730883 | -19.57 | 19.2233324730883 | 9.26651795460035 | 1.62342421967462 |
| 313.13 | 38.4289131230785 | 38.4289131230785 | -19.68 | 18.7489131230785 | 8.29116881160942 | 1.38297269178863 |
| 333.15 | 37.9468713894125 | 37.9468713894125 | -19.51 | 18.4368713894125 | 7.31122068730195 | 1.14630540072808 |
| 353.15 | 37.4732312544000 | 37.4732312544000 | -17.87 | 19.6032312544001 | 7.80967416164805 | 1.15511165758985 |
| | | | AMP | | | |
| 298.15 | 37.4469762578401 | 37.4469762578401 | -38.15 | -0.7030237421599 | -10.6598382606479 | -1.86752345324692 |
| 313.15 | 37.0689043098887 | 37.0689043098887 | -38.18 | -1.11109569011131 | -11.5688400015804 | -1.92969051304986 |
| 333.15 | 36.5732099779229 | 36.5732099779229 | -37.54 | -0.966790022077099 | -12.0924407241877 | -1.89593922861544 |
| 353.15 | 36.0853921449826 | 36.0853921449826 | -37.19 | -1.1046078550173 | -12.8981649477693 | -1.90773909183698 |
| | | | 1-AP | | | |
| 298.15 | 39.5762564656342 | 39.5762564656342 | -26.11 | 13.4662564656342 | 3.50944194714629 | 0.614827822322505 |
| 313.15 | 39.1987096174900 | 39.1987096174900 | -26.18 | 13.0187096174900 | 2.56096530602092 | 0.427170784158423 |
| 333.15 | 38.6998646858752 | 38.6998646858752 | -25.69 | 13.0098646858753 | 1.88421398376470 | 0.295420526625342 |
| 353.15 | 38.2115217530083 | 38.2115217530083 | -24.73 | 13.4815217530083 | 1.68796466025629 | 0.249663125029825 |
| | | | AMPD | | | |
| 298.15 | 57.6181648881200 | 57.6181648881200 | -53.49 | 4.12816488811999 | -5.82864963036797 | -1.02113555753046 |
| 313.15 | 57.1282466553614 | 57.1282466553614 | -53.18 | 3.94824665536139 | -6.50949765610768 | -1.08578871088159 |
| 333.15 | 56.4792231445983 | 56.4792231445983 | -52.73 | 3.74922314459834 | -7.37642755751222 | -1.15652899958845 |
| 353.15 | 55.8380761325025 | 55.8380761325025 | -51.75 | 4.08807613250256 | -7.70548096024949 | -1.1397006712816 |
| | | | SAPD | | | |
| 298.15 | 54.9753369510657 | 54.9753369510657 | -45.56 | 9.41533695106570 | -0.541477567422263 | -0.094862795461093 |
| 313.15 | 54.5668092071642 | 54.5668092071642 | -45.23 | 9.33680920716424 | -1.12093510430484 | -0.186972750615111 |
| 333.15 | 54.0327825804991 | 54.0327825804991 | -44.72 | 9.31278258049913 | -1.81286812161143 | -0.284234412759578 |
| 353.15 | 53.5071575526666 | 53.5071575526666 | -44.30 | 9.20715755266664 | -2.58639954008541 | -0.382548643912593 |
| | | | 2-AEE | | | |
| 298.15 | 41.4629405064873 | 41.4629405064873 | -24.57 | 16.8929405064873 | 6.93612598799935 | 1.21515708217481 |
| 313.15 | 40.6506109180385 | 40.6506109180385 | -24.81 | 15.8406109180385 | 5.38286660656943 | 0.897865872662339 |
| 333.15 | 39.5699552665004 | 39.5699552665004 | -24.69 | 14.8799552665004 | 3.75430456438984 | 0.588626685228168 |
| 353.15 | 38.4793227162456 | 38.4793227162456 | -25.44 | 13.0393227162457 | 1.24576562349361 | 0.184258442098497 |
| | | | 2-AP | | | |
| 298.15 | 39.5001169760129 | 39.5001169760129 | -31.02 | 8.48011697601286 | -1.47669754247510 | -0.258706298021893 |
| 313.15 | 39.1971343177103 | 39.1971343177103 | -30.76 | 8.43713431771031 | -2.02060999375876 | -0.337039144373799 |
| 333.15 | 38.8006838721051 | 38.8006838721051 | -30.38 | 8.42068387210510 | -2.70496683000546 | -0.424104020196089 |
| 353.15 | 38.4115848255390 | 38.4115848255390 | -29.80 | 8.61158482553905 | -3.18197226721300 | -0.470638490660115 |

Table B.9: Gaussian output of the ideal gas relative gibbs free energies (in Hartree) of the most stabe conformer of the neutral ($RNH_2$), protonated ($RNH_3^+$) and carbamate forms ($RNHCO_2^-$) of th each amine using different QM method. The values were used in calculation of the data in table B.5 and table B.6. The calculation were performed at $P^0$=1.0 bar and T=298.15 K.

| | MEA | AMP | 1AP | AMPD | SAPD | 2AEE | 2AP |
|---|---|---|---|---|---|---|---|
| | | | | G4 | | | |
| RNH2 | -210.285299 | -288.857045 | -249.573028 | -364.056233 | -324.769447 | -364.034805 | -249.570793 |
| RNH3+ | -210.634676 | -289.214133 | -249.923214 | -364.418092 | -325.12759 | -364.398438 | -249.924582 |
| RNHCOO- | -398.293192 | -476.863713 | -437.581215 | -552.070243 | -512.782752 | -552.042817 | -437.578533 |
| | | | | CBS-QB3 | | | |
| RNH2 | -210.06686 | -288.533647 | -249.302145 | -363.676932 | -324.44235 | -363.656377 | -249.299868 |
| RNH3+ | -210.415436 | -288.889989 | -249.653102 | -364.037841 | -324.799754 | -364.018328 | -249.652869 |
| RNHCOO- | -397.914019 | -476.379884 | -437.149633 | -551.530808 | -512.295374 | -551.504015 | -437.146933 |
| | | | | CBS-APNO | | | |
| RNH2 | -210.321709 | -288.904251 | -249.615545 | -364.119546 | -324.826468 | -364.098073 | -249.612288 |
| RNH3+ | -210.670136 | -289.261335 | -249.966309 | -364.480967 | -325.184759 | -364.461601 | -249.966062 |
| RNHCOO- | -398.369167 | -476.952184 | -437.663316 | -552.175296 | -512.881042 | -552.147366 | -437.660556 |
| | | | | G3B3 | | | |
| RNH2 | -210.250444 | -288.809444 | -249.531892 | -363.996301 | -324.715811 | -363.975037 | -249.529529 |
| RNH3+ | -210.599806 | -289.166597 | -249.883628 | -364.358171 | -325.073898 | -364.338465 | -249.88336 |
| RNHCOO- | -398.227019 | -476.785267 | -437.508851 | -551.979774 | -512.698138 | -551.952187 | -437.50623 |
| | | | | G3 | | | |
| RNH2 | -210.246513 | -288.803158 | -249.527303 | -363.988275 | -324.708517 | -363.966891 | -249.524152 |
| RNH3+ | -210.595275 | -289.160347 | -249.878373 | -364.350685 | -325.066862 | -364.330733 | -249.878045 |
| RNHCOO- | -398.218287 | -476.774792 | -437.499248 | -551.967875 | -512.686963 | -551.940741 | -437.496583 |

Table B.10: Gaussian output of the ideal gas relative gibbs free energies (in Hartree) of the most stabe conformer of the neutral ($RNH_2$), protonated ($RNH_3^+$) and carbamate forms ($RNHCO_2^-$) of th each amine using different QM method. The values were used in calculation of the data in table B.5 and table B.6. The calculation were performed at $P^0$=1.0 bar and T=313.15 K..

| | MEA | AMP | 1AP | AMPD | SAPD | 2AEE | 2AP |
|---|---|---|---|---|---|---|---|
| | | | | G4 | | | |
| RNH2 | -210.286980 | -288.859032 | -249.574877 | -364.058353 | -324.771426 | -364.037051 | -249.572640 |
| RNH3+ | -210.636381 | -289.216153 | -249.925088 | -364.420220 | -325.129575 | -364.400544 | -249.926457 |
| RNHCOO- | -398.295172 | -476.865983 | -437.583362 | -552.072585 | -512.785015 | -552.045157 | -437.580689 |
| | | | | CBS-QB3 | | | |
| RNH2 | -210.068536 | -288.535626 | -249.303989 | -363.679044 | -324.444321 | -363.658624 | -249.301710 |
| RNH3+ | -210.417139 | -288.892005 | -249.654974 | -364.039966 | -324.801738 | -364.020433 | -249.654741 |
| RNHCOO- | -397.916001 | -476.382151 | -437.151779 | -551.533150 | -512.297635 | -551.506353 | -437.149090 |
| | | | | CBS-APNO | | | |
| RNH2 | -210.323431 | -288.906237 | -249.617439 | -364.121668 | -324.828455 | -364.100289 | -249.614135 |
| RNH3+ | -210.671845 | -289.263356 | -249.968186 | -364.483105 | -325.186756 | -364.463722 | -249.967940 |
| RNHCOO- | -398.371161 | -476.954454 | -437.665472 | -552.177719 | -512.883270 | -552.149732 | -437.662723 |
| | | | | G3B3 | | | |
| RNH2 | -210.252126 | -288.811435 | -249.533744 | -363.998428 | -324.717793 | -363.977263 | -249.531379 |
| RNH3+ | -210.601515 | -289.168627 | -249.885510 | -364.360310 | -325.075892 | -364.340579 | -249.885242 |
| RNHCOO- | -398.229010 | -476.787549 | -437.511009 | -551.982129 | -512.700396 | -551.954538 | -437.508398 |
| | | | | G3 | | | |
| RNH2 | -210.248238 | -288.805155 | -249.529201 | -363.990406 | -324.710509 | -363.969123 | -249.526009 |
| RNH3+ | -210.596993 | -289.162382 | -249.880264 | -364.352803 | -325.068874 | -364.332871 | -249.879936 |
| RNHCOO- | -398.220292 | -476.777083 | -437.501419 | -551.970252 | -512.689246 | -551.943126 | -437.498761 |

Table B.11: Gaussian output of the ideal gas relative gibbs free energies (in Hartree) of the most stabe conformer of the neutral ($RNH_2$), protonated ($RNH_3^+$) and carbamate forms ($RNHCO_2^-$) of th each amine using different QM method. The values were used in calculation of the data in table B.5 and table B.6. The calculation were performed at $P^0$=1.0 bar and T=333.15 K..

| | MEA | AMP | 1AP | AMPD | SAPD | 2AEE | 2AP |
|---|---|---|---|---|---|---|---|
| | | | | G4 | | | |
| RNH2 | -210.289256 | -288.861739 | -249.577389 | -364.061244 | -324.774116 | -364.040106 | -249.575149 |
| RNH3+ | -210.638691 | -289.218905 | -249.927633 | -364.423122 | -325.132276 | -364.403414 | -249.929005 |
| RNHCOO- | -398.297862 | -476.869080 | -437.586283 | -552.075782 | -512.788097 | -552.048348 | -437.583622 |
| | | | | CBS-QB3 | | | |
| RNH2 | -210.070808 | -288.538321 | -249.306493 | -363.681922 | -324.447001 | -363.661679 | -249.304212 |
| RNH3+ | -210.419446 | -288.894753 | -249.657517 | -364.042863 | -324.804436 | -364.023299 | -249.657286 |
| RNHCOO- | -397.918691 | -476.385244 | -437.154699 | -551.536346 | -512.300714 | -551.509540 | -437.152025 |
| | | | | CBS-APNO | | | |
| RNH2 | -210.325764 | -288.908941 | -249.620012 | -364.124560 | -324.831156 | -364.103304 | -249.616644 |
| RNH3+ | -210.674160 | -289.266109 | -249.970736 | -364.486020 | -325.189472 | -364.466610 | -249.970492 |
| RNHCOO- | -398.373866 | -476.957550 | -437.668404 | -552.181025 | -512.886303 | -552.152957 | -437.665671 |
| | | | | G3B3 | | | |
| RNH2 | -210.254405 | -288.814147 | -249.536260 | -364.001327 | -324.720489 | -363.980292 | -249.533892 |
| RNH3+ | -210.603832 | -289.171393 | -249.888067 | -364.363228 | -325.078604 | -364.343459 | -249.887800 |
| RNHCOO- | -398.231714 | -476.790663 | -437.513946 | -551.985344 | -512.703472 | -551.957745 | -437.511349 |
| | | | | G3 | | | |
| RNH2 | -210.250576 | -288.807875 | -249.531779 | -363.993311 | -324.713217 | -363.972160 | -249.528532 |
| RNH3+ | -210.599323 | -289.165154 | -249.882834 | -364.355690 | -325.071611 | -364.335783 | -249.882505 |
| RNHCOO- | -398.223013 | -476.780207 | -437.504372 | -551.973497 | -512.692364 | -551.946379 | -437.501725 |

Table B.12: Gaussian output of the ideal gas relative gibbs free energies (in Hartree) of the most stabe conformer of the neutral ($RNH_2$), protonated ($RNH_3^+$) and carbamate forms ($RNHCO_2^-$) of th each amine using different QM method. The values were used in calculation of the data in table B.5 and table B.6. The calculation were performed at $P^0$=1.0 bar and T=353.15 K. .

| | MEA | AMP | 1AP | AMPD | SAPD | 2AEE | 2AP |
|---|---|---|---|---|---|---|---|
| | | | | G4 | | | |
| RNH2 | -210.291573 | -288.864510 | -249.579953 | -364.064207 | -324.776866 | -364.043229 | -249.577711 |
| RNH3+ | -210.641042 | -289.221725 | -249.930232 | -364.426097 | -325.135037 | -364.406351 | -249.931607 |
| RNHCOO- | -398.300605 | -476.872255 | -437.589271 | -552.079063 | -512.791252 | -552.051620 | -437.586621 |
| | | | | CBS-QB3 | | | |
| RNH2 | -210.073119 | -288.541081 | -249.309049 | -363.684870 | -324.449739 | -363.664803 | -249.306766 |
| RNH3+ | -210.421795 | -288.897567 | -249.660114 | -364.045834 | -324.807194 | -364.026234 | -249.659884 |
| RNHCOO- | -397.921436 | -476.388415 | -437.157685 | -551.539627 | -512.303866 | -551.512808 | -437.155025 |
| | | | | CBS-APNO | | | |
| RNH2 | -210.328138 | -288.911709 | -249.622636 | -364.127522 | -324.833915 | -364.106385 | -249.619204 |
| RNH3+ | -210.676517 | -289.268928 | -249.973340 | -364.489009 | -325.192247 | -364.469566 | -249.973097 |
| RNHCOO- | -398.376624 | -476.960724 | -437.671403 | -552.184415 | -512.889408 | -552.156262 | -437.668684 |
| | | | | G3B3 | | | |
| RNH2 | -210.256725 | -288.816925 | -249.538828 | -364.004299 | -324.723244 | -363.983418 | -249.536458 |
| RNH3+ | -210.606191 | -289.174227 | -249.890679 | -364.366221 | -325.081378 | -364.346408 | -249.890413 |
| RNHCOO- | -398.234473 | -476.793856 | -437.516950 | -551.988644 | -512.706620 | -551.961032 | -437.514366 |
| | | | | G3 | | | |
| RNH2 | -210.252955 | -288.810661 | -249.534411 | -363.996287 | -324.715984 | -363.975265 | -249.531108 |
| RNH3+ | -210.601694 | -289.167994 | -249.885459 | -364.358648 | -325.074409 | -364.338764 | -249.885129 |
| RNHCOO- | -398.225790 | -476.783411 | -437.507392 | -551.976828 | -512.695555 | -551.949712 | -437.504756 |

Table B.13: Gaussian output of the ideal gas relative gibbs free energies (in Hartree) of the small molecules using different QM method. The values were used in calculation of the data in table B.5 and table B.6. The calculation were performed at $P^0$=1.0 bar and T=298.15-353.15 K. .

| | $HCO_3^-$ | $H_2O$ | $CO_2$ |
|---|---|---|---|
| | | T = 298.15 K | |
| G4 | -264.40865 | -76.414912 | -188.555973 |
| CBS-QB3 | -264.187558 | -76.355139 | -188.392774 |
| CBS-APNO | -264.461903 | -76.428200 | -188.594605 |
| G3B3 | -264.363493 | -76.402061 | -188.525095 |
| G3 | -264.35775 | -76.399650 | -188.520977 |
| | | T = 313.15 K | |
| G4 | -264.410181 | -76.415996 | -188.557199 |
| CBS-QB3 | -264.189089 | -76.356222 | -188.394001 |
| CBS-APNO | -264.463424 | -76.429280 | -188.595826 |
| G3B3 | -264.365028 | -76.403179 | -188.526326 |
| G3 | -264.359275 | -76.400731 | -188.522202 |
| | | T = 333.15 K | |
| G4 | -264.412246 | -76.417454 | -188.558849 |
| CBS-QB3 | -264.191155 | -76.357681 | -188.395653 |
| CBS-APNO | -264.465475 | -76.430734 | -188.597471 |
| G3B3 | -264.367099 | -76.404683 | -188.527984 |
| G3 | -264.361331 | -76.402186 | -188.523852 |
| | | T = 353.15 K | |
| G4 | -264.414337 | -76.418928 | -188.560517 |
| CBS-QB3 | -264.193246 | -76.359155 | -188.397323 |
| CBS-APNO | -264.467552 | -76.432204 | -188.599133 |
| G3B3 | -264.369196 | -76.406202 | -188.529660 |
| G3 | -264.363414 | -76.403657 | -188.525519 |

# Appendix C

# Supporting Information: Prediction of Alkanolamine pKa Values by Combined Molecular Dynamics Free Energy Simulations and ab Initio Calculations

Table C.1: The raw intrinsic hydration free energies (in kJ·mol$^{-1}$) of the neutral forms of the 29 alkanolamines of this study from different charge models and from SMD continuum solvent simulations at $T = 298.15$ K and $P = 1.0$ bar.

| | RESP | | | | |
|---|---|---|---|---|---|
| amine | HF/6-31G* | B3LYP | MP2-TZ+SCRF | AM1-BCC | SMD |
| MEA | -30.79 | -27.07 | -29.8 | -28.93 | -31.72 |
| 3-AP | -30.52 | -26.05 | -28.12 | -32.35 | -26.93 |
| EDA | -38.59 | -34.37 | -39.50 | -35.60 | -33.17 |
| PA | -21.33 | -18.19 | -20.63 | -14.06 | -15.60 |
| 2-MPA | -15.09 | -11.30 | -14.99 | -13.66 | -11.44 |
| AMP | -33.36 | -30.43 | -33.39 | -24.6 | -29.17 |
| AMPD | -56.48 | -51.28 | -52.9 | -44.82 | -43.12 |
| AEPD | -52.16 | -49.21 | -53.38 | -41.19 | -37.75 |
| 2-AP | -38.11 | -33.47 | -36.32 | -26.72 | -31.58 |
| DEA | -47.3 | -42.28 | -45.91 | -43.26 | -47.52 |
| 2AEE | -29.74 | -26.56 | -31.82 | -42.44 | -40.6 |
| 2DIPA | -14.57 | -12.86 | -18.3 | -11.08 | -10.15 |
| DIPA | -45.22 | -40.94 | -46.61 | -38.779 | -46.68 |
| MDEA | -40.95 | -34.29 | -36.15 | -39.23 | -31.05 |
| N-CHEA | -25.06 | -22.23 | -26.05 | -25.19 | -26.53 |
| SAPD | -50.52 | -45.27 | -47.44 | -46.71 | -44.61 |
| TBAE | -18.3 | -16.45 | -21.13 | -21.44 | -24.77 |
| THMAM | -76.27 | -71.97 | -68.99 | -57.24 | -62.09 |
| 3-DMAP | -15.28 | -13.24 | -18.75 | -24.01 | -16.32 |
| DMIPA | 2.62 | 3.31 | 1.57 | -9.12 | -6.06 |
| T-BDEA | -43.84 | -39.08 | -21.13 | -32.33 | -31.1 |
| TREA | 5.94 | 6.34 | 4.03 | 7.79 | -2.74 |
| 1AP | -32.96 | -29.68 | -32.52 | -27.08 | -29.78 |
| MAE | -18.99 | -14.99 | -15.85 | -25.29 | -30.23 |
| EAE | -24.09 | -20.66 | -22.11 | -24.32 | -17.2 |
| IPAE | -20.47 | -17.54 | -20.1 | -22.52 | -19.76 |
| MPAE | -18.13 | -15.74 | -16.95 | -19.3 | -11.21 |
| IBAE | -19.45 | -15.98 | -16.02 | -21.23 | -27.68 |
| EAMP | -25.71 | -19.89 | -24.91 | -19.26 | -16.88 |

Table C.2: The raw intrinsic hydration free energies (in kJ·mol$^{-1}$) of the protonated ($RNH_3^+$) forms of the 29 alkanolamines of this study from different charge models and from SMD continum solvent simulations at $T = 298.15$ K and $P = 1.0$ bar. The value of the Galvani potential for TIP3P water[261, 251] (-48.24 kJ·mol$^{-1}$) should be subtracted from the raw SMD values for comparison purposes.

| | RESP | | | | |
|---|---|---|---|---|---|
| amine | HF/6-31G* | B3LYP | MP2-TZ+SCRF | AM1-BCC | SMD |
| MEA | -239.86 | -237.57 | -243.18 | -246.93 | -290.07 |
| 3-AP | -218.05 | -216.29 | -222.98 | -227.37 | -269.22 |
| EDA | -225.99 | -222.7 | -231.07 | -233.00 | -275.69 |
| PA | -222.14 | -218.93 | -235.98 | -234.01 | -286.49 |
| 2-MPA | -215.24 | -211.47 | -229.8 | -228.13 | -281.14 |
| AMP | -222.05 | -216.09 | -226.45 | -223.6 | -270.38 |
| AMPD | -229.95 | -221.62 | -227.79 | -229.16 | -264.27 |
| AEPD | -218.22 | -212.35 | -217.50 | -222.35 | -257.13 |
| 2-AP | -232.91 | -229.51 | -236.64 | -233.86 | -278.63 |
| DEA | -213.28 | -208.1 | -207.33 | -213.99 | -248.44 |
| 2AEE | -216.08 | -213.07 | -223.77 | -227.13 | -262.57 |
| 2DIPA | -158.3 | -152.28 | -156.27 | -153.25 | -216.76 |
| DIPA | -198.66 | -193.21 | -193.19 | -190.684 | -245.23 |
| MDEA | -199.84 | -195.19 | -192.56 | -191.47 | -238.66 |
| N-CHEA | -187.64 | -179.66 | -189.3 | -186.75 | -237.47 |
| SAPD | -236.36 | -230.24 | -234.27 | -241.74 | -273.28 |
| TBAE | -184.80 | -179.84 | -187.22 | -188.06 | -243.31 |
| THMAM | -235.58 | -224.43 | -225.93 | -232.68 | -258.88 |
| 3-DMAP | -174.24 | -173.21 | -173.18 | -174.78 | -227.04 |
| DMIPA | -174.15 | -173.01 | -179.83 | -173.55 | -242.86 |
| T-BDEA | -174.28 | -166.5 | -168.5 | -168.45 | -229.38 |
| TREA | -164.02 | -160.55 | -169.56 | -162.44 | -231.43 |
| 1AP | -232.91 | -229.67 | -237.16 | -238.23 | -284.80 |
| MAE | -212.62 | -210.71 | -213.99 | -214.95 | -266.18 |
| EAE | -201.41 | -200.1 | -203.41 | -204.07 | -256.79 |
| IPAE | -193.42 | -188.52 | -195.73 | -194.72 | -250.00 |
| MPAE | -186.9 | -180.61 | -188.13 | -189.32 | -241.81 |
| IBAE | -187.77 | -183.99 | -193.15 | -193.77 | -248.04 |
| EAMP | -188.24 | -182.16 | -189.8 | -185.25 | -241.25 |

Note that SMD values for the hydration free energy of charged species are absolute and include the surface contribution. For the FF simulations, the values reported here are intrinsic values and the Galvani surface potential of TIP3P water (-48.25 $kJ \cdot mol^{-1}$) must be added before comparing with the SMD values.

# Appendix D

# Supporting Information for: Force–Field–Based Computational Study of the Thermodynamics of a Large Set of Aqueous Alkanolamine Solvents for Post–Combustion $CO_2$ Capture

Table D.1: Coefficients of the fit to $\frac{\Delta G^{IG}}{RT} = A^0 + B^0/T + C^0 ln(T)$ of the ideal gas reaction free energy of the deprotonation reaction $RNH_3^+ + H_2O{=}RNH_2{+}H_3O^+$. $R^2$ values are smaller than 0.001 in all cases.

| **Amine** | $A^0$ | $B^0$ | $C^0$ |
|---|---|---|---|
| 1AB | -1.7709 | 28971.9471 | 0.1095 |
| 1AP | -1.639 | 28539.283 | 0.0798 |
| 2AB | -1.7845 | 29823.7425 | 0.1168 |
| 2AEE | -2.1655 | 33274.8689 | -0.364 |
| 2AP | -2.0784 | 29344.3398 | 0.1456 |
| 2DIPA | -1.7133 | 37312.6541 | 0.0511 |
| 2MPA | -0.6631 | 28084.1253 | -0.0903 |
| 2PIPE | -3.2131 | 36526.0553 | 0.2995 |

*Continued on next page*

Table D.1 – *Continued from previous page*

| **Amine** | $A^0$ | $B^0$ | $C^0$ |
|---|---|---|---|
| 2PIPM | 3.7909 | 33810.3877 | -0.7983 |
| 3AP | -2.4697 | 31484.7204 | 0.1493 |
| 3DMAP | -1.8628 | 36037.8328 | 0.1495 |
| 3PIPM | -0.658 | 35640.9672 | -0.3225 |
| 4AB | -1.422 | 32993.7242 | -0.0429 |
| 4PIPM | 3.5531 | 34186.2686 | -0.8755 |
| AEPD | -0.9279 | 31844.7058 | 0.3375 |
| AMPD | -0.5097 | 31910.1481 | -0.147 |
| AMP | -2.7791 | 30396.15 | 0.265 |
| DA | -1.9806 | 31670.7906 | 0.0193 |
| DEA | -2.4838 | 33911.4959 | 0.1502 |
| DIPA | -5.4594 | 35309.6218 | 0.5354 |
| DMIPA | -0.9796 | 33850.3361 | -0.0601 |
| EAE | -2.4362 | 32557.5202 | 0.2104 |
| EAMP | -1.9331 | 34576.7974 | 0.1778 |
| EDA | 1.1834 | 31070.4922 | -0.5132 |
| IBAE | -2.4934 | 33472.5984 | 0.2381 |
| IPAE | 4.3804 | 33243.2002 | -0.8523 |
| IPA | -0.8489 | 28098.6201 | -0.0492 |
| MAE | -2.4472 | 31399.6998 | 0.2024 |
| MDEA | -3.0616 | 35521.1045 | 0.1839 |
| MEA | -1.6917 | 27821.1662 | 0.0767 |
| MPAE | -2.0906 | 34139.022 | 0.1288 |
| nCHEA | -1.4521 | 34601.234 | 0.0355 |
| nCPEA | -2.0814 | 31332.7732 | 0.1513 |
| nCPnEA | -2.9696 | 34069.1829 | 0.2134 |
| PA | -2.25 | 27654.6742 | 0.1466 |
| SAPD | -2.0719 | 30854.522 | 0.0791 |
| TBAE | -2.4516 | 34438.9691 | 0.2024 |
| TBA | -1.218 | 29398.4886 | 0.0057 |
| tBDEA | 20.0224 | 36925.7149 | -3.1926 |
| TREA | -416.4317 | 55625.1955 | 60.8012 |
| 12HEPP | -1.6905 | 31977.1237 | 0.249 |
| 1DEA2P | -3.2134 | 36267.8139 | 0.3045 |
| 1DMA2P | -2.7259 | 34097.9319 | 0.2681 |

*Continued on next page*

Table D.1 – *Continued from previous page*

| **Amine** | $A^0$ | $B^0$ | $C^0$ |
|---|---|---|---|
| 1M2PPE | -3.8139 | 37412.6123 | 0.4305 |
| 1PE | -2.908 | 35620.9668 | 0.2847 |
| 1PP | -3.4169 | 37804.3396 | 0.3578 |
| 3APD | -3.5509 | 31492.0037 | 0.3712 |
| 3DEA1P | -5.662 | 37969.4525 | 0.6806 |
| 3MDA1P | -3.442 | 36112.2929 | 0.3827 |
| 3PPE | -4.6577 | 36628.8977 | 0.6086 |
| 4IPB | -3.7798 | 36969.628 | 0.355 |
| 5AP | -0.4463 | 34626.3821 | -0.6294 |
| 6AH | -1.9823 | 34627.7249 | -0.5397 |
| BAE | -2.2562 | 33425.9771 | 0.1656 |
| BA | -1.1995 | 28090.2011 | -0.0275 |
| DEA12PD | -4.1105 | 36473.3663 | 0.4616 |
| DEAB | -3.8251 | 38308.543 | 0.4021 |
| DEAEEO | -3.7242 | 40395.0125 | -0.14 |
| DMA12PD | -4.8047 | 34753.1136 | 0.6043 |
| DMA22DP | -4.3401 | 36757.7882 | 0.4704 |
| DMA2M1P | -2.4766 | 35794.0183 | 0.2194 |
| DMAH | -3.6662 | 37364.8295 | 0.4409 |
| EDEA | -2.7973 | 36683.4952 | 0.1496 |
| DEEA | -2.5767 | 35750.5359 | 0.1973 |
| IBA | -0.7848 | 28091.3383 | -0.0689 |
| IPAP | -9.4752 | 36371.7638 | 1.2319 |
| PA2 | -0.8129 | 28332.1993 | -0.0843 |
| PAE | -2.9101 | 33083.4722 | 0.2839 |
| PRLD12PD | -5.046 | 36389.4178 | 0.5256 |
| PRYE | -2.3462 | 34981.3927 | 0.2237 |
| SBA | -1.1829 | 28871.283 | 0.0089 |
| TEA | -2.7899 | 36083.7427 | 0.6225 |
| TMPOL | -1.3739 | 34774.0414 | -0.0894 |
| TRC | -2.963 | 33488.7853 | 0.6594 |

Table D.2: Coefficients of the fit to $\frac{\Delta G^{IG}}{RT} = A^0 + B^0/T + C^0 ln(T)$ of the ideal gas reaction free energy of the carbamate reversion reaction $RNHCO_2^-$ + $H_2O$ = $RNH_2$+$HCO_3^-$. $R^2$ values are smaller than 0.001 in all cases.

| **Amine** | $A^0$ | $B^0$ | $C^0$ |
|---|---|---|---|
| 1AB | -8.8006 | 5984.7715 | 0.8286 |
| 1AP | -8.6156 | 5751.163 | 0.813 |
| 2AB | -45.7933 | 7440.4122 | 6.2814 |
| 2AEE | -9.2782 | 7063.7404 | 0.2731 |
| 2AP | -8.6904 | 5661.3724 | 0.8554 |
| 2MPA | -11.2721 | 1741.3204 | 1.394 |
| 2MPIP | -13.8762 | 3181.1511 | 1.7907 |
| 2PIPE | -15.4999 | 7219.5487 | 1.7615 |
| 2PIPM | -9.9054 | 5975.3381 | 0.8838 |
| 3AP | -11.2186 | 6385.3666 | 1.1626 |
| 3PIPM | -10.6277 | 8106.7717 | 0.8194 |
| 4AB | -11.5565 | 5592.4179 | 1.2541 |
| 4PIPM | -12.9709 | 4840.6054 | 1.6782 |
| AEPD | -7.985 | 7733.0638 | 0.5434 |
| AMPD | -7.8625 | 8217.2526 | 0.4601 |
| AMP | -9.4659 | 5547.8388 | 0.8911 |
| DA | -5.3486 | 1439.4713 | 0.5532 |
| DEA | -8.3226 | 11189.1564 | 0.5906 |
| DIPA | -9.2112 | 11548.7737 | 0.7007 |
| EAE | -11.6103 | 6746.0512 | 1.189 |
| EAMP | -11.4599 | 4369.0695 | 0.9831 |
| EDA | -18.8288 | 3174.6189 | 2.4044 |
| IBAE | -11.2913 | 7420.9313 | 1.2404 |
| IPAE | -5.3182 | 6275.5327 | 0.2368 |
| IPA | -10.9208 | 832.4404 | 1.3563 |
| MAE | -11.0349 | 6525.5853 | 1.2259 |
| MEA | -8.2703 | 5640.0695 | 0.7686 |
| MPAE | -11.4999 | 7135.4392 | 1.1624 |
| nCHEA | -17.4203 | 7152.1889 | 2.053 |
| nCPEA | -11.8382 | 6656.6602 | 1.2693 |
| nCPnEA | -12.1726 | 6682.1417 | 1.2874 |
| PA | -11.242 | 1188.0222 | 1.3777 |

*Continued on next page*

Table D.2 – *Continued from previous page*

| **Amine** | $A^0$ | $B^0$ | $C^0$ |
|---|---|---|---|
| SAPD | -8.4162 | 7619.9573 | 0.7408 |
| TBAE | -12.068 | 4475.2118 | 1.0949 |
| TBA | -8.2227 | 473.7842 | 0.6201 |
| 4IPB | -15.8751 | 5357.6517 | 1.8391 |
| 5AP | -51.1472 | 9253.0437 | 6.5924 |
| 6AH | -11.629 | 9195.0102 | 0.5305 |
| BAE | -24.0521 | 7742.878 | 3.0328 |
| BA | -17.0813 | 1680.4657 | 2.2363 |
| IBA | -10.9873 | 1727.3807 | 1.3522 |
| IPAP | -14.7675 | 6219.5837 | 1.7549 |
| PA2 | -16.5328 | 1785.8608 | 2.1546 |
| PAE | -16.3061 | 7291.6771 | 1.9508 |
| SBA | -10.4223 | 1168.775 | 1.3237 |
| TMPOL | -19.6017 | -19.4552 | 2.3569 |
| TRC | -11.9189 | 15789.4523 | 0.9495 |

Table D.3: Coefficients of the fit to $\frac{\mu_i{}^{res\infty}}{RT} = a^{res} + b^{res}/T + c^{res}ln(T)$ for the small molecules.

| **molecule/ion** | $a^{res}$ | $b^{res}$ | $c^{res}$ | $R^2$ |
|---|---|---|---|---|
| $CO_2$ | 79.1899 | -4499.66 | -11.1688 | 0.0044 |
| $H_2O$ | 27.2591 | -5988.09 | -3.15944 | 0.0013 |
| $HCO_3^-$ | -99.6984 | -48119.3 | 17.9077 | 0.0337 |
| $H_3O^+$ | 124.002 | -59320.3 | -15.7999 | 0.0330 |

Table D.4: Coefficients of the fit to $\frac{\mu_i{}^{res\infty}}{RT} = a^{res} + b^{res}/T + c^{res}ln(T)$ of the neutral amines considered in this work.

| **Amine** | $a^{res}$ | $a^{res}$ | $a^{res}$ | $\mathbf{R}^2$ |
|---|---|---|---|---|
| 1AB | 210.4576 | -16073.2359 | -29.3384 | 0.0424 |
| 1AP | 71.0732 | -9044.3069 | -9.0724 | 0.0225 |
| 2AB | 205.8978 | -15512.5395 | -28.7641 | 0.0109 |
| 2AEE | 189.0121 | -17453.9019 | -25.7452 | 0.0525 |
| 2AP | 181.3051 | -14317.0121 | -25.2698 | 0.0659 |

*Continued on next page*

Table D.4 – *Continued from previous page*

| **Amine** | $a^{res}$ | $a^{res}$ | $a^{res}$ | $\mathbf{R}^2$ |
|---|---|---|---|---|
| 2DIPA | 403.1422 | -23780.8268 | -57.5741 | 0.4576 |
| 2MPA | 183.6791 | -12966.5084 | -25.5579 | 0.0019 |
| 2PIPE | 782.7360 | -43647.8031 | -113.5969 | 0.6021 |
| 2PIPM | 279.7805 | -20204.1674 | -39.3299 | 0.0623 |
| 3AP | -30.6572 | -4442.0201 | 5.7385 | 0.1245 |
| 3DMAP | 355.1848 | -22688.7714 | -50.6598 | 0.2676 |
| 3PIPM | 197.6844 | -17725.4382 | -26.8807 | 0.0042 |
| 4AB | 126.5239 | -12075.7200 | -17.3699 | 0.2605 |
| 4PIPM | 151.3932 | -15822.4896 | -19.9879 | 0.0864 |
| AEPD | 212.8097 | -18754.6764 | -29.2756 | 0.0357 |
| AMPD | 154.9861 | -16079.7149 | -20.8482 | 0.0464 |
| AMP | 134.5980 | -12035.5836 | -18.2805 | 0.0154 |
| DA | 242.9101 | -16007.6894 | -34.0247 | 0.0059 |
| DEA | 145.4630 | -15524.5142 | -19.4967 | 0.4645 |
| DIPA | 262.4441 | -21098.2889 | -36.3091 | 0.0441 |
| DMIPA | 191.0841 | -13217.0023 | -26.4091 | 0.0115 |
| EAE | 165.7390 | -13809.3166 | -22.6601 | 0.0112 |
| EAMP | 110.6176 | -10561.5717 | -14.4915 | 0.5318 |
| EDA | 68.6756 | -10621.8368 | -8.3261 | 0.0087 |
| IBAE | 218.0455 | -16463.9598 | -30.0964 | 0.0328 |
| IPAE | 160.9893 | -13750.7891 | -21.7777 | 0.0167 |
| IPA | 201.6689 | -13770.9357 | -28.2912 | 0.0039 |
| MAE | 181.9803 | -14354.8711 | -25.2710 | 0.0073 |
| MDEA | 161.4050 | -14883.1149 | -22.0024 | 0.1014 |
| MEA | 140.3623 | -12223.8270 | -19.4521 | 0.0359 |
| MPAE | 116.8421 | -10958.8731 | -15.4626 | 0.2835 |
| nCHEA | 305.5471 | -21497.1145 | -42.7842 | 0.0441 |
| nCPEA | 171.4751 | -13743.9572 | -23.5932 | 0.0721 |
| nCPnEA | 160.7804 | -14406.0214 | -21.5765 | 0.0458 |
| PA | 185.4105 | -12929.0773 | -25.9232 | 0.0043 |
| SAPD | 111.3119 | -13980.3092 | -14.5841 | 0.0290 |
| TBAE | 244.9174 | -17733.2481 | -34.0476 | 0.0627 |
| TBA | 219.5646 | -14663.9893 | -30.7945 | 0.0024 |
| tBDEA | 232.2342 | -18328.2130 | -32.1963 | 0.0693 |
| TREA | 289.3663 | -18236.0776 | -40.6017 | 0.0017 |

*Continued on next page*

Table D.4 – *Continued from previous page*

| **Amine** | $a^{res}$ | $a^{res}$ | $a^{res}$ | $\mathbf{R}^2$ |
|---|---|---|---|---|
| 12HEPP | 0.0000 | -0.0000 | -0.0000 | 0.0000 |
| 1DEA2P | 278.2159 | -18612.1331 | -38.9590 | 0.0297 |
| 1DMA2P | 271.3263 | -18400.2172 | -38.1471 | 0.0477 |
| 1M2PPE | 972.6835 | -54851.1325 | -140.4900 | 6.7791 |
| 1PE | 248.6462 | -17969.9730 | -34.6375 | 0.0391 |
| 1PP | 449.6205 | -28363.7239 | -63.9835 | 0.6404 |
| 3DEA1P | 211.2548 | -16339.5569 | -28.9356 | 0.1829 |
| 3MDA1P | 154.1696 | -13064.6259 | -21.0567 | 0.3039 |
| 3PPE | 233.2995 | -19305.4523 | -31.9402 | 0.2136 |
| 4IPB | 521.7880 | -31045.3895 | -75.0021 | 0.7836 |
| 5AP | 189.4600 | -17287.8613 | -25.6866 | 0.0076 |
| 6AH | 246.0961 | -20165.1838 | -33.9294 | 0.0089 |
| BAE | 326.0884 | -21829.7309 | -45.9604 | 0.0145 |
| BA | 204.9936 | -14049.4511 | -28.6721 | 0.0098 |
| DEA12PD | 342.6799 | -23471.3487 | -48.2837 | 0.0417 |
| DEAB | 311.6800 | -21525.6692 | -43.4165 | 1.0433 |
| DEAEEO | 186.6435 | -17685.8268 | -24.6286 | 0.2180 |
| DMA12PD | 172.0676 | -15309.0986 | -23.4149 | 0.0307 |
| DMA22DP | 798.6723 | -44174.0627 | -115.4575 | 1.1717 |
| DMA2M1P | 185.6981 | -14142.7873 | -25.5217 | 0.0676 |
| DMAH | 281.4987 | -21856.7487 | -38.7805 | 0.0204 |
| EDEA | 133.6756 | -13680.5376 | -17.7377 | 0.1901 |
| DEEA | 417.7298 | -25937.1158 | -59.3312 | 0.9908 |
| IBA | 182.2697 | -12907.4863 | -25.3456 | 0.0099 |
| IPAP | 295.6218 | -20310.4799 | -41.6642 | 0.4899 |
| PA2 | 220.4286 | -14844.7744 | -30.8655 | 0.0071 |
| PAE | 253.9065 | -18145.3148 | -35.4871 | 0.0234 |
| PRLD12PD | 295.7216 | -22256.9582 | -41.2403 | 0.0052 |
| PRYE | 232.0390 | -17192.2640 | -32.2676 | 0.0309 |
| SBA | 194.0099 | -13553.4275 | -27.0278 | 0.0022 |
| TEA | 123.4115 | -15972.3180 | -16.0236 | 0.0405 |
| TMPOL | 252.6900 | -20781.6228 | -34.4284 | 0.0077 |
| TRC | -108.3534 | -9758.5817 | 18.7755 | 0.1275 |

Table D.5: Coefficients of the fit to $\frac{{\mu_i}^{res\infty}}{RT} = a^{res} + b^{res}/T + c^{res}ln(T)$ of the protonated amines considered in this work.

| **Amine** | $a^{res}$ | $b^{res}$ | $c^{res}$ | $\mathbf{R}^2$ |
|---|---|---|---|---|
| 1AB | 208.4933 | -41869.6063 | -28.4563 | 0.0903 |
| 1AP | 84.7962 | -36123.4917 | -10.4555 | 0.0969 |
| 2AB | 173.3823 | -39485.5929 | -23.3440 | 0.0521 |
| 2AEE | 51.1282 | -32901.2906 | -5.5572 | 0.0764 |
| 2AP | 84.4223 | -35616.0023 | -10.3967 | 0.0390 |
| 2DIPA | 280.2058 | -36589.4663 | -38.5251 | 0.0156 |
| 2MPA | 215.2401 | -41029.6299 | -29.7965 | 0.0162 |
| 2PIPE | 257.4210 | -37940.2993 | -35.5761 | 0.1894 |
| 2PIPM | 171.4724 | -35883.3810 | -22.8890 | 0.0081 |
| 3AP | 21.7710 | -31102.6887 | -1.5471 | 0.1745 |
| 3DMAP | 249.7019 | -35914.8412 | -34.9675 | 0.1786 |
| 3PIPM | 269.2084 | -39702.5271 | -37.4319 | 0.4821 |
| 4AB | 182.1690 | -38261.1348 | -24.8486 | 0.4884 |
| 4PIPM | -60.9870 | -25043.5132 | 11.1671 | 2.2221 |
| AEPD | 131.5062 | -37156.6117 | -16.7832 | 0.0655 |
| AMPD | 118.2720 | -37279.1308 | -15.0068 | 0.0539 |
| AMP | 148.8536 | -37798.6455 | -19.6830 | 0.0141 |
| DA | 223.2376 | -37362.0560 | -30.9622 | 0.0129 |
| DEA | 173.9547 | -38053.8957 | -23.2681 | 0.0363 |
| DIPA | 234.8420 | -40200.3544 | -31.7032 | 0.0240 |
| DMIPA | 184.5325 | -32771.1915 | -25.2982 | 0.0094 |
| EAE | 162.0187 | -35838.1692 | -21.7521 | 0.0144 |
| EAMP | 228.1947 | -37432.0148 | -31.0892 | 0.1015 |
| EDA | 174.8196 | -39559.6977 | -23.8700 | 0.0184 |
| IBAE | 268.4411 | -40270.3132 | -37.0630 | 0.0358 |
| IPAE | 198.7507 | -36960.2866 | -26.9015 | 0.0130 |
| IPA | 204.4520 | -40141.8467 | -28.3356 | 0.0121 |
| MAE | 133.3731 | -35231.7345 | -17.8338 | 0.0123 |
| MDEA | 118.2682 | -32784.4091 | -15.1167 | 0.0391 |
| MEA | 122.7887 | -38539.1442 | -16.3015 | 0.0081 |
| MPAE | 255.8795 | -39262.0001 | -35.1864 | 0.0196 |
| nCHEA | 334.4773 | -43223.8771 | -46.4862 | 0.0146 |
| nCPEA | 178.3916 | -35744.8311 | -24.0269 | 0.0150 |

*Continued on next page*

Table D.5 – *Continued from previous page*

| **Amine** | $a^{res}$ | $b^{res}$ | $c^{res}$ | $\mathbf{R}^2$ |
|---|---|---|---|---|
| nCPnEA | 301.0135 | -41836.8616 | -41.6981 | 0.0118 |
| PA | 170.6268 | -39024.1915 | -23.3825 | 0.0070 |
| SAPD | 155.5230 | -40292.4838 | -20.6687 | 0.0269 |
| TBAE | 253.3340 | -39098.8790 | -34.7262 | 0.0088 |
| TBA | 190.4882 | -38692.4586 | -26.0768 | 0.0183 |
| tBDEA | 227.3878 | -35993.6242 | -30.6283 | 0.0925 |
| TREA | 234.3821 | -34354.8356 | -32.3516 | 0.0159 |
| 12HEPP | 229.5047 | -37100.9425 | -31.5937 | 0.0264 |
| 1DEA2P | 199.9093 | -34183.3294 | -26.6598 | 0.0973 |
| 1DMA2P | 155.3352 | -33072.3241 | -20.7301 | 0.0102 |
| 1M2PPE | 309.4926 | -38193.8691 | -43.2394 | 0.1058 |
| 1PE | 206.5230 | -35070.8867 | -28.0201 | 0.0187 |
| 1PP | 70.8655 | -26536.2470 | -8.1215 | 0.5269 |
| 3DEA1P | 232.0149 | -34107.1037 | -31.6974 | 0.4378 |
| 3MDA1P | -159.1977 | -15975.7688 | 25.0783 | 0.5774 |
| 3PPE | 15.3116 | -27033.0175 | 0.4718 | 0.9537 |
| 4IPB | 408.2547 | -45116.0522 | -57.2888 | 1.1804 |
| 5AP | 720.6705 | -63814.3852 | -104.3024 | 0.3480 |
| 6AH | 604.3737 | -56066.4876 | -88.2549 | 5.8223 |
| BAE | 180.1525 | -36123.1724 | -24.1195 | 0.0103 |
| BA | 185.5792 | -39527.4476 | -25.4842 | 0.0207 |
| DEA12PD | 340.1534 | -42052.6703 | -47.3709 | 0.9826 |
| DEAB | 264.9119 | -34412.1806 | -36.8851 | 0.6176 |
| DEAEEO | 419.5276 | -43885.2591 | -59.1751 | 0.6087 |
| DMA12PD | 73.8921 | -30002.5383 | -8.9455 | 0.7154 |
| DMA22DP | -112.4257 | -17201.5428 | 18.5433 | 1.0505 |
| DMA2M1P | -259.1693 | -12306.0831 | 40.4442 | 5.6613 |
| DMAEOE | 96.5972 | -29267.0639 | -12.2415 | 0.0642 |
| DMAH | 244.7945 | -35378.6039 | -34.1408 | 3.7970 |
| EDEA | 186.1138 | -35037.3269 | -24.9723 | 0.0727 |
| DEEA | 150.0239 | -31818.6491 | -19.7207 | 0.2663 |
| IBA | 193.2756 | -39868.6826 | -26.6155 | 0.0235 |
| IPAP | 192.2776 | -34502.9251 | -26.0549 | 0.1849 |
| IPDEA | 507.0265 | -50216.6599 | -71.7737 | 0.4039 |
| MMOR | 160.7449 | -34000.2279 | -21.7330 | 0.0205 |

*Continued on next page*

Table D.5 – *Continued from previous page*

| **Amine** | $a^{res}$ | $b^{res}$ | $c^{res}$ | $\mathbf{R}^2$ |
|---|---|---|---|---|
| MOR | 143.4922 | -35898.8691 | -19.3428 | 0.0076 |
| MPP | 264.9223 | -38793.2962 | -36.9959 | 0.1543 |
| PA2 | 235.9420 | -41937.9335 | -32.7492 | 0.0117 |
| PAE | 223.6380 | -38403.2958 | -30.6079 | 0.0068 |
| PRLD12PD | 39.0800 | -28655.2194 | -3.0962 | 1.2876 |
| PRYE | 139.7385 | -32312.0522 | -18.3166 | 0.0248 |
| SBA | 218.8915 | -40576.2858 | -30.2688 | 0.0220 |
| TEA | 297.7615 | -42576.3363 | -41.1050 | 0.1435 |
| TMPOL | -547.8666 | -716.0436 | 83.0995 | 7.3983 |
| TRC | 213.5585 | -44795.3992 | -28.0414 | 0.2360 |

Table D.6: Coefficients of the fit to $\frac{{\mu_i}^{res\infty}}{RT} = a^{res} + b^{res}/T + c^{res}ln(T)$ of the carbamate form of the primary and secondary amines considered in this work.

| **Amine** | $a^{res}$ | $b^{res}$ | $c^{res}$ | $\mathbf{R}^2$ |
|---|---|---|---|---|
| 1AB | 78.5090 | -55391.5553 | -7.6030 | 0.0329 |
| 1AP | -408.1027 | -31799.1007 | 63.7690 | 4.6979 |
| 2AB | 59.0699 | -54280.9452 | -4.8050 | 0.0604 |
| 2AEE | 260.5727 | -67291.9908 | -34.4141 | 0.5913 |
| 2AP | 7.1245 | -51053.3996 | 2.5627 | 0.0409 |
| 2MPA | 94.1556 | -58486.1668 | -9.8468 | 0.0182 |
| 2PIPE | 173.3941 | -57880.1352 | -21.6250 | 0.1888 |
| 2PIPM | 149.2997 | -58433.3063 | -17.9581 | 0.0340 |
| 3AP | -25.5928 | -50648.5266 | 7.4424 | 0.8737 |
| 3PIPM | 668.0674 | -89854.8359 | -91.6848 | 4.0733 |
| 4AB | 368.3351 | -69923.3208 | -50.7193 | 0.8269 |
| 4PIPM | 2366.2316 | -168941.3290 | -343.8127 | 75.0574 |
| AEPD | 161.4551 | -58647.5839 | -19.6495 | 0.1287 |
| AMP | 157.1279 | -59025.7403 | -19.1432 | 0.1253 |
| AMPD | 16.9623 | -51344.7798 | 1.2168 | 0.5439 |
| DA | 116.0914 | -59292.0726 | -12.9911 | 0.0073 |
| DEA | -57.8792 | -45238.2151 | 12.0425 | 0.0301 |
| DIPA | 200.2722 | -57464.4487 | -25.5988 | 0.1413 |
| EAE | 100.7821 | -55302.7734 | -11.0512 | 0.0155 |

*Continued on next page*

Table D.6 – *Continued from previous page*

| **Amine** | $a^{res}$ | $b^{res}$ | $c^{res}$ | $\mathbf{R}^2$ |
|---|---|---|---|---|
| EAMP | 186.0125 | -59786.0822 | -23.2903 | 0.0067 |
| EDA | 38.8362 | -57200.4420 | -1.5928 | 0.0175 |
| IBAE | 149.2167 | -57865.5900 | -17.9239 | 0.0443 |
| IPA | 123.3613 | -55637.0559 | -14.3035 | 0.0104 |
| IPAE | 58.5788 | -56473.5938 | -4.7090 | 0.0074 |
| MAE | 131.3362 | -57455.7339 | -15.5789 | 0.0252 |
| MEA | 22.6664 | -52582.1056 | 0.2267 | 0.0760 |
| MPAE | 191.7098 | -58837.1893 | -24.2539 | 0.0096 |
| nCHEA | 185.3666 | -58774.7075 | -23.1786 | 0.0209 |
| nCPEA | 63.3273 | -51960.2725 | -5.6055 | 0.0313 |
| nCPnEA | 116.6365 | -54848.0269 | -13.2522 | 0.0082 |
| PA | 101.3030 | -59039.1347 | -10.9628 | 0.0015 |
| SAPD | 98.9386 | -56594.6597 | -10.7247 | 0.2964 |
| TBAE | 147.1174 | -57285.9022 | -17.6530 | 0.0051 |
| TBA | 115.4493 | -59831.8006 | -12.8857 | 0.0085 |
| 4IPB | 236.8104 | -64156.9904 | -29.8728 | 1.8856 |
| 5AP | -138.6563 | -46649.3239 | 24.2461 | 4.6510 |
| 6AH | 1033.3136 | -104095.9295 | -147.6718 | 6.4134 |
| BAE | 165.2381 | -58327.9238 | -20.2168 | 0.6386 |
| BA | 152.6880 | -61542.3649 | -18.3711 | 0.5293 |
| IBA | 125.4644 | -60258.8584 | -14.3242 | 0.4841 |
| IPAP | 485.5124 | -74736.1711 | -67.0451 | 1.9948 |
| PA2 | 167.7751 | -62495.9731 | -20.3998 | 0.5478 |
| PAE | 175.3433 | -59554.5621 | -21.7655 | 0.6613 |
| SBA | 122.1271 | -59720.1183 | -13.8274 | 0.5650 |
| TMPOL | 242.3183 | -67122.9008 | -30.5258 | 0.9078 |
| TRC | -59.5351 | -45482.3847 | 13.0306 | 2.2549 |

Table D.7: Coefficients of the fit to $-\ln K = A + B/T + Cln(T)$ of the deprotonation reaction $RNH_3^+ + H_2O$=$RNH_2$+$H_3O^+$.

| **Amine** | $A = A^0 + A^{res}$ | $B = B^0 + B^{res}$ | $C = C^0 + C^{res}$ |
|---|---|---|---|
| 1AB | 96.9363 | 1436.1075 | -13.4131 |
| 1AP | 81.3809 | 2286.2578 | -11.1776 |
| 2AB | 127.4739 | 464.5859 | -17.9438 |

*Continued on next page*

Table D.7 – *Continued from previous page*

| **Amine** | $A = A^0 + A^{res}$ | $B = B^0 + B^{res}$ | $C = C^0 + C^{res}$ |
|---|---|---|---|
| 2AEE | 232.4613 | -4609.9524 | -33.1925 |
| 2AP | 191.5473 | -2688.88 | -27.368 |
| 2DIPA | 217.966 | -3210.9164 | -31.6384 |
| 2MPA | 64.5188 | 2815.0368 | -8.4922 |
| 2PIPE | 618.8448 | -22513.6585 | -90.3618 |
| 2PIPM | 208.8419 | -3842.6087 | -29.8797 |
| 3AP | 41.845 | 4813.179 | -5.2056 |
| 3DMAP | 200.363 | -4068.3074 | -28.1833 |
| 3PIPM | 24.5609 | 4285.8461 | -2.4118 |
| 4AB | 39.6758 | 5846.929 | -5.2047 |
| 4PIPM | 312.6762 | -9924.9178 | -44.671 |
| AEPD | 177.1185 | -3085.5689 | -24.7954 |
| AMPD | 132.9473 | -222.646 | -18.6289 |
| AMP | 79.7082 | 2827.0019 | -10.973 |
| DA | 114.4348 | -307.0528 | -15.6837 |
| DEA | 65.7674 | 3108.6674 | -8.7189 |
| DIPA | 118.8856 | 1079.4773 | -16.711 |
| DMIPA | 102.3149 | 72.3153 | -13.8115 |
| EAE | 98.027 | 1254.1628 | -13.3381 |
| EAMP | -22.7673 | 8115.0305 | 4.135 |
| EDA | -8.2177 | 6676.1431 | 2.3902 |
| IBAE | 43.8539 | 3946.7418 | -5.4358 |
| IPAE | 63.3619 | 3120.4877 | -8.369 |
| IPA | 93.1109 | 1137.3211 | -12.6453 |
| MAE | 142.9029 | -1055.6468 | -19.8753 |
| MDEA | 136.8181 | 90.1887 | -19.3423 |
| MEA | 112.6248 | 804.2734 | -15.7144 |
| MPAE | -44.3851 | 9109.939 | 7.2121 |
| nCHEA | 66.3606 | 2995.7866 | -8.903 |
| nCPEA | 87.745 | 1.4371 | -12.0555 |
| nCPnEA | -46.4598 | 8167.8131 | 7.6945 |
| PA | 109.2766 | 417.5784 | -15.0346 |
| SAPD | 50.4599 | 3834.4866 | -6.4768 |
| TBAE | 85.8747 | 2472.39 | -11.7595 |
| TBA | 124.6013 | 94.7479 | -17.3525 |

*Continued on next page*

Table D.7 – *Continued from previous page*

| **Amine** | $A = A^0 + A^{res}$ | $B = B^0 + B^{res}$ | $C = C^0 + C^{res}$ |
|---|---|---|---|
| tBDEA | 121.6117 | 1258.9161 | -17.4011 |
| TREA | -264.7046 | 18411.7435 | 39.9106 |
| 12HEPP | -134.4523 | 15745.8562 | 19.2022 |
| 1DEA2P | 171.8361 | -1493.1998 | -24.6352 |
| 1DMA2P | 210.0081 | -4562.1712 | -29.7894 |
| 1M2PPE | 756.1199 | -32576.8611 | -109.4606 |
| 1PE | 135.9581 | -610.3295 | -18.9732 |
| 1PP | 472.081 | -17355.3473 | -68.1447 |
| 3DEA1P | 70.3208 | 2404.7893 | -9.1981 |
| 3MDA1P | 406.6682 | -14308.7742 | -58.3928 |
| 3PPE | 310.0731 | -8975.7471 | -44.4439 |
| 4IPB | 206.4964 | -2291.9193 | -29.9988 |
| 5AP | -434.9139 | 27820.696 | 65.3459 |
| 6AH | -263.517 | 17196.8187 | 41.1453 |
| BAE | 240.4226 | -5612.7914 | -34.3158 |
| BA | 114.9578 | 235.9876 | -15.8559 |
| DEA12PD | 95.1589 | 1722.4779 | -13.0917 |
| DEAB | 139.6859 | -2137.1556 | -18.7698 |
| DEAEEO | -139.8654 | 13262.2348 | 21.766 |
| DMA12PD | 190.1137 | -3885.6567 | -26.5056 |
| DMA22DP | 1003.5008 | -43546.9417 | -146.1709 |
| DMA2M1P | 539.1337 | -19374.8959 | -78.387 |
| DMAH | 129.7809 | -2445.5253 | -16.8393 |
| EDEA | 41.5074 | 4708.0745 | -5.2563 |
| DEEA | 361.8721 | -11700.1408 | -52.0537 |
| IBA | 84.9522 | 1720.3246 | -11.4395 |
| IPAP | 190.6119 | -2768.001 | -27.0179 |
| PA2 | 80.4166 | 2093.1484 | -10.8411 |
| PAE | 124.1013 | 9.2432 | -17.2358 |
| PRLD12PD | 348.3385 | -10544.531 | -50.259 |
| PRYE | 186.6972 | -3231.0291 | -26.3678 |
| SBA | 70.6784 | 2561.9313 | -9.3906 |
| TEA | -80.397 | 9355.551 | 13.0634 |
| TMPOL | 895.9256 | -38623.7478 | -130.2578 |
| TRC | -228.132 | 15193.3928 | 34.8358 |

Table D.8: Coefficients of the fit to $-\ln K = A + B/T + Cln(T)$ of the carbamate reversion reaction $RNHCO_2^- + H_2O = RNH_2 + HCO_3^-$.

| **Amine** | $A = A^0 + A^{res}$ | $B = B^0 + B^{res}$ | $C = C^0 + C^{res}$ |
|---|---|---|---|
| 1AB | -3.8096 | 3171.8857 | 0.16034 |
| 1AP | 343.599 | -13625.0692 | -50.96066 |
| 1MPIP | -44.0773 | 4629.3353 | 5.98794 |
| 2AB | -25.9258 | 4077.7455 | 3.38994 |
| 2AEE | -207.7954 | 14770.5737 | 30.00904 |
| 2AP | 38.5317 | 266.5913 | -5.90986 |
| 2MPA | -48.7064 | 5129.7845 | 6.75004 |
| 2PIPE | 466.8839 | -20679.3031 | -69.14316 |
| 2PIPM | -6.3828 | 2073.2998 | 0.57924 |
| 3AP | -143.2396 | 10460.6211 | 20.52574 |
| 4AB | -380.327 | 21308.895 | 55.67084 |
| 4PIPM | -2354.7789 | 115828.8133 | 346.57194 |
| AEPD | -83.5864 | 5494.6882 | 11.98414 |
| AMPD | -136.9606 | 9032.0103 | 19.82204 |
| AMP | -18.782 | 2725.556 | 2.46014 |
| DA | -5.4867 | 2592.6089 | 0.58664 |
| DEA | 68.062 | -1228.3466 | -9.88146 |
| DIPA | -73.9954 | 5783.6608 | 11.05734 |
| EAE | -73.6098 | 6108.2454 | 10.64704 |
| EAMP | -213.8122 | 11462.3692 | 30.84904 |
| EDA | -115.9413 | 7621.7445 | 16.73734 |
| IBAE | -69.4208 | 6691.393 | 10.13524 |
| IPAE | -94.6479 | 6030.5986 | 13.82974 |
| IPA | 5.2121 | 1403.8774 | -1.15876 |
| MAE | -87.349 | 7495.2699 | 12.60104 |
| MEA | -17.5342 | 3867.2481 | 2.15734 |
| MPAE | -213.3252 | 12882.5535 | 31.02094 |
| nCHEA | -24.1973 | 2298.57 | 3.51454 |
| nCPEA | -30.65 | 2741.8670 | 4.34904 |
| nCPnEA | -94.9856 | 4992.9113 | 14.03014 |
| PA | -54.092 | 5166.8686 | 7.48444 |
| SAPD | -122.9981 | 8102.9867 | 17.94824 |
| TBAE | -41.2254 | 1896.6498 | 5.76744 |

*Continued on next page*

Table D.8 – *Continued from previous page*

| **Amine** | $A = A^0 + A^{res}$ | $B = B^0 + B^{res}$ | $C = C^0 + C^{res}$ |
|---|---|---|---|
| TBA | -31.0642 | 3510.3504 | 3.77834 |
| 4IPB | 142.1433 | -3661.8762 | -22.22286 |
| 5AP | 150.0037 | -3516.3277 | -22.27206 |
| 6AH | -925.8012 | 50994.4144 | 135.33964 |
| BAE | 9.8418 | 2109.8081 | -1.64386 |
| BA | -91.7314 | 7042.0833 | 13.00214 |
| IBA | -81.1416 | 6947.6453 | 11.39824 |
| IPAP | -331.6171 | 18514.1357 | 48.20324 |
| PA2 | -90.8357 | 7305.7962 | 12.75584 |
| PAE | -64.7031 | 6569.8392 | 9.29674 |
| SBA | -65.4957 | 5204.1956 | 9.19034 |
| TMPOL | -136.1879 | 4190.6311 | 19.52144 |
| TRC | -187.6845 | 9381.5555 | 27.76004 |

*Continued on next page*

Table D.9: Reaction enthalpy (in kJ/mol) at T=313.15K for the amine de-protonation (R1) and carbamate reversion (R2) reactions.

| **Amine** | $\Delta H^{deprot}$ | $\Delta H^{carb}$ |
|---|---|---|
| 1AB | 46.86 | 25.96 |
| 1AP | 48.11 | 19.4 |
| 2AB | 50.58 | 25.08 |
| 2AEE | 48.09 | 44.68 |
| 2AP | 48.9 | 17.6 |
| 2DIPA | 55.68 | t |
| 2MPA | 45.52 | 25.08 |
| 2PIPE | 48.08 | 8.09 |
| 2PIPM | 45.85 | 15.73 |
| 3AP | 53.57 | 33.53 |
| 3DMAP | 39.55 | t |
| 3PIPM | 41.91 | 91.11 |
| 4AB | 62.17 | 32.22 |
| 4PIPM | 33.79 | 60.69 |
| AEPD | 38.9 | 14.48 |
| AMPD | 46.65 | 23.49 |

*Continued on next page*

Table D.9 – *Continued from previous page*

| **Amine** | $\Delta H^{deprot}$ | $\Delta H^{carb}$ |
|---|---|---|
| AMP | 52.07 | 16.26 |
| DA | 38.28 | 20.03 |
| DEA | 48.55 | 15.52 |
| DIPA | 52.49 | 19.3 |
| DMIPA | 36.56 | t |
| EAE | 45.16 | 23.07 |
| EAMP | 56.71 | 14.98 |
| EDA | 49.29 | 19.79 |
| IBAE | 46.97 | 29.25 |
| IPAE | 47.74 | 14.13 |
| IPA | 42.38 | 14.69 |
| MAE | 42.97 | 29.51 |
| MDEA | 51.11 | t |
| MEA | 47.6 | 26.54 |
| MPAE | 56.97 | 26.34 |
| nCHEA | 48.09 | 9.96 |
| nCPEA | 31.4 | 11.47 |
| nCPnEA | 47.88 | 4.98 |
| PA | 42.62 | 23.47 |
| SAPD | 48.75 | 20.64 |
| TBAE | 51.17 | 0.75 |
| TBA | 45.97 | 19.35 |
| tBDEA | 55.77 | t |
| TREA | 49.17 | t |
| 12HEPP | 80.92 | t |
| 1DEA2P | 51.73 | t |
| 1DMA2P | 39.63 | t |
| 1M2PPE | 14.14 | t |
| 1PE | 44.33 | t |
| 1PP | 33.13 | t |
| 3DEA1P | 43.94 | t |
| 3MDA1P | 33.07 | t |
| 3PPE | 41.09 | t |
| 4IPB | 59.05 | 27.41 |
| 5AP | 61.17 | 28.75 |

*Continued on next page*

Table D.9 – *Continued from previous page*

| **Amine** | $\Delta H^{deprot}$ | $\Delta H^{carb}$ |
|---|---|---|
| 6AH | 35.85 | 71.61 |
| BAE | 42.68 | 21.82 |
| BA | 43.25 | 24.7 |
| DEA12PD | 48.41 | t |
| DEAB | 31.1 | t |
| DEAEEO | 53.6 | t |
| DMA12PD | 36.7 | t |
| DMA22DP | 18.51 | t |
| DMA2M1P | 43.0 | t |
| DMAH | 23.51 | t |
| EDEA | 52.83 | t |
| DEEA | 38.25 | t |
| IBA | 44.09 | 28.09 |
| IPAP | 47.33 | 28.43 |
| PA2 | 45.63 | 27.53 |
| PAE | 44.95 | 30.42 |
| PRLD12PD | 43.19 | t |
| PRYE | 41.79 | t |
| SBA | 45.75 | 19.34 |
| TEA | 43.77 | t |
| TMPOL | 18.01 | -15.98 |
| TRC | 35.62 | 5.72 |